Development and Characterisation of Next Generation Stylus for Micro Coordinate Measuring Machine

by

Mohd Anuar Bin Ismail

A thesis submitted in partial fulfilment of the requirement for the degree of
Doctor of Philosophy in Engineering

University of Warwick, School of Engineering
In collaboration, with
National Physical Laboratory United Kingdom

April 2017

Table of content

List of tables

List of figures

Acknowledgement

All thanks and praises to God the Almighty for His blessing that made this work possible and completed.

I would like to express my earnest gratitude to many people who have contribute to the completion of my PhD thesis. First and foremost, I must thanks to National Physical Laboratory (NPL), and my industrial Supervisor, Professor Richard Leach, a former principle research scientist in NPL, for providing me the opportunity to start my PhD research project and working with one of the world class research group in this field. Thanks Richard for your continuing advices and support throughout my PhD project.

Special thanks must also go to Dr James Claverley, my industrial supervisor in NPL. Thanks James, for your continuing support and guidance in technical knowledge, especially for your patience and enthusiasm in shaping me to become a researcher in this field.

I could not have navigated the academic requirements without the guidance of my academic supervisors. I would also like to thanks Professor Derek Chetwynd for your continuing guidance in this research project especially in ensuring that this works achieved certain level above the requirement set by the university, for the PhD study.

I would also like to express my gratitude to my colleagues from Surface metrology group, engineering measurement division, NPL, especially to Dr Claudiu Giusca, Dr Andrew Henning, Mrs Lakshmi Nimishakavi, Dr Christopher Jones, Dr Wenjuan Sun and Dr Giuseppe Moschetti. I would also like to thanks to my project collaborator from Taiwan, Professor Dong-Yea Sheu and Mr Kuo-Yu Tseng.

This work was funded by the NMS Engineering & Flow Metrology Research Programme, and through EMRP Project IND59.

My biggest thanks go to my family. To my mother, Hjh Rokiah Yusoff, without you, none of my success would be possible, and all of my brothers for your unconditional love and support. This thesis is dedicated to my late father, who is always in my heart.

And my deepest appreciation must go to my wife, Fatimatuzzahra Thaifor, whom I love, without you, this journey will not be able to reach to its final destination.

Declaration

The majority of this thesis, submitted to the University of Warwick for the degree of Doctor of Philosophy, is the work of the author alone. A few specific contributions of several colleagues at NPL and other external collaborators, which are properly referenced throughout the text, are specified here.

The set of micro- styli investigated (in section 5.2) were manufactured by Kuo-Yu Tseng (Institute of Mechatronic Engineering, National Taipei University of Technology, Taiwan). He also assisted on the development of the control software (section 5.3.5) and helped, in conducting preliminary performance testing (section 5.4) and the stylus testing (section 5.5 and section 5.6) for some of the micro-styli. The stylus holder (section 5.3.1) designed by Dong-Yea Sheu (Institute of Mechatronic Engineering, National Taipei University of Technology, Taiwan).

James Claverley and Andrew Henning (both NPL) contributed to the development of the concept of the sphericity measurement strategy (section 6.2) and to ideas for the preliminary investigation measurement (section 6.3.4). James Claverley also assisted in the preparation of the sample (section 6.3.2). Andrew Henning was also involved in the initial stage of the development of the stitching algorithm (section 6.4.2) especilaly in the concept and algorithm for stitched error.

Publications by the author

A list shown below is publications that were produced by the author during the period of registration For PhD study.

1) **M. A. Ismail**, J. D. Claverley, R. K. Leach, & D. G. Chetwynd, "Design considerations for the development of stylus systems for micro-CMMs," Eu**spen**'s 15th International Conference & Exhibition, 2015

2) **M. A. Ismail**, J. D. Claverley, A. J. Henning, R. K. Leach, & D. G. Chetwynd, "Strategy for the measurement of micro-spheres using coherence scanning interferometry," Eu**spen** Micro/Nano Manufacturing Workshop, 2015

3) **M. A. Ismail**, J. D. Claverley, A. J. Henning, R. K. Leach, & D. G. Chetwynd, "Measurement of micro-spheres using coherence scanning interferometery and data fusion techniques," Warwick Postgraduate symposium, school of Engineering, University of Warwick, 2016

4) **M. A. Ismail**, K-Y Tseng, J. D. Claverley, D-Y Sheu, D. G. Chetwynd, &, R. K. Leach, "Investigating mechanical characteristics of styli for micro-CMMs," Eu**spen**'s 16th International Conference & Exhibition, 2016

Abstract

Products are routinely being manufactured with features having dimensions below 50 µm, with consequent of increasing demand for micro-coordinate measuring machines (micro-CMMs) that have stylus systems with tip diameters of 10 µm or less. However, current commercially available micro-CMMs are unable to fulfil this demand reliably. Therefore, with this in mind, the development of a stylus system with a significantly smaller dimension and the potential to fulfil this demand is reported.

After an initial review of the current state of the art and the projected needs, this thesis examine in detail the design considerations and analytical modelling of stylus systems. A key factors affecting styli as their dimension is reduced down to the micrometre level are identified and discussed. Based on five important groups of theses influence factors, a new comprehensive set of design rules and analytical models is constructed and the relationship among these rules observed. Maintaining a stylus contact force that reliably detect the measured surface at reasonable operation speeds while having a sufficiently slender and strong stylus shaft become an issue of particular importance.

Experimental investigation of a set of prototype micro-styli is used both to demonstrate the effectiveness of the design rules and to compare different manufacturing methods that have been proposed elsewhere. The model underlying the design rules are shown to be generally consistent within existing uncertainty, except for anomalies with one of manufacturing process which is a combination process of Wire Electro-Discharge Grinding (WEDG) and micro-electrochemical (ECM) process for manufacturing of stylus shaft.

The surface quality of spherical form deviation of stylus tip is also a major factor in the uncertainty in the scale of measurement. Therefore, the final part of this work develops and demonstrate a new measurement technique for spherical form error of the micro-styli with tip diameter below than 10 µm. This methods employed a coherence scanning interferometry, together with new rotational referencing manipulation system and new technique of data fusion. Practical testing was conducted to 300 µm diameter sphere, with a typical uncertainty below 30 nm being obtained.

Abbreviations

CMMs	Coordinate Measuring Machines
micro-CMMs	Micro Coordinate Measuring Machines
NPL	National Physical Laboratory
TUE	Eindhoven University Of Technology,
METAS	Institute Of Metrology And Standardization Of Switzerland
PTB	Physikalisch-Technische Bundesanstalt, (National Metrology Institute Of Germany)
FIB	Focused Ion Beam
WEDG	Wire Electro-Discharge Grinding
OPED	One-Pulse Electro Discharge
ECM	Electrochemical Machine
micro-ECM	Micro Electrochemical Machine
RANSAC	Random Sample Consensus
CSI	Coherence Scanning Interferometer
NA	Numerical Aperture
FOV	Field Of View

Chapter 1: Introduction

1.1. Aim and motivation

A micro coordinate measuring machine (micro-CMM) is at the cutting edge of technology for 3D measurement in dimensional metrology. It is a tactile measuring instrument for millimetre and sub-millimetre range of dimensional measurement with sub-micrometre accuracy. It also offers better accuracy and accessibility to the measured workpiece compared to the optical-CMMs [1].

Over the last decade the main focus for micro-CMM research and development activities has been associated with their probing systems[2][3][4]. The detection mechanism of micro CMMs probes plays a major part in probing error and uncertainty in micro-CMM measurements. However, in recent years, with complex miniature products being manufactured in increasing volume, research in the field of micro-CMMs has focused on shrinking the dimensions of the stylus system itself. Demand for dimensional metrology of miniature products, with feature dimensions below 50 µm, is increasing, and currently available stylus systems for micro-CMMs are becoming unsuitable.

Therefore, the focuse of this thesis is upon developing the next-generation stylus system of micro-CMMs for fulfilling the increasing demand for miniature product. The **Thesis Aim** for this research work has been defined as:

> *"The aim of this study is to develop and characterize a contact stylus with a tip diameter below 10 µm that fit on any micro-CMM probing system and has appropriate aspect ratio to measure micro features*".

Based on this **Thesis Aim,** specific **Thesis Objectives** and **Research Questions** can be established**.**

1.2. Thesis Objectives

Several **Thesis Objectives** have been developed associated with the **Thesis Aim**. These **Thesis Objectives** will be discussed further in the following chapters and specific and relevant **Research Questions** will also be refined.

- ☐ ***Thesis Objective 1***: To design a new stylus for tactile probes with a stylus tip diameter less than 10 μm and investigate the required manufacturing techniques
- ☐ ***Thesis Objective 2***: To characterize the mechanical properties of the new stylus and hence verify the design.
- ☐ ***Thesis Objective 3***: To reduce measurement uncertainties by developing new technique for 3D spherical form measurement of micro-sphere.

1.3. Research approach

To achieve the **Thesis Aim** and **Thesis Objectives** outlined above, several strands of research are needed before the main questions can be studied properly. It is necessary to verify that the contact method of micro-CMM remains competitive for the area of 3D measurement of micrometre size products. The state of the art of micro-dimensional metrology and its limitations should also be established. Furthermore, the critical factors in designing next-generation styli need to be identified. Also, the current limitations of the methods of manufacturing and characterising the stylus system will be reviewed.

1.4. Thesis layout

Chapter 1 has defined the direction of the research work in this thesis by explaining the **Thesis Aim**, **Thesis Objective** and research approach. In Chapter 2, background information from a critical review of relevant literature is presented to provide a context to this research work. This includes the review of the currently available micro-CMMs probes, manufacturing techniques for stylus systems and a review of spherical form measurement of the sphere surfaces.

The technical work is first reported in Chapter 3. In this chapter, the critical factors have been determined and considered in designing the stylus system with tip diameter of sub-10 µm. Chapter 4 and Chapter 5 are dedicated to investigate the mechanical behaviour of the stylus system. In Chapter 4, based on the defined design consideration factors in Chapter 3, the relationship of the dimension of the stylus with several mechanical parameters have been studied and modelled. Chapter 5 will explain in detail the testing conducted to characterise mechanical behaviour of the stylus. As the testing of the stylus are conducted independently without fitting to the micro-probe and micro CMMs, the focus of this mechanical characterisation is to investigate the strength of the stylus shaft in a presence of forces. The experimental results, uncertainty evaluation and discussion of these testing will be reported later in the chapter.

In Chapter 6, a newly-invented technique and strategy for 3D spherical form measurement of micro sphere is reported. The details of the measurement, setup procedure and result are presented. This new measurement technique will lead to the better understanding of the issues when determining the spherical form deviation and uncertainty for stylus tip spheres with tip diameter of sub-10 µm range. The overall conclusions of the thesis, along with suggestions for future work, will be described in Chapter 7.

Chapter 2: Background and Literature review

2.1. Introduction

The aim of this chapter is to provide supporting information and a review on the current research work related to this project. The background knowledge of dimensional metrology and micro-CMMs will be described first. Then, the review of the research work related to the stylus of probing systems for micro-CMMs, the manufacturing routes of micro-styli and the sphericity measurement for characterisation of the surface condition of the stylus tip will be explained. At the end of the chapter, based on this review, the knowledge gaps will be specified and the **Research Questions** will be identified.

2.2. Dimensional metrology

Dimensional metrology has been defined in many of engineering, metrology and measurement related texts [1] [5][6][7][8]. In general, dimensional metrology is the science associated with length measurement. This includes linear displacement measurement, features size and shape measurement, coordinate measurement, angle measurement, form and roundness measurement, surface texture and areal topography measurement. Measurements taken in dimensional metrology should be traceable to the realisation of metre. The metre is defined as “the length of the path travelled by light in vacuum during a time interval of (1 /299792458) of a second” [9].

The coordinate measuring machine (CMM) is an important type of metrological instrument which is used widely in many fields of engineering, including automotive, manufacturing and aeronautic engineering. Its capability to collect coordinate data over a set of individual points and so perform shape, dimension and form measurement in 1D, 2D and 3D, has made it a popular choice among other coordinate measuring techniques in many fields. With the advancement of the technology, various types of CMM have been developed, such as tactile CMMs, multi sensor CMMs, non-tactile CMMs, portable arm CMMs and micro-CMMs.

2.3. Micro-CMMs

A micro coordinate measuring machine or micro-CMM is a small version of CMM. The concept of the micro-CMM was first proposed by a group of researchers from Japan [10] in 1996. Ideally, micro-CMMs are proposed to have accuracies in the range between tens of micrometres and hundreds of nanometres in x, *y*, and *z* direction. All major components of micro-CMM such as scales, actuators, table and probe system will have specifications scaled by perhaps 1/1000 or 1/100 if compared to traditional CMMs. The continued development of micro-CMM is essential due to increasing numbers of miniature industrial products. Thus, the needs of having three dimensional metrological instruments with accuracies in the nanometre range are becoming a crucial matter.

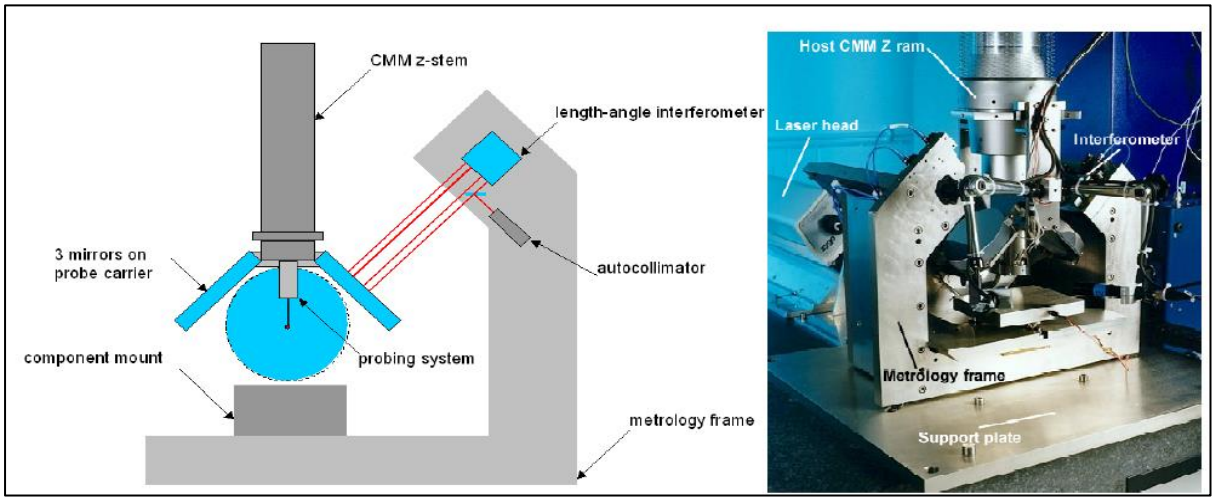

Figure 2. 1: NPL Small Volume CMM (SCMM) [11]

The rapid developments of micro-CMM design and technique have been successfully conducted by many groups of researchers. One of the earliest micro-CMMs was successfully developed in 1999 at the UK National Physical Laboratory (NPL) [11][12] and is known as the NPL Small Volume CMM (SCMM). The SCMM, as illustrated in Figure 2.1 is capable of measuring (50 x 50 x 50) mm working volume with a target uncertainty of 50 nm. It has been retrofitted to a conventional CMM and thus motion control, programming and data analysis are also synchronised using this conventional CMM. Three interferometers were used in SCMM to monitor six degrees of freedom of the reflector and thus make the SCMM traceable to the metre. In this setup, SCMM used a probing system with stylus tip of either 0.3 mm or 0.5 mm diameter and a capacitance sensor as a detection mechanism. The positional

resolution is 3 nm and its probing force was recorded at 0.1 mN. The development of micro-CMMs was then actively continued by many groups of researchers around the world such as those from University of Tokyo [13], Physikalisch-Technische Bundesanstalt (PTB) [14], Hefei University of Technology [15] and others.

There are also several Micro-CMMs that have been commercialized. One of them is Carl Zeiss F25 micro-CMM as in Figure 2.2 [16]. The Carl Zeiss F25 was initially developed by the Technical University of Eindhoven (TUE) [17], and commercialized by Carl Zeiss. The unique design of its kinematic system allows the F25 to eliminate some geometric errors and thus increase the stiffness and accuracies of the machine [1]. The claimed measurement capability is (100 x 100 x 100) mm with resolution of 7.5 nm and measurement uncertainty of 250 nm. The F25 uses a probing system with silicon membrane chip with piezoresistive sensor for its detection mechanism and a stylus tip of 100 µm to 700 µm in diameter. The probing force recorded in this micro probe was less than 0.5 mN μm^{-1} [16].

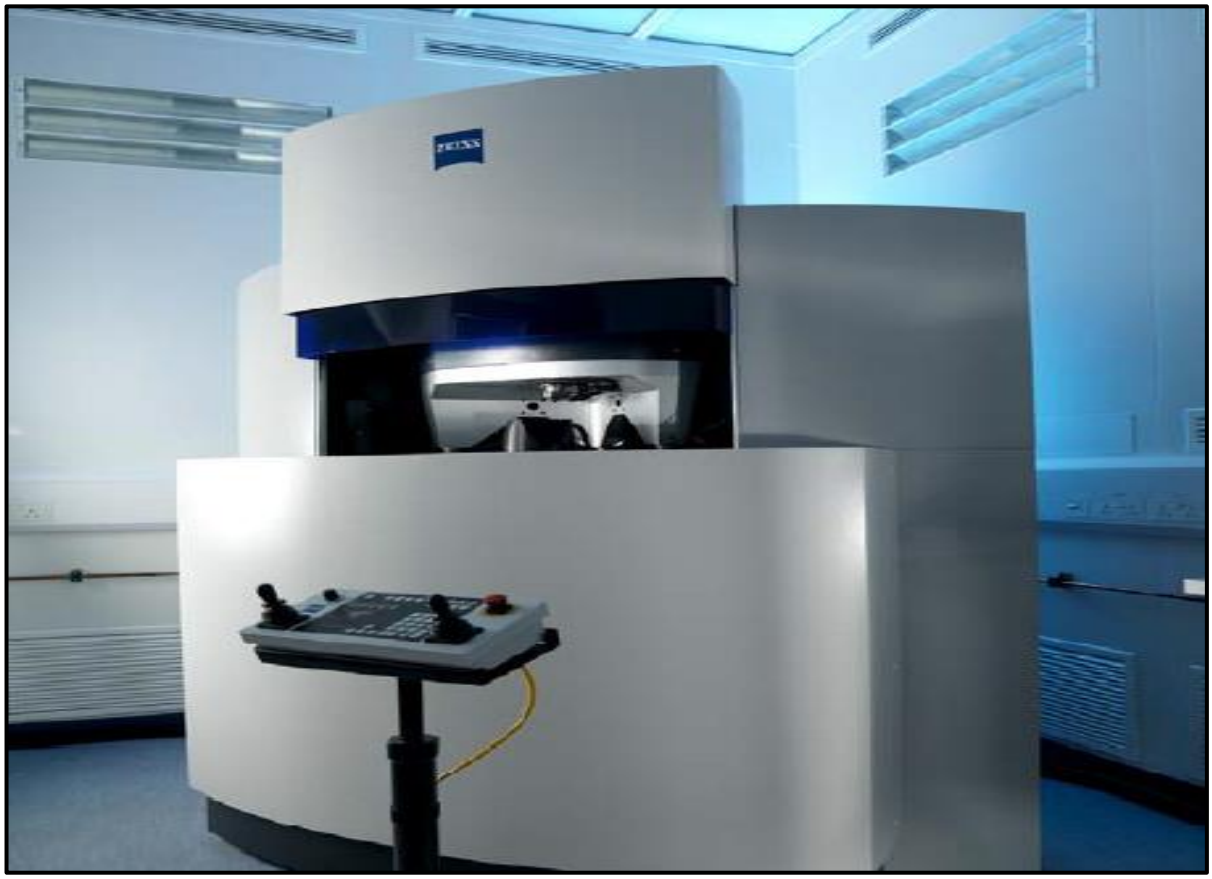

Figure 2. 2: Carl Zeiss F25 micro-CMM

2.4. Probing system for micro-CMMs

The stylus shaft and stylus tip are major components influencing micro-probes for micro-CMMs. As defined in ISO 10360-1 [18] for conventional CMM, the probe is defined as the complete devices that generates a signal during probing while the stylus is the mechanical devices that consist of a stylus shaft and a stylus tip. The stylus also establishes the physical contact with the workpieces, coupling its positional information to the probe sensor. Figure 2.3 illustrates the components of probing system.

Over the last decade, research and development of micro-probes for Micro-CMM have focused on the sensor mechanism of the probes rather than the stylus system. It can be understood that the detection mechanism in the micro-probes makes a major contribution to probing error and the source of uncertainty in measurements. Thus, it is essential to find the best approaches for detection mechanisms in different probe systems. These include, for instance, using mechanical techniques, capacitive sensors, optical techniques and vibration detection technique. However, in recent years, the increasing numbers of complex miniature products have driven research in micro probes to focus increasingly on shrinking the dimension of the stylus system itself. To provide context, the following section will review several probing systems of micro CMM which have been developed previously.

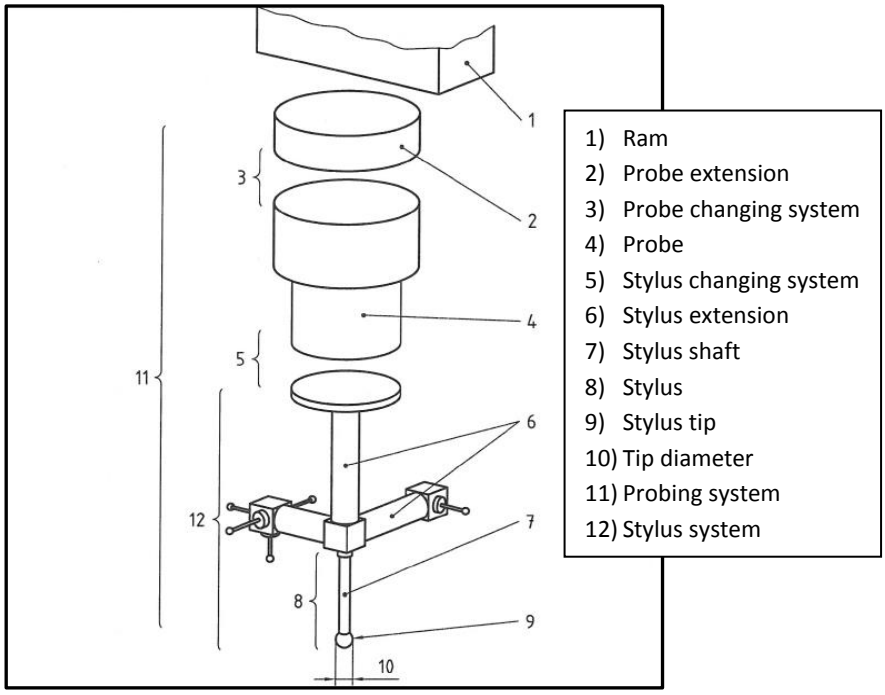

Figure 2. 3: Probing system according to ISO 10360-1 [18]

2.4.1. Conventional tactile Styli for Micro CMM probing system

The stylus systems categorised in this group are those for micro CMMs that have a similar design to those for the conventional CMM probing systems. As described in the ISO 10360-1 [18], the stylus systems mentioned have a spherical stylus tip, a rigid, straight and cylindrical stylus shaft, and (means of coupling to) a sensing element. These styluses operate in contact mode.

2.4.1.1. UMAP Mitutoyo probing system

The Mitutoyo UMAP stylus system was first developed by a group of researchers in 1993 to 1999 at the University of Tokyo, Japan [19]. After that, this research has been continued by the Mitutoyo Research Centre Europe and commercialised by the Mitutoyo Company [20]. There are three models of the stylus system, which are *UMAP 103*, *UMAP 110* and *UMAP 130*. *UMAP 103* consists of the smallest diameter of a sphere stylus tip, which is 30 µm, with a stylus shaft of 20 µm in diameter and 3 mm in length. The UMAP 110 consists of a stylus sphere tip diameter of 100 µm, with a stylus shaft diameter of 80 µm and a stylus length of 10 mm. The UMAP 130 consists of a stylus sphere tip of 300 µm, a stylus shaft diameter of 200 µm and a stylus length of 10 mm. Figure 2.4 shows the construction and components of the stylus system [20].

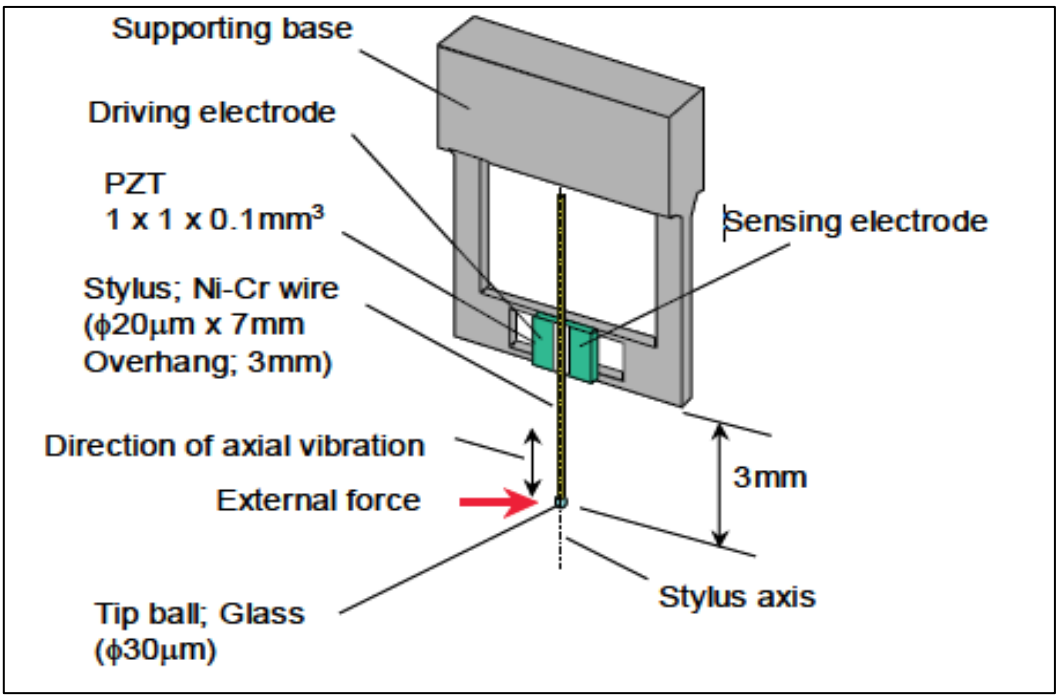

Figure 2. 4: Construction of UMAP stylus system [20]

This stylus system was initially developed for the profile measurement of ink jet and fuel injection nozzles. For this intention, it was designed to have a long and thin stylus which can access a micro-hole to some depth. Thus, one of the advantages of this stylus is it can perform high aspect ratio measurements [21]. Most of the literature that described this stylus system focused on the sensor mechanism when in contact with the workpieces. The UMAP stylus uses a piezoelectric force sensor as the driving and sensing electrode. The stylus is vibrated in its axial resonant state at approximately 350 kHz by the driving electrode. Meanwhile, the sensing electrode will detect any changes in the stylus' vibration amplitude, phase or resonant frequency [2] [21].

In terms of the fabrication process of the stylus system, the stylus shaft is made of nickel-chromium (Ni-Cr) and the stylus tip sphere is made of glass. By using the glass to metal sealing technology, melted glass is mounted like a water drop at the tip of Ni-Cr wire stylus shaft. The surface tension of the glass will form the sphere shape. The assembly process occurs in a vacuum chamber. One of the reasons that a Ni-Cr stylus shaft was selected in this design is because of its affinity towards the glass is extremely high[21][2]. Other important feature of the UMAP stylus system is the ability to mount to the Mitutoyo micro-CMM. The repeatability of the UMAP 103 is less than 0.1 µm. The measuring range of the UMAP 103 is (245 x 200 x 200) mm, with a contact force of 0.15 µN to 10 µN and stiffness of 21 kN/m. The UMAP 103 stylus system can also be removed, installed, and replaced easily by the user.

2.4.1.2. NPL capacitive SCMM probe

This probing system was first developed in 1999 [12], as shown in Figure 2.5. It uses three flexures in a triangular arrangement, which is manufactured from a 50 µm thick beryllium copper sheet. The stylus shaft is connected to the centre of the disk that consists of three tungsten carbide tubes. Three capacitance sensors electrode are also fabricated onto the three flexures. Displacement of the probe tip is detected by the translation or rotation of the centre tungsten carbide body, which is suspended on the three flexures. Thus, the gap between one or more capacitance sensor and an aluminium target disk will change when the stylus moves, the sensors will record each gap, and the position of the probe tip can be calculated [21][2].

This design provides equal stiffness of the suspension for all horizontal probing directions. It also has a light structure with a low probing force. The probing force is approximately 0.1 mN with a probing deflection of 10 µm, and the weight of the probe is 350 mg. Other characteristics of this design are, the stylus shaft is made of tungsten carbide, the stylus tip sphere is made of silicon nitride and the diameter of stylus tip is 1mm. The positional uncertainty of this design is between 50 nm and 100 nm [12].

The main contribution of this NPL stylus system is the generation at that time of knowledge about how to achieve equal stiffness in each axis and the low probing force. However, it is considered as the first generation of stylus system for micro-CMM, where the 1 mm in diameter for the stylus tip is no longer relevant to current needs. Nevertheless, the information on the material and design used in the stylus tip and shaft can be a reference to this study.

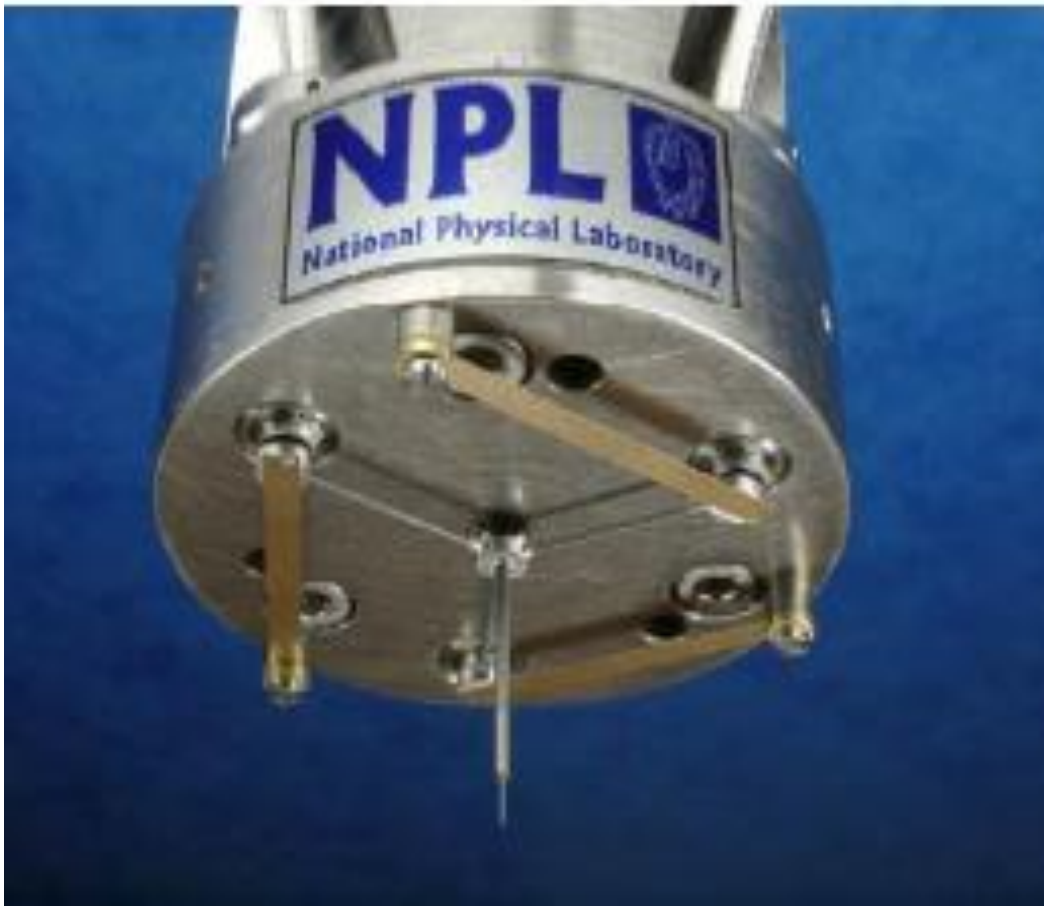

Figure 2. 5: NPL Capacitive Stylus [12]

2.4.1.3. TUE/ XPRESS Gannen Stylus

This probe stylus system was first developed by the Eindhoven University of Technology, TUE [22]. The TUE probe has later been commercialised by a company named Xpress Precision Engineering in the Netherlands [23] [24] . Figure 2.6 illustrate this probing system. The TUE probe was successfully developed with a nanometre capability in uncertainty, and with a low probing force around the range of mili-newtons. This probe consists of a silicon membrane, three slender rods with triangular orientation, and stylus system. The stylus system comprises of stylus tip with a diameter ranging from 50 µm to 500 µm. This orientation is designed in order to achieve the thermal and mechanical stability. On the centre is a moving platform of this chip where a stylus is attached at the end of the probe tip. An elastic deformation of the three slender rods is expected to be occurred during displacement of the probe tip and it is measured by piezo resistive strain gauges [23].

Figure 2. 6: Image of the first prototype of TUE probe (left) [22] , and it had been improved and commercialised by Xpress Precision engineering (right) [23]

Other important feature of this stylus is that it has low moving mass, which is 25 mg including the stylus shaft and tip. The stiffness of the probe is 480 Nm^{-1} with a hysteresis of 0.05 % and the standard deviation of repeatability is recorded at 2 nm, while the 3D uncertainty is 10 nm. This stylus also gives equal measurement sensitivity in every axis [23].

2.4.1.4. METAS probing system

This probing system has been developed and commercialised by the Institute of Metrology and Standardization of Switzerland (METAS) [25][26][4]. The component and construction of this probe are illustrated in Figure 2.7. The displacement of the probe stylus tip is measured via the deflection of a suspension based on three elastic flexure hinges using

three inductive sensors that are mounted on the probe housing. During single point probing, the probe deflection is recorded at different positions to obtain a force-distance curve for the measurement point. The flexures hinges are made from aluminium by using the milling and EDM processes. One of the unique features in this system is all the axes are inclined by 45 degrees and thus, will have equivalent orientation with respect to gravity when the probe is mounted on a CMM. A permanent magnet is also located in the system to eliminate the sagging phenomena due to gravity [21][2].

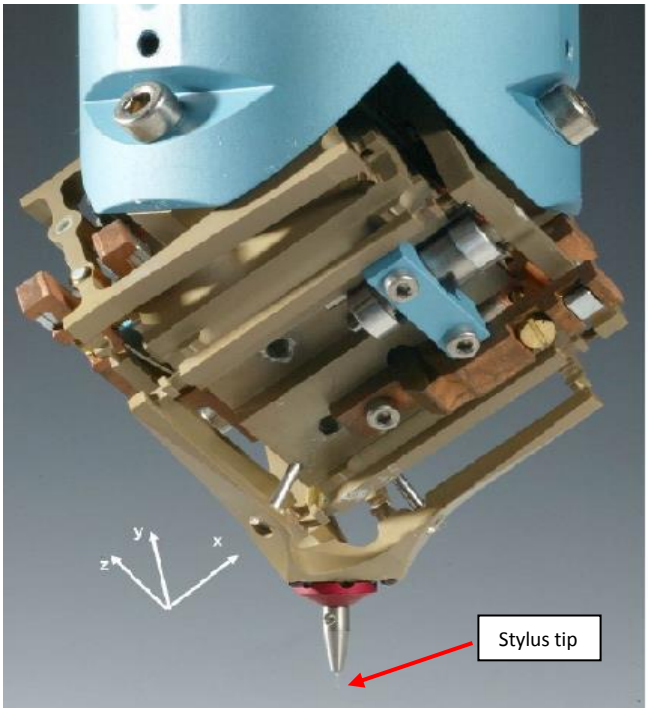

Figure 2. 7: image of component and construction of METAS Probing and stylus System [23]

The diameter used for this stylus tip sphere is 100 µm to 300 µm while probing force is below 0.5 mN, and the stiffness of the probe was recorded at 20 Nm^{-1}. The moving mass is 7 g, which is quite high and as a result, a plastic deformation may occur either on the surface of the measured workpiece or stylus tip itself. An elastic element is used to reduce the influence of colliding mass [2] [21]. A completed series of performance tests on this stylus system, especially covering repeatability and isotropy have also been conducted [25]. The probing acceptance method based on ISO 10360-2 [27] was also conducted. From these tests, the repeatability is 5 nm and the roundness deviation is 40 nm for the sphere with a 300 µm diameter tip [25].

2.4.1.5. Piezoresistive based stylus

A piezoresistive based stylus for the micro-CMM is another new stylus system developed by a group of researchers in PTB Germany [28][29], as shown in Figure 2.8. Similar to other types of stylus systems that have been discussed previously, the focus of this research is mainly on the sensing mechanism part of the probing system, as this probe uses a silicon membrane with diffused piezoresistor as the sensing element.

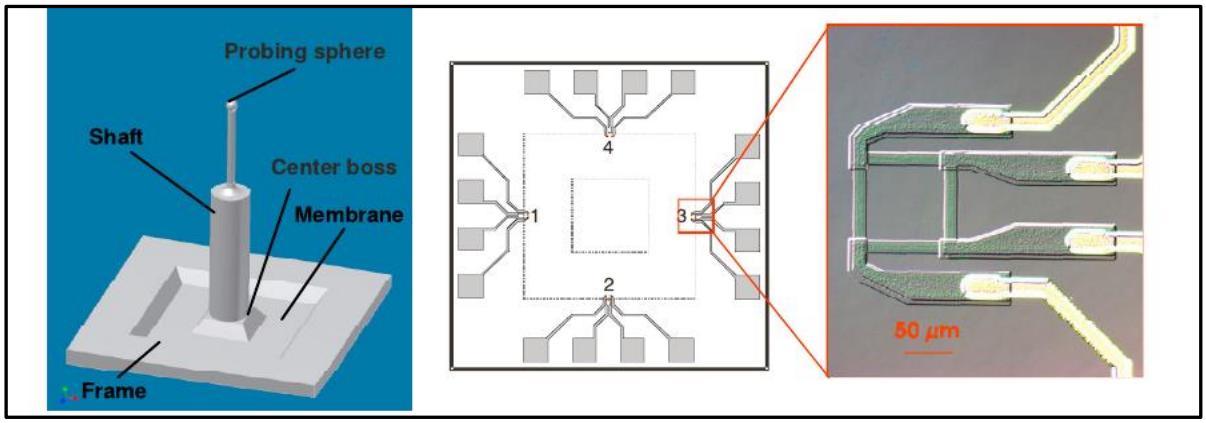

Figure 2. 8: Piezoresistive stylus system [28]

This stylus consists of a silicon membrane with the piezoresistor layer at the back side of the membrane, which is used as the sensing element, a 7 mm effective length of stylus and a 300 µm in diameter of the stylus tip sphere. The silicon membrane is fabricated using the KOH-etching technique while the piezoresistor layer is fabricated using standard micro fabrication technique for insulation, diffusion and metallization. The stylus shaft is glued at the centre boss of the membrane. Figure 2.8 shows the components of this stylus.

In theory, as shown in Figure 2.9 the silicon membrane will sense any deformation and mechanical stress caused by any deflection of the stylus tip when it is in contact with the surface. The piezoresistors will transform the deformation and mechanical stress into electrical output signal through changing their electrical resistance, where the change of electrical resistance is proportional to the mechanical stress.

Several test programs and characterisations were conducted to this stylus, such as for the force calibration, probing repeatability and probing qualification. As a result, the maximum probing force was estimated at 0.73 mN and the sensitivity is in the nanometre range. Further testing and characterisation work were carried out in 2010 to determine the best designs to improve stiffness at the suspension and its sensitivity [28].

A few designs have been investigated at PTB to improve the sensitivity of the probe and the stiffness of the suspension. From the finite element analysis, adding aperture design to the membrane will increase the sensitivity of the probe [28]. A double triangle design of the silicon membrane was proposed to improve the stiffness of the suspension. With this new design, the results showed that the original anisotropic stiffness could be improved to a nearly isotropic stiffness of suspension.

In contrast, there is no further information on the reaction of this stylus towards the surface interaction force during measurements. The physical characteristic of the stylus, such as the roughness error of the stylus tip sphere and the diameter of the stylus shaft were also not mentioned in this research. Moreover, the investigation of performance for this stylus system should be continued with a smaller stylus tip sphere diameter of less than 300 µm because the probe qualification test, which was conducted in this research may not be suitable when testing the smaller sphere tip diameter.

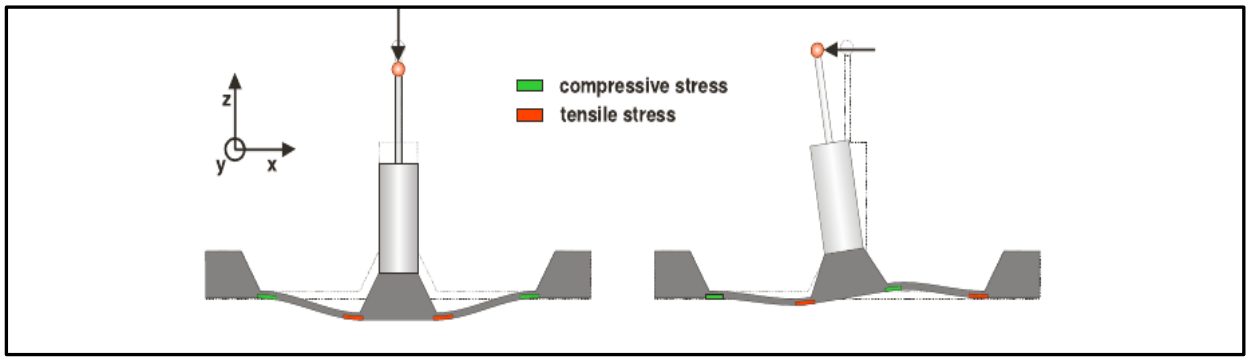

Figure 2. 9 : working principle of stylus deformation [28]

2.4.1.6. Fizeau Interferometer based Stylus

This type of stylus uses a Fizeau laser interferometer as the sensor mechanism at the probing head to detect the deflection of stylus tip sphere when contacting the measured surface. This stylus had first been demonstrated by T. Liebrich and W. Knapp (2010) [30]. The details of this stylus are as shown in Figure 2.10. Theoretically, the laser interferometer will detect the different in the fringe pattern cause by any change of position and orientation between the reference surface and the moveable surface during the test. As the stylus shaft and stylus tip are attached to the moveable surface under test, any deflections in the stylus will cause it to move and, hence, the position of the stylus can be detected by a laser

interferometer. The probing force and probing stiffness behaviour of this stylus system, theoretically and experimentally, are also investigated and reported by the authors [30].

This Fizeau interferometer stylus was successfully demonstrated for probing in millinewton range. The drawbacks of this stylus include an ability to operate in 1D measurement only, and the stiffness not being similar in all axes. However, no further information was mentioned about the probing force characteristics, bending behaviour and physical information of the stylus shaft and stylus tip sphere, including the diameter of the stylus shaft and stylus sphere, materials used, roughness and roundness of the sphere. The focus of the paper is more on the behaviour and characteristic of the sensing element and the mechanism of this stylus system.

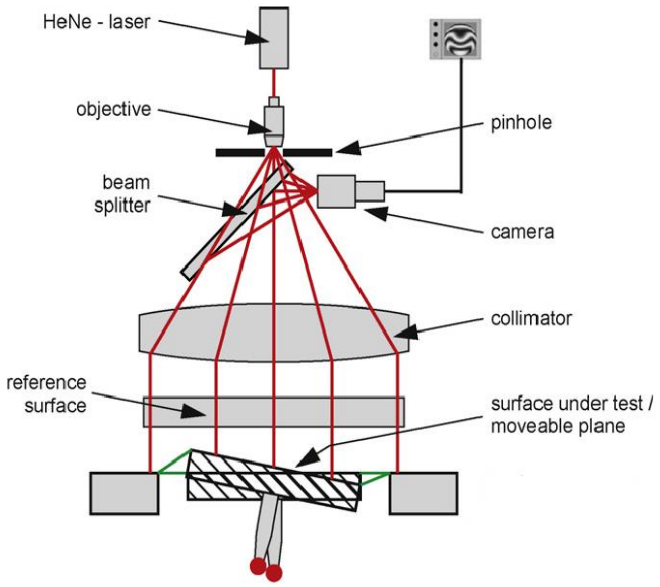

Figure 2. 10: Fizeu interferometer stylus system [30]

2.4.1.7. NPL Vibrating Stylus

The design of the vibrating stylus is based on the NPL capacitive stylus using the triskelion design as shown in Figure 2.11 [31],[32],[33], [32], [34]. This probe is an improved version of the NPL capacitive SCMM probe (refer to section 2.4.1.2). The stylus shaft is mounted onto the hub at the centre of a micro-fabricated suspension which consists of three relatively rigid beams, each connected to beam flexure element. The stylus shaft is 46 µm in diameter, with a 70 µm diameter stylus tip sphere and an aspect ratio of 20. Six thin-film piezoelectric actuators deposited on the flexures are used to vibrate the probe and the stylus system. The vibration is controlled so that the stylus tip always vibrates normal to the

measurement surface and its acceleration is sufficient when contacting the measurement surface. The frequency of oscillation is about 1.6 kHz and vibration amplitude is 1 µm [31]. Any interaction between the stylus tip and measurement surface will cause the change in amplitude and will be captured by the two piezoelectric sensors at either end of the flexures. The probe stiffness determined from the modelling is estimated around 15 Nm^{-1}.

A broad simulation and characterisation of this stylus has been reported [33], including the understanding of the load parameter, the surface force characteristic, the snap in and snap out phenomena, and the sensitivity of the stylus in vertical and lateral direction. However, these characterizations seemed to focus more on the functionality of the sensing element in the probing system itself rather than the characterisation of the stylus system, including the quality of the stylus, the form and roughness error of stylus sphere tip, and the probe tip calibration, which were not addressed in details.

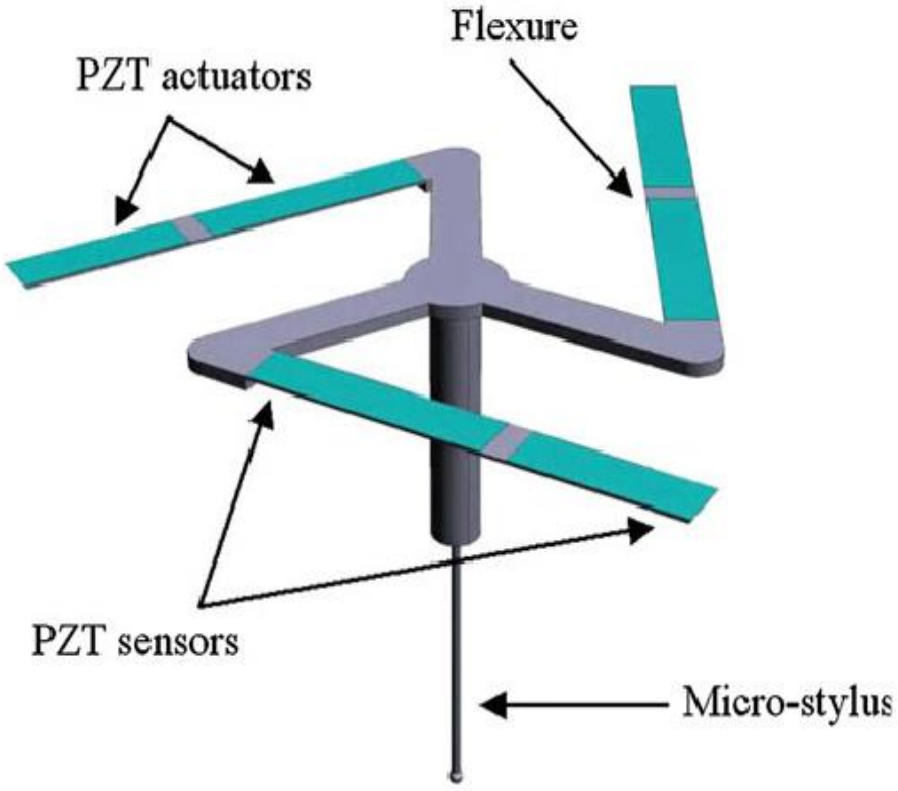

Figure 2. 11: NPL vibrating stylus [31]

2.4.1.8. IBS Triskelion Ultra-Precision Touch Probe.

As shown in Figure 2.12, this probe uses a stylus shaft made from tungsten carbide and ruby for the stylus tip. The diameter of the stylus tip recorded in the literature is between 70 µm to 500 µm, while the diameter of the stylus shaft is 50 µm. The flexure used in this system was made from monolithic metal foil and it is elastically suspended, thus, allowing deflection of the tip during probing measurement. The displacement of these targets is measured with the capacitive sensors and can be used to determine the *X*, *Y*, and *Z* deflection of the probe [35]. Other features of this stylus system are the stiffness are: 70 Nm^{-1} isotropic in every axis, the suspended mass of 160 mg, measurement range of 10 µm, and 3D measurement error recorded is less than 15 nm [36][37].

Figure 2. 12: IBS Triskelion Ultra-Precision Touch Probe

2.4.1.9. Differential Capacitor Based Stylus

Capacitive sensing is not a new technology in micro-CMM probing. The capacitive based stylus system was first developed by NPL, which was discussed in section 2.4.1.2. However, a group of researchers from China in 2013 [38] has developed a new design of the micro CMM stylus system based on the micro-fabricated capacitive and by using the differential capacitor technique to sense any displacement of a spring-suspended floating plate during contact measurement between the surface and stylus tip sphere as shown in Figure 2.13. This new stylus is able to measure in 3D. Other than that, this stylus has a nanometre range sensitivity and can measure a high aspect ratio measurement down to 2.3 mm in depth with a dimension larger than 0.3mm. This means that the minimum stylus tip sphere diameter used is 300 µm.

As shown Figure 2.13, the micro capacitive sensors consist of a floating plate and a fixed plate. Four pillars are used to separate them, hence, making a nominally uniform gap between the floating and fixed plate. The fixed plate itself has been separated into four equal parts that are connected electrically by wires. The sensing principle can be summarised as follows; when the stylus tip sphere contacts the measured surface, the probing force will be exerted by the system. This probing force will cause translational motion in the *Z* direction and tilt motion about the *X* and *Y* axes of the floating plate. The four sections of the fixed plate will experience differently varying capacitances with the floating plate caused by its translational and tilt motion. These capacitance differences are sent to a computer via signal processing circuit for analysis to determine the tip motion.

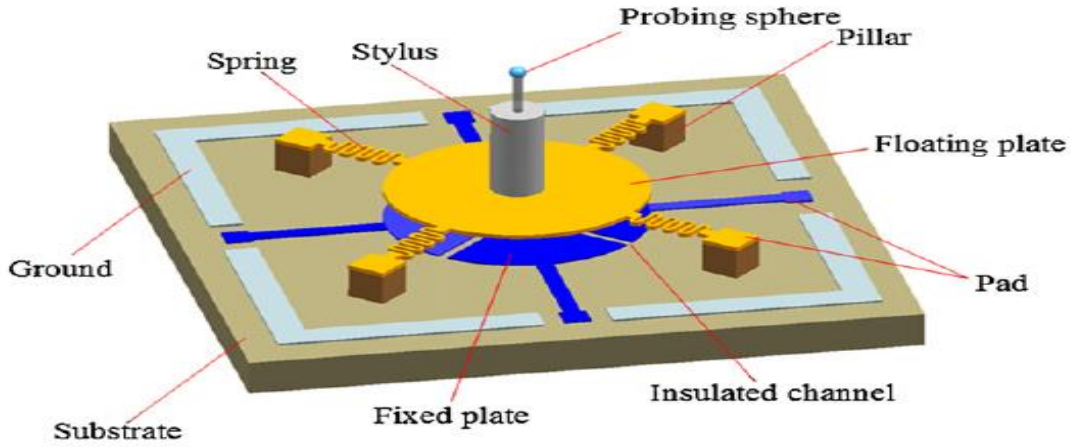

Figure 2. 13: Differential capacitor based stylus system

The micro capacitive sensor was made by MEMS fabrication technology and a precision piezoelectric nano-positioning stage was used to assemble the capacitive sensor with the stylus shaft and stylus tip sphere. However, there is no clear information on the techniques being used to fix the stylus onto the capacitive sensor, either by using the glue technology or other techniques. Other than that, similar to the other types of stylus that were discussed previously, there is no information about the manufacturing or fabrication technique of the stylus shaft and stylus tip where there is no characteristic information on the physical form of the stylus shaft and stylus tip, such as the stylus tip and shaft diameter, and its roughness. This is because more focus was put onto the sensor mechanism. Although this stylus is capable of measuring high aspect ratio measurements, it is yet able to measure many of the products that required dimensions of less than 0.3 mm, such as the micro gear, injection nozzle, and micro ring artefact.

2.4.1.10. Tri-Switch Stylus

The tri-switch stylus system has been developed by a research group from the National Taipei University of Technology, in 2013 [39][40]. As compared to the other stylus systems that have been discussed in this chapter, this research does not only focus on the sensing element, but also the information on the stylus shaft and tip. As shown in Figure 2.14, the diameter of the stylus tip sphere used is 80 µm and is made of glass, while the diameter of the stylus shaft is expected to be smaller than the diameter of the stylus tip sphere. The stylus shaft is made of wire electro-discharge grinding (WEDG) process and adhesive hybrid technology was used to assemble the stylus tip sphere onto the stylus shaft. For the sensing element, this stylus uses the concept of triggering mechanical system. The metal plate with three micro wire rods was placed on the supporting base. The sensing wire rods were fixed onto the micro wire. The stylus shaft will then be assembled in the centre of the metal plate. The sensing wire rod will function as the on-off switch. When force is applied to the stylus tip, the metal plate will oscillate and thus, causing the contact point between the sensing wire and micro wire like the on-off switch. At the same time, the signal from the on-off switch will be triggered by the electronic systems. Additionally, the sensitivity of this probe is only in the micrometre range and need to be improved for micro-CMMs application.

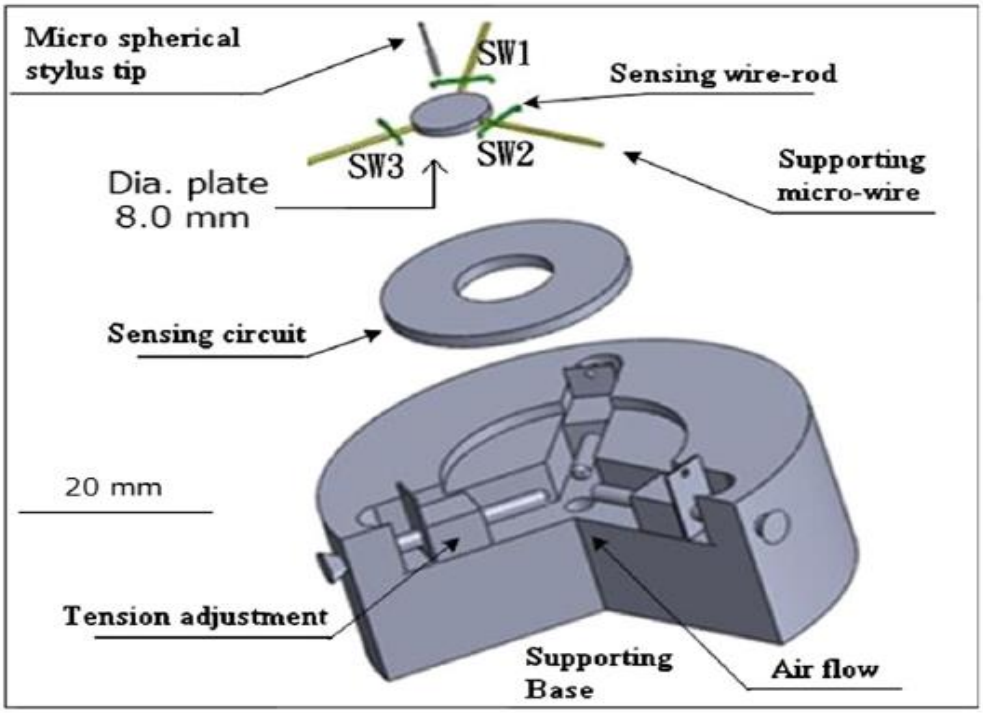

Figure 2. 14: Image of the component of Tri-Switch Stylus System [28]

2.4.1.11. Variable Stiffness Probing System

A completely new concept of probing systems with tuneable stiffness and a description of the operating procedure is presented in this paper [41] [42]. The design of the sensor mechanism for a variable stiffness probing system was based on a novel suspension structure that allows compressive force to be applied to the main spring elements within the structure. The spring element is made of a long slender beam for the wide range of geometrical measurement can be performed. The loads can be applied using a piezo-electric or other similar form of actuator at the end of each beam. This design structure allows a probing system to operate in either “stiff” or “flexible” mode at which can be selected at a certain position. A stiff mode is selected when approaching the measured workpiece, while at the certain predetermined location where the distance between the stylus tip and measured workpiece is small, the stylus is operated in the flexible mode when the stiffness at a minimum to ensure a low contact force occurred. Then, after measurement contact is performed, the stylus is switched back to the stiff mode [42].

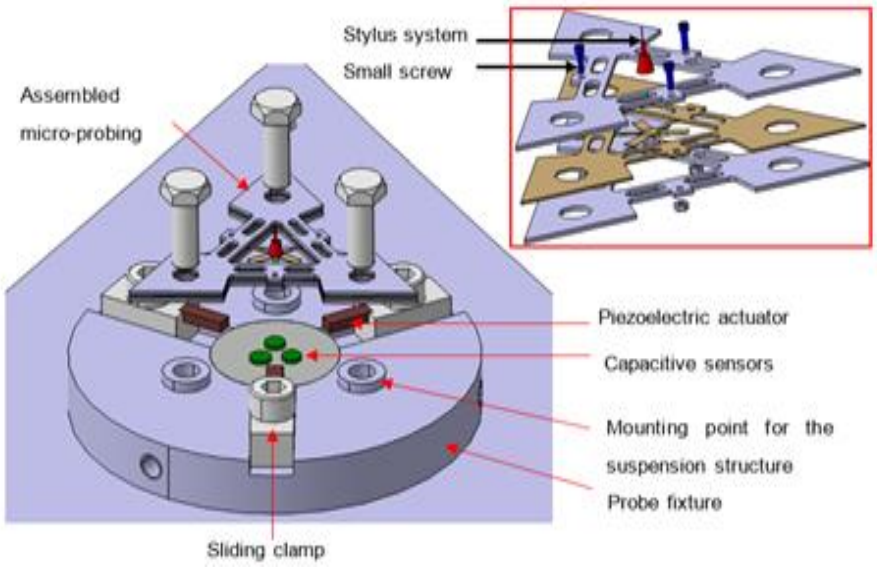

Figure 2. 15: Schematic diagram for variable stiffness probe [42]

A schematic diagram of the variable stiffness micro-scale probing system is shown in Figure 2.15. The sensor suspension is assembled in triangular-shaped object with a stylus system of a 300 µm diameter spherical tip is mounted on top of it. Displacements of the stylus system during probing are measured as a function of suspension structure displacement whereby it is quantified by mounting the suspension structure above three high precision capacitive displacement sensors. The three sensors are mounted within the probe fixture to

allow an accurate position relative to the suspension structure. The vertical positions of the sensors are varied within the probe fixture to allow an optimum working gap at an approximately 100 µm. In order to allow stiffness modulation of the suspension structure, three piezoelectric actuators with 8 µm maximum displacement are mounted to the probe fixture. A set of three sliding clamps are employed to ensure that the actuators are positioned in intimate contact with the load application points on the suspension structure. [43]. The probe stiffness is varies from 914 Nm^{-1} to 2853 Nm^{-1} in vertical direction while from 410 Nm^{-1} to 610 Nm^{-1} in lateral direction [43]. The first promising experiment conducted resulted in an uncertainty of the probing system in about 60 nm which shows that the issue of drift and stylus tip displacement while switching the stiffness need to be resolved [4].

2.4.2. Non-conventional tactile styli design of probing system for micro-CMM

There are two criteria for stylus systems to be categorised here as 'non-conventional'. The first criterion is the styluses have a unique design, which is not following the normal design of the stylus system of micro CMM described generally by ISO 10360-1 [18] (as illustrate in Figure 2.3 in section 2.4). For the normal design of the stylus system as discussed before, the stylus with a rigid, straight, and cylindrical stylus shaft, a spherical stylus tip is attached at the end of stylus shaft and an interface between the stylus and the sensing element. The second criterion is that, while having important characteristics in common with a tactile stylus system, it actually functions as a non-contact stylus when measuring the surface. Thus, the stylus systems discussed in this section either do not have a stylus shaft, or a stylus tip sphere or are operated in a non-contact mode when measuring the surface.

2.4.2.1. PTB-Werth Fibre Stylus

The fibre probe stylus system was first developed by the PTB, which has been patented and commercialised by the Werth Messtechnik Company [44] [45]. As shown in Figure 2.16, this stylus system is unique as it uses optical fibre as the stylus shaft and a glass sphere with the smallest diameter of 10 µm as stylus tip. The stylus length is between 2.5 mm to 150 mm and probing force is low, which is between 1 µN to 100 µN. With this specification, this stylus is suitable for the measurement of small parts, such as rubber goods, plastic parts, gauges, miniature gear, fuels injection nozzles, and calibration of optical components.

This stylus system uses optical imaging in the detecting mechanism. In detail, as the stylus tip comes into contact with the workpiece, the stylus tip will be deflected, and this deflection is detected by a camera system of the optical Micro CMM where the position of the probing point is calculated by high accuracy image processing [21][44]. The measurement can be done either by the use of backlight illumination, which measures the resulting shadow of the ball tip or detects the position of a self-illumination probing (hence the use of an optical fibre). The stylus tip sphere in this stylus system was initially used for both tactile probing and optical measurements by the camera system. Thus, problems could occur when the optical light path was disturbed by, for instance, effects resulting from the penetration depth in a small, deep hole. Such effects would consequently lead to measurement error. Nevertheless, this problem has been solved by adding a second sphere that is located on the fibre shaft, above the stylus tip sphere. This second sphere is used for optical detection of the fibre deflection, but does not penetrate the measured structure, as shown in Figure 2.17 [21].

Figure 2. 16: Opto-Tactile PTB-Werth Fibre Probe [45]

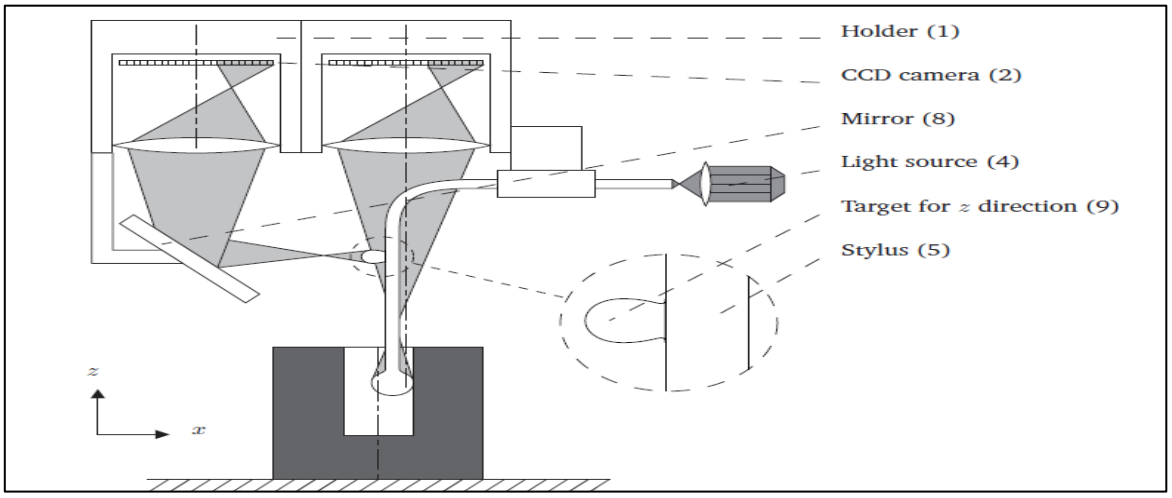

Figure 2. 17: Component of the PTB-WERTH Fibre Stylus Probe [21]

In the early developmental stage of this stylus system, it was unable to sense in the *z*-direction; hence, it was only used for 2D measurements. However, through recent development of application of additional speckle pattern evaluation and stereo-photogrammetry principle, this stylus is now able to detect the deflection in z-direction [44]. Other specifications of this stylus include a single-point repeatability with 50 nm standard deviation, probe uncertainty of 0.2 µm to 0.5 µm, working distance of 0.01 mm to 3 mm and up to 1 mm depth to be measured. In addition, advantages and disadvantages of the stylus system have been discussed and explained elsewhere [2], [21].

2.4.2.2. Laser trapping stylus system

Demonstration of the first stylus for the micro CMM to use a laser trapping principle was reported by Y. Takaya *et al*. (1999) [46]. The research and development of this stylus are continued to improve the resolution and measurement range [47] [22]. The laser trapping stylus is a non-contact tactile stylus. It uses a laser interferometer as the sensing element while a microsphere made from glass with 8 µm in diameter is used as the stylus tip. The uniqueness of this "stylus" is that it does not have a physical stylus shaft. A laser trapping force or a standing wave scale (SWS) generated by the fibre laser is used to hold the stylus tip sphere as in shown in Figure 2.18 and Figure 2.19.

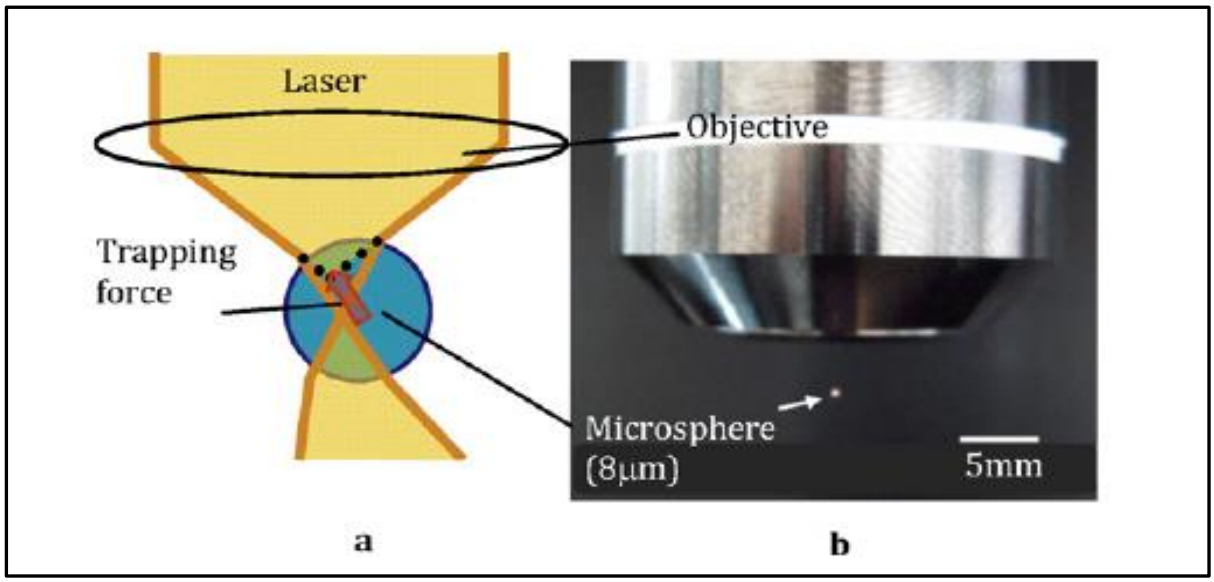

Figure 2. 18: Laser trapping stylus system [35]

The working principle of this probe, the stylus system senses its displacement associated with an object surface. Then, a laser diode that excited the fibre laser is used to capture an 8 µm in diameter of the microsphere stylus tip, which then produces its standing wave. A laser diode illuminates the microsphere coaxially to determine the actual micro-probe axial movement. Backscattering light that is associated with the laser diode out of the micro-sphere is spotted by the photodetector. Several parts of the detected output voltage are applied to be the probe displacement signal.

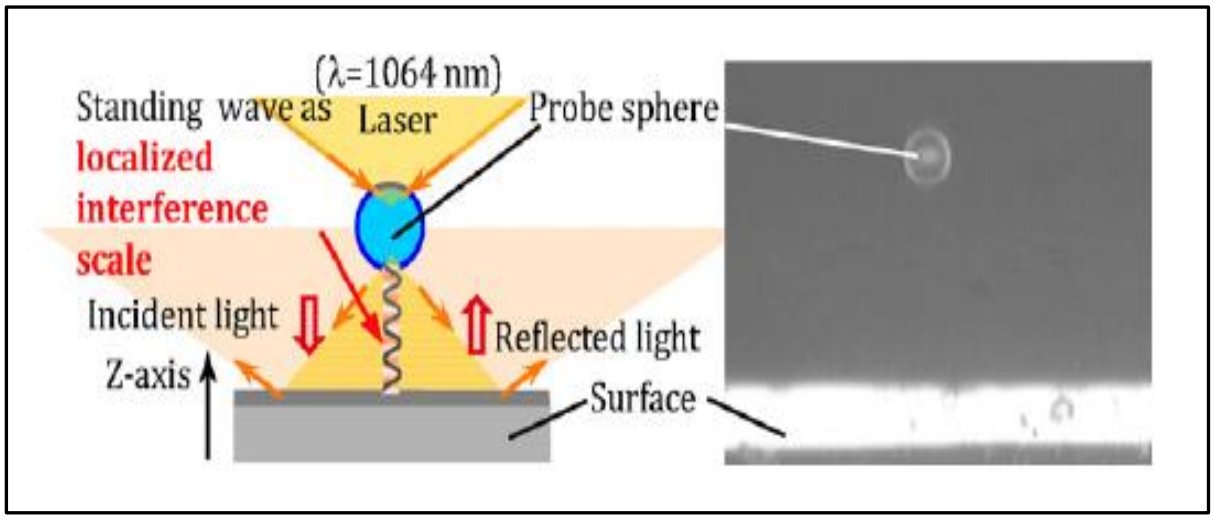

Figure 2. 19 : Principle of standing wave scale or laser trapping [35]

2.4.2.3. Standing wave stylus (Virtual probe)

Standing wave stylus was developed by Bauza *et al.* (2005), illustrated in Figure 2.20 [48] [49]. This tactile stylus operates in the contact stylus mode and is able to measure a high aspect ratio measurement up to 500:1. Compared to the the conventional design of styli, this stylus system does not have a stylus tip and only have a stylus shaft. The standing wave stylus consists of the displacement sensor and the quartz crystal oscillator as a sensing element, while the stylus shaft is attached to the end of the oscillator that is made from micro-fibre, which is 7 µm in diameter and 3.5 mm in length. The stylus shaft is vibrated at 32 kHz using a quartz crystal oscillator to produces a mechanical standing wave.

Other characteristics of this stylus are the ability to measure in 3D and the contact force recorded is approximately 20 nN to 50 nN, which was calculated using the beam bending theory. In addition, this stylus can avoid having any adhesive interaction force and sticking

problem to the measurement surface. This stylus also has a high stability in standing wave amplitude up to several tens of micrometres.

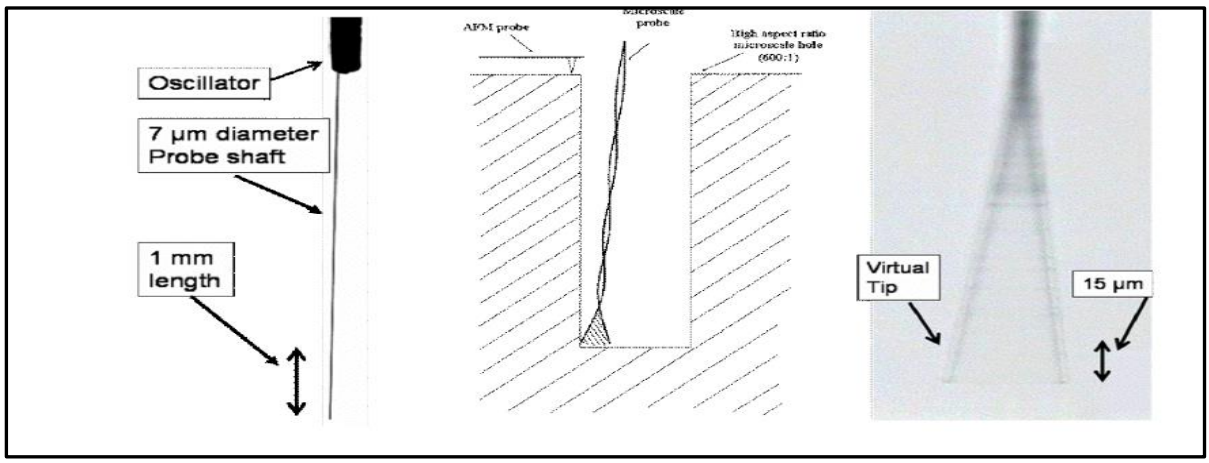

Figure 2. 20: Standing Wave Stylus [36]

In addition, an interesting part of this stylus is about the bending and stiffness of the stylus shaft. For a conventional stylus system, the stylus shaft needs to be stiff enough in order to measure the surface, however, in this virtual stylus, the stiffness is not an important parameter and it can be operated with a low stiffness of the stylus shaft.

2.4.2.4. Spherical Capacitive Plate Based Stylus

The spherical capacitive based stylus was developed to deal with the high aspect ratio measurement [50]. This stylus comprises of a probe head, a stylus shaft with a 2.2 mm in diameter and 100 mm in shaft length, while the stylus tip sphere consists of a 3 mm in diameter as shown in Figure 2.21. This probing system has 1 μm measurement range and the resolution is better than 5 nm.

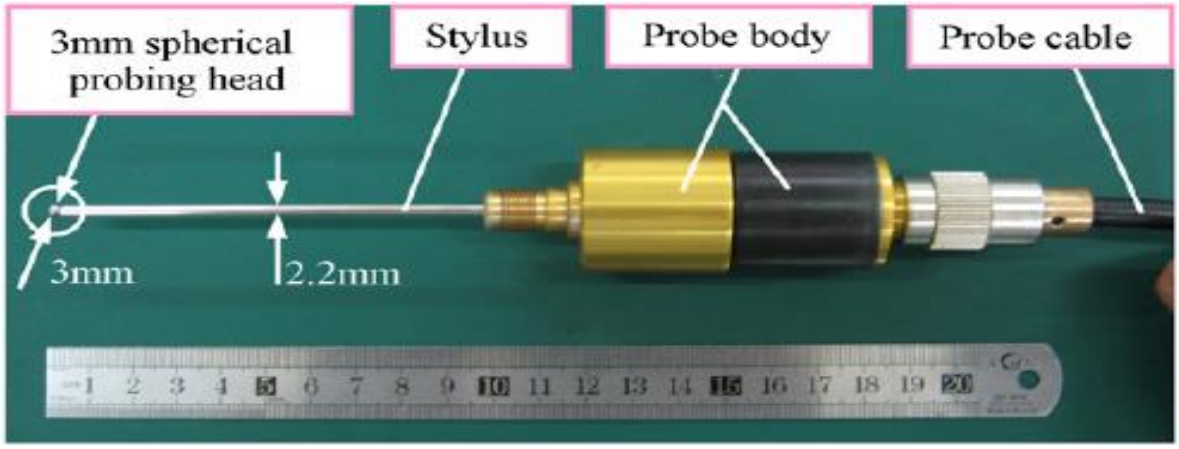

Figure 2. 21: Spherical Capacitive plate based Stylus [38]

This tactile-like stylus operates in a non-contact mode using the principle of the spherical capacitive plate as shown in Figure 2.22. In detail, when the stylus tip approaches the measured surface, a gap (δ) between them will become small enough for a measurable capacitance to be created. As the electrical fields between the stylus tip and measured surface are non-uniform 3D spatial field, the capacitance is calculated based on the electrical image method and this sensing characteristic is nonlinear and need to be corrected during the signal processing. Other important features of the spherical capacitive plate's principle are its sensing characteristic is identical in any arbitrary spatial direction, and thus, it will not be affected by any change of position and depth in the measured surface or in re-mounting of the probe. Furthermore, the electric field's lines of the spherical capacitive plate are focused within a very small region between the plate and the measured surface, hence, acting approximately similar to the point sensing characteristic [50].

With a 3 mm diameter stylus tip and a 2.2 mm diameter stylus shaft, this particular dimension of stylus is not suitable for a micro CMM stylus system and is not capable of measuring small products such as nozzles and micro-gears. However, this stylus can solve the high aspect ratio challenge in many industrial products, such as holes in aviation parts. Nevertheless, this detection mechanism employed in this stylus can be potentially explored for the development of micro-probes for micro-CMMs application.

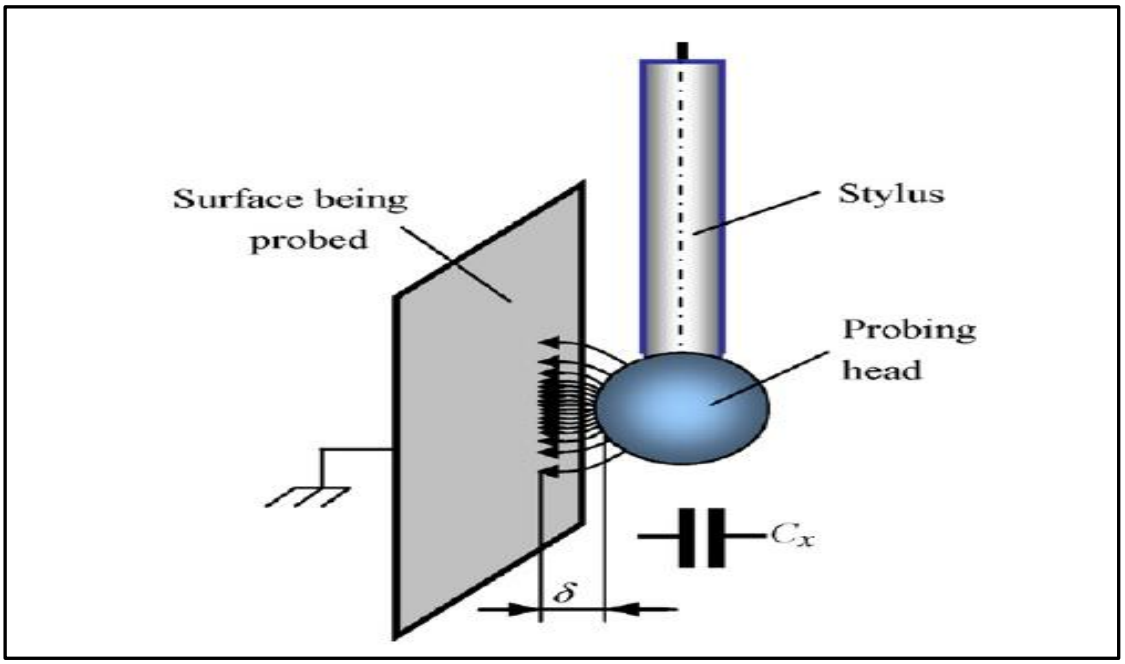

Figure 2. 22: Principle of spherical capacitive plate [38]

2.4.2.5. Acoustic Emission (AE) Wire Based Stylus

The AE wire based stylus system was discovered by Goo *et al*. (2012) [51]. This stylus uses an acoustic emission sensing principle by means of an adjacent sensing element and a rotating stylus with a 100 µm diameter alloy steel wire acting as the stylus tip. The stylus tip diameter is defined as D_p when the wire rotates at the angle of α_p as shown in Figure 2.23. The design of the stylus tip makes it different from the conventional stylus systems for micro-CMMs. The stylus tip is mounted to the stylus shaft and the fabrication of the stylus is claimed to be simpler than the normal spherical stylus tip. This stylus is expected to solve the problem of snap in and sticking effects during contact with the measurement surface.

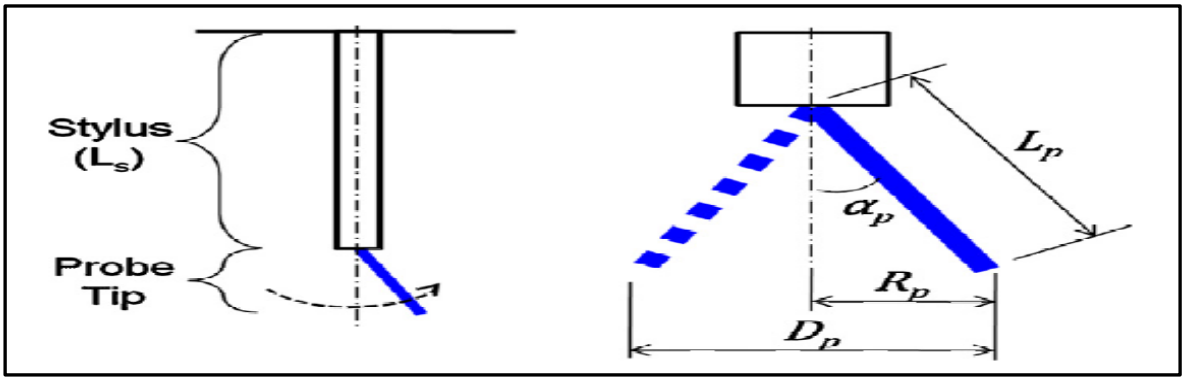

Figure 2. 23: AE Wire Based Stylus system [39]

The working principles of this AE wire based stylus can be summarised as shown in Figure 2.24. When the spinning or rotating stylus tip is in contact with the measured object, the stylus tip will rub the measured surface and thus, the AE signal will be generated and will be sensed by the AE sensor. The stylus will stop when a pulse is generated, which is caused by a situation where the root-mean-square (RMS) value of the AE signal is larger than the threshold value. Then, the position of the stylus will be recorded.

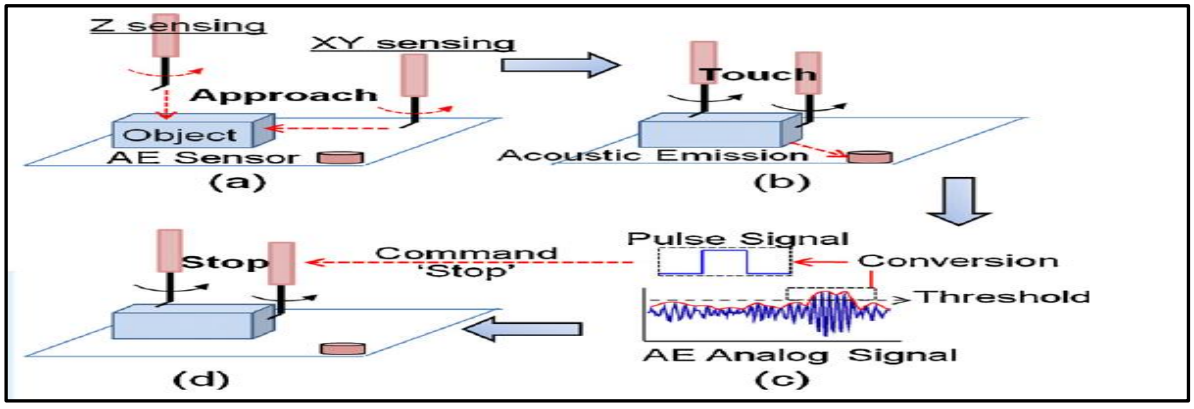

Figure 2. 24: Sensing Principle of Acoustic Emission Torch stylus system [39]

2.4.2.6. Uniaxial resonant probe

The uniaxial resonant probe is the tactile stylus that operates in a non-contact mode when measuring the surface, as shown in Figure 2.25. The stylus was first developed by B. Goj and M. Hoffmann from the Ilmenau University of Technology [52] [53], and mainly focused on solving the sticking effect from the capillary force. This probe consists of a ruby sphere stylus tip with 200 µm in diameter, the stylus shaft and two electrostatic actuators. The actuators will drive the stylus in a resonant motion.

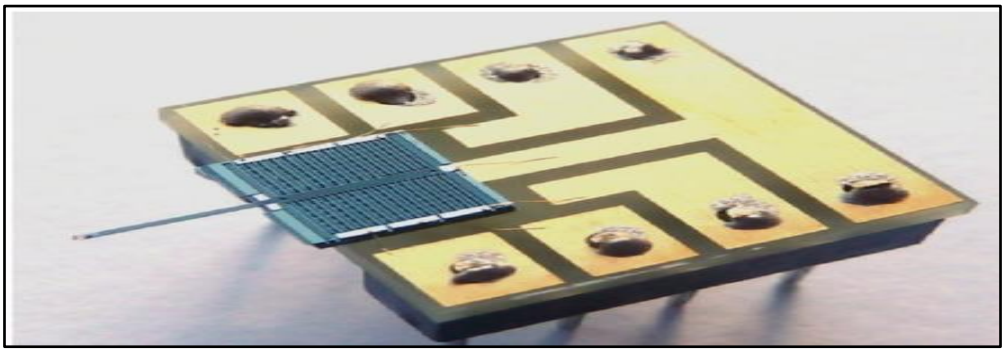

Figure 2. 25: Uniaxial Resonant probe stylus [40]

The electrostatic actuators are located on the silicon on insulator (SOI) substrate and normal semiconductor fabrication, such as lithography, deep reactive ion etching process, evaporation, wet etching and vapour etching are involved in the manufacturing of the electrostatic systems and stylus shaft. The assembly of the ruby sphere at the end of the stylus shaft is done by gluing using a thermally cured epoxy. However, the strength of bonding between the end of the stylus shaft and the stylus tip sphere were not mentioned in this research [53].When the stylus approaches near to the measurement surface, the actuators will oscillate the stylus. The oscillation of the stylus will cause damping in the *x*-direction and rotation in the *y*-direction. The damping in the *x*-direction will cause the change in capacitance, while the rotations in the *y*-direction will generate the torque around the stylus. The position of the stylus will be captured by the sensor when the actuators produce the output voltage, which is proportional to the change in capacitance. The amplitude of the output voltage will evaluate the torque generated from the rotation motion of the stylus [53].

2.4.3. Summary of the review of probing systems

Section 2.4.1 and 2.4.2 have reviewed experimental and commercial probing systems for micro-CMMs. In this review, all probes are categorised based on the styli design. The

discussions in this review are focused on the stylus system used in these probing systems and therefore the sensing mechanism is not explained in detail. The focus of this project is on tactile styli of relatively conventional design. Nevertheless, it is also beneficial to overview non-conventional stylus designs for the better understanding of the current technology on the probing system in micro-CMM and other micro- and nanometre instruments.

Table 2.1 summarise the parameters of the stylus system for some of the reviewed probing system. From section 2.4.1, which covers the conventional design of styli, it is observed that the stylus tip used in all reviewed probing systems have a diameter higher than 50 µm and the applied probing forces that can be imparted to the probing systems are bigger than 0.01 mN. These capabilities, in general are not suitable for micro products which might often contain features of less than 50 µm. Of all reviewed probe system, the stiffness of the stylus shaft was not reported. This can be understood that majority of the reviewed probing system employed micro-styli that have tip diameters above 300 µm, and thus, it is expected that stiffness of their stylus shaft is bigger than the stiffness of the suspension of the probing sensor mechanism. This condition is important to ensure the sensitivity of the probing system (later will be discussed in details in section 3.4.4). However, when the stylus system shrink down to the dimension of sub-10 µm, it is crucial to conduct testing to determine the stiffness of the stylus shaft.

From Table 2.1, only Metas probing system had reported a value of the spherical form error of the stylus tip. This parameter is difficult to be examined due to the limited establish metrological instrument and measurement technique. In theory, due to an imperfection in spherical shape of the stylus tip, its spherical form deviation should be determined. Nevertheless, this parameter is not relevant in conventional CMM as its value is much smaller compared to the CMM's stage positional error. Furthermore, for probing system of micro-CMM that have styli tip diameter larger than 300 µm, the spherical form error of the stylus tip can be compensated by conducting probe qualification procedure based on ISO 10360:5 [54]. However, this procedure is becoming unsuitable and difficult to be applied to the stylus with the tip diameters less than 300 µm Therefore, this parameter is a limiting factor when dealing with the stylus system with tip diameters less than 300 µm.

Table 2.1: summary of the parameters for the several reviewed probing systems of the micro -CMM in the category of the conventional tactile styli design. The parameter reported as (-) are either not provided by its literature or not applicable. Please note that most report do not clearly differentiate between the stiffness of the stylus system and the overall probing system.

Probing system	Probing Force (mN)	probing mass (g)	Stylus Tip Diameter (µm)	stylus length (mm)	spherical form error of the stylus tip (nm)	stiffness at tip lateral Nm^{-1}	stiffness at tip vertical Nm^{-1}	Material of stylus system	Ref
Metas probe	**< 0.5**	**7**	**100 to 300**	**<5**	**33**	**20**	**isotropic**	-	[25][26]
NPL SCMM probe	**0.1**	**0.35**	**300**	**>5**	**-**	**10**	**isotropic**	**Shaft: Tungsten carbide Tip: silicon nitride**	[12]
IBS Triskelion A250	**0.07**	**0.16**	**500**	**8.5**	**-**	**70**	**isotropic**	**Shaft: Tungsten carbide Tip: ruby**	[34]
IBS Triskelion B-35	**0.07**	**0.075**	**70**	**6**	**-**	**13**	**20**	**Shaft: Tungsten carbide Tip: -**	[34]
IBS Triskelion C-500	**0.07**	**0.3**	**1000**	**-**	**-**	**35**	**113**	**Shaft: Tungsten carbide Tip: ruby**	[34]
Xpress Gannen Xm	**>0.01**	**0.045**	**50 to 500**	**-**	**-**	**10**	**50**	**Shaft: Tungsten carbide Tip: -**	[24]
Xpress Gannen Xp	**0.4**	**0.05**	**120 to 500**	**-**	**-**	**400**	**isotropic**	**Shaft: Tungsten carbide Tip: -**	[52]
PTB piezoresistive Probe	**<0.73**	**-**	**<300**	**7**	**-**	**-**	**-**	-	[27]
NPL Vibrating Probe	**<0.1**	**-**	**70**	**1**	**-**	**15**	**isotropic**	**Shaft: Tungsten Tip: Tungsten**	[31][32] [33]
Tri-switch Probe	**1.3**	**-**	**70**	**1.5**	**-**	**-**	**-**	**Shaft: Tungsten Tip: Glass**	[37][38]
Variable stiffness probe	**<1**	**-**	**300**	**5.6**	**-**	**410 to 610**	**910 to 2853**	-	[39] [40].

2.5. Manufacturing route of styli for micro-CMMs

As a conventional design of tactile micro-styli (which has been discussed in Section 2.4.1) is the focused in this project, the following section will provide information on the manufacturing techniques that normally used to fabricate these micro-styli. In general, advance and non-traditional machining process have been employed for this fabrication of micro-styli. These are included focused ion beam (FIB), wire electro-discharge grinding (WEDG), one-pulse electro discharge (OPED), micro electrochemical machine (micro-ECM). Furthermore, the combination of these techniques for fabrication of micro-styli are also investigated and will be explained in the later of this section.

2.5.1. Focused Ion Beam technique

Focused ion beam (FIB) is one of fabrication technique employed to manufacture stylus shaft of micro CMM. In general, FIB has been used in many fields for fabribrication of various type of devices and component including semiconductor devices and micro tools with various shapes and dimensions.

In this process, a group of high intensity ion beam in a vacuum chamber is directed to the substrate material. High energy ions that hit the target surface material will create various ion-target interactions such as swelling, deposition, milling, sputtering, implantation, backscattering, nucleation and others. However, some of these interactions are not completely separable which lead to unwanted side effects, and hence need to be avoided for some specific applications. For FIB physical sputtering process, after the ion beam hits the target surface, some atoms from this target material have been removed, and by controlling this process, the required shape, in this case is the micro tool or stylus shaft can be fabricated [55]. A sputtering yield is defined as the number of atoms ejected per incident ion, functioning as indicator for the material removal efficiency. The yield is normally in the range of 1-50 atoms per ion depending on many variables such as ion mass and target atoms, ion energy, direction to the surface of the target, target temperature and ion flux [56]. This technique, however, is not suitable for mass production as it is time consuming.

2.5.2. Wire electro discharge grinding

Wire electro-discharge grinding (WEDG) is a micro fabrication process that uses an electrical discharge in a dielectric fluid to erode material from conductive wires and produce micro shafts [57]. It is a popular technique employed in manufacturing stylus shaft with the dimension less than 100 µm in diameter [58][59][31]. WEDG has also been used to manufacture monolithic stylus system (stylus shaft and stylus tip). However, form deviation and surface finish of the stylus tip was relatively poor[60]

This fabrication method was first demonstrated by Masuzawa *et al* (1985) to manufacture micro cylinder electrodes [61]. Since then, research on WEDG concentrated on either characterising, optimising or applying the process to manufacture particular microstructures[57][62][63][64][65].

The details explanation of working principle of WEDG process can be found in many of the literature [57][61]. In general, as illustrate in Figure 2.26(a), an electrical discharge between the workpiece (cathode) and a metal alloy wire (anode) is produced from electrical pulse. The workpiece which is mounted vertically is rotated and then slowly fed in the z-direction. A wire guide is used to support the wire while its position is controlled in the *x*- and *y*-directions. As refer to Figure 2.26(b), there are three general process steps involved in producing micro shaft. The first step involves positioning the workpiece above the travelling wire and the end of the shaft is machined by feeding the wire or guide in the x- direction. Next, a rough cut is made to the shaft and the diameter of the stock material is reduced by feeding the workpiece in the z- direction. The final step is to finish the shaft cut [57].

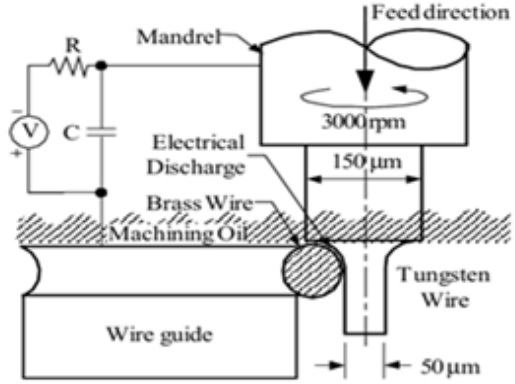

(a)

Operation	Geometry	Process Conditions
Step 1: Flat End		V = 100 V C = 1 Fh = 30 µm/s Fl = 2 µm/s
Step 2: Rough Cut		V = 110 V C = 1 Fh = 30 µm/s Fl = 3 µm/s
Step 3: Finish Cut		V = 70-80 V C = 4 Fh = 20 µm/s Fl = 30 µm/s

(b)

Figure 2. 26: (a) is the basic principle of WEDG while (b) is a typical step and condition for WEDG [57]

There are several critical criteria in WEDG that need to considered. One of this criteria is the selection of the material [58]. This is because WEDG can only fabricate a measure workpiece which its materials have a specific value of hardness and toughness. Tungsten and tungsten carbide are the two examples of material that have the hardness and toughness properties that are suitable for WEDG process. Other important criteria is, in order to get an adequately straight line in the stylus shaft, the rod material needs to be closely and correctly aligned on the rotary axis.

2.5.3. One-pulse electro discharge (OPED)

One-pulse electro discharge (OPED) technique is normally employed to manufacture the stylus tip. It is a process to form a sphere of a stylus tip on the end of the stylus shaft. In this process, a single and high energy electro discharge pulse is exposed to the end of the stylus shaft in order to melt a small part of it which later will form a sphere due to the surface tension forces before solidifying [66].

There are two crucial parameters that need to be controlled: a peak current and a discharge duration [58]. The peak current is functioned to control growth of the diameter and sphericity deviation of the stylus tip. In constrast, The volume rod material melted also increases with the increasing value of discharge energy. Besides these two parameters, the quality obtained by OPED is also dependent on the material used to make the spherical stylus tip whereby single element metal is more suitable as compared to an alloy [58].

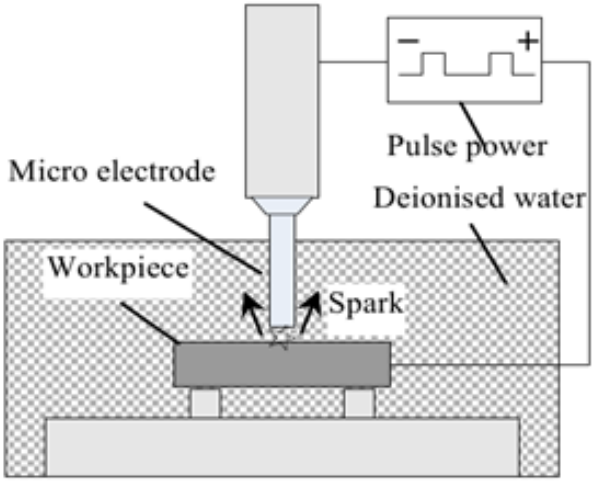

Figure 2. 27: schematic diagram of OPED process [67]

Figure 2.27 shows the schematic diagram of OPED. As explained in literature [67], this process is carried out by producing controlled electric pulse sparks in between the stylus shaft and the workpiece which are both immersed in a dielectric fluid. The distance between them is approximately less than 1 µm. Once the workpiece has been detected, the multi-function machine will generate one pulse electro discharge between the negative and positive polarity by switching it into transistor discharge type. Due to this electric discharge energy, some metal from the workpiece and the stylus shaft are melted instantaneously. This molten metal or alloy is then frozen immediately, resultant from a great cooling capacity of the deionised water in this process. Consequently, a sphere is formed on top of the stylus shaft under the liquid surface tension [67]. During these processes, predominant parameters such as the applied voltage and electric discharge duration especially the peak current were being studied [67].

2.5.4. Micro Electro-chemical machine

Micro electrochemical machine (micro-ECM) is the process of chemical erosion between the electrode and a sample material during an electrolysis process [68]. It has the capability to manufactutre a smaller diameter of the stylus shaft as compared to WEDG process and therefore is used to fabricate stylus shaft that has a diameter in less than 40 µm [69].The principles of operation for this process are well discribed in the literature, such as in [69] [70] [71] [72] [73]. In general, the electrode and the sample material are separated by the electrolyte. To manufacture a stylus shaft, a cylindrical rod of required material is used as sample material. A thin layer called a double layer is formed at the interface between the electrode and the electrolyte. The sample material is dissolved locally when the electric current is applied to the electrolyte. This process is continued until the sample material is dissolved to the required diameter.

However, in a micro-ECM process for fabrication of a stylus shaft, it is crucial to control some of the paramerers in order to obtain a required diameter of the shaft .These are the feeding rate, direction of the electrolyte, gap current, concentration and temperature of the electrolyte. [69]. To date, the main problems in this process for stylus shaft fabrication are poor surface roughness and the occurrence of pitting [73]. This might be due to the creation of localised electrochemical dissolution considering that, during machining the area of dissolution is larger than the area of the electrode tool (machining delocalisation).

2.5.5. Assembly of stylus system hybrid manufacturing technique

So far, Section 2.5 has focused on the individual techniques of manufacturing process for stylus systems. In recents years, there are a growing numbers of research works that attempts to intergrate these techniques in manufacturing the micro-styli. These are called hybrid manufacturing techniques. In 2004, Sheu [58] has demonstrated the application of the WEDG technique in combination with the OPED technique to assemble the stylus system. WEDG is used to fabricate the stylus shaft and OPED is utilised to form the spherical stylus tip at the end of the stylus shaft. However, this technique is consistently stable only for a stylus tip that has diameter above 70 µm. An attempt to fabricate diameters less than 50 µm will form an uneven spherical shape for the stylus tip. Further active investigations to optimise the OPED process are being conducted[58][74].

Other than that, Small [75] in 2010, also suggested the fabrication technique using a focused ion beam machine (FIB) and scanning electron microscope (SEM) to manufacture a stylus shaft and stylus tip sphere. This assembly process was done in the FIB/SEM chamber. Using this assembling technique requires high operator skill and is time consuming. Thus, it is not suitable for mass production. In 2012, Sheu [76] has introduced micro-styli which combines WEDG and assembly using adhesive material of commercial-available micro-ball made from glass on a micro-EDM stage. However, a poor surface condition of the stylus tip and weak bonding of the adhesive material limits the potential of this styli. To optimise this hybrid technique, some factors of control parameters need to be studied and altered. These include: sufficient time is needed for curing the adhesive material and to prevent disintegration; the amount of adhesive material applied during the adhering process between the stylus shaft and the stylus tip needs to be controlled to prevent epoxy drifting on the material of the stylus tip surface [76]: an optimisation study of the adhesion strength factor, as it depends on the amount of epoxy glue material and diameter of the stylus shaft [76][77][39].

The latest research work on this hybrid technique is the combination of the ECM process with the OPED manufacturing technique [69]. However, to date, with the current manufacturing parameters and settings, ECM techniques make it difficult to predict precisely the diameter of the stylus shaft. Nevertheless, from this work, it shows a promising candidate to manufacture micro-styli with dimensions of sub-10 µm.

2.5.6. Summary of the manufacturing route of micro-styli

From literatures describes in this section, micro-styli with tip diameter between 70 µm to 300 µm had been successfully manufactured using micro-machining techniques (which have been briefly explained above). However, some of these techniques are struggling to manufacture a micro-styli with the dimensions less than 50 µm due to the limitation in their technology. In addition, the quality of the surface condition and the uniformity of the required dimension of a micro styli are arising issues that need to further investigated especially for fabrication of micro styli with diameters less than 50 µm.

2.6. Spherical form measurement of stylus tip surface

As explained in section 2.4.3, most of the current reviewed micro-probes do not report the spherical form error of the stylus tip for their micro-styli. This is due to the lack of establish metrological instrument that capable to measure this parameter especially for the micro-styli that have tip diameter less than 300 µm.

For the micro styli with tip diameter larger than 300 µm and a stylus of conventional CMM, a form deviation of the stylus tip is smaller than the probing error [4] and can be compensated by finding the relative tip diameter in probe qualification procedure [5]. Based on the ISO 10360-5 [54], the qualification of the probe is carried out by measuring a hemisphere of the standard sphere artefact with 25 evenly distributed probing points and determining the associated least squares sphere [5]. Nevertheless, this specific qualification procedure is difficult to be conducted on the micro styli with tip diameter less than 300 µm. This is because, currently, there is no available establish calibrated reference standard [31].

However, when the diameter of stylus tip is less than 100 µm, the probing error in measurement is expected in the range of micrometre and sub-micrometre. Hence, the form deviation of the stylus tip is crucial to be determined and could not be neglected [78]. Therefore, it is beneficial in this section to review current techniques and technology used to measure form deviation of the sphere surface, especially on the stylus tip of micro-styli. Previous research works that had been conducted to measure this parameter will also be reviewed. Prior to that, fundamental of form error in 2D and 3D measurement will be described.

2.6.1. Definition of roundness and sphericity in surface geometry

Roundness in 2-D measurement and a sphericity in 3-D measurement are parameters used to describe the form deviation of the surfaces. In general, the roundness is defined as the deviation from ideal or nominal circle shape while the sphericity is the deviation from the ideal or nominal sphere shape [79][80].

2.6.2. Method of data fitting for roundness and sphericity calculation

There are several mathematical data fitting methods to determine the roundness and sphericity since a computed reference of ideal geometrical shape needed could not be physically calculated. Numerous studies have discussed these data fitting modelling methods and their improvements such as the least squares method [81], minimum zone method [82][83], maximum inscribed method [83][84], minimum circumscribed method [85][86] [84]and random sample consensus (RANSAC) method [87]. The modelling of sphericity calculation is more complicated as compared to roundness calculation, however, the basic principle behind these methods are similar. The summary of the methods mentioned above is explained as follow:

2.6.2.1. Least Squares method

A least squares sphere (LSS) or least squares circle (LSC) is fitted to lie in the mid-range of the profile where the sum of the squares of the radial residual, that is radial distances between the individual profile ordinates the circle, is minimised. A circumscribed and an inscribed circle are drawn using the centre of the LSC on the polar profile and the out of roundness value is the radial separation of these two circles. The uniqueness of the least squares circle and its centre is that there is only one that complies with the definition and the accuracy depends on the number of points measured. The latest digital instruments simplify the laboured and time consuming manual LSC calculation [81].

2.6.2.2. Minimum Zone method

The roundness error is measured using two concentric circles as references-pairs in this method. One of the circles is drawn outside to cover the whole roundness profile and the other circle is drawn inside the roundness profile to inscribe the profile. The difference between the radius of the two circles is the roundness error [81].

2.6.2.3. Maximum Inscribed method

This is the method that fits the largest possible circle inside the profile. Once the circle has been drawn, the out of roundness value is the maximum radial distance between the average profile and the inscribed circle [81].

2.6.2.4. Minimum Circumscribed method

In this method, the centre of the circle is determined by drawing a circle that has the smallest radius but still completely contains the polar plot profile. An inscribed circle is then drawn inside the profile based on the centre of the minimum circumscribed circle. The difference between the radii of the inscribed and circumscribed circle is the out-of-roundness value [81].

2.6.2.5. Random Sample Consensus (RANSAC) method

This method was first introduced in 1981 and was proposed by Fischler and Bolles [88]. Since then, this method has been applied and improved in fitting the data in various of shape dimensions [87][89][90][91]. The advantage of RANSAC among many is that this method does not constrain to a specific dimension and shape.

RANSAC is an iterative method to estimate the mathematical model from a set of observed data that contains outliers. A standard RANSAC algorithm proceeds in the following general way. First, a randomly selected minimal data subset of the input data is computed using a suitable method of model parameters fitting. Second, the support data from all other data that are tested against the fitted model is selected as consensus set for this model. Lastly, the model parameters are estimated from the consensus set. This procedure is repeated for a fix number of iterations resulting either a model is rejected because not enough points as part of the consensus or a refined model together with a corresponding consensus set size [91].The RANSAC paradigm extract shapes by randomly drawing minimal sets from the point data and construct the corresponding shape primitively. A type of geometric primitive is uniquely defined by the smallest number of points required or called as a minimal set. The candidate shapes are then tested against all points in the data to determine the number of the points that are well approximated by the primitive (called the score of the shape). After a certain number of trials, the shape that approximates the most points is extracted and the algorithm continues the remaining data. [87].

2.6.3. Review on Roundness and sphericity measurement techniques on spheres

In this section, the measurement techniques and instrument used to measure roundness and sphericity of a sphere surface will be reviewed. This review will be divided into two parts: first part is reviewing the measurement technique and technology for sphere with diameter in the millimetre and larger range while second part is for sphere with diameter less than 500 µm.

2.6.3.1. Roundness and spherical form measurement for sphere diameter larger than 500 µm

For roundness measurement, there are variety of models (from standard industry ones to high accuracy special system) of commercial metrological roundness measuring machine available in the market such as instrument from Taylor Hobson [92], Mahr [93] and Mitutoyo [94] . Also, many commercial conventional CMMs are capable to perform roundness measurement of the part diameter larger than 500 µm. Nevertheless, only one commercial metrology instrument is found to measure sphericity directly. This instrument is known as sub-aperture stitching interferometer manufactured by QED technology [95]. Its technology consists of the combination of Fizeau interferometer, sub-aperture stitching technique and variable optical null technique. It can measure aspheric surface up to 200 mm in diameter and suitable for optical lens measurements [95] [96].

There are also numbers of research work focusing on the development of the sphericity measurement for the large diameter sphere. Griesman *et al* from National Institute of Standards and Technology (NIST) have developed a metrological instrument known as 'XCALIBIR' diameter and form of sphere [97]. This instrument consists of spherical Fizeau interferometer along with a setup of optical components and also employs stitching algorithm technique. A silicon sphere with nominal radius of 46.8 mm is used in this work. The form error is estimated about 88 nm. PTB also develops the interferometer for sphere measurement [98][99][100]. It consists of two spherical Fizeau interferometers with the combination of two side measurement principles. Absolute diameter and topography of the sphere are obtained from this measurement. A silicon sphere with 93 mm in diameter is used in this measurement. The uncertainty of measurement of 5 nm is estimated from this measurement. Hagino *et al* [101] from Mitutoyo also developed a sphericity measurement system which targeted suitable industrial accuracy application. Several sphere with diameter

from 10 mm to 30 mm several material are employed as the test-workpiece. In this system, a sphere will be manipulated using a manipulation stage and a Fizeau interferometer is applied to the sphere. Stitching algorithm technique is also employed.

2.6.3.2. Roundness and spherical form measurement for sphere diameter less than 500 µm

Over the last decade, the high accuracy measurement of a roundness and sphericity of the sphere with diameter less than 500 µm have been difficult to conduct, due to the limitations of the measuring technologies. Thus, there is lack of commercial metrological instrument available for this purpose. Nevertheless, in recent years, with the enhancement of the knowledge and technologies, there are research works conducted by several researchers to measure this surface quality of the stylus tip sphere. For the roundness measurement of a circle with diameter less than 500 µm, Fan *et al* [78] had developed a roundness measuring system. This system consists of two traceable miniatures Michelson interferometer, together with application of two point methods for error separation. The sphere with diameter of 250 µm is used and rotated. The roundness error obtained in this experiment is approximately about 100 µm. In contrast, for sphericity measurement, Kung *et al* [102][25][4], have established the absolute calibration technique which applied error separation method for diameter and sphericity of the stylus tip sphere. This method uses three nominally identical sapphire sphere with 1 mm in diameter. This three identical sphere are measured against each other in various configurations using micro-CMM and thus the result of absolute diameter and sphericity mapping error will be obtained. This meant that a standard calibration artifact does not require in this method. This measurement produces a promising result where it forms error of 33 nm [4].The traceability of this calibration method rely on the particular micro-CMM. However, because of the limitation of this particular micro-CMM, this method is difficult to be measured and applied to the stylus tip sphere that have diameter below 100 µm. Another research had been conducted by Chen [59], determined the sphericity deviation of micro stylus using optical microscope together with the surface reconcruction techniques. The micro styli used in this work have tip diameter of 50 µm. By using volumetric intersection algorithm, derived from optical projection principle, and 3D mapping algorithm with least square optimization, a 3D volumetric data of the stylus tip are obtained. The minimun zone optimization is also employed to evaluate the sphericity deviation of the styli. This system including the optical

microscope have been calibrated using calibrating block and thus metrological characteristic related to the positional error have been traceable to the primary standard of length. However, because of the optical distortion and abberation of the lens, and also optical behaviour of the measurement, the measurement uncertainty of sphericity deviation are within 500 nm. Alternatively, a new technique of probe qualification proedure of micro stylus are also been proposed [103]. This technique employed a standard gauge block as the standard reference artefact. This gauge block consists of one standard gauge block and another two support gauge blocks which had wrung at the edge of gauge block. The micro-styli involved in this process have a tip diameter of 50 µm. By conducting this new probe qualification procedure, the sphericity deviation of the micro-stylus tip can be compesated and the unceratinty of this procedure was reported as 72 nm.

2.7. Key knowledge gap and research question

Throughout this chapter, the background information for the context of this work has been presented. This includes the main context on the review of probing system of micro-CMMs, manufacturing route for stylus system and spherical form measurement of the stylus tip sphere. From this review, there are three key knowledge gap can be identified associated with the development of the stylus system of the micro-CMMs.

The first key knowledge gap is about the dimension of the stylus system. Majority of the current available probing systems employ the stylus system with the tip diameter bigger than 50 µm. With the increasing demand in measuring a feature of micro-product with dimension less than 50 µm, the current available stylus system will become unsuitable for this measurement task. However, It is a challenging task to shrink the tip diameters of stylus systems to the dimension of sub-10 µm, as there is a lack of established development methods able to address the known scaling issues. Therefore, the critical issues affecting the stylus system should be determined.

The second key knowledge gap is about the characterisation method of the stylus system. The needs to characterise the critical parameter of the stylus system become important when the dimension of the stylus is shrinking down. This includes the mechanical strength of the stylus system in a present of the applied forces. To date, majority of the

characterisation works reported in the literature focused on the sensing mechanism of the probing system.

As the spherical form deviation of the stylus tip surface is vital to be determined, there are difficulties, in practical, to be measured especially for the stylus tip with dimension in less than 300 µm. This is due to the lack of the appropriate metrological intsrumensts that have capabilities in accuracy to perfom the measurement. Hence, it would be a challegging task in development of micro-styli with the dimension in sub-10 µm. Therefore this limitation, which is recognised as the final key knowledge gap, should be addressed in this thesis.

From these key knowledge gaps, the **Thesis Objective** has been derived, and hence a set of **Research Questions** can be defined. These **Research Questions** associated with the three **Thesis Objectives** and are numbered accordingly.

- **Research Questions** related to **Thesis Objective 1**: To design a new stylus for tactile probes with a stylus tip diameter less than 10 µm and investigate the required manufacturing techniques
  - 1.1) What are the influence factors to develop stylus in sub-10 µm dimension and how will they differ from those of a stylus above 100 µm?
  - 1.2) What is the maximum workable aspect ratio that a stylus with tip dimension in sub-10 µm region could have? How could the optimum aspect ratio of stylus be determined?

- **Research Questions** related to **Thesis Objective 2:** To characterize the mechanical properties of the new stylus and hence verify the design.
  - 2.1) Can the strength of the new styli under certain loads be tested? If it can be tested, how might it be possible to validate the result of the experiment?
  - 2.2) What is the result of this styli test? Are there any differences between high aspect ratio styli with low aspect ratio styli and how is the performance compared to the design rule?

2.3) From this testing result, is it suitable for the new stylus to be fitted to current available micro-probe and can it be used to perform high aspect ratio measurement?

- **Research Questions** related to **Thesis Objective 3:** To reduce measurement uncertainties by developing new technique for 3D spherical form measurement of micro-sphere. By developing this new technique, a reference standard from micro sphere can be potentially realised for qualification of micro-probe with stylus tip diameter less than 10 µm

3.1) Can the 3D form error of the spherical surface of the stylus tip with a stylus tip diameter in less than 50 µm be examined?

3.2) How is the performance of the new measurement technique of micro sphere measurement?

Chapter 3: Design consideration of the stylus system for micro-CMMs

3.1. Introduction

As the aim of this thesis is to develop the stylus system of micro-CMM that consists of dimension in sub-10 µm, the influence factors to develop the stylus at that scale need to be identified. In general, it is a challenging task to scale down styli from the smallest commercially-available dimensions (of the order of 100 µm) to a diameter of 50 µm or less. Many issues which are not relevant at the macro-scale, will be significant at the micro- and nano-scale. Therefore, in this chapter, a set of design rules will be introduced that address the influence factors affecting micro-CMM measurements at micro- and nano-scale. This set of design rules developed for the eventual manufacture of stylus systems with diameters of the order of 10 µm. These influence factors are all interlinked; hence, for a better description of design rules, the influence factors have been divided into five categories. The suggested categories of influence factors are geometrical consideration, forces during measurement, physical condition, material selection, and manufacturing process and technique. This design rules are written in a general way, intended to be universal enough to be a guideline in designing the stylus system for many micro-CMM applications.

3.2. Geometrical consideration

3.2.1 Background

The selection of geometrical dimensions of the stylus system is crucial in fulfilling an increasing demand for high aspect measurement of miniatures product using micro-CMMs. This is because, a stylus with suitable combination of geometrical dimension of stylus shaft and stylus tip will help to optimise other influence factors such as the stiffness of the stylus, effect of forces and probing speed during measurement and hence the measurement error is expected to be minimum in value. However, selection of geometrical dimension of the stylus also depend on the application of the stylus itself and hence, to an extent, compromises between some influence factors are needed. For instance, to have a high aspect ratio

measurement, the effective length of the stylus should be increased. Consequently, the stiffness will be decreased and a larger error in measurement may occur.

In this section, the design rules on stylus shaft and stylus tip dimensions including length and diameter will be identified and explained. Although only few papers discuss the geometrical considerations of stylus system (see chapter 2), it can be understood that these influence factors are unwritten general rules known by researchers. Therefore, the general views on the stylus shaft and tip dimensions and aspect ratio of the stylus will be formalised in section 3.2.2 and 3.2.3. In addition, the mathematical relationship between diameter of stylus shaft and tip, and effective length of stylus will be explained in 3.2.4.

3.2.2 Diameter of Stylus shaft and stylus tip

To start the technical discussion associated with the geometry considerations of the stylus system, the geometrical dimension of the stylus shaft and the stylus tip are the first aspect to be discussed. Based on ISO 10360 [18], the stylus tip is the component of the stylus system that establishes a contact with the measured workpiece while the stylus shaft is the component that connects the stylus tip to the probing sensor. Normally, the design of stylus shaft has two parts, which are the upper part of the stylus shaft and the effective part of the stylus shaft as shown in Figure 3.1. The upper part of the stylus shaft function as a holder of the stylus for connection to the probing system while the effective stylus shaft transmits the position of the stylus tip during measurement to the probing sensor.

The first design rules relate to the diameter of the stylus tip. The diameter of the stylus tip sphere must be smaller than the dimensions of any entrance features of the surface to be measured. Furthermore, the diameter of the stylus tip should be bigger than the diameter of the effective stylus shaft. These two common rules have been implemented by researchers and scientists in terms of design and selection of the stylus system for micro-CMMs. These rules have been mentioned specifically in some literature [32] [5]. As features of workpieces or measured surfaces get smaller, the current stylus systems for micro probes will not be able to measure them. As a result, nowadays, increasing research focuses on shrinking the stylus system for micro probes. Other reason to have smaller diameter of stylus shaft compared to stylus tip is to allow flexibility in the direction of approach relative to the probe body of the stylus tip in measuring the workpiece. In addition, the centre of the stylus tip sphere should

be manufactured aligned with the centre axis of the stylus shaft. Alternatively, if this design rule or this condition cannot be achieved, the difference in distance between the centre of the stylus tip and the centre axis of the shaft has to be specified and applied in the measurement.

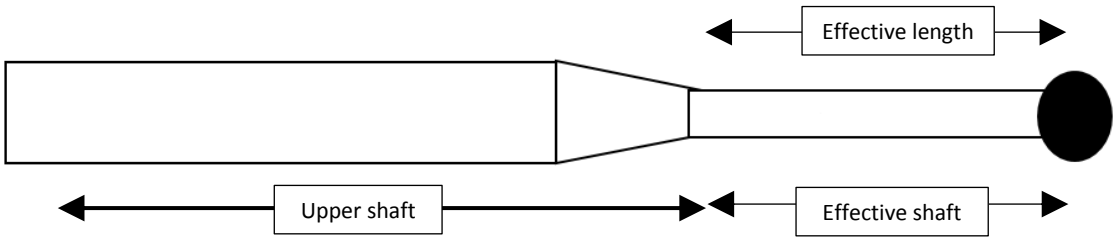

Figure 3.1: structure of stylus system

3.2.3 Effective length and Aspect ratio

The aspect ratio of the stylus should be higher than the aspect ratio of the features that it is intended to be measured. The maximum aspect ratio of the measured surface needs to be determined before selecting the suitable aspect ratio of the stylus for micro probes. As in Figure 3.2, the aspect ratio is defined as the length divided by the width. Generally, for the stylus system, there are two types of definition of aspect ratio for stylus shaft; effective aspect ratio and mechanical aspect ratio. The effective aspect ratio describes the overall aspect ratio of the stylus that is involved in the measurement. In this case, the effective aspect ratio of the stylus is defined as the effective length of stylus divided by the diameter of the stylus tip. In contrast, the mechanical aspect ratio demonstrates the properties of the stylus shaft. Therefore, the mechanical aspect ratio of the stylus is defined as the effective length divided by the diameter of the stylus shaft. Note also that, for a few designs and applications of the stylus, the aspect ratio is defined by the total length of the stylus rather than effective length of stylus. Thus, the effective length and diameter of the stylus shaft, and the diameter of stylus tip are the important parameters in defining the aspect ratio of the stylus for micro probes.

Ideally, the stylus shaft should be as short as possible to increase the stiffness of the stylus [32], hence, avoiding stick slip phenomena in measurement. This means that a low aspect ratio of stylus will be seen as a ‘good’ stylus for general manufacture. However, the demand to measure high aspect ratio of the features conflict with this idea of the good stylus. Thus, there are considerable to produce the stylus that is stiff enough, free from stick slip

problem, and that is able to measure the high aspect ratio of the features on the measured surface. The selection of appropriate effective aspect ratio of stylus is also crucial to avoid collisions between the stylus shaft and the edge of some features of measured workpieces due to the deflection of the stylus during probing. Thus, the determination of the maximum effective aspect ratio of a stylus used in a measurement is influenced by the applied contact forces, the elastic deflection of stylus and the material properties of the stylus tip and the measured workpiece. Therefore, the maximum effective aspect ratio is expected to vary depending on the material of the stylus tip and measured workpiece. Further explanation of the effect of forces and material properties will be described later in section 3.3 and section 3.5.

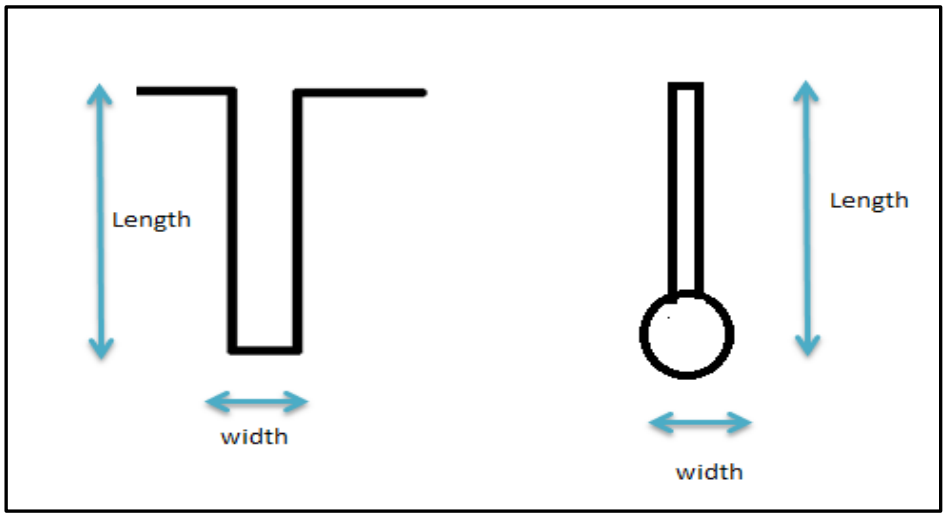

Figure 3. 2: Aspect ratio of the measured surface and stylus

3.2.4 Relationship between stylus tip diameter, effective length and diameter of stylus shaft

In the previous discussion, the general rules related to the diameter of the stylus tip, diameter and length of the stylus shaft have been reviewed. For the next discussion, the mathematical relationship between diameter of the stylus shaft, length of the stylus shaft and diameter of the stylus tip will be formulated. These derivations draw directly on several well-known theoretical models and so first-principles detail is mostly omitted here. The first equation is based on the Hertz theory of the acceptable probing force [25]. Note that section 3.3.2.1 provides discussion on the practical probing force. This equation is also known as the equation of allowable probing force, has previously been formulated as [26]:

$$F_p = 21\ \frac{\sigma^3\ {r_t}^2}{E^{*2}} \tag{3.1}$$

Where,

F_p : Allowable probing force,
r_t : Radius of stylus tip,
E^* : Reduced Young's modulus,
σ : Material's yield strength

Any bending or other distortion of the stylus shaft during probing, resulting from a probing force, constitutes an error in transmitting the position of the stylus tip to the rest of the probe. So, a second equation is used to define the amount of elastic deformation of the stylus shaft expected under acceptable probing force [2]. Lateral displacement of the free end of the shaft relative the fixed end is the only significant error term and it will be dominated by bending effects for all practicable aspect ratios. Then, using simple elastic deflection beam theory with the assumptions that the stylus shaft is a laterally end-loaded uniform cylindrical cantilever gives:

$$W_s = \frac{64\ F_p\ \ l^3}{3\pi\ E\ \ d_s^4} \tag{3.2}$$

Where,

W_s : Elastic deflection,
l : Length of the stylus shaft
d_s : Diameter of stylus shaft
E : Young modulus of the stylus shaft material

The third equation is related to allowable stylus deflection, W_a [51]. Figure 3.3 describes the details for better understanding of Wa. The equation is stated in the equation (3.3) below

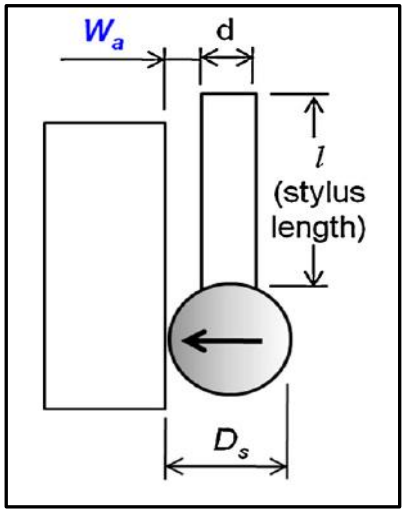

Figure 3. 3: Allowable stylus deflection, Wa [51]

$$w_a = \frac{1}{2}(d_{tip} - d_s) \tag{3.3}$$

Where,

W_a : Allowable stylus deflection
d_{tip} : Diameter of stylus tip

A collision between stylus and workpiece will occur if the stylus elastic deflection is larger than the allowable stylus deflection: $W_s > W_a$ [51]. For the condition when $W_s = W_a$, the equation 3.2 (substitutes equation 3.1 into equation 3.2) and equation 3.3 becomes:

$$\frac{1}{2}(d_{tip} - d_{shaft}) = \frac{64\ (21\frac{\sigma^3 {r_t}^2}{E^{*2}})\ l^3}{3\pi\ E\ d_s^4} \tag{3.4}$$

The equation 3.4 can be solved for $\boldsymbol{d_{tip}}$, giving:

$$\boldsymbol{d_{tip}} = \frac{d_{shaft}^4 \pm \sqrt{d_{shaft}^8 - 4\left(\frac{224\,\sigma^3\ l^3}{\pi\ E\ E^{*2}}\right) d_{shaft}^5}}{2\left(\frac{224\,\sigma^3\ l^3}{\pi\ E\ E^{*2}}\right)} \tag{3.5}$$

Through the combination of these three-related theoretical idea, the equation (3.5) demonstrates that acceptable value of the arrangement of the diameter of the stylus shaft, the diameter of the stylus tip and the length of the stylus shaft can be calculated. Selecting some geometrical dimensions to meet the application needs, others can be set explicitly (this equation (3.5) can also be altered accordingly in order to find the diameter of the stylus shaft). If the parameters satisfy equation (3.5) (or the relevant inequality based on it), the stylus will operate in the elastic region and the force exerted to the stylus will not damage the surfaces of stylus tip and test-workpiece, and also there is low possibility for a collision between stylus shaft and test- workpiece.

3.2.5 Summary of the design rules for geometry conditions:

(i) The diameter of stylus tip sphere must be smaller compared to the dimensions of the features of the surface to be measured.

(ii) The diameter of the stylus tip should be bigger than the diameter of the stylus shaft.

(iii) The aspect ratio of the stylus should be higher than the aspect ratio of the features that intends to be measured

(iv) Selection for the diameter of the stylus tip is depend on the geometrical condition of the stylus shaft, including its diameter and effective length. The mathematical relationship between the diameter of the stylus shaft, length of the stylus shaft and the diameter of the stylus tip is:

$$d_{tip} = \frac{d_{shaft}^4 \pm \sqrt{d_{shaft}^8 - 4\left(\frac{224\,\sigma^3\ l^3}{\pi\ E\ E^{*2}}\right) d_{shaft}^5}}{2\left(\frac{224\,\sigma^3\ l^3}{\pi\ E\ E^{*2}}\right)}$$

3.3. Forces during measurement

3.3.1 Background

Forces play critical roles in micro-CMM measurement and become more crucial when measuring microscale products with smaller stylus systems. It is important to understand the effect of forces in measurement and select a suitable value of force in order to avoid damage in both stylus and measured workpiece, as well as to minimise the error in measurement. There are several types of forces that have to be considered for the design rules of the stylus system of the micro-CMM. The main types of forces are those involved in single point probing mode, additional ones occurring in scanning mode and forces associated with the bending of the stylus as illustrated in Figure 3.4. These forces will be introduced and discussed in detail in section 3.3.2, section 3.3.3 and section 3.3.4.

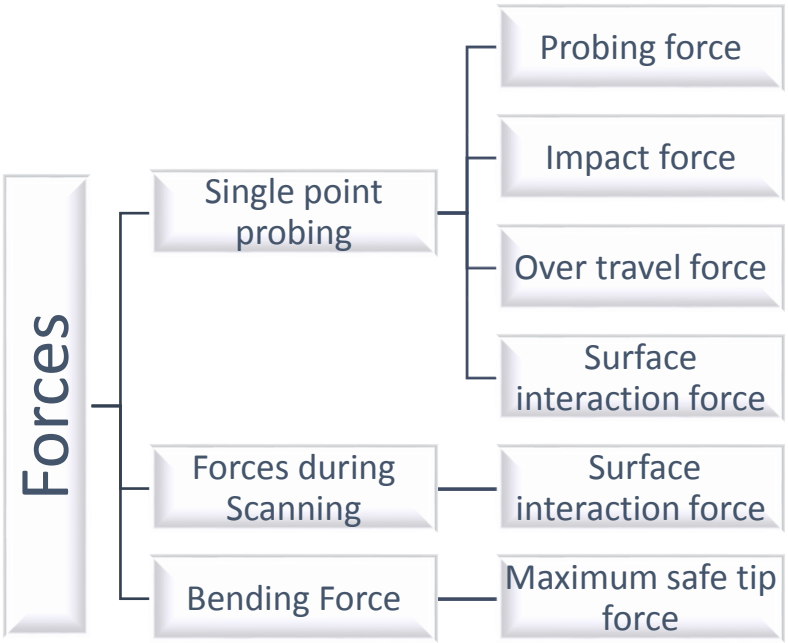

Figure 3.4 : Type of forces during micro-CMM measurement

3.3.2 Force during single point probing

Force exerted during the cycle of single point probing can be categorised according to several phenomena as illustrated in Figure 3.4. As a touch triggering probe [104] [105][106] is a common and widely used in conventional CMM, it is a good example to explain the overview of force during single point probing. Nevertheless, as the type and operation of the sensor mechanism varies among current available probing system in the market, some of the forces described for touch trigger probe, may not occur during particular examples of single point probing.

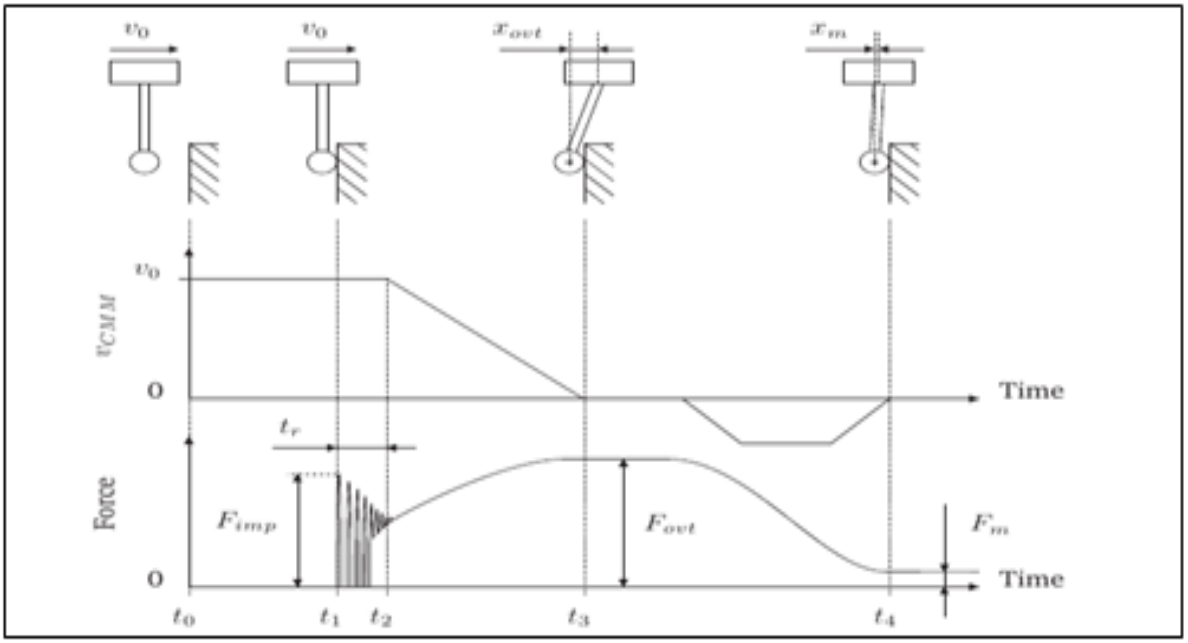

Figure 3. 5 : Probing Force during Single Point Probing for touch triggering force [21]

Figure 3.5 is graph of a behaviour of force applied to a touch trigger probe and a behaviour of the velocity of the CMM, which both behaviours observed against time during process of approach, contact and retract cycle of single point probing. It shows that the Impact force occurs at time t_1 when the stylus tip first contacts the surface. After the first contact with the surface, the tip will bounce several times before the contract is registered and a signal is sent to the micro-CMM controller after time t_2. To prevent macroscopic plastic deformation between probe tip and the surface, the velocity during second and subsequent collisions must be smaller than first contacts. This impact force has a strong relationship with the probing speed, the effective mass at the probe tip and material properties of the stylus system [107][21].

Overtravel force occurs after initial contact at time t_1 until the time t_3 where the probe has stopped moving toward the surface [107]. This force occurs due to the stiffness at stylus tip (later, the detail of stiffness will be explained in section 3.4.4). In Figure 3.5, notice that there are overlapping regions between overtravel force and impact force between time t_1 and t_2.

The effect of surface tension from adsorbed films should also be considered during probing. Thus, a surface interaction force should be added to the probing force. There are four major types of surface interaction force: the Van der Waals force; the Casimir force; the electrostatic force; and the hydrostatic force. The effect of this surface force during measurement is very significant in micro scale measurement. The surface interaction force depends on the environmental condition such as temperature and humidity [21].

3.3.2.1. Allowable Probing force

The forces exerted during single point probing is often known as probing force or, in some literature, contact force. It could consist of one or a combination of impact force, overtravel force and surface interaction forces. It might also involve other force which is not specified above, such as a triggering force (depending on the type and sensor mechanism of the probe). In the majority of the research conducted in this field, the value of the probing force is one of the main parameters that has been reported. This is because an excessive probing force will cause damage to the surface of the stylus tip or measured workpiece.

Clearly, with the development of stylus tips for micro-CMMs having sub-micrometres scale, the probing forces need to be reduced in order to prevent plastic deformation either on the surface of the stylus tip or the measured workpiece. However, there are arguments about the value of probing force that should be applied without damaging the stylus tip or the surface of test workpiece. Generally, Dai [29] states that the value probing force should be in order of micro-newton. Leach *et al* [32]has suggested that probing force should be less than 0.1 mN, while Liebrich [30] stated that the maximum value of probing force is 0.2 mN. Fan [108] also suggests that the probing force should be less than 1 mN. In contrast, the existing styli of micro-CMMs have various values of probing force. For instance, probing force for the METAS stylus system is less than 0.5 mN, for the NPL capacitive stylus system is 0.1 mN, and for the TUE/Gannen stylus system is less than 0.4 mN. All of these three stylus

systems use a stylus tip greater than 100 µm in diameter. For stylus systems with stylus tip diameter less than 100 µm such as PTB/Werth fiber Probe and Mitotuyo UMAP stylus system, the value of probing force is recorded in the micronewtons range. This wide variation in the design values of the probing force can be understood in practical term. In order to avoid damaging on either surface, the selection of probing force depends on the material properties, the radius of the stylus tip itself and the compliance of the probe system.

To estimate the appropriate probing force to be applied in a measurement, a theoretical value which is called the allowable probing force is introduced. The allowable probing is defined (using ideas from Hertz contact theory) as the force where the shear stress at a point somewhat below the surface exceeds a critical value and plastic deformation starts[22][26]. It can be calculated using equation (3.1) from section 3.2.4 [26]. However, this definition is difficult to measure in practised, and therefore, it is used only as a theoretical guideline in the selection of the suitable force applied to a measurement. Alongside this theoretical definition is exerted force, the combination values of all components of probing forces, which should not exceed the value of allowable probing force as calculated in the equation (3.1). This is because, with the consideration of the material properties and the requirements of the stylus tip diameter in this equation, calculated value of allowable probing force is expected to be the maximum force that can be applied in order for the stylus to operate in the elastic region (or the stresses occurring during contacting process do not exceed the plastic deformation condition of both surfaces). The detailed explanation of the relationship of material properties with allowable probing force will be described in section 3.5.

3.3.2.2. Impact force

In single point probing, introduced in section 3.3.2, impact force is the first force that occurs when the stylus tip contacts the surface under test. This impact force has been discussed in detail by Pril [22], Meli [26] and Bos [21][107]. The impact force has been recognised as a force resulting from the almost instantaneous stopping of the tip (while the probe continues to have some forward velocity) and the effective mass of the probe at the point of contact. The effective mass in this scope covers the net effect at the tip of all the masses and moments of inertia of the probing systems that are involved in accelerating the

probe tip including any components attached to it [22][107]. The impact force has been expressed [21][22][26] :

$$F_{imp} = \sqrt[5]{\frac{125}{36}\, m_t^3\ \Delta v^6\ \ E_{red}\, r_t} \tag{3.6}$$

With,

$$\frac{1}{E_{red}} = \frac{1-v_1^2}{E_1} + \frac{1-v_2^2}{E_2} \tag{3.7}$$

Where,

F_{imp} : Impact force
m_t : Effective Mass at stylus tip
Δv : Stylus speed
r_t : Radius of stylus tip
E_{red} : Reduced Young's modulus
E_1 : Young's modulus for material of stylus tip sphere
E_2 : Young's modulus for material of measured surface
v_1 : Poison ratio of material for material of stylus tip sphere
v_2 : Poison ratio for material of measured surface

According to the relationship in equation (3.6), the impact force is greatly influenced by the mass of the stylus, the stylus speed, material properties and diameter of the stylus tip. In developing the smaller stylus, the impact force needs to be reduced to prevent plastic deformation during probing. Hence the mass of the stylus and the stylus speed also need to be reduced. Nevertheless, the mass of the stylus and the stylus speed are the two parameters which are not directly proportional to each other. These parameters and the relationship between them will be discussed in detail in section 3.4.2.

3.3.2.3. Overtravel force

As briefly described in section 3.3.2, overtravel force occur after an initial contact between the stylus tip and the measured surface. Once a small, pre-set deflection of the stylus has been registered to the probing system to trigger the position measurement, the micro CMM will be instructed to stop, but the micro CMM, and so the probe body, needs some travel distance to decelerate before it can come to a complete stop. This travel distance is called overtravel distance and causes the overtravel force. The overtravel force is resulted from overtravel distance and the effective stiffness at the stylus tip. Assuming, reasonably,

that the effective stiffness is constant over the distances involved, the overtravel force is [22][107]

$$F_{ovt} = C_t \ x_{ovt} \tag{3.8}$$

Where,

C_t : Effective stiffness at stylus tip
x_{ovt} : overtravel distance

The overtravel distance, mainly depends on the movement parameters of the micro-CMM and its probing system. Because the overtravel distance is defined as the distance travelled by the stylus tip from initial contact until the micro-CMM has finished decelerating, an assumption that the machine acceleration is approximately constant allows it to be expressed simply as [22]:

$$x_{ovt} = v_0 t_r \ + \ \frac{v_0^2}{2a_{cmm}} \tag{3.9}$$

Where,

v_0 : Stylus approach speed
t_r : Reaction time
a_{cmm} : Acceleration of micro-CMM (assumed constant)

Hence, the overtravel force depends on the stylus speed, for which there is further discussion in section 3.4.2, and on the stiffness at a stylus tip, which will be discussed in the section 3.4.4. According to the discussion on the probing force earlier in section 3.3.2.1, it is clear that the overtravel force needs also to be reduced as the probing force is suggested to be reduced for the development of smaller stylus systems. This will lead to reducing the effective stiffness of the stylus tip and the overtravel distance. In contrast, the overtravel force will also influence the selection of the stylus approach speed. Based on the equation 3.9, the stylus speed can be derived as

$$V_{ovt} = -t_r a_{cmm} \ + \ \sqrt[2]{t_r^2 \ a_{cmm} \ + \ \frac{170 \, r_t \, \sigma_y^3 \quad a_{cmm}}{c_t \, E_r^2}} \tag{3.10}$$

Where,

V_{ovt} : overtravel stylus speed
t_r : Reaction time
a_{cmm} : Acceleration of CMM
r_t : Radius of stylus tip
c_t : effective Stiffness at stylus tip
σ_y : yield strength

At this stage of the discussions, recognising that the aim is to reduce the probing force, it has been established that the stylus speed, effective mass, stiffness of the stylus and the material characteristics of both stylus system and measured surface are parameters of significant influence on the probing forces. Therefore, each of these parameters will be addressed in a following section of this chapter: stylus speed will be discussed in section 3.4.2, stiffness in section 3.4.4 and material characteristics in section 3.5

3.3.2.4. Surface interaction force

In dealing with micrometre-sized stylus systems, the surface interaction force needs to be considered as one of the potentially significant components in the probing force. This is because for any components, including a measured surface or a stylus tip sphere, that have dimensions less than one millimetre, the surface forces exerted on the bodies become dominant as compared to gravitational forces [109]. Thus, for micro CMM measurement, the effect of surface force is becoming significant and cannot be neglected automatically, especially when using a smaller stylus tip to measure a miniature product.

Van der Waals force, electrostatic attraction force, Casimir Forces, and hydrostatic or capillary force are types of surface forces. Van Der Waals forces are the inter-molecular forces that occur due to the polarization between atoms and molecules in the surfaces interacting during the probing process. The Van Der Waals forces are related to the Hamaker constant, the separation distance between the closest regions of the test surface and the the stylus's tip sphere and the diameter of the stylus tip. The van der Waals force is expected to increase with decreasing diameter of the stylus tip. The Hamaker constant is important in calculation of the Van Der Waals force, but is itself acquired from several calculation methods based on empirical data [110]. Thus the value of the van der Waals force will be different, dependent on the application and situation.

The significant effect of the van der Waals forces is this force will be influenced by the surface roughness of the stylus tip and the surface under test [21] [110]. The van der Waals force is reduced with the increasing of surface roughness from both stylus tip sphere and measured surface[111][109]. Moreover, the contact area between stylus tip sphere and measured surface will cause plastic deformation of the roughness peaks in the surface. This plastic deformation will increase with the increasing of contact area during probing force [21].

To reduce the van der Waals force, the contact area between the surfaces needs to be as smaller as possible. Therefore, it is suggested that a hard material is preferable as the stylus tip material because harder material will reduce the local deformation in the situation of high contact pressure [109] [21].

The second type of surface force is electrostatic attraction force. Electrostatic attraction force arises from the electrical charge generation or charge transfer between two bodies, in this case the stylus tip surface and surface under test. The charge generation between bodies may arise from friction and difference in contact potential [112][107]. Charge theoretically will flow between materials with different contact potentials when they are brought into contact together until both materials have reached an equal (local) contact potential [109]. The magnitude of this force strongly depends on the materials of the both bodies [110]. The electrostatic force between spheres can be written as [111]:

$$F_e = \frac{4\pi\sigma_1\,\sigma_2\,r_1^1 r_2^2}{\varepsilon_0 d_{cc}^2} \tag{3.11}$$

Where,

σ	: Surface charge density
ε_0	: Permittivity in vacuum
$\mathrm{d_{cc}}$	: Distance between the sphere centers
r	: sphere radius

Equation (3.11) shows that the electrostatic force is increased rapidly when the separated distance between two materials is reduced. The magnitude of the charge density will be higher when the separation distance is smaller than the mean free path for air if compared to the surface charge density when the separation is by air at atmospheric pressure [109].

To reduce the electrostatic force, methods of grounding conductor materials and the use of insulator materials are applied in some circumstances [113]. However in the development of the micro styli for micro CMM , it is suggested as better to select materials so that there is a small contact potential difference between the stylus tip and the measured surface [109], [21].

Casimir force arises due to attraction of two uncharged material bodies due to modification of zero-point energy related with the electromagnetic modes in the space between this two bodies [21]. This type of surface force is considered weak and can often be

neglected, especially when the separation distance between stylus tip and surface larger than 0.2 µm [21]. However the Casimir force will become stronger than van der Waals Force and electrostatic attraction force when the separation distance between stylus tip and measured surfaces is below several hundred nanometres [114]. Thus, the existence of the Casimir force during probing in micro CMM measurement could not be neglected.

Hydrostatic or capillary force is usually a dominant force in micro structure scale [110]. The equation of capillary force can be simplified using [112]

$$F_s = 4\pi r_t \gamma \tag{3.12}$$

Where r_t is stylus tip radius while γ is the surface tension of the liquid. Hydrostatic force occurs due to the surface tension in the thin layer of liquid film between two surfaces caused by condensation and contamination processes. This force will increase with high humidity, long contact time and large radius of curvature [107]. When the two surfaces are brought together, the liquid films of both surfaces will join together. Surface tension will then tend to maintain a liquid bridge even if the surfaces separate slightly. In other words, an adhesion effect will occur [110], [115]. The adhesion force created from these phenomena are influenced by the shape of the liquid bridge and the amount of condensed water [115]. The hydrostatic force will increase with increasing relative humidity and will decrease when the surface roughness of the contact area is increased [21]. In order to reduce the surface force related to capillary effects, it is has been recommended that the relative humidity should be below 60% and preferably between 30 to 40% RH [21].

In relation to these surface interaction forces, the research studies by Arai [111], Bos [21], and Van Brussel [109] on the comparison of the types of surface interaction forces and the gravitational forces shows an important point. In these studies, as illustrate in Figure 3.7, Arai used the SiO_2 sphere that contacts with silicon plane surface, while Bos (as shown in Figure 3.8) used sapphire sphere with aluminium plane surface. In Figure 3.9, Van Brussel used silicon sphere with contact of flat jaw surface of gripper. Although they used different materials in their research, all of them draw the same conclusion. The gravitational force from all of these studies is observed to be dominant when the sphere diameter is in the millimetre range but the surface forces are dominant in the micro-scale range. The results of these studies also show that the hydrostatic force and electrostatic force are dominant within

the surface force at the micro-scale range. This concludes that in the measurement and handling of miniature products, the surface interaction forces are important and must be considered. According to the concept of allowable probing force in section 3.3.2.1, the sum of forces occurring during measurement have to be reduced if the geometrical dimension of the stylus is reduced, and thus the sum of the surface interaction force should also be reduced. However, when the dimension of the stylus are in micro scale range, as the sum of surface interaction force is dominant over the gravity force, its value should be carefully investigate and selected in order to avoid adhesion condition between surface of stylus tip and measured surface and hence reduced measurement error.

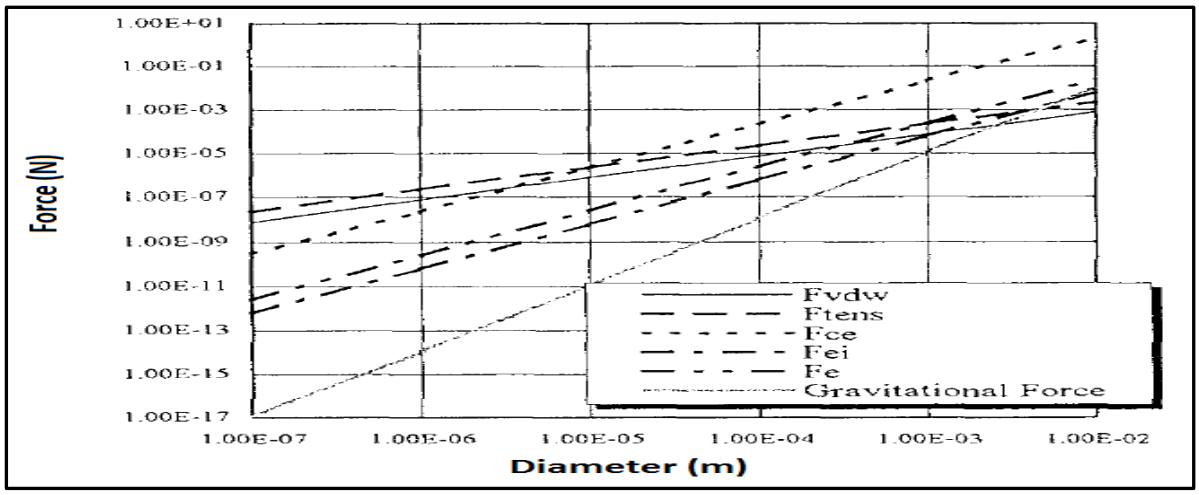

Figure 3. 6 : Comparison between surface forces and gravitational force of the SiO2 sphere and Si surface plane [111]

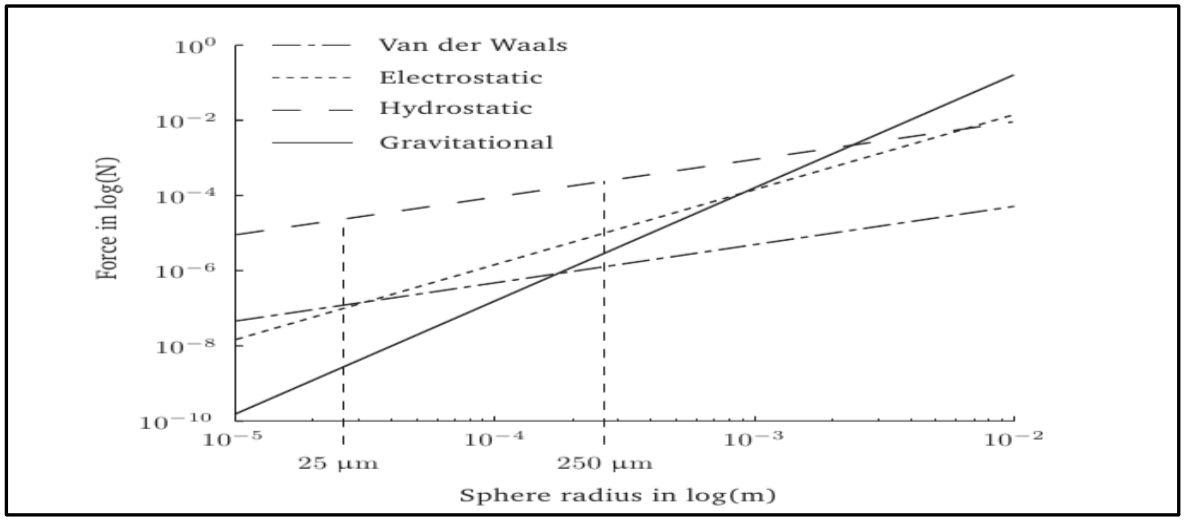

Figure 3. 7: Comparison between surface forces and gravitational force of the Sapphire sphere and Al surface plane [21]

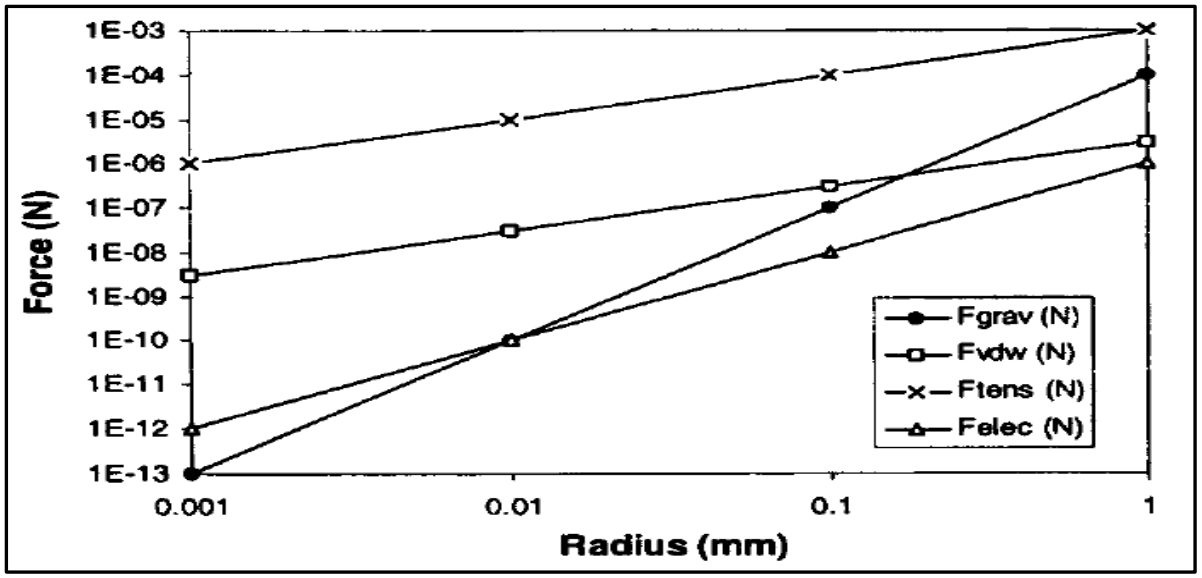

Figure 3. 8 : Comparison between type of surface forces and gravitational force for Si sphere and gripper [109]

3.3.3 Force during scanning

Generally, micro-CMMs can perform single point probing and also act in scanning mode. Section 3.3.2 focuses on the forces related to single point probing method. In this section the forces involved with the scanning method will be explained.

Scanning is the mode of probing where the stylus tip makes continuous contact to the surface. The stylus tip is guided along a straight line on the surface continuously to take a set of surface data on the fly. The scanning mode has the capability to take more point data compared to single point probing mode. However, the scanning mode is less precise as compared to the single point probing as the scanning mode often tends to suffer additional uncertainty due to stylus shaft bending and change in probe head sensitivity as the tip contact changes [116]. Other than that, stick slip effect and the deformation in the metrological reference loop could occur during scanning [21].

Forces associated with the scanning mode include surface interaction forces, and static and dynamic friction force. The static friction force will limit the smallest data to be measured while dynamic friction force will cause stick slip effect in the measurement in the scanning mode [107]. This stick slip effect could be described by this equation:

$$\Delta y = \mu\ (\Delta x\ + \frac{F_s}{C_t}) \tag{3.13}$$

Where,

Δy : Stick slip distance
Δx : Probe deflection during scanning
μ : Friction coefficient
C_t : Effective stiffness at a tip
F_s : Surface interaction force

Hence, in the scanning mode, the surface interaction force and the stiffness at the stylus tip play critical roles. The importance of both parameters can be understood as the surface interaction force increased in the continues and long contact in certain time between stylus tip and measured surface while the stiffness properties will determine the bending of the stylus shaft during scanning mode. It can also be seen that the stick slip effect will be large when the stylus tip has a low stiffness. To reduce the stick-slip effect and improve the scanning measurement, as suggested in the literature [21], a vibrating stylus system for micro CMMs should be used to reduce the friction coefficient, μ, and attempts made to optimize the suspension stiffness of the probe system.

3.3.4 Force associates with bending or deflection of the stylus

So far, the discussion of forces during micro-CMM measurement in section 3.3.2 and 3.3.3 has been related to the forces that could cause damage either on the surface of the stylus tip or the surface of measured test-workpiece and consequently might introduce to the measurement error. In this section, the effect of force on the stylus shaft will be investigated. When the probing force is applied to the stylus, the stylus shaft will bend or deflect.

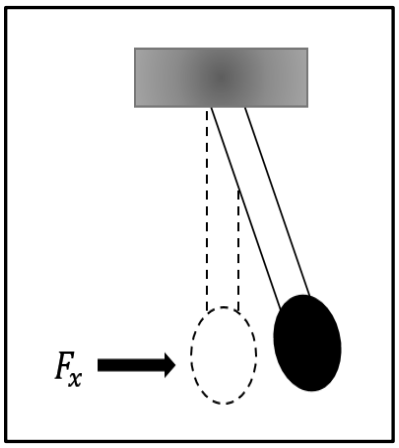

Figure 3. 10: Force in the horizontal direction

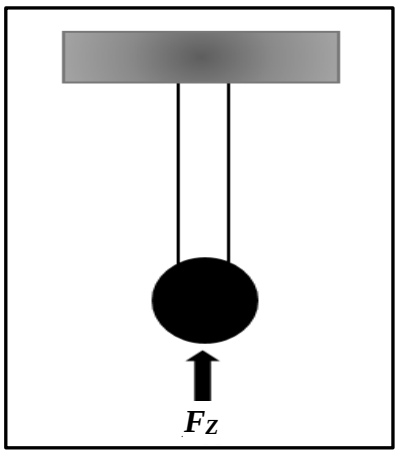

Figure 3. 9: force in vertical direction

Normally the probing or contacting force is applied (or can be resolved) in two directions. One force (component) *Fz,* is in the vertical direction, that is, parallel to the orientation of the stylus shaft, while other component of applied contacting force F_x is in the horizontal direction, perpendicular to the orientation of the stylus shaft. Figure 3.9 and Figure 3.10 illustrate these directions of applied forces. This external horizontal force causes stylus shaft bending, which can be calculated using the theory of simple cantilever deflection, as in equation (3.2) in section 3.2.4 where the elastic deflection W_s is introduced. Note that, among other restrictions, equation 3.2 applies only for the elastic deflection of the stylus shaft.

This force needs to be accurately determined or estimated. This is because the bending of the stylus shaft will affect the measurement in three ways. Firstly, the bending of shaft will introduce a measurement error. As mentioned in section 3.2.2, the function of the stylus shaft is to send the signal of position of the stylus tip to the probing sensor during measurement and the bending of the stylus will be included in the positional signal, leading to an error in the measurement result. Secondly, the bending of the stylus could cause a collision between the stylus shaft and the test-workpiece and this collision must be avoided during measurement. Consequent measurements resulting from such collisions may not be valid as the principle of micro-CMM measurement permits only that the stylus tip should be contacting the test-workpiece. Thus, an allowable stylus deflection, W_a, was introduced and has been described in equation (3.3) [51]. Furthermore, to avoid the collision, the elastic deflection, W_s, should be smaller than allowable stylus deflection, W_a.. The third condition for restricting the bending of the stylus shaft is to avoid permanent damage to the stylus system. When the bending of the shaft reaches the elastic limit point of the shaft and a plastic deformation occurs, the stylus cannot be used anymore. The stylus shaft will break if the ultimate strength of the shaft is reached, but prior to this any yielding will introduce a permanent set to the shape of the shaft and so confound the probe calibration. This condition depends crucially on the magnitude of the horizontal force applied. A vertical force applied to the tip contributes to the stress in the shaft and so reduces the maximum stress available to support bending without yield, but in practical designs the difference is generally small enough to be neglected. Therefore, the force before the elastic limit is reached and the plastic behaviour starts to occur should be determined, with consideration only of bending adequate

for this purpose. In these design rules, a special term for this force is introduced and called the maximum safe tip force. The maximum safe tip force is then defined as the transverse force on the stylus tip that causes initial plastic behaviour in the stylus shaft. To have a good stylus system, a maximum safe tip force should be bigger than the allowable probing force to ensure that the actual contacting forces are only determined by the allowable probing force.

3.3.5 Summary of design rules for forces

(v) In the micro-scale range, the probing force for single point probing is a combination of impact force, overtravel force and surface interaction forces. The actual probing force must always be less than allowable probing force. The allowable force depends on the material properties and the radius of stylus tip. Using the previously defined notation, the allowable probing force should obey the relationship:

$$F_p = 21\,\frac{\sigma^3\, r_t}{E^2}$$

(vi) The impact force in the single point probing will be influenced by the probing speed, material properties, probing mass and stylus tip diameter with this relationship:

$$F_{imp} = \sqrt[5]{\frac{125}{36}\, m_t^3\ \Delta v^6\ E_{red}\, r_t}$$

(vii) The overtravel force depends on the stylus stiffness with the following relationship

$$F_{ovt} = C_t\ x_{ovt}$$

(viii) The surface interaction force has potential contributions from the van der Waals force, electrostatic attraction force, Casimir force, and hydrostatic or capillary force. The surface interaction force has an important influence in micro-scale range compared to the gravitational force and cannot be neglected.

(ix) To reduce the van der Waals force, the contact area between the surface should be as small as possible and it is preferable to select a hard material for the stylus tip.

(x) To reduce the electrostatic force, a stylus tip material with a small contact potential difference between the tip and the measured surface is preferred.

(xi) In order to reduce the surface force related to the hydrostatic or capillary force, it is recommended that the relative humidity should be above 10% and below 60%, with a preference that it should be between 30 to 40% RH.

(xii) The scanning mode is influenced by the surface force, friction force and the stylus stiffness with the following relationship:

$$\Delta \boldsymbol{y} = \boldsymbol{\mu}\,(\Delta \boldsymbol{x} + \frac{\boldsymbol{F_s}}{\boldsymbol{C_t}})$$

(xiii) To avoid the collision between stylus shaft and measured workpiece, elastic deflection of the stylus shaft , W_s, should be smaller than allowable stylus deflection, W_a

(xiv) The maximum safe tip force should be determined and should be bigger than allowable probing force.

3.4. Physical condition

3.4.1 Background

In this section the parameters associated with the physical aspects of the stylus system for micro CMMs will be discussed. The general aspects of geometrical condition have been introduced in section 3.2, while in section 3.3, the aspects related to the force during probing have been discussed. To continue the discussion of design rules, this section will focus on other important physical conditions such as the moving mass of the entire probe system, stylus speed during probing and stiffness both at the stylus shaft and at the stylus tip. Also, the surface quality of the stylus tip sphere will be considered, especially the 3D spherical form of the sphere surface. These discussions of the physical conditions have been placed after the discussion of the forces (section 3.3) because all of them have influences on the forces during measurement by a micro CMM. Thus, constraints and effects of the forces in probing are best introduced first.

3.4.2 Probing speed vs moving mass

Equation (3.6) in section 3.3.2.2 shows that the probing speed and mass of the entire stylus system play an important factor in reducing the impact force. As the impact force can be a major component of the probing force, both probing speed and moving mass need to be reduced. However, to achieve a specified impact force, there is an inverse relationship, so decreasing the mass enables the use of rather higher stylus speeds. Derived from equation (3.6) in section 3.3.2.2, the velocity to cause a specified impact stress (in effect, a maximum allowable probe speed) can be expressed as [21] :

$$\Delta v_{imp} = \sqrt[2]{\frac{(1.61\pi)^5 \ r_t \ \sigma_{0.2}^5}{30 \ E_{red}^4 \ m_t}} \tag{3.14}$$

Where,

m_t : Effective mass at stylus tip
E_{red} : Reduced young modulus
r_t : Radius of stylus tip sphere
$\sigma_{0.2}$: yield strength

Equation (3.14) shows how the selection of a maximum probing speed must be compromised against the effective mass at the stylus tip in order to avoid damage. Section 3.3.2.2 provides the definition of the effective mass at the stylus tip. Using this equation, Bos [21] has calculated that with a stylus tip diameter of 150 µm and probing speed of 1 mms^{-1}, the effective mass should be below 35 mg. Pril [22] has estimated the mass should be below 20 mg to allow a probing speed of 1 mms^{-1} for a 300 µm stylus tip diameter. Clearly, previous research has considered 1 mms^{-1} stylus speed leading to an effective stylus mass in the milligram range. However, the stylus tips were always above 100 µm in diameter and there is no evidence that this speed can be applied to the stylus tip with diameter below 100 µm. The current demands of miniature products need smaller diameter stylus tips to perform the measurement and according to equation (3.14), in order to reduce the impact forces, the stylus needs to move slower with lighter effective moving mass.

To discuss the question of selecting reasonable values for the stylus speed and the effective mass for a micro-CMM stylus having a tip sphere diameter of less than 100 µm, two basic conditions need to be comprehended. The first condition is the stylus should, for practical reasons, move relatively fast and the individual probing event itself should be

finished within 10 µs in order to reach the probing uncertainty of 10 nm [22]. The second condition is the higher stylus speed can cause damage to the surface under test. Vliet had discovered that the surface can be damaged during probing using a stylus speed of 3 mms^{-1}, stylus tip 1 mm and force higher than 10 N [117][118]. Hence, based on this two conditions and the equation (3.14), it is suggested that for stylus tip diameter less than 100 µm, the stylus speed should be less than 0.1 mms^{-1} [34]. As the stylus tip diameter gets smaller, into the sub-10 µm region, the stylus should move even slower. Thus, a problem could then arise over the time constraint in probing and probing uncertainty. On the other hand, some experiments done previously have shown that the acceptable experimental stylus speed is higher by factor of ten compared to the calculated theoretical prediction [26]. Since the effective mass has relationship with the stylus speed, its maximum value can be easily calculated after the selection of the stylus speed. From the discussion above, to decide the reasonable value of stylus speed or effective mass, information about the stylus tip diameter, the probing uncertainty and material properties of the stylus also need to be considered.

3.4.3 Surface quality condition of stylus tip sphere

Surface quality at the stylus tip is another factor to be considered when designing the stylus system for a micro-CMM. This is because the surface quality of the stylus tip sphere will contribute to the probing uncertainty of measurement as imperfections in the stylus tip surface geometry will introduce systematic errors during measurement.

In the majority of stylus designs for conventional CMMs, a sphere is employed as the shape of stylus tip. This is because the sphere offers a symmetrical shape which provides isotropy for the point of contact in measurement [5]. To have a good surface quality, the stylus tip sphere must have a low surface roughness, uniform sphere diameter, small centric offset of the sphere from the stylus shaft and a small spherical form error. The spherical form error is particularly important here because, in practice, this parameter becomes more difficult to control and to determine when the dimension of the stylus system becomes smaller. If the stylus tip sphere were perfect, only information on the effective sphere diameter would be needed.

There is not much in the literature that specifically discusses the theoretical aspects and guidelines on surface quality of the stylus tip for micro-CMMs. Nevertheless, the important notes about this matter stress that the surface roughness and roundness of the stylus tip sphere must be smaller than the surface roughness and roundness of the surface to be measured [32]. The values of roundness and centre offset errors have been targeted to be less than 1 µm [119]. For the last decade, there have been difficulties in measuring surface roughness and surface roundness of the micro-CMMs stylus tip sphere, due to the lack of appropriate metrological instruments that have the capabilities and accuracy needed. Nevertheless, as reviewed in section 2.6.3.2, recent enhancement of the technologies has allowed several researchers to attempt to measure this surface quality of the stylus tip sphere.

The other important matter related to the surface quality condition of the stylus tip sphere is that the stylus tip sphere should be free from contamination or, at least, the contamination at the stylus tip surface should be minimized. The sources of contaminations at the surface of stylus tip sphere may originate from metal oxide particle, loose debris such as particles and atmospheric contaminates [120][121]. The stylus tip tends to pick up the particles or debris from the surface under test during scanning. The present of contaminate particles at the stylus tip sphere will cause unexpected geometrical error and bias error during repeated measurements and hence will affect the uncertainty of measurement [120]. The appropriate cleaning method at the stylus tip surface should be applied to ensure that the contaminations level at the stylus tip sphere have been minimized or eliminated. Further investigation on the effect of contamination on the stylus tip spheres and effective cleaning methods to eliminate contamination particles can be found in the literatures [120] [122][123].

3.4.4 Stiffness of stylus system

During probing, effective stiffness at tip is an important parameter that needs to be considered. A probing system of a micro-CMM with high stiffness will have a higher natural frequency and so a minimum tendency to oscillate excited by forces exerted at the tip or from inertia during acceleration compared to low stiffness stylus system. It also induces higher mechanical stress in the sensor and thus the electrical sensitivity will be increased. Therefore,

even a small amount of deflection will produce a good electrical signal to noise ratio. However, a high stiffness stylus system will require more probing force to deflect the flexure/suspension of the probe sensor. For a smaller stylus tip sphere, high surface pressures will be occurred due to the high forces in the measurement [28]. As a result, significant elastic or even plastic deformation will occur, leading to measurement error. In contrast, a stylus with low stiffness will face a problem from the stick slip effect during scanning. In this section, the stiffness at the stylus shaft, stiffness at the region of contact and the issue of the isotropy in the stiffness will be discussed.

Contributions to stiffness relevant during measurement can be observed in the three parts of a micro-CMM, which are in the micro-CMM itself, in the probing system and at the region of contact between the stylus tip sphere and the measured surface [21]. The stiffness of the micro-CMM can be compensated with the calibration process of the CMM. Since the stiffness of the CMM has a higher order of magnitude compared to stiffness of probing system, it can be neglected here. Moreover, the stiffness of the CMM is out of scope of this document. In contrast, the stiffness of the probing system consists of the stiffness at the sensor mechanism and the stiffness at the stylus shaft. Various research into the stiffness analysis and modelling at the sensor mechanism of the probing system includes the investigation of the optimum sensor designs for normal probes [22][124][125], and fibre probes [108][126][127]. In this section, to address the ***Thesis Aim***, the stiffness at the stylus system will be the main focus of discussion.

The stiffness of the stylus system is defined as the capability of a styli to resist deflection when subjected to an applied contacting force and can be mathematically described using Hooke's law. How the contact force relates to the deflection of the stylus has been explained in section 3.3.4. As the function of the micro-CMM is to position the probe and stylus tip sphere on the measured surface, the measurement data will also be influenced by the deflection of the stylus shaft. Consequently, as explained in section 3.3.4, the lateral (or transverse) deflection of the shaft will introduce an error in measurement. Hence, it is important to determine the stiffness value of the shaft prior to measurement and to estimate the deflection so as to minimise the error in measurement. It is usually suggested that the stylus shaft be as stiff as possible to avoid bending [32]. In addition, the stiffness value of stylus shaft will limit the suitable probing sensor mechanism that it can be attached or

mounted to. This is due to fact that the stiffness at the stylus shaft should be higher than the stiffness of the suspension for probe sensor mechanism or that the overall movement at the stylus tip arising from the suspension is bigger than the estimated deflection of the stylus shaft [114]. When the stiffness at the stylus shaft is higher than the stiffness of the probing sensor mechanism, the force applied to the stylus during probing and the positioning motion of the stylus tip will be transferred directly to the probing sensor mechanism [114]. Moreover, the sensitivity of the measurement will be decreased when the stiffness of the stylus shaft is similar to the stiffness of the suspension for probe sensor mechanism [21].

Now, an analysis of stiffness of the stylus shaft will be considered. To start the stiffness analysis, the direction of the applied force needs to be determined. As mentioned in section 3.3.4, the direction of force can be applied at the z-axis and in xy-axis (in Figure 3.6 and Figure 3.7 in section 3.3.4). Since the stylus shaft has an upper part and an effective part as illustrated in Figure 3.1, the analysis of stylus stiffness has to consider both parts. Also, there are several variant designs in styli in micro-CMM probing systems and thus the calculation equations for their stiffness also will be different. In this section, four case studies of the stiffness will be described: stiffness equation at the effective part of stylus shaft, stiffness for total length for conventional stylus system, stiffness for total length for taper design of stylus system and the stiffness of the fibre probe. All of these analyses are derived from a model using cantilever beam theory [128].

Because it is so directly involved in the measurement, determining the stiffness of the effective part of stylus shaft is crucial. Based on the well-known models for an axially loaded rod and a simple cantilever with a transverse end load, the stiffness at effective stylus shaft for the deflection in the horizontal direction ($K_{x,y}$) and vertical direction (K_z) can be calculated based on the following equations:

$$K_{x,y} = \frac{3EI}{l^3} \tag{3.15}$$

$$I = \frac{1}{4}\pi r_{shaft}^4 \tag{3.16}$$

$$K_z = \frac{AE}{l} \tag{3.17}$$

Where, $K_{x,y}$ is a stiffness in the *x*, *y* directions, K_z is a stiffness in the *z* direction , I is the second moment of area of the stylus shaft, E is Young's modulus of shaft material, l is effective length of the stylus shaft, r_{shaft} is radius of stylus shaft and A is a cross sectional area of the stylus shaft. These equations assume the shaft is a uniform circular cylinder.

To analyse the stiffness of the overall length of the stylus shaft, two designs of styli have been considered. The stylus shown in Figure 3.12 is the conventional design for micro-CMM styli while the design in Figure 3.13 is normally used for styli manufactured by electro chemical machining (ECM). The stiffness calculation for both designs will involve the diameters of the upper and effective parts of the stylus shaft and the total length and effective length of the stylus. The stiffness analyses for both designs are based on the solution suggested for two series-connected uniform cylindrical cantilever beams that have different diameters [128].

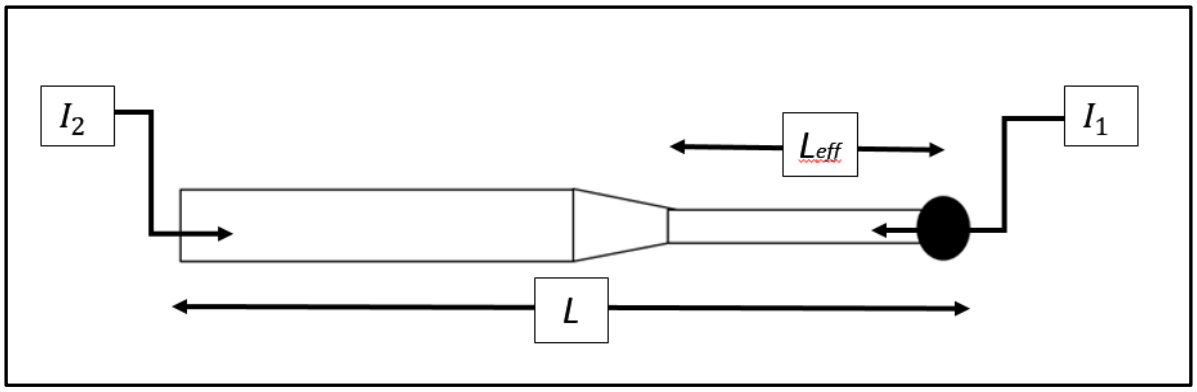

Figure 3. 11: structure of conventional design styli

For the conventional design in Figure 3.8 and with the force is applied in the perpendicular direction to the orientation of the stylus, the stiffness is

$$K_{xy} = \frac{3EI_2}{L_{eff}^3 + L^3 - [L_{eff}^3 (I_2/I_1)]} \tag{3.18}$$

$$I_1 = \frac{1}{4}\pi r_{eff}^4 \tag{3.19}$$

$$I_2 = \frac{1}{4}\pi r_{upp}^4 \tag{3.20}$$

where L_{eff} is the effective length of the stylus shaft, L is the total length of stylus, I_1 is the second moment of area of the effective part of stylus shaft, I_2 is the second moment of area of the effective part of stylus shaft, r_{eff} is the radius of the effective part of the stylus shaft and r_{upp} is the radius of the upper part of the stylus shaft.

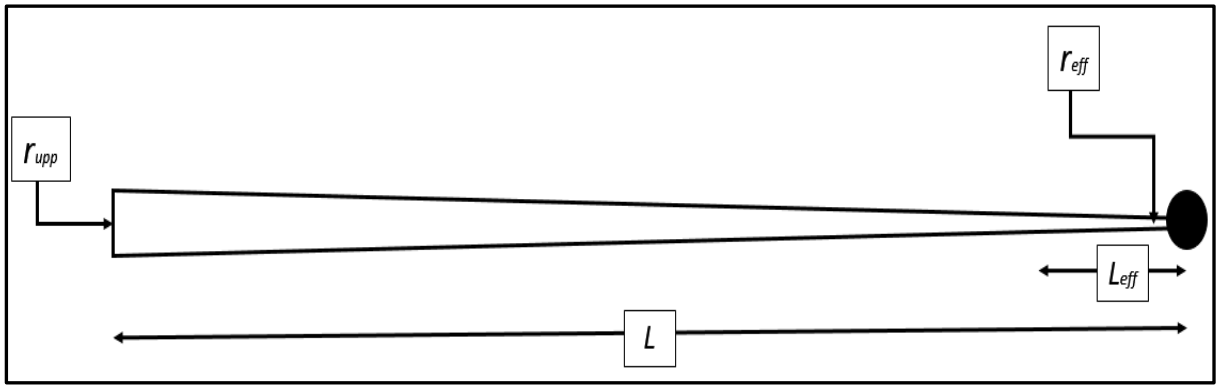

Figure 3. 12: structure of tapered design of styli

Similar to the stiffness analysis of conventional design of stylus, the calculation of taper based design of stylus with the force direction applied perpendicular to the orientation of the stylus, the stiffness can be calculated based on the following equation:

$$K_{xy} = \frac{3E\pi r_{upp}^3 r_{eff}}{4L^3} \tag{3.21}$$

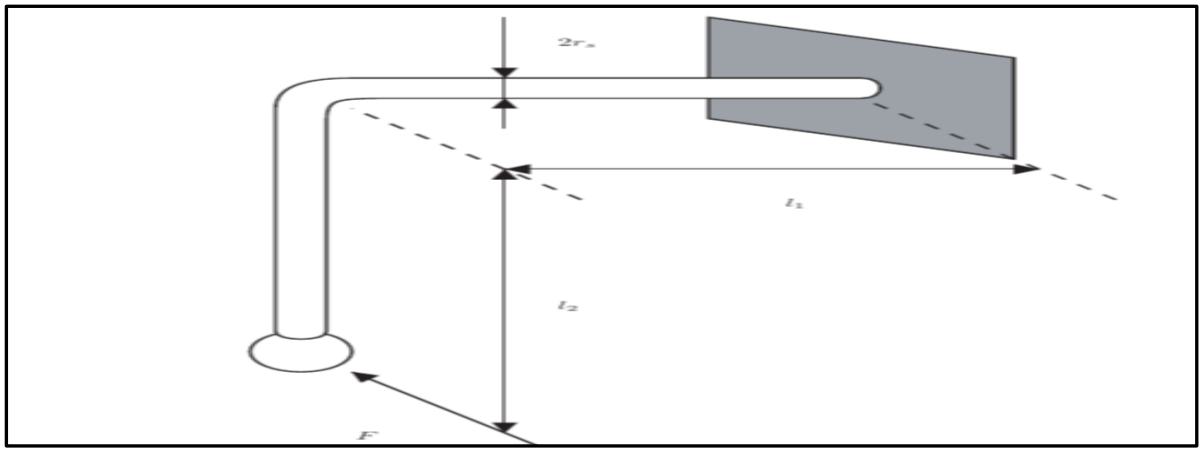

Figure 3. 13: Stiffness model for the fibre probe [21]

For a more complicated construction design of the stylus shaft, such as the fibre probe in Figure 3.14, the stiffness analysis will also be more complicated. The fibre probe consists of a fibre as a stylus shaft and is assumed to have uniform properties with a constant diameter circular cross-section. If the bend is a right angle and has a small radius, the stiffness can be modelled as a pair of connected cantilevers for which the equation has been given as [21]:

$$K = \frac{3E\pi r_{shaft}^4}{4l_1^3+4l_2^3+12l_1l_2^2(1+v)} \tag{3.22}$$

Where v is poisson ratio of the material.

Note that, from all these analyses, the stiffness at the stylus shaft depends on the lengths and diameters of each section of the stylus shaft and the Young's modulus of its material. Note, also, that the effective stiffness at the stylus tip will depend as well on the type of suspension or probing that stylus shaft is attached to.

As mentioned previously, the third part of micro-CMM where the stiffness is important to be considered is at the region of contact between the stylus tip sphere and the measured surface. This is because, it can potentially cause deformation at the measured surface. As discussed in section 3.3.2.3, the stiffness at the stylus tip sphere influences the overtravel force and the overtravel force will increase with the increasing of the stiffness. Thus it will also affect the stylus speed, as in equation 3.8 in section 3.3.2.3. As mentioned in section 3.4.2, the stylus speed not only has a relationship with the effective mass, but is also limited by the stiffness at the stylus tip. Furthermore, the stiffness at the tip can cause significant effects in the scanning mode of probing. Equation (3.13) in section 3.3.3 shows that the stiffness at the tip regulates, in combination with the surface force, the stick slip effects. It can be seen that, the effect of surface interaction force during scanning will increase when the stiffness at the tip is decreased. The stick slip effect during scanning also increases with the decreasing of the stiffness at the tip. The relationship between stiffness and surface interaction force would be more crucial for stylus tip below 100 µm. This is because at and below this dimension the surface interaction force is incrementally increased, causing more serious adhesion conditions between the surface of the stylus tip sphere and the measured workpiece. Thus, to prevent this probing error condition, the effective stiffness at the stylus tip, and so also the stiffness of the stylus shaft, needs to be increased [114].

Isotropy of the stiffness is a crucial parameter in the probing system of the micro CMM. Isotropy of the stiffness means that the stiffness of the stylus system has the same stiffness value in all directions. Although it is very challenging to achieve complete isotropy, it is very important for a probing system (both the suspension and stylus shaft) to have a similar stiffness in all directions, otherwise the contact force will vary for different contact vectors, as will the deflection of the stylus. As the micro CMM movement is based on the deflection of the stylus, this will lead to a measurement error. Thus, when the stiffness of the stylus is not isotropy, the movement of the stylus needs to be referenced to the direction of the stylus movement and not simply to its deflection [107][28]. Fan [108], Nesterov [125], and Claverley [114] have demonstrated that the stiffness of their probe designs are isotropic.

3.4.5 Summary of design rules for physical condition

(xv) Relationship between (maximum) stylus speed and effective mass for a given maximum contact stress due to the impact is (using the previously defined notation):

$$\Delta v_{imp} = \sqrt[2]{\frac{(1.61\pi)^5 \; r_t \; \sigma_{0.2}^5}{30 \; E_{red}^4 \; m_t}}$$

(xvi) In general, higher stylus speeds are preferred in order to reduce overall measurement times, reduce risk of thermal drift, and so on. Selection of the stylus speed depends on the effective mass, stiffness at the stylus tip, diameter of stylus tip sphere, and material properties of both stylus tip and measured workpiece.

(xvii) A good surface quality is necessary at the stylus tip sphere, evaluated in comparison to the desired measurement precision and uncertainty. It should have a low surface roughness, a uniform sphere diameter, a small value of roundness deviation and a small centric offset of the sphere from the stylus shaft.

(xviii) The surface roughness and roundness of the stylus tip sphere must be smaller than the surface roughness and the (local) roundness of features on the measured surface.

(xix) The contamination at the surface of stylus tip sphere should be minimized (ideally, eliminated) by using appropriate cleaning methods..

(xx) The effective stiffness at the stylus contact point depends on the stiffness of the stylus shaft, which is influenced by the length and diameter of the stylus shaft and the Young's modulus of its material, and the type of suspension or probing that the stylus shaft is attached to.

(xxi) Stiffness of the stylus shaft should be higher than the stiffness of the suspension for probe sensor mechanism or that the overall movement at the stylus tip arising from the suspension is bigger than the estimated deflection of the stylus shaft.

(xxii) Stiffness should be isotropic (or in practical terms, nearly equal in all directions).

(xxiii) As mentioned in design rule (VII), (XII), and (XIV), the stiffness at stylus tip sphere will give significant effect to the probing force, stylus speed, surface force and stick slip effect during scanning

3.5. Material selection for stylus system

3.5.1 Background

From the early discussion in section 3.3.2.1, the material properties of the stylus play an important role in the probing, especially on the force exerted in the measurement. Young's modulus is one of the most important material properties to be considered when selecting the material for the stylus shaft and stylus tip.

For conventional CMMs, steel, ceramic and tungsten carbide are all materials regularly used for stylus shafts. However, for micro-probes, tungsten and tungsten carbide are the most popular materials for stylus shafts [31][39][12]. Tungsten and tungsten carbide are preferred because they have a high Young's Modulus, favourable strength, toughness and hardness properties, and can be used reliably for manufacture using micro-machining processes[58][76].

The materials for the stylus tip sphere in micro-probes, both currently available in the market or in the research and development, are usually glass, silicon nitride, ruby, and sapphire [21][37][129]. However, for a stylus tip with diameter in the range of ten micrometres, only glass materials are available for manufacturing the stylus tip, owing to current limitations in manufacturing techniques. Another important point is that the selection material for the stylus tip sphere must also refer to material of the surface to be measured. The details of these material properties will be discussed in the next section.

3.5.2 Young's modulus of material

Young's modulus or elastic modulus is a measure of stiffness of an elastic material. The Young's modulus of a material is defined as the ratio of stress to engineering strain during the linear elastic behaviour. For a device of given geometry, selecting a material with higher value of Young's modulus will lead to the need for higher stress to generate a certain strain, that is it will require more load or force to deform its shape. Therefore, because a stylus system should be stiff (hard to distort), a high value of Young's modulus is a characteristic needed in the stylus shaft [34]. However, the Young's modulus of the stylus shaft material is not the only major factor that determines the stiffness of the stylus shaft. As discussed in section 3.4.4, the length and the diameter of the stylus shaft are strong factors that influence the stiffness of the stylus shaft. A key functional requirement is the ability of the stylus shaft to resist bending deflection during probing. Equation (3.2) in section 3.2.4 shows that bending stiffness is proportional to Young's modulus and so a high modulus material should be selected for the stylus shaft in order to minimize its bending.

Elastic deflection, or distortion, at the contact point between the stylus tip sphere and the measured surface will also directly affect the measurement. This effect (modelled in equation 3.1 in section 3.2.4) depends on the scale of the contact and the effective Young's modulus (reduced modulus) of the contact region. The reduced Young's modulus between the stylus tip sphere and the measured surface can be calculated using equation 3.6 in section 3.3.2.2. It is mainly scale-independent, but might increase when the contact size approaches the grain size of the workpiece [26]. Selection for a higher reduced Young modulus can lead to larger allowable probing forces, implying generally that a material with a high Young's modulus should be used for the tip sphere.

So, a material with high Young's modulus is most suitable for the stylus shaft and stylus tip sphere because it is an important factor that favourably influences the stiffness at the stylus shaft, amount of bending at the stylus shaft, and also the allowable probing force.

3.5.3 Yield strength of the measured workpiece

For the micro CMM measurement at the micro- and nano-scales, it is important to ensure that the applied contact forces during probing do not cause plastic deformation on the surfaces of either the stylus tip or the measured workpiece. To avoid such plastic damage, the yield strengths of the materials for both surfaces are considered in the estimation of the allowable probing forces, as discussed in section 3.3.2.1. For the case where the material of measured workpiece is softer than the material of stylus tip, the yield strength of measured workpiece is the crucial one for the calculation of allowable probing force. However, if a measured workpiece of a harder material than the stylus tip, the yield strength of the stylus tip should be used in order to avoid plastic deformation and permanent damage occurring at the surface of the tip. Therefore, it is crucial to determine the material of the measured workpiece prior to selecting suitable styli and conducting the measurement task.

3.5.4 Adhesive and abrasive wear

The selection of material for the stylus tip sphere should also take note of the material of the surface intended to be measured. This is because an appropriate stylus tip material will avoid or minimise adhesive and abrasive wear when contacting the measured surface. This is clearly more critical in the scanning mode of probing. In essence, adhesive wear as the local pressure between asperities on two surfaces causes them to temporarily 'weld' together and subsequently break, pulling a small particle from one surface that might become free or might stay adhered. Material pick up, one of the important concerns in the present context, is the phenomenon where the stylus tip sphere will collect the particle or contamination on the measured surface during probing [2]. This transfer process of the particle may happen through the process of local adhesion at the microscopic level and break off during sliding. This adhesion of the particle to the stylus tip is permanent and cannot be removed by normal cleaning processes. Thus it will affect the shape of the stylus tip which will lead to the measurement error [121]. For instance, adhesive wear could occur when a stylus tip made

from ruby contacts a measured surface made from aluminium [121][2][21]. Adhesive wear also arises when the measured surface is repeatedly scanned by the stylus tip sphere as has been demonstrated previously in the literature [26].

Abrasive wear on the other hand occurs when a small hard particle is pushed into and removes a small piece of a softer counter-face. Free hard particles might be present in the contact region (perhaps including ones created by the oxidation of debris from adhesive wear) or a harder asperity on one surface might act similarly. Small particles might be removed from one or both surfaces during the probing process. Abrasive wear may occur due to several factors; some particle in the stylus act as abrasive, and atomic attraction between the materials may occur [121][21]. Stylus tips made from ruby are found to be good for measuring workpieces made from stainless steel and titanium but are not suitable for aluminium workpieces. Silicon nitride is the alternative material for stylus tips to measure aluminium workpiece. Zirconia and tungsten carbide are suitable materials for the stylus tips to measure workpieces made from cast iron [121].

Thus, the abrasive and adhesive wear between the stylus tip surface and the measured surface are factors needed to be considered when selecting the appropriate materials for stylus tip spheres. This factor is of greater importance for scanned probing, but even point probing in practice involves a small amount of sliding motion in the contact region.

3.5.5 Summary of design rules for material selection

(xxv) With reference to design rules number (V) and number (XIX), the material for stylus shaft with higher value of Young's modulus will reduced the allowable probing force and will influence the stiffness of the stylus shaft.

(xxvi) The material of the measured workpiece should be considered in designing a measurement task and selecting the appropriate styli in order to avoid plastic deformation in the measurement. Generally, though, a stylus tip material has high Young's modulus and higher strength will be preferable.

(xxvii) The selection material for stylus tip sphere should take account of the material of the surface intended to be measured to avoid or minimize the abrasive and adhesive wear.

3.6. Manufacturing technique and process

3.6.1 Manufacturing techniques and the effect of control parameters

As discussed in section 2.5, there are several potential manufacturing processes that have the capability to manufacture a stylus with a dimension less than 100 µm. In summary, for manufacturing of the stylus shaft, they focus on ion beam (FIB), wire electro discharge grinding (WEDG) and electro chemical machining (ECM), while for manufacturing of the stylus tip, one pulse electro discharge (OPED) or a hybrid technique using adhesives is used. In the future, it is believed that new manufacturing techniques and processes will be developed for the manufacturing of the stylus with the dimension less than 100 µm.

With the range of variants of currently available plus possible future techniques, it is not practical for this chapter to formulate specific design rules for each of these manufacturing process. Nevertheless, as manufacturing technique is one of the important factors that influences the performance of the styli in micro-CMM measurement, some general design rules should be formalised.

It is crucial to ensure that manufacturing techniques are capable of making devices that can achieve the performance required by the design rules discussed earlier in this chapter, especially the design rules about geometrical considerations in section 3.2 and physical conditions in section 3.4. For instance, the stylus is expected to have a good surface quality and adequately uniform diameter of the stylus shaft and stylus tip after manufactured. Of course, with the limitations in all real manufacturing processes and techniques, the perfect match to the required stylus parameters will not be achieved, but near-optimum values that adhere closely to the theoretical results are expected to be produced.

Each manufacturing technique and process depends on its own control parameters. A good combination of control parameters during manufacturing process will result a stylus that has optimum performance for its required parameters. For example, in the WEDG process, the rod material needs to be accurately aligned on the rotary axis to get good straightness in the stylus shaft. Also, the WEDG process can only manufacture artefacts in a material that has good hardness and toughness [58]. In contrast, for an ECM process, feeding rate and direction of the electrolyte flow need to be controlled. Moreover, the chemical erosion rate and

dimensional accuracy of the ECM process also depend on the gap current, concentration and temperature of the electrolyte. To achieve the required diameter of the stylus shaft, feed rate and current gap must be especially closely controlled [69].

3.6.2 Summary of design rules for manufacturing process and assembly of stylus

xxviii) Manufacturing techniques applied to styli must be able to deliver consistent control over sizes, tolerances and so on sufficient to achieve the performance required in the stylus design rules, especially those for geometrical considerations and physical condition.

xxix) As there are variants manufacturing techniques and processes for producing stylus systems for micro-CMMs, the important control parameters associated with these manufacturing processes depend on their specific manufacturing technique themselves. The relevant factors must be properly investigated and understood before any process is introduced.

3.7. Discussion

Five main categories of influence factors in developing styli for micro-CMM with dimension below 100 µm have been discussed. These influence factors are important measurement performance and must be considered carefully, especially in micro- and nano-scale work. This is because, many factors, which are not relevant at the macro-scale, will become significant at the micro- and nano-scale. For example, low contacting forces during micro-CMM measurement are often desirable to ensure no significant surface damage occurs. However, a low force probing introduces susceptibility to surface interaction forces, such as surface tension from adsorbed water layers, resulting in surface stiction effects both parallel and normal to the surface and consequently in reduced measurement consistency. In addition, other parameters such as the stiffness of the stylus shaft and form error of stylus tip which are not necessarily so significant in macro scale measurement, will always be important factors to be determined in the micro and nanoscale. As discussed earlier, in micro-scale measurement, the stiffness plays important roles not only in determining the sensitivity of the measurement and minimising the stick slip error during scanning, it also critical in selecting the appropriate probing speed of the micro CMM. The form error of the stylus tip needs to be small or to be determined (ideally, both) in order to minimise the systematic errors.

As mentioned earlier, all of these main categories of influence factors are interrelated. A new, wide-ranging set of design rules has been developed here from the main influence factors. Some of these design rules are general and qualitative rules while some can be quantitatively modelled. For instance, the relationship between the geometrical dimensions of the stylus, allowable probing force, surface interaction force, elastic deformation and stiffness of stylus shaft can be calculated and estimated using specific equations. However, the best values for factors such as stylus speed, surface form for the stylus tip and abrasive wear characteristics at the stylus tip could not be determined by a specific mathematical equation, depending in too complex ways on the other influence factors. Furthermore, maximum safe tip force and control parameter in manufacturing process can be determined practically during experiments prior to setting up 'routine' measurements.

In the detail investigation, the effects of forces are the main critical factors influencing the design of a new stylus with a dimension less than 100 µm. In summary, besides introducing a measurement error, the ultimate effect of forces in measurement could damage the surface of the workpiece and stylus tip sphere. Also, the stylus shaft might be broken, or its excessive bending might cause collision between the stylus shaft and the measured workpiece. Therefore, to avoid these conditions, the ideas of allowable probing force and maximum safe tip force are introduced to be limiting factors in selecting an appropriate applied contact force in measurement. These two forces are different in nature. The allowable probing force concerns the interaction between stylus tip sphere and the measured workpiece, whereas the maximum safe tip force concerns the (bending) strength of the stylus shaft under a certain applied force. Whilst the value of the maximum safe tip force of any stylus is expected to be constant, the material properties of the stylus tip and measured workpiece are the limiting factors of the allowable probing force, as discussed in section 3.5. This means that the value of the allowable probing forces varies depending on the measurement tasks. Therefore, it is crucial for a maximum safe tip force to be known for a particular situation, because it will be a limiting factor in selecting a working range of allowable probing force, and, hence, in designing the measurement task. This is based on the practical assumption that the value of maximum safe tip force should be higher than allowable probing force as described in section 3.3.4. In addition, the value of maximum safe tip force is difficult to estimate from theoretical equations.

Allowable probing force is also used in formulating the relationship between the diameter of the stylus tip, effective length and diameter of the stylus shaft, as illustrated in equation (3.5) in section 3.2.4. From this equation (3.5), a suitable diameter of the stylus tip can be calculated from the input parameter of the effective length and diameter of the stylus shaft. In addition, this equation can also be altered to determine the appropriate diameter of the stylus shaft. Also, this equation is intended to be a guideline in determining the geometry of the styli as the result of this equation will be used to define the maximum values of their dimensions. The solution of this equation is quadratic and more than one value is expected from it. As long as the values from these equations obey the design rule (ii) in section 3.2.5, they can be used in the estimation of the dimensions of the geometry for styli.

Equation (3.5) is also indirectly demonstrates the relationship between the maximum effective aspect ratio with the allowable probing force, elastic deflection of the stylus and the material selection of the measured workpiece and stylus tip sphere. As this equation only considered the condition where the maximum elastic deflection is equal to or less than the allowable stylus deflection, only an input value of effective length that obey this condition will give result value of diameter of stylus tip or stylus shaft. Otherwise the output value will contradict with design rule (ii) in section 3.2.5. Therefore, the maximum effective aspect ratio can be predicted through this equation when the maximum stylus deflection is equal to allowable stylus deflection. Moreover, since the material properties of both stylus tip and measured workpiece are considered in formulating the allowable probing force (which is used in the calculation of maximum stylus deflection), the maximum effective aspect ratio also depends on both materials. Hence, the maximum effective aspect ratio will be different when a different material is selected as a measured workpiece or stylus tip. Nevertheless, when using a stylus which have effective aspect ratio that does not satisfy equation (3.5) and hence, in theory, not obey the design rule (xiii) in section 3.3.5, other influence factors should be considered. For instance, during actual measurement, the deflection of the stylus must be ensured not to exceed the allowable stylus deflection and the applied force imparted on the stylus should be monitored below the allowable probing force. Furthermore, the approach probing speed also needs to be carefully selected, so that the impact and overtravel forces can be minimised.

As the intention of this project is to develop micro-styli with dimensions in the sub-10 µm range, the sum of forces exerted to the styli has to be a small value. To reduce this sum of forces, the stiffness at the region of contact (in the metrology loop), mass and speed of the probe should also be reduced. However, several challenges will arise. By reducing this stiffness, the stick slip effects during scanning will be increased, which can also cause a probing error. Moreover, when the dimension of the styli is in the micro-scale range, the sum of the surface interaction forces is larger compared to gravitational forces, which might cause a similar measurement error to the stick slip phenomena. Therefore, the surface interaction forces need to be investigated in detail. In contrast, as discussed in section 3.4.2, in order to reduce the impact forces, the effective mass of the probing system is inversely proportional toward its speed and therefore, both of them cannot be reduced at the same time. Another challenge is to fulfil the current demand in producing the high aspect ratio micro-styli with dimensions in sub-10 µm region. This is because the stiffness of the stylus shaft should be higher than the stiffness at the probing sensor in order to increase the sensitivity of measurement and resistance towards bending of the stylus. A higher stiffness of the stylus shaft can be achieved by reducing its aspect ratio.

Another key fact to remember is that some of the parameters in the design rules can only be examined when the styli are attached to their probing systems. These include the probing force, impact and overtravel force, stylus speed and stick slip effect during scanning. In contrast, some parameters can be examined on the styli itself without paying any direct attention to the probing system. For instance, the form error of the stylus tip, the stiffness of stylus shaft, control parameters of the manufacturing process and the maximum safe tip force are some of the parameters in this category.

In this chapter, the discussion on the influence factors that lead to the design rules for new stylus systems are based on the general functions expected of stylus systems for tactile probing with micro-CMMs. For a specifically functionalised type of stylus, such as vibration styli in which a stylus is vibrating during measurement, other specific influence factors related to its specific function (for example, its natural frequency) need to be considered.

3.8. Conclusion and summary of design rules

This chapter describes the newly-formulated set of design considerations for stylus systems for micro-CMMs and micro scale measurement. Five major factors that influence the measurements using micro-CMMs, especially at micro- and nanometre scales, have been identified. These influence factors then lead to the development of the design considerations for a new stylus with tip diameter in the sub-10 µm region. Thus, the outcome of this chapter is a set of the design rules which are interlinked to each other, satisfying Thesis Objective 1. Moreover, the explanation of the influence factors and the development of design rules are essential in answering Research Question 1.1. This set of design rules is also expected to be a general recommendation in manufacturing and properties characterization of styli. In summary, the set a design rules can be listed as follows:

(i) The diameter of Stylus tip sphere must be smaller compared to the dimensions of the features of the surface to be measured.

(ii) The diameter of the stylus tip should be bigger than the diameter of the stylus shaft.

(iii) The aspect ratio of the stylus should be higher than the aspect ratio of the features that intends to be measured

(iv) Selection for the diameter of the stylus tip is depend on the geometrical condition of the stylus shaft, including its diameter and effective length. The mathematical relationship between the diameter of the stylus shaft, length of the stylus shaft and the diameter of the stylus tip is:

$$d_{tip} = \frac{d_{shaft}^4 \pm \sqrt{d_{shaft}^8 - 4\left(\frac{224\,\sigma^3\, l^3}{\pi\, E\, E^{*2}}\right) d_{shaft}^5}}{2\left(\frac{224\,\sigma^3\, l^3}{\pi\, E\, E^{*2}}\right)}$$

(v) In the micro-scale range, the probing force for single point probing is a combination of impact force, overtravel force and surface interaction forces. The actual probing force must always be less than allowable probing force. The allowable force depends on the material properties and the radius of stylus tip. Using the previously defined notation, the allowable probing force should obey the relationship:

$$F_p = 21\,\frac{\sigma^3\, r_t}{E^2}$$

(vi) The impact force in the single point probing will be influenced by the probing speed, material properties, probing mass and stylus tip diameter with this relationship:

$$F_{imp} = \sqrt[5]{\frac{125}{36}\, m_t^3\ \Delta v^6\ E_{red}\, r_t}$$

(vii) The overtravel force depends on the stylus stiffness with the following relationship

$$F_{ovt} = C_t\ x_{ovt}$$

(viii) The surface interaction force has potential contributions from the van der Waals force, electrostatic attraction force, Casimir force, and hydrostatic or capillary force. The surface interaction force has an important influence in micro-scale range compared to the gravitational force and cannot be neglected.

(ix) To reduce the van der Waals force, the contact area between the surface should be as small as possible and it is preferable to select a hard material for the stylus tip.

(x) To reduce the electrostatic force, a stylus tip material with a small contact potential difference between the tip and the measured surface is preferred.

(xi) In order to reduce the surface force related to the hydrostatic or capillary force, it is recommended that the relative humidity should be below 60%, with a preference that it should be between 30 to 40% RH.

(xii) The scanning mode is influenced by the surface force, friction force and the stylus stiffness with the following relationship:

$$\Delta y = \mu\ (\Delta x\ +\ \frac{F_s}{C_t})$$

(xiii) To avoid the collision between stylus shaft and measured workpiece, elastic deflection of the stylus shaft , W_s, should be smaller than allowable stylus deflection, W_a

(xiv) The maximum safe tip force should be determined and should be bigger than allowable probing force

(xv) Relationship between (maximum) stylus speed and effective mass for a given maximum contact stress due to the impact is (using the previously defined notation):

$$\Delta v_{imp} = \sqrt[2]{\frac{(1.61\pi)^5 \; r_t \; \sigma_{0.2}^5}{30 \; E_{red}^4 \; m_t}}$$

(xvi) In general, higher stylus speeds are preferred in order to reduce overall measurement times, reduce risk of thermal drift, and so on. Selection of the stylus speed depends on the effective mass, stiffness at the stylus tip, diameter of stylus tip sphere, measurement range travels by stylus, and the sensitivity of the measurement.

(xvii) A good surface quality is necessary at the stylus tip sphere, evaluated in comparison to the desired measurement precision and uncertainty. It should have a low surface roughness, a uniform sphere diameter, a small value of roundness deviation and a small centric offset of the sphere from the stylus shaft.

(xviii) The surface roughness and roundness of the stylus tip sphere must be smaller than the surface roughness and the (local) roundness of features on the measured surface.

(xix) The contamination at the surface of stylus tip sphere should be minimized (ideally, eliminated) by using appropriate cleaning methods..

(xx) The effective stiffness at the stylus contact point depends on the stiffness of the stylus shaft, which is influenced by the length and diameter of the stylus shaft and the Young's modulus of its material, and the type of suspension or probing that the stylus shaft is attached to.

(xxi) Stiffness of the stylus shaft should be higher than the stiffness of the suspension for probe sensor mechanism or that the overall movement at the stylus tip arising from the suspension is bigger than the estimated deflection of the stylus shaft.

(xxii) Stiffness should be isotropic (or in practical terms, nearly equal in all directions).

(xxiii) As mentioned in design rule (VII), (XII), and (XIV), the stiffness at stylus tip sphere will give significant effect to the probing force, stylus speed, surface force and stick slip effect during scanning

(xxiv) With reference to design rules number (V) and number (XIX), the material for stylus shaft with higher value of Young's modulus will decrease the allowable probing force and will influence the stiffness of the stylus shaft.

(xxv) The material of the measured workpiece should be considered in designing a measurement task and selecting the appropriate styli in order to avoid plastic

deformation in the measurement. Generally, a stylus tip material with high Young's modulus and higher strength will be preferable.

(xxvi) The selection material for stylus tip sphere should take into account the material of the surface intended to be measured to avoid or minimize the abrasive and adhesive wear

(xxvii) Manufacturing techniques applied to styli must be able to deliver consistent control over sizes, tolerances and so on sufficient to achieve the performance required in the stylus design rules, especially those for geometrical considerations and physical condition.

(xxviii) As there are variant manufacturing techniques and processes for producing stylus systems for micro-CMMs, the important control parameters associated with these manufacturing processes depend on their specific manufacturing technique themselves. The relevant factors must be properly investigated and understood before any process is introduced.

Finally, the next step is to bring these design rules together and consult with the manufacturer for the manufacturing a stylus system with the dimension of stylus tip less than 10 µm or in sub-10 µm range. In addition, prior to characterising the new stylus design, analytical modelling based on the design rules will be explored in chapter 4

Chapter 4: Exploration of design rule parameters using analytical models

4.1. Introduction

To address ***Research Question 1.3*** in ***Thesis objective 1*** and ***Research Question 2.1*** in ***Thesis objective 2,*** extended works of exploring some of important parameters suggested in newly-developed design rules of micro-styli (chapter 3) have been modelled in this chapter. There are three different cases which have been studied. The first case is the exploration work of suitable parameters for a micro-styli with tip diameter less than 10 µm. Based on the design rules, a preliminary analytical modelling has been constructed. A set of preliminary input design of parameters and conditions has been defined prior to this modelling and the analytical solution for this model has been discussed in detail in section 4.2. This works is important to determine the state of the art of the new stylus system with smaller geometrical dimension in practicality to be fitted to the current available micro probe technology, hence, identified the challenges in realisation of the stylus with dimension less than 10 µm in micro probes.

The second case is dedicated for discussion on the analytical modelling of the mechanical properties of the stylus system for micro-CMM. As mentioned in discussion in Chapter 3, section 3.7, some of the parameters of influenced factors in developing stylus system can be tested on the styli itself without attaching to the probing system. Therefore, in order to investigate the mechanical properties of the stylus, the stylus will be tested separately without attaching to the micro-probes. Thus, the characterisation of the mechanical properties will start by calculating the important parameters regarded to mechanical properties of the stylus. As referred to the design rules in Chapter 3, to determine the mechanical properties of the stylus, some parameters related to the strength behaviour of the stylus system need to be identified and tested. The identified parameters include the stiffness of the shaft, allowable deflection, maximum deflection of the stylus shaft and maximum safe tip force.

In contrast, as an increasing demand of the high aspect ratio measurement using micro-CMM, the development of the stylus with high aspect ratio is becoming more important. However, according to the design rules in section 3.2.3, the aspect ratio of stylus could not simply selected because it depends on the other geometrical dimension, applied probing force and the properties of both material of stylus tip and measured workpiece. This means that the maximum workable aspect ratio of stylus might be varies according to the specific measurement task. Therefore, as part of addressing the ***Research Question 1.2,*** the third case in this extended works will demonstrate the effect of different material selected as a measured workpiece toward the effective aspect ratio of the styli. From this modelling, a prediction of ideal maximum workable aspect ratio of styli can be estimated.

4.2. Preliminary modelling of micro-stylus with tip diameter less than 10 µm

To start modelling of stylus system designs according to formulate by the new design rules, a set of preliminary input design of parameters and conditions needs to be established. A stylus tip sphere is assigned to have diameter of 8 µm. Tungsten is selected as a material for both stylus tip and stylus shaft. In addition, to simplify the modelling, the measured workpiece will also be made from tungsten material in this case. The solution of this preliminary modelling is summarised in Table 4.1 and illustrated in Figure 4.1.

Table 4.1: Preliminary analytical solution of stylus design model

Analytical model parameter	Output	Calculated based on
Length of the stylus shaft	0.28 mm	Equation (3.5)
Maximum diameter of the stylus shaft	6.9 µm	Equation (3.5)
Maximum allowable probing force	3.42 µN	Equation (3.1)
Stiffness of the stylus shaft in lateral direction	6.28 Nm^{-1}	Equation (3.15)
Stiffness of the stylus shaft in axial direction	54.9 kNm^{-1}	Equation (3.17)

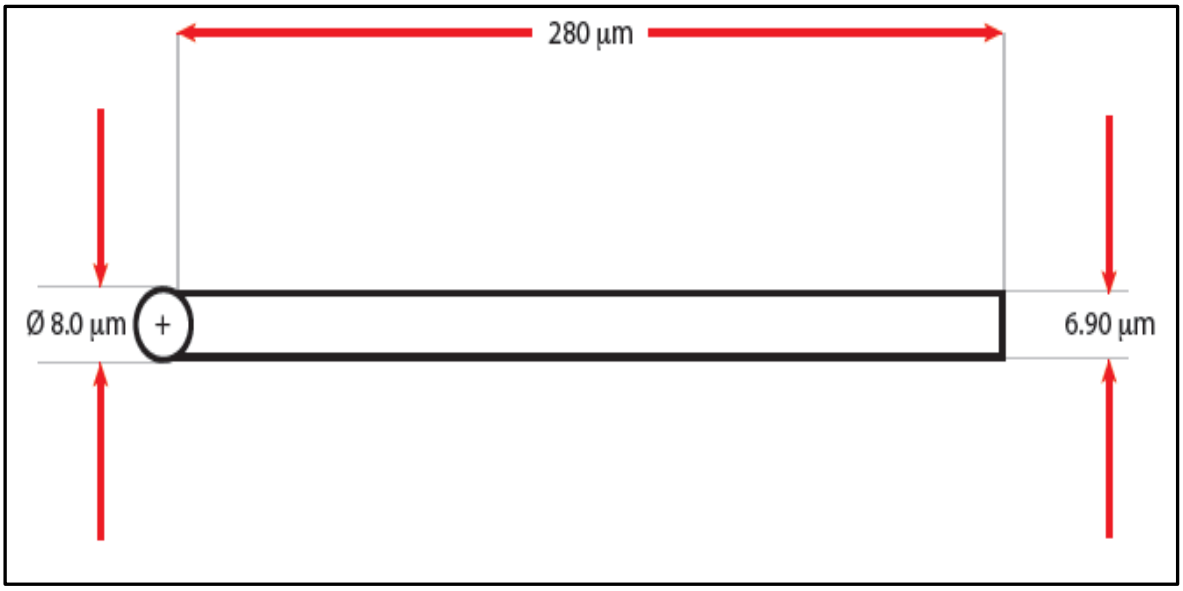

Figure 4.1: stylus design based on the preliminary analytical design model (µm)

The details of the aspect in the preliminary solution are described as follow:

Geometry dimension on stylus. The dimension of the shaft including diameter and length is defined based on the equation (3.5) in section 3.2.4. From this equation, calculated based on the preliminary set of input design of parameters and conditions (which had been set prior to this modelling), the maximum effective aspect ratio is 35 (based on the equation (3.5), any larger value than this will cause the stylus to disobey design rules (ii) and (xii) (referred to section 3.8)), the maximum effective length is 280 µm and the diameter of the stylus shaft is 6.9 µm. In this model, only effective length of stylus shaft is considered because of its involvement in measurement while the geometry dimension of upper part of the stylus shaft can be customised according to a holder of micro-probes so that the stylus can be fitted to micro-probes.

Allowable probing force. This value is the estimated of the maximum contact forces that can be applied to this stylus. Beyond this value, the plastic deformation will occur at both surface of stylus tip and measured workpiece. According to the design rules, the allowable probing force should be lower than the maximum safe tip force of the stylus. Therefore, the calculation of this force is beneficial in selecting the styli with appropriate capability of maximum safe tip force.

Stiffness. The stiffness of the shaft in horizontal direction (which applied force is perpendicular to the orientation of the stylus) is 6.28 Nm^{-1} while the stiffness in vertical direction is 54.9 kNm^{-1}. As the design rules state that the stiffness of the shaft should be bigger than the stiffness at the sensor mechanism of the probing system, this stylus is unlikely seems difficult to be fitted to most of the current available micro-probes.

Material selection. Tungsten is widely used as the stylus shaft because of its properties which consists of high young modulus. As discussed in section 3.5.2, material with higher value of Young modulus will also contribute to the stiffer styli. In addition, the tungsten is also selected as a material for measured workpiece. The reason of this selection is because to ensure that, the yield strength of both stylus tip and measured workpiece have a similar value, and thus, are expected to have same deformation capability. From this condition, based on the discussion in section 3.5.3, the maximum allowable probing force and the maximum elastic deformation for this specific stylus can be estimated.

Surface quality at stylus tip. The stylus tip should have a uniform sphere diameter, good sphericity form error and roughness, and small centric offset of the sphere from the stylus shaft. Also, the measurement uncertainty of surface form and roughness deviation at of stylus tip should be less than the surface form and roughness deviation at the measured workpiece.

4.3. Analytical Modelling for mechanical properties of stylus:

As the purpose of **Thesis Objective 2** is to investigate the mechanical properties of the stylus, it is beneficial to first establish a theoretical analytical modelling, so that a good design parameters for physical experiments of the stylus can be identified. Since the stylus shaft is mostly affected in a presence of the forces or load during measurement, its mechanical behaviour is crucial to be investigated. Hence, the deflection of the stylus shaft, the stiffness and the maximum safe tip force are the important parameter in order to characterise the mechanical properties of the stylus system. In this case, the relationships of these parameters with the geometry condition of the stylus shaft are observed. For the start, a set of styluses with specific geometrical conditions have been selected, and their important parameters related to the mechanical properties have been calculated and shown in Table 4. 2.

Table 4. 2: Analytical modelling for mechanical properties of the stylus

Geometrical condition						Analytical modelling			
Styli No	Effective aspect ratio	mechanical aspect ratio	Max shaft diameter	tip diameter	effective length	Allowable probing force	Allowable deflection (Wa)	Effective elastic deflection (Ws)	effective stiffness (xy)
			(µm)	(µm)	(µm)	(µN)	(µm)	(µm)	(Nm^{-1})
1	5	5	9.5	10	50	8.8	0.25	0.002	3944
2	10	11	9.5	10	100	8.8	0.25	0.018	493
3	15	17	9	10	150	8.8	0.50	0.075	118
4	20	25	8	10	200	8.8	1.00	0.280	31
5	30	43	7	10	300	8.8	1.50	1.600	5
6	40	47	8.5	10	400	8.8	0.75	1.800	5
7	50	56	9	10	500	8.8	0.50	2.800	3
8	10	20	10	20	200	35.0	5.00	0.470	75.7
9	15	38	10	25	375	55.0	7.50	4.800	11.5
10	20	54	10	27	540	64.0	8.50	17.000	3.8
11	30	90	10	30	900	79.0	10.00	95.000	0.8
12	40	120	10	30	1200	79.0	10.00	230.00	0.4
13	10	15	23	35	350	110.0	6.00	0.270	395.1
14	14	18	20	25	350	55.0	2.50	0.240	225.9
15	25	35	10	14	350	17.0	2.00	1.200	14.1
16	35	44	8	10	350	8.8	1.00	1.500	5.8
17	43.75	58	6	8	350	5.6	1.00	3.100	1.8

In Table 4. 2, seventeen styli have been selected with the stylus tip diameter between 10 µm to 40 µm, and the effective length less than 1200 µm. These particular value are based on actual styli (later will be explained in section 5.2) which have been successfully manufactured and will be used in this testing work. The selection of these styli are based on their geometrical conditions which obey the equation (3.5) in section 3.2.4 (two geometrical condition parameters of the styli is selected arbitrarily, either tip diameter, maximum shaft diameter or effective aspect ratio. Other geometrical parameters will be calculated according to these two arbitrary parameters). In this modelling, all material for stylus tip, stylus shaft and measured workpiece are made from Tungsten. The stiffness of the styluses is calculated by using equation (3.16) in section 3.4.4, considered only the stiffness at the effective stylus

shaft and in the case where the force is perpendicular to the orientation of the stylus. Maximum stylus deflection and allowable stylus deflection are calculated based on the equation (3.2) and equation (3.3) in section 3.2.4. In contrast, the maximum safe tip force is difficult to model using analytical equation but can be determined through experiment. However, in this table, the allowable probing force is calculated as indicator so that, in ideal condition, the maximum safe tip force should be higher than the allowable probing force (please refer section 3.3.4 for detail discussion on the maximum safe tip force). From these tables, the allowable probing forces are in the range of 1 to 100 μN.

To observe the relationship between the geometrical condition with the allowable probing force and stiffness of the stylus shaft, the data in the Table 4.2, the graphs in Figure 4.2, Figure 4.3, Figure 4.4, Figure 4.5, Figure 4.6, Figure 4.7, and Figure 4.8 are plotted. All of these graphs are represented by their least square best fit line. Although the allowable probing force is the theoretical value, it represents the maximum value of all interaction force between stylus tip and measured workpiece surfaces which can be exerted on the styli during measurement. Therefore, it is crucial to investigate its behaviour toward the geometrical condition of the styli. Figure 4.2 shows the arising curve of graph which follow the square-law dependency relationship of equation (3.1) in section 3.2.4. Nevertheless, for the effect of allowable probing force toward effective length of the stylus (Figure 4.3), diameter of stylus shaft (Figure 4.4) and mechanical aspect ratio (Figure 4.5), the unique definitive mathematical equations are difficult to be derived for these relationships. Although the allowable probing force in the least square best fit line of these graphs are seen exhibit a proportional relationship to square root to the effective length of stylus (Figure 4.3), and square to both stylus shaft diameter (Figure 4.4) and mechanical aspect ratio of stylus (Figure 4.5), they might also have other type of relationship, for instance, a linear relationship. In overall observation of these relationships, the force exerted to styli during measurement will increase with the increasing of all geometrical dimensions of the styli itself. As for now, we also assume that the maximum safe tip force follow the same trend as the allowable probing force (although the function for both are not the same as discussed in Chapter 3).

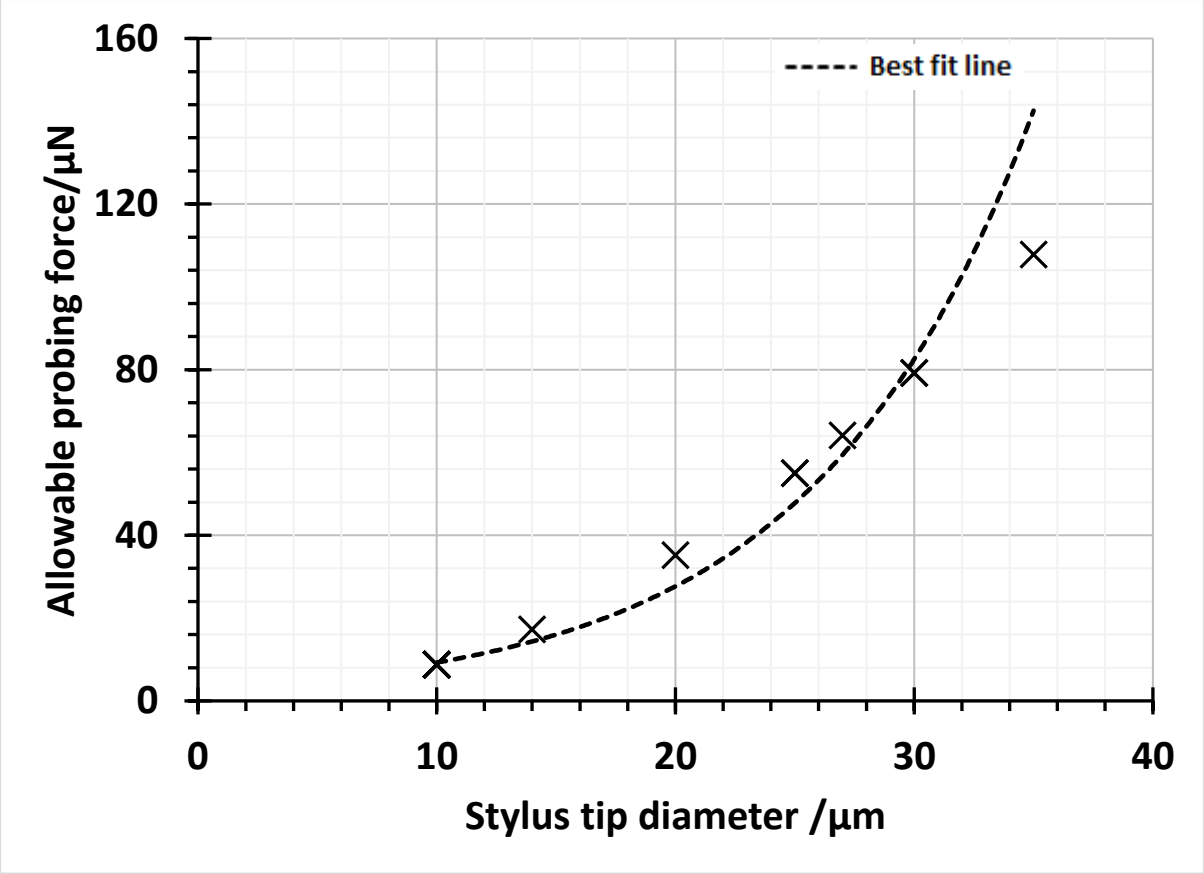

Figure 4. 2: Effect of stylus tip diameter in the function of allowable probing force

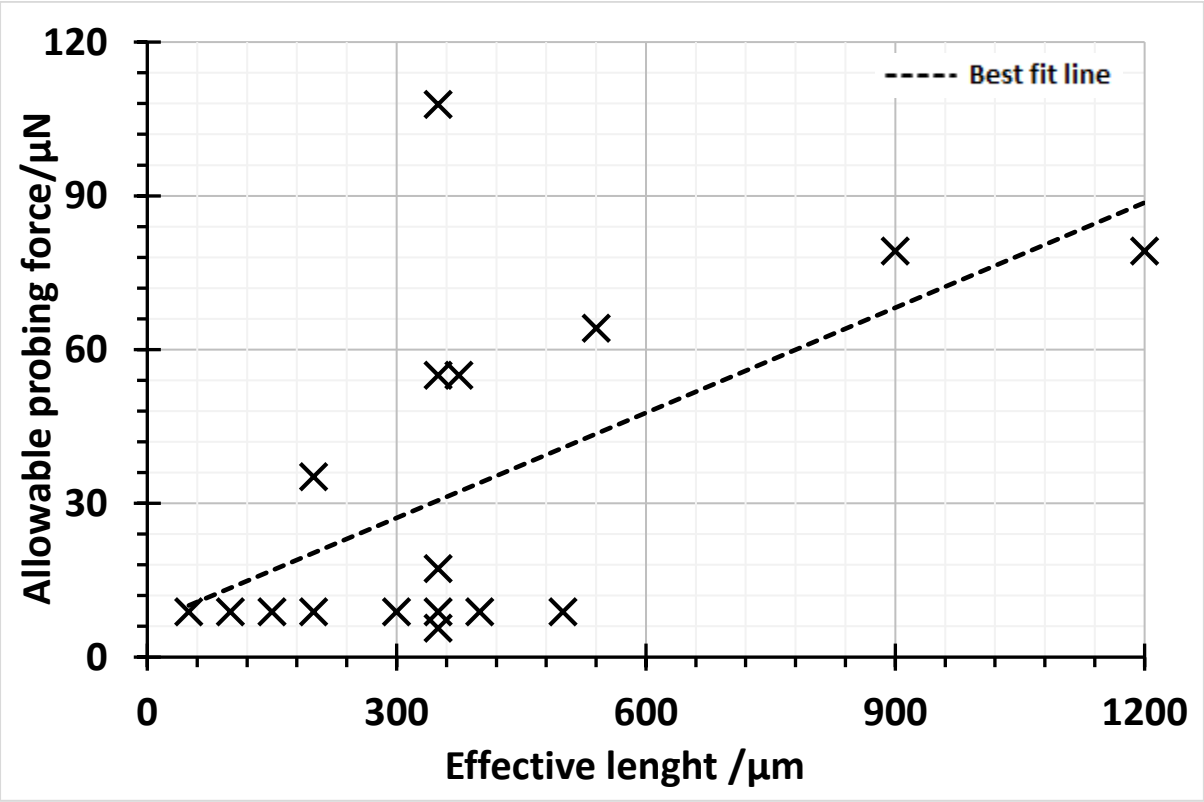

Figure 4. 3 : Effect of effective length in the function of allowable probing force

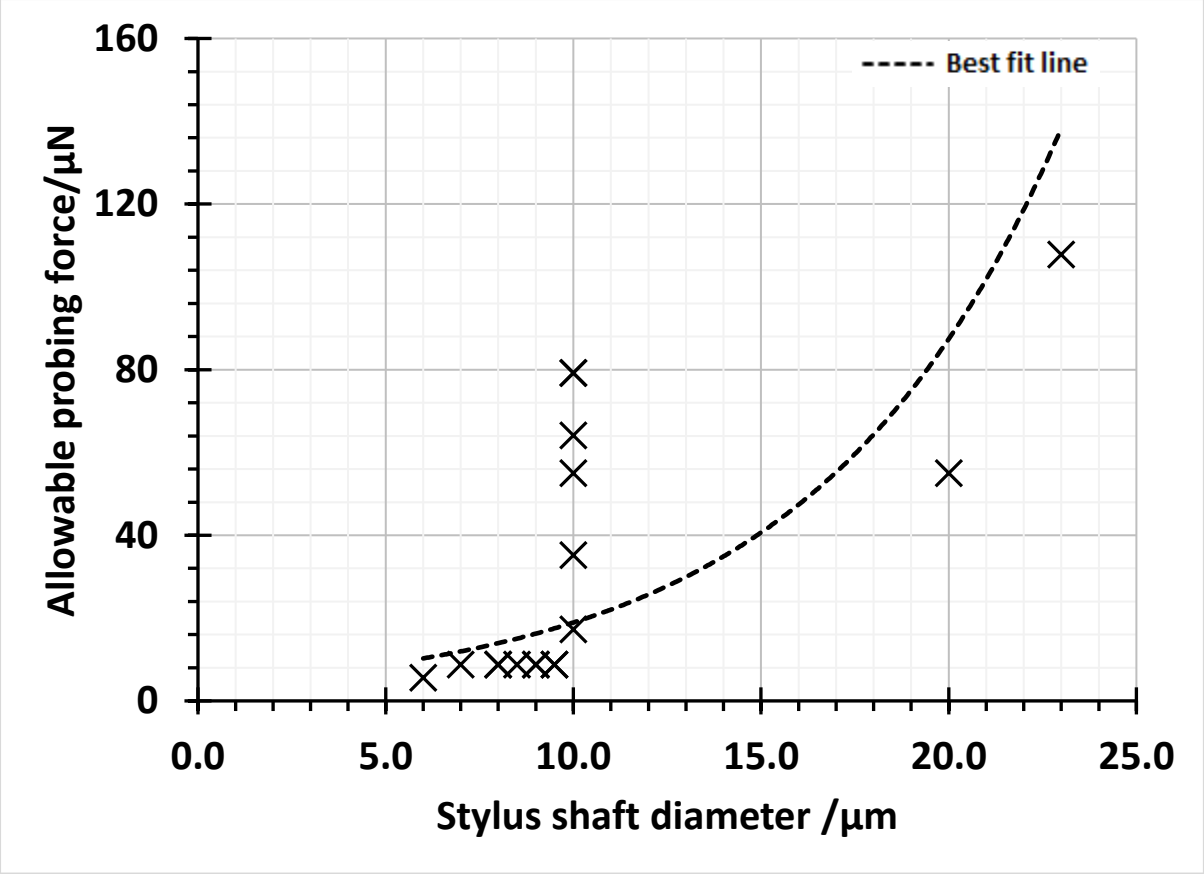

Figure 4. 4: Effect of stylus shaft diameter in the function of allowable probing force

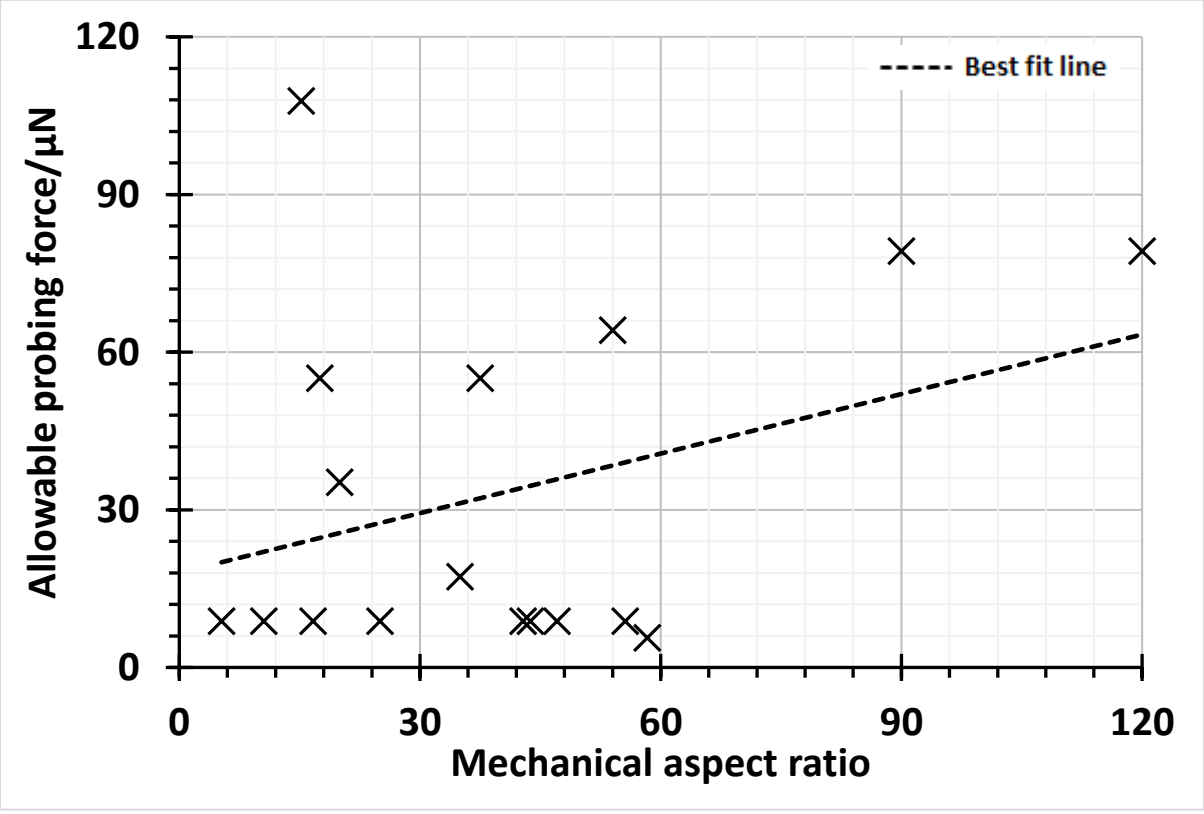

Figure 4. 5: Effect of mechanical aspect ratio in the function of allowable probing force

In contrast, the effective length of the stylus, mechanical aspect ratio and diameter of the stylus shaft are the parameters of geometrical condition that affected the stiffness of the stylus shaft, and therefore their characteristics are observed in the graph Figure 4.6, Figure 4.7, and Figure 4.8. As the relationship of stiffness and geometrical dimension of stylus shaft derived from the theory of cantilever [128], it is expected that the stiffness have a decreasing in trend throughout the effective length of the stylus and increasing in trend throughout the diameter of the stylus shaft. Furthermore, the relationship between stiffness and mechanical aspect ratio is observed to have a decreasing in trend. Thus, in theory, the development of the smaller stylus with higher aspect ratio will produce lower stiffness of the stylus. Therefore, from this modelling result, in the development of a smaller stylus dimension with high aspect ratio, it must understand that this stylus have a low stiffness. Thus its value has to be determined so that the specified measurement task including critical parameters (i.e. applied force) can be designed accordingly.

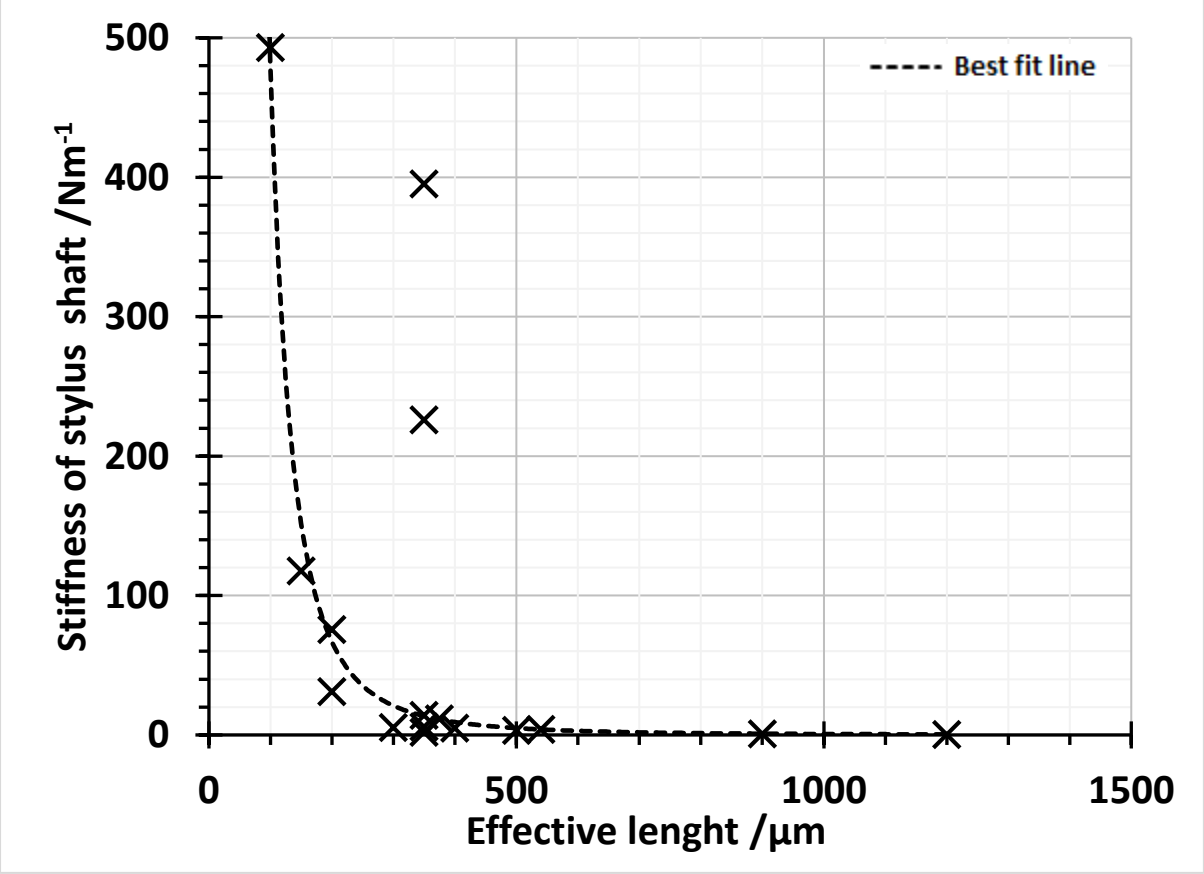

Figure 4. 6: Effect of effective length in the function of stiffness of the stylus

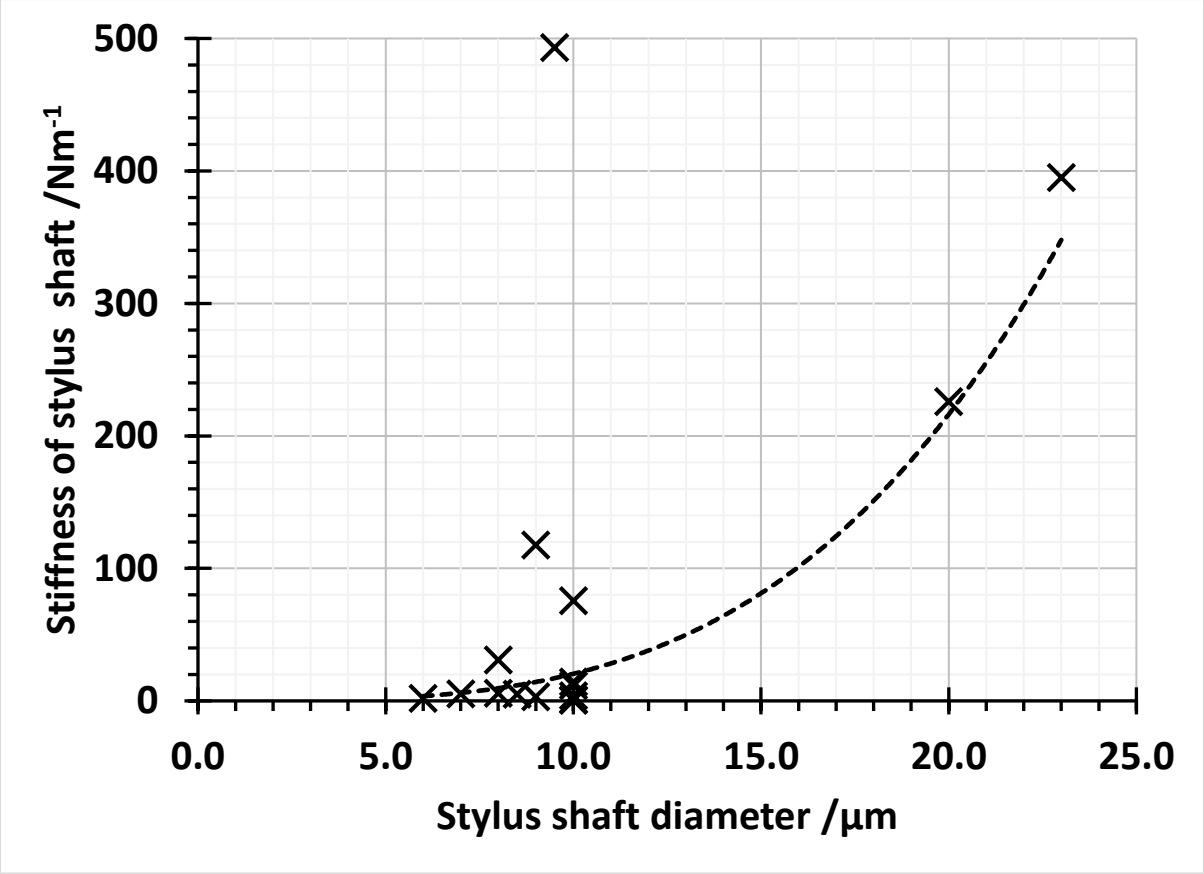

Figure 4. 7: Effect of diameter of shaft in the function of stiffness of the stylus

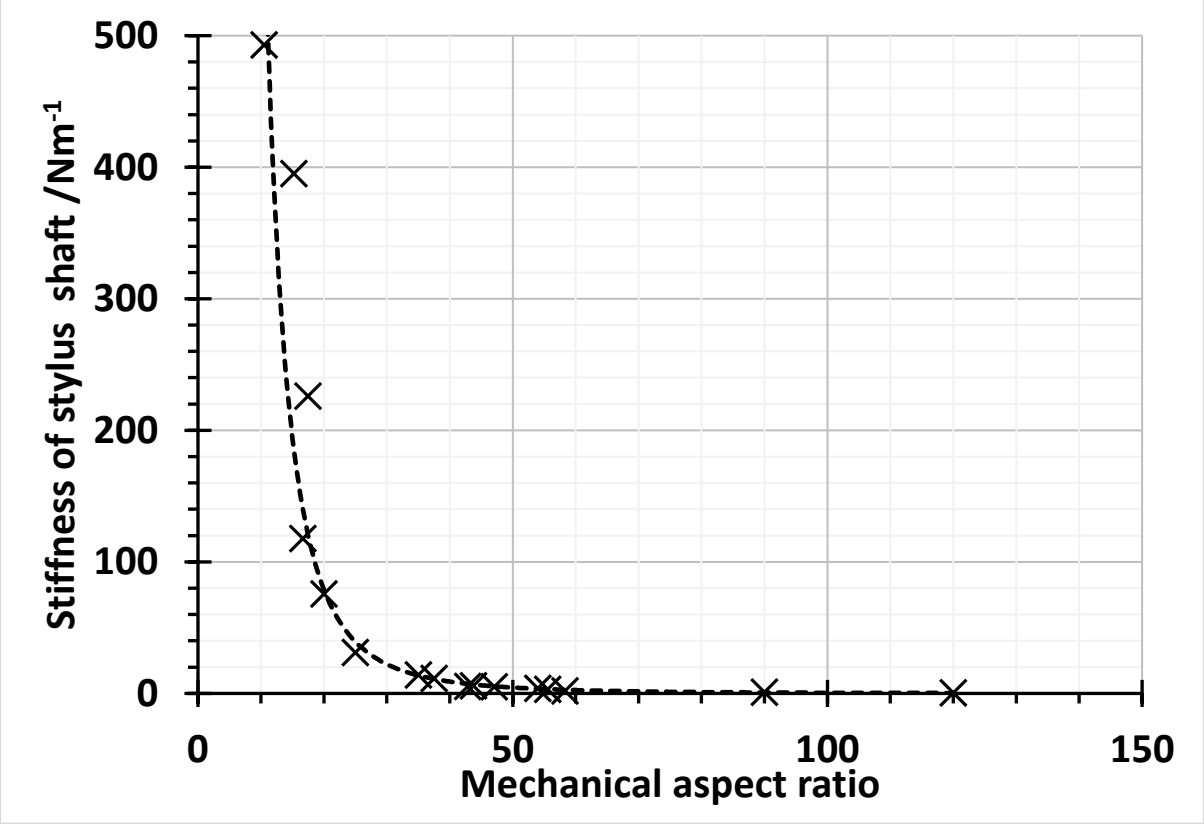

Figure 4. 8: Effect of mechanical aspect ratio in the function of stiffness of the stylus

4.4. Modelling the relationship between aspect ratio and material properties

The selection of an effective stylus ratio appropriate to the particular measurement task on a micro-CMM will not only optimum the measurement but also to avoid the measurement error due to the collision between stylus shaft and measured workpiece or stick slip phenomena. As explained in the discussion of design rule in section 3.7, the decision of selecting a suitable effective aspect ratio stylus should be based on the material used in stylus tip and features of the measured workpiece intended to be measured. Therefore, for this purpose, the relationship of the maximum effective aspect ratio with the material properties for both parts will be investigated and modelled. In this case, a set of styli, all having their stylus tip made from tungsten, are selected to measure three different materials of measured workpiece. All styli will have a constant value of diameter of stylus shaft and stylus tip, which is 8 µm and 10 µm respectively. However, the effective lengths of styli in this set will vary so that the effective and mechanical aspect ratios of the styluses will also be different. The three measured workpieces in this model are made from tungsten, aluminium and cast iron alloy. The related properties of these materials are summarised in Table 4. 3

Table 4. 3: Material properties of Tungsten, Aluminium and Cast Iron [130] [131]

Material	**Young's modulus**	**Yield strength**	**Poison ratio**
	GPa	MPa	
Tungsten	411	941	0.28
Aluminium	69	100	0.33
Cast Iron	211	126	0.29

For each of measurement between the stylus and measured workpiece, the allowable probing force, the allowable stylus deflection and elastic deflection for each of the stylus are calculated based on the equation (3.1) and equation (3.2) in section 3.2.4. Then, the behaviour of the maximum stylus deflection and allowable stylus deflection as a function of effective aspect ratio are plotted as illustrated in Figure 4.9, Figure 4.10, and Figure 4.11.

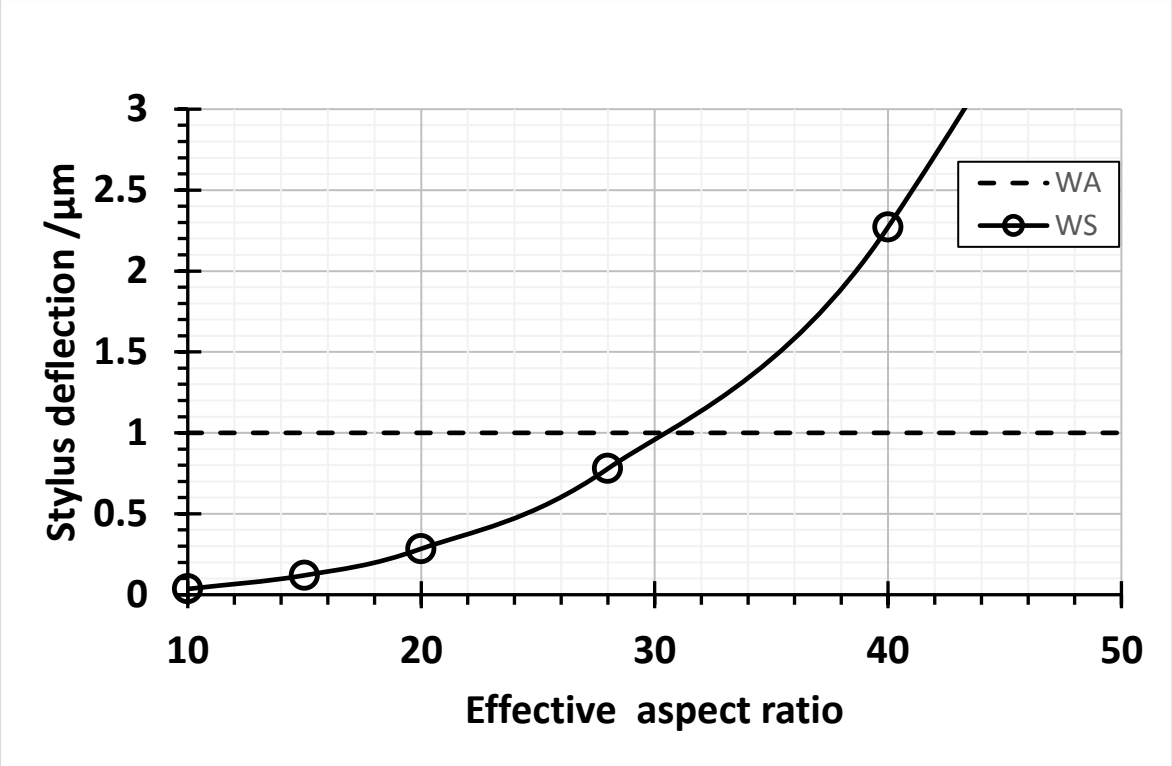

Figure 4. 9: Behaviour of elastic deflection (Ws) and allowable stylus deflection (Wa) in the function of effective aspect ratio when stylus tip made from tungsten is contacting measured workpiece made also from **Tungsten.**

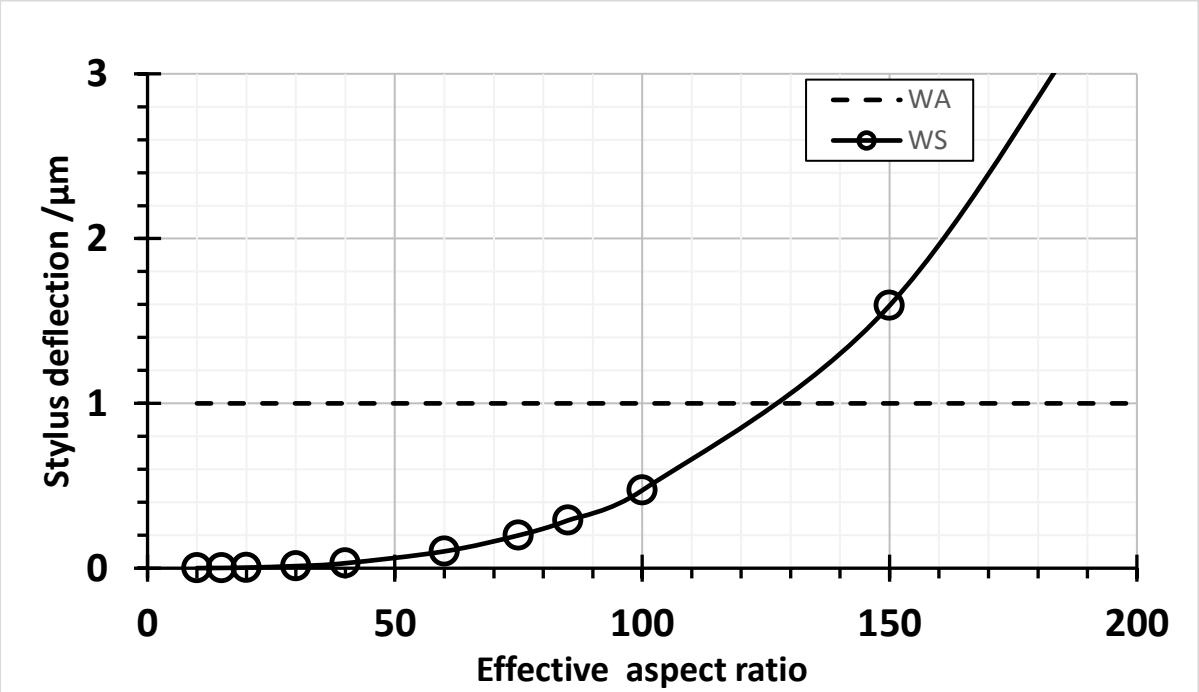

Figure 4. 10: Behaviour of elastic deflection (Ws) and allowable stylus deflection (Wa) in the function of effective aspect ratio when stylus tip made from tungsten is contacting measured workpiece made from **Aluminium**

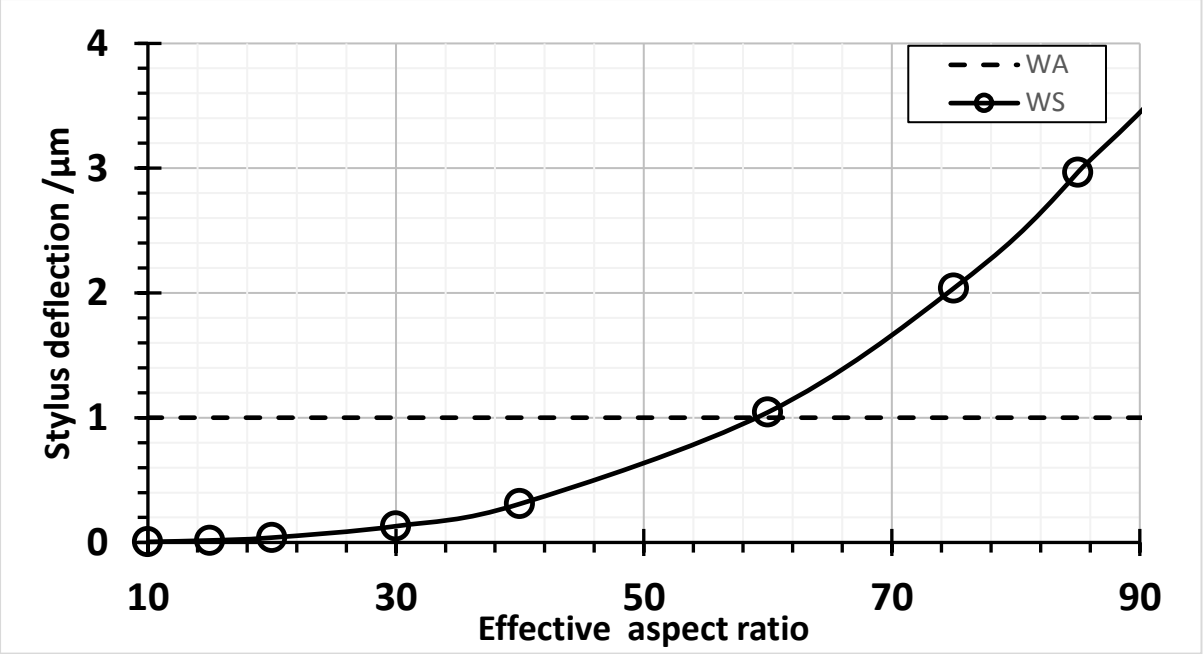

Figure 4. 11: Behaviour of elastic deflection (Ws) and allowable stylus deflection (Wa) in the function of effective aspect ratio when stylus tip made from tungsten is contacting measured workpiece made from **Cast Iron alloy**

Figure 4.9 illustrates the behaviour of the elastic deflection *(*Ws) and allowable stylus deflection (Wa) for the case of measurement on the Tungsten measured workpiece while Figure 4.10 and Figure 4.11 show the same behaviours for the measurement on the measured workpiece made from aluminium and cast iron alloy. The intersection between the allowable stylus deflection (which is constant throughout this study) and elastic deflection for each Figure 4.9, Figure 4.10 and Figure 4.11 are at different point of effective aspect ratio which are at effective aspect ratio of 30, 130, and 65. As the design rules state that the maximum elastic deflection should be lower than the allowable stylus deflection in order to avoid collision between stylus shaft and measured workpiece, the intersection between the plots of these parameters represents a boundary condition where the deflection of the stylus is at its allowable maximum. Therefore, the aspect ratio where these intersections occur should be considered as the maximum effective aspect ratio of the stylus that can be selected for the measurement. The result from this model study indicates that the stylus is allowed to have higher effective aspect ratio when probing the softer material for the measured workpiece. This is because the measurement task is restricted by the allowable probing force and maximum elastic deflection of the stylus. The allowable probing forces that should be applied during probing the softer material are smaller compared to the hard material. Consequently, the deflection of the stylus is also smaller. Thus, this condition allowed the stylus to have

longer effective length and higher aspect ratio because the tendency for the stylus shaft is colliding with the measured workpiece become smaller. Therefore, the model proves that the material both stylus tip and measured workpiece is important factor in determining the optimum effective aspect ratio for the stylus in the measurement.

4.5. Conclusion

In conclusion, three different cases have been modelled using the new rules developed in Chapter 3, in order to explore the plausible range of practical designs for very small styli systems. The first study considered the case where the dimension of stylus tip diameter is less than 10 µm. The preliminary conditions set prior to this model are the stylus tip diameter is 8 µm and the material for both stylus tip and measured workpiece are tungsten. Based on the design rules in chapter 3, the required parameters have been calculated and will be set as the theoretical maximum value for the properties of the stylus. The outcome of this modelled exhibits the small value of some of the important parameter such as the stiffness of the stylus shaft and the allowable probing forces which are difficult to be fulfilled by many of the current available probing probes. Therefore, to address the ***Research Question 1.3,*** based on the result of the stylus stiffness and allowable probing force in the first analytical modelling, the current available probing system (as summarised in Table 2.1 in section 2.4.3) are not suitable for the this styli to be fitted to. This is because the resultant stylus stiffness(which is calculated from their geometrical condition) is lower than the probe stiffness which leads to the false signal to the probing sensor. Nevertheless, this analytical modelling is significant to the future improvement work for the development of probing system of micro CMM that capable in micro and sub-micro scale measurement.

The second analytical modelling is essential to investigate the relationship between geometrical dimension of the stylus and mechanical properties of the stylus. The first study of this relationship is between geometrical condition of stylus and the allowable probing force of the stylus. Although the allowable probing force are difficult to be tested in practical, the results show that, in order to have smaller value of all parameter of the geometrical condition, the allowable probing force should be reduced. Also, the relationship of effective length of stylus, diameter of the stylus shaft and mechanical aspect ratio with stiffness of the stylus shaft had been modelled and plotted. The challenge in development of high aspect ratio

micro-styli, as shown in the graphs are the stiffness of the stylus will be decreased as the effective length of the stylus is increased and smaller diameter of the stylus shaft is used. As discussed in section 3.4.4, the sensitivity of measurement is decreased when the stiffness is equal with the stiffness of the sensor in probing system[107] and the stylus cannot be used if the stiffness of the stylus shaft is less than the stiffness of the sensor of probing system. The resultant from this model will be used as the preliminary theoretical value for the following testing work and will be compared to the experimental result which will be presented in chapter 5.

In contrast, to address the ***Research Question 1.2,*** the third modelling has been presented. This modelling describes the relationship between the aspect ratio of the stylus with the selection of material for stylus tip and measured workpiece. This factor is often neglected in CMM for macro scale measurement. The finding from the modelled suggest that the aspect ratio of the stylus could not been easily selected as many of the factors such as of the stiffness of the stylus, applied contact force in during probing and the materials use as the stylus tip and measured workpiece should be considered. Otherwise, the collision between the stylus shaft and measured workpiece could happen, and hence will damage the either the stylus of the measured workpiece.

Chapter 5: Mechanical testing of prototype styli

5.1. Introduction

In this chapter, two experiments have been conducted to characterise the mechanical properties of some new prototype micro-styli. These experiments are linked to the ***Thesis Objective 2***, which is concerned with the characterisation of the mechanical behaviours of the micro-stylus. The aim of this chapter is to test the mechanical behaviour of the stylus itself under certain loadings so as to verify the analytical modelling and design considerations proposed in this work. Two main parameters related to the mechanical properties of the stylus will be tested: stiffness and maximum safe tip force of the stylus.

The experiments have been designed to focus on the important parameters that have been discussed in chapter 3 and the resultant theoretical modelling in Chapter 4. As described previously, the behaviours of some of the stylus parameters can only be examined when the stylus is attached to the probing system of a micro-CMM. These parameters include the probing contact forces, the interaction surface forces, behaviours during scanning, probing speed, the mass of the probing system and the isotropy of the probing stiffness. Meanwhile, some of the parameters such as the material properties and those related to manufacturing are not easily tested. Therefore, these two experiments in this chapter are intended to characterise the capability of the stylus itself under certain loads.

Next, section 5.2 will describe the styluses used in this experiment. Then, a thorough description of the experimental setup involved in the work will be completed in section 5.3. This experimental setup is designed and developed to test both experiments. To inspect the performance of each main component in the setup before the experiments are carried out, preliminary test are conducted and are explained in detail in section 5.4. The preliminary testing is also important to determine the source of uncertainties in the experiment. Section 5.5 and section 5.6 will explain the main experimental procedures for both testing. Section 5.7 will describe the method of analysis both measurement. The results of both experiments are presented and discussed in section 5.8, while the uncertainty evaluation is discussed in section 5.9.

5.2. Manufacturing techniques for the test micro styli

As explained in chapter 2, there are several currently available technique capable of manufacturing a stylus system with dimensions below 100 µm. In summary, fabrication of stylus shaft might use the wire electro-discharge grinding (WEDG), and electro-chemical machining (ECM), while one pulse electro-discharge machining (OPED) or available glass micro-sphere technology is used for fabrication of the stylus tip. Therefore, for this project, four variant hybrid manufacturing techniques are used, namely:

Manufacturing technique Type 1: A combination of wire electro discharge grinding (WEDG) and one pulse electro discharge machining (OPED) [58]. The stylus shaft is manufactured by a WEDG process while the stylus tip is directly formed at the end of the stylus shaft using *OPED*, so creating a monolithic structure. This styli will be referred to as *Type 1 styli* (Figure 5.1).

Manufacturing technique Type 2: Assembly of the stylus using an adhesive material to attach a stylus tip sphere on the end of the stylus shaft [76]. The stylus shaft is manufactured using a process similar to that for *Type 1 styli* and a commercially available micro-sphere made from glass is used as the stylus tip. Styli manufactured using this technique will be referred to as *Type 2 styli* (Figure 5.2).

Manufacturing technique Type 3: monolithic manufacture technique similar to manufacturing technique in *Type 1 styli* except that when manufacturing the stylus shaft, an electro chemical machining (ECM) process is introduced after the *WEDG* process. The ECM process is expected to increase the stiffness of the stylus by improving the surface and geometrical quality of the stylus shaft. The detail of this *ECM* process is well described in a previous paper [132]. Styli manufactured using this technique will be referred to as *Type 3 styli* (Figure 5.3).

Manufacturing technique Type 4: The stylus shaft is made by only ECM process while the stylus tip is added monolithically using OPED. To date, ECM appears to be the promising technique for manufacturing stylus shaft with dimension below than 20 µm. Referred to as *Type 4* styli, these have smallest stylus dimension among the type use here (Figure 5.4).

Type 1 styli and *Type 2 styli* have been tested previously to investigate their ultimate yield strength [133], while with the enhancement in the experimental setup and procedure, *Type 3 styli and Type 4 styli* which are manufactured using new combination of manufacturing techniques, are tested here for the first time and their mechanical characteristics are compared to *Type 1* and *Type 2* styli. The result from these testing for *Type 3 styli and Type 4* styli are vital in understanding the ECM process as it is a promising manufacturing technique in fabricating the stylus system with dimension in sub 10 micrometre.

Figure 5. 1: Type 1 styli – combination of WEDG and OPED manufacturing process

Figure 5. 2: Type 2 styli – Combination of WEDG manufacturing process for stylus shaft and commercial glass sphere for stylus tip

Figure 5. 3: Type 3 styli – combination of WEDG and ECM process for stylus shaft and OPED for stylus tip

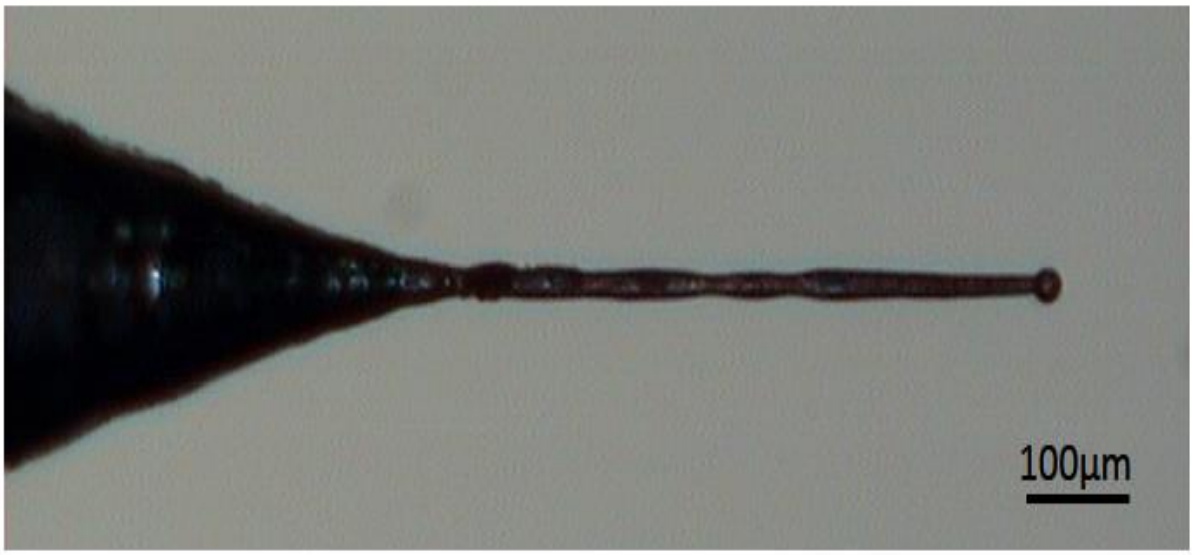

Figure 5. 4: Type 4 styli – smallest dimension (less than 20 µm) using ECM process and OPED

Table 5. 1: Geometrical dimension and analytical modelling data for the micro- styli manufactured using the variant hybrid manufacturing techniques (type1 to type4). * The value of effective maximum deflection are calculated based on the upper value of effective shaft diameter.

STYLUS			GEOMETRICAL DIMENSION						ANALYTICAL MODELLING				
	Stylus Name	Stylus Code	Effective Shaft Diameter		Stylus Tip Diameter	Effective Length	Effective Aspect Ratio	Mechanical Aspect Ratio	Allowable Probing Force	Allowable Deflection (Wa)	Effective Maximum Deflection*	Effective Stiffness	
			lower value	upper value								lower value	upper value
			(µm)	(µm)	(µm)	(µm)			(mN)	(µm)	(µm)	Nm^{-1}	Nm^{-1}
TYPE 1	1a	0506-1-2	38	44	75	669	9	16	2.04	16	3.1	347	649
	2a	0430-4-5	39	46	73	709	10	17	1.9	16	2.6	344	735
	3a	0504-1-2	38	46	62	691	11	16	1.4	9	1.9	317	742
TYPE 2	2a	0509-1-2	34	40	68	720	11	20	9.66	16	26	182	361
	2b	511-1-2	35	43	90	742	8	20	17	26	38	187	445
TYPE 3	3a	0517-4-5	31	39	49	593	12	16	0.9	7	1.8	188	475
	3b	0521-3-4	34	42	77	642	8	16	2.1	18	3.6	249	586
	3c	0521-9-10	36	43	73	713	10	18	1.9	16	3.85	235	509
TYPE 4	4a	0602-1-2	15	17	26	156	6	10	0.3	5.5	2.0	45	125
	4b	0602-5-6	10	15	21	171	8.4	16	0.2	5	1.3	28	143
	4c	0607-2-3	18	25	32	343	11	16	0.4	5.5	1.2	72	215
	4d	0602-7	17	18	24	573	23	33	0.24	3.3	2.1	50	115

Table 5.1 shows the micro styli that have been manufactured using the four variants of hybrid manufacturing technique and used in the present experiment to examine their mechanical properties. These styli are selected based on their geometrical dimension which obey the design rules for geometrical consideration (discussed in section 3.2) including equation (3.5) in section 3.2.4. However *Type 2 styli* seem not to obey this equation, because their effective maximum deflection is larger than their allowable deflection. Therefore, to make these styli to obey to this equation, in the following experiments, it will be ensured that the force imparted to them will not exceed the allowable probing force and hence its deflection will not exceed the allowable deflection.

The geometrical dimension (diameter of the stylus shaft and stylus tip) for each of these styli have been measured using optical microscope made from Alicona Imaging GmbH [134]. During this measurement for each stylus, it is noticed that the diameter of the stylus shaft is varied along the effective length of the stylus shaft. Thus, in this work, the diameter is measured at different location of the stylus shaft and the upper and lower results value are recorded in the Table 5.1. Therefore, this upper and lower limits of stylus shaft diameter are used to determine the upper and lower limit of the calculated stiffness from this analytical model. Also, the mean value between the lower and upper value of stylus shaft diameter is used to calculate the mechanical aspect ratio.

The table provide information on the geometrical dimension and analytical modelling calculations for each stylus. *Type 4 styli* have the smallest geometrical dimension in this set. As required in the ***Thesis Aim*** for the characterisation of the stylus with dimension in sub-10 µm**,** Type 4 styli will be a major focus in this testing. Stylus 4b (stylus code 0602-5-6) has the smallest dimension of the styli while stylus 4d (stylus code 0602-7) has the highest aspect ratio among all the styli. The analytical modelling results are calculated based on the requirement that the stylus tip is contacting a test-workpiece made from the copper. This choice is because, pure copper is a soft material that has unfavourable material properties compared to tungsten and glass [131].

5.3. Details of experimental Set-up

The experimental set up are presented in Figure 5.5. The experimental setup comprises four main groups of component: stylus holder, force sensing system, stylus movement, and monitoring and alignment. The outputs from all of these groups are well integrated and captured by the control software. This setup is the base setup for both the stylus stiffness measurement and maximum safe tip force measurement. The differences between these two experiments are in the aspect of the experimental procedures and the analysis methods, as will be explained in detail in section 5.5, section 5.6 and section 5.7.

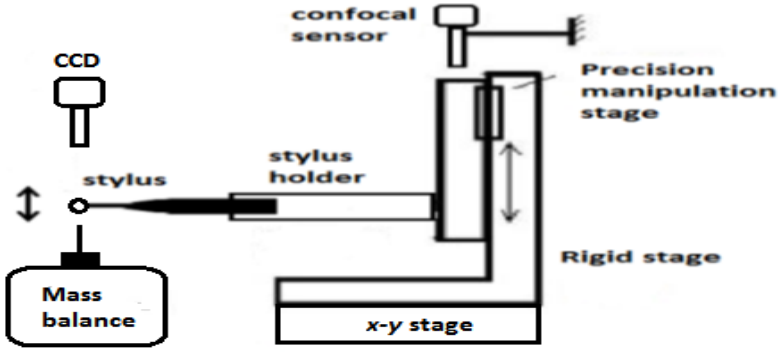

Figure 5. 5: Schematic diagram of overall base experimental setup

In this setup, the stylus is attached to the stylus holder while stylus holder is mounted at a manual stage and micro translational stage. The stylus is positioned in the horizontal axis and its intended movement is in vertical axis. In the general experimental procedure of both testing regimes, the stylus is moved into contact with test workpiece made from cooper sheet in the nominally vertical direction by a precision micro translation stage. The test workpiece is located on a precision mass balance. The precision mass balance is used as a force sensor and records results during the contact between stylus and cooper sheet. A chromatic confocal point displacement sensor records the movement of the precision translation stage. For stiffness testing, during contacts, the stylus moves a few micrometres toward the test workpiece and then returns to its initial position before contact. In contrast, for the maximum safe tip force testing, the downward movement of the stylus is only stopped after the stylus breaks. The anti-vibration table is used in this setup while the environmental conditions of the laboratory are control, with a temperature gradient of better than 0.1°C per hour, and a humidity of between 40%RH and 65%RH. The construction of this experimental setup will be explained in section 5.3.1 to section 5.3.5.

5.3.1. Design of stylus holder

It is very important to ensure that the stylus is securely mounted in the experimental setup to avoid gross movements and vibrations of the stylus that might confound measurements of its bending deflection. As described previously in section 5.2, each stylus has two parts to its stylus shaft with different diameters. The upper part of stylus shaft is very important to act as an interface to the holder, which would normally be part of the probe. To attach the stylus to the experiment setup, special holder has been designed and manufactured as shown in Figure 5.6. This stylus holder will securely mount the stylus by holding the upper part of stylus shaft securely tight by using a small M2 screw. With this design, the holder is expected to minimise the vibration error. There are also two parts to this stylus holder, an extension part and holder part. These two parts are joined together using a thin stainless sheet. The extension part of the holder (shown on the left in Figure 5.6) is attached to the precision translation stage (and the manual XY stage for coarse alignment) for stylus motion as will be explained in detail in the next section.

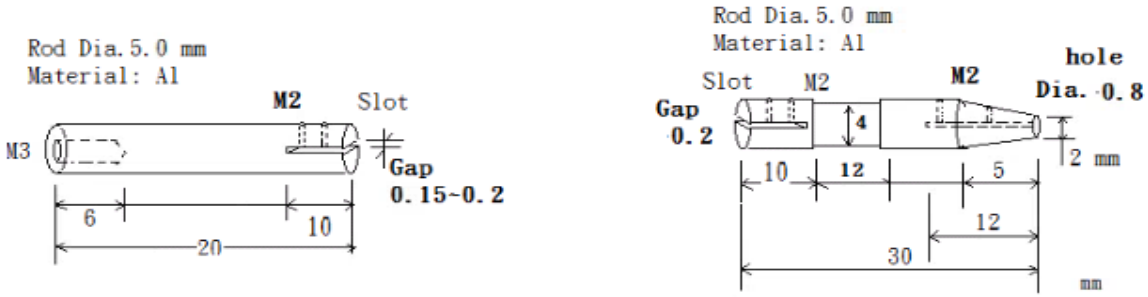

Figure 5. 6: Engineering drawing of stylus holder

5.3.2. Force sensing mechanism

A precision mass balance and a lightweight test workpiece are used in sensing the force during the experiments. The test workpiece functions as a representative measured workpiece and is placed on the mass balance as shown in Figure 5.7. The precision mass balance records the results when the stylus touches the test workpiece. Later, in data analysis, by using gravitational acceleration constant, the results reported in in mass units will be converted to forces. The copper sheet is used as a test workpiece. The precision mass balance used in this experiment is manufactured from Mettle Toledo (model AT20) which has the resolution of 2 µg and weighing capacity up 22 g [135].

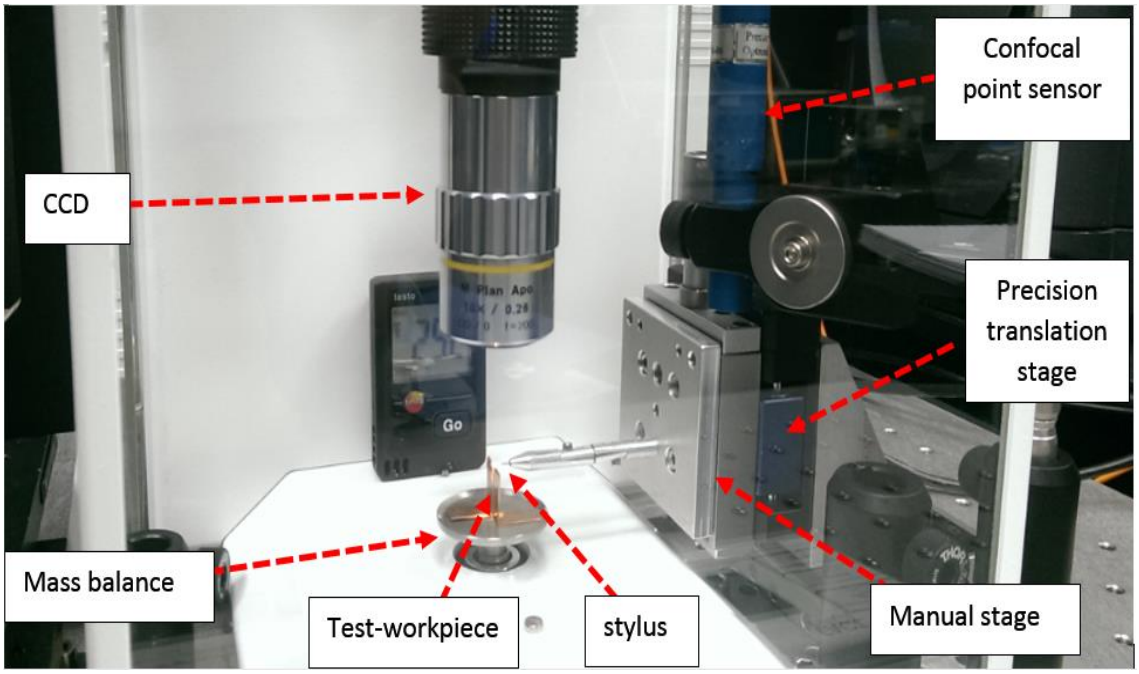

Figure 5. 7: test workpiece is placed on the precision mass balance to function as force sensing mechanism

5.3.3. Motion mechanism for the stylus

The stylus is required to be moved in the vertical direction toward the test workpiece to make contacts. For this purpose, the stylus holder which was introduced in section 5.3.1 is attached to a precision translation stage. The required motion of the stylus must resolve well into sub-micrometre range and provide close control over sub-tens-micrometres ranges, based on theoretical values of maximum deflection given in Table 5.1. Also, the stylus must be able to move over wide vertical travel ranges to facilitate the setting up and to model CMM approaches. The precision translation stage must have capability to fulfil all the requirements. In this experiment, a model M-110.1 micro translation stage from Physik Instrumente (PI) is selected. Its travel range is 5 mm, with a resolution of 7 nm and minimum incremental motion of 50 nm [136]. The translation stage is connected and controlled by the control software (latter will be explained in section 5.3.5). To record the displacement of the stylus motion, a traceable chromatic confocal point sensor is employed. The chromatic confocal point sensor focused on the micro translation stage to measure the displacement of the stylus motion during the experiment as shown in Figure 5.7. The working range of this chromatic confocal point sensor is up to 250 µm with resolution of 10 nm.

5.3.4. Positioning, alignment and Monitoring components

Before starting the experiment, the tip sphere of the stylus has to be positioned accurately toward the top of the test workpiece without contacting it. This can be achieved by using a manual translation stage which functions as coarse alignment in vertical direction for the stylus motion. This manual translation stage is placed between the stylus holder and the precision micro translation stage. For horizontal positioning, another manual translation stage is also attached to the stylus. A CCD camera are also employed to assist positioning the stylus during the alignment process. Furthermore, the CCD camera are also important in monitoring the stylus condition during the entire experiment.

5.3.5. Control software

An interface that controls and gathers all experimental results has been developed in LabVIEW software [137]. The data from the precision mass balance, chromatic confocal point sensor are input to this control software. Furthermore, it also controls the movement of the precision micro translation stage, with each movement being recorded. The movement step of this stage will be explained latter in section 5.6.2.

5.4. Preliminary performance testing of each component

To understand the operational behaviour of the main components in this setup, preliminary performance testing was conducted. Such testing is very important to ensure the result from the experiments are reliable and to establish confidence. As the precision mass balance and chromatic confocal point sensor are used to record mass (for force data) and the displacement of the stylus during the experiment as explained in the previous section, the noise and drift of both instruments need to be determined. Section 5.4.1 and 5.4.2 explain in detail the procedures and results of this noise testing. In section 5.4.3, the stability of mass balance plate is another very important factor, has been determined. The basic principle of operation of the mass balance involves the displacement of its plate in order to measure an imposed weight. It is crucial to measure the changes of displacement of the mass balance plate occurring during the present experiments as it will contribute to the measurement uncertainties. To select an optimised process parameter for the stylus motion, the backlash and delay time of the precision translation stage were measured, as described in

section 5.4.4. In addition, trial-run testing of overall experimental setup is explained in section 5.4.5. Conducted at the beginning of each experiment, this initial testing ensured that all main components in experiment setup operated properly in combination and produced results as expected in the designated experiment. Otherwise, the experimental set-up was inspected again and troubleshooting done as necessary.

5.4.1. Testing of noise for precision mass balance

The noise of the precision mass balance was determined by monitoring and capturing the reading of the mass balance every 10 seconds over period of 40 minutes. In this noise testing, the mass balance was running without measuring any test specimen. This experiment was repeated for the second time and the graph of mass against time was plotted. These graphs are shown in Figure 5.8 and Figure 5.9. All graphs are close to normal distribution with slightly left skewed. Also, these graphs show consistency indicating that a noise of the mass balance, as determined from the difference between maximum and minimum values is 0.17 mg and 0.24 mg. This information will be used in the evaluation of measurement uncertainty.

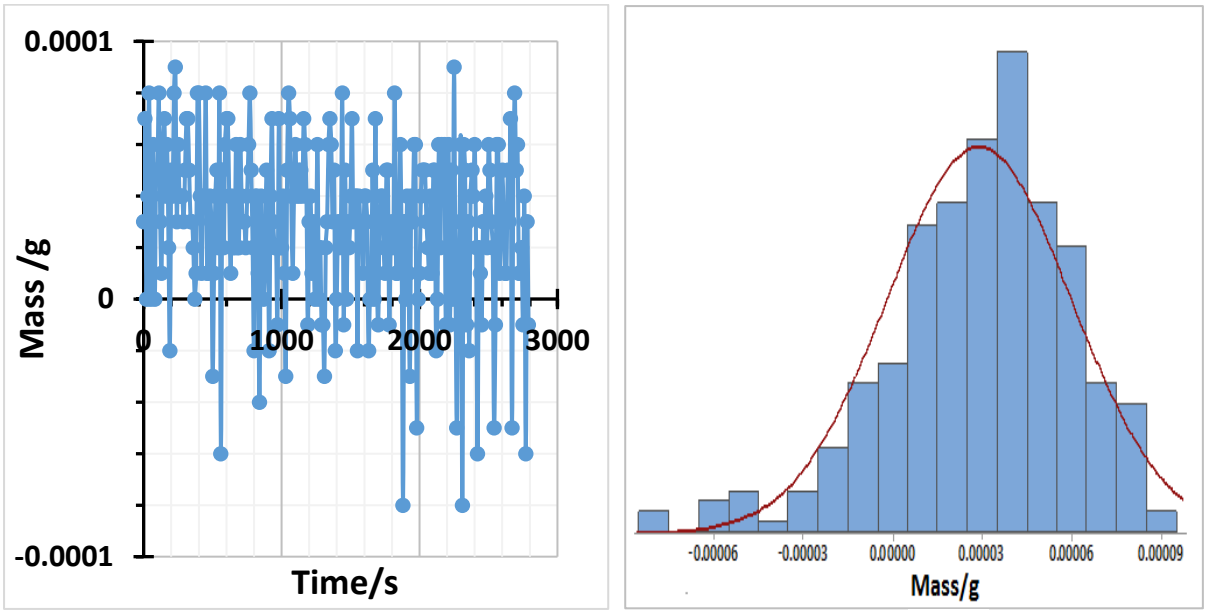

(a) (b)

Figure 5. 8: Result of first run testing for noise of precision mass balance. (a) is representing the raw measurement data point while in (b) shows its distribution. With mean of 0.029 mg, standard deviation of 0.031 mg, kurtosis of 0.9 and skewness of -0.74, the points of this data is slightly headed to the left of distribution

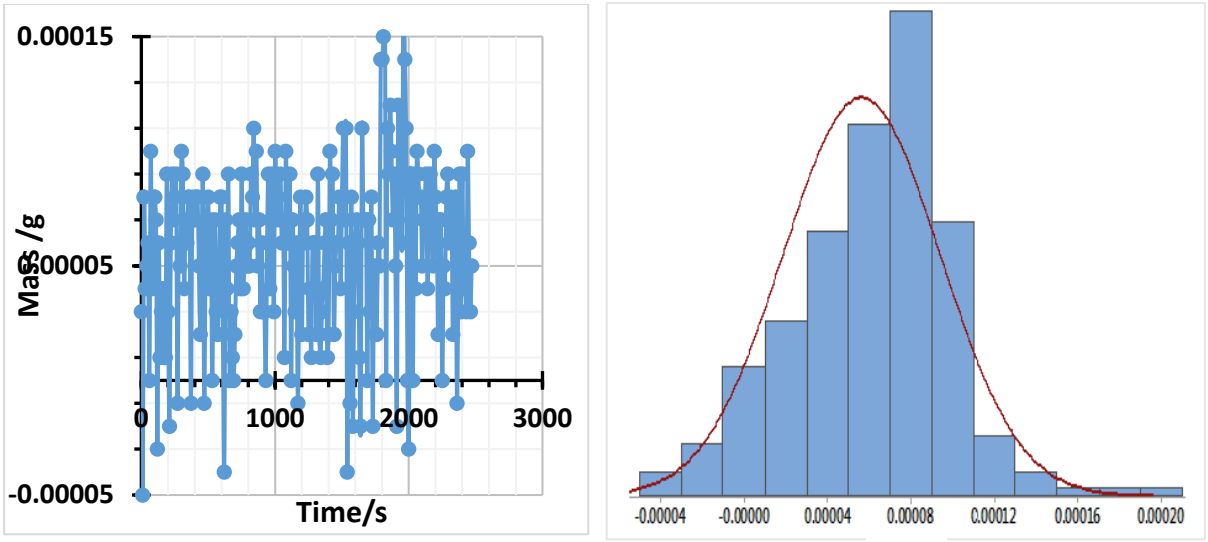

(a) (b)

Figure 5. 9: Result of second run testing for noise of precision mass balance. (a) is representing the raw measurement data point while in (b) shows its distribution. With mean of 0.06 mg, standard deviation of 0.04 mg, kurtosis of 0.7 and skewness of -0.11, the points of this data is slightly headed to the left of distribution

5.4.2. Noise level of the chromatic confocal sensor

The chromatic confocal sensor is focused onto the manual translation stage in the experimental setup. The manual translation stage is mounted using fix holder. For this noise test, all components in the instrument set-up including the manual translation stage are in a fixed position without any motion. The reading of the chromatic confocal sensor is captured every 10 seconds over a period of 2 hours. A s similar to the noise testing for the mass balance in section 5.4.1, the noise value for chromatic confocal sensor can be calculated by determining the different between maximum and minimum value in this result. Figure 5.10 plots the chromatic confocal sensor output vs time, recorded over almost two hours from initially setting it up. Initially, there is a notable consistent positional drift, typical due thermal and electronic fluctuation, which is likely to be the primary cause here. The system stabilises after about 40 minutes, to a more-or-less constant, noisy level. Figure 5.11 shows a magnified extract of the trace in Figure 5.10, beginning after 40 minutes and taken to represent the steady-state noise level; actually there might be a small contribution from environmental drift over the more than an hour-long period shown, so this represents a conservative estimate of operational noise levels. The peak-to-peak noise from the displacement sensor was 40 nm, while the root-mean-square (rms) noise over shorter periods is generally well below 10 nm.

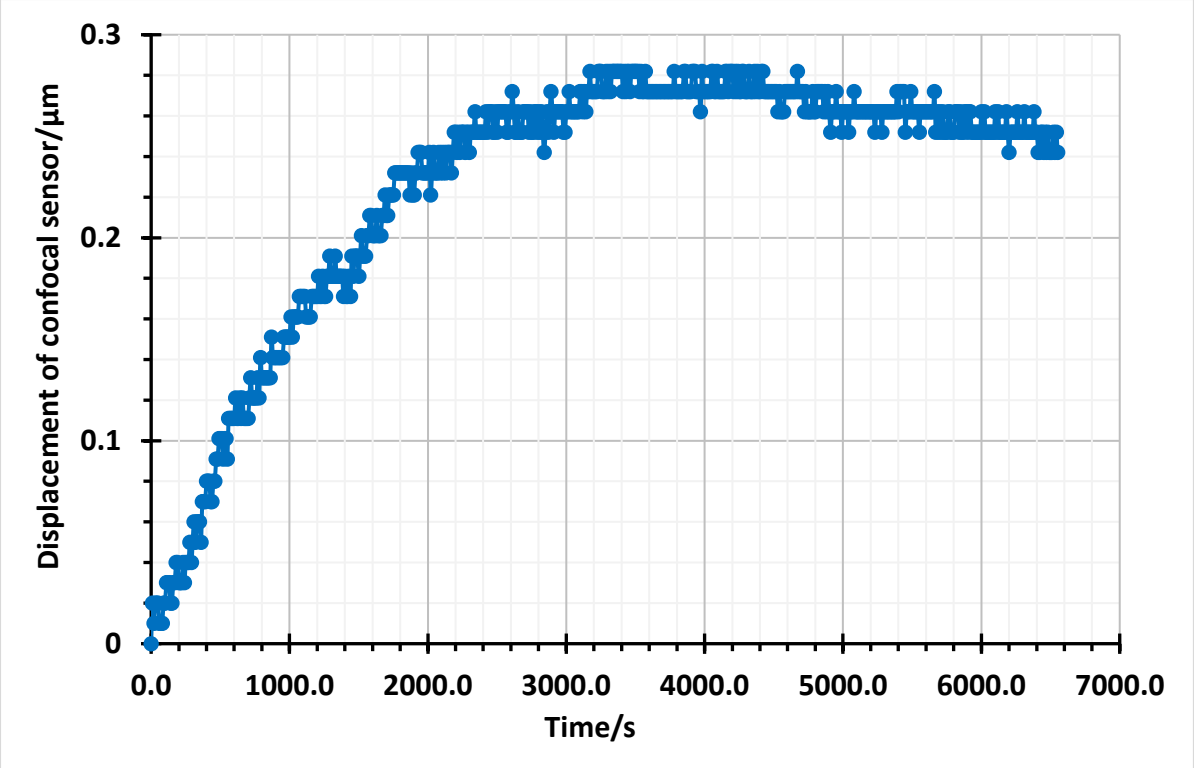

Figure 5. 10: The drift and noise of the chromatic confocal sensor over period of time from initially setting up

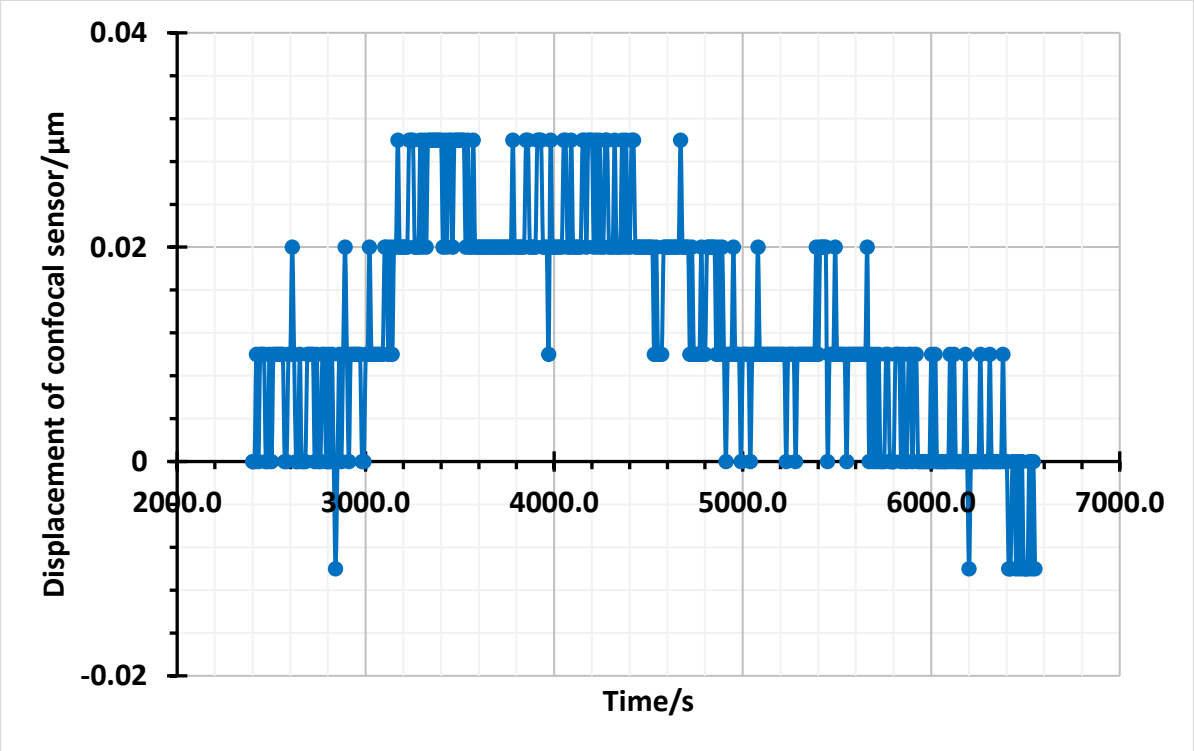

Figure 5. 11: The noise behaviour of chromatic confocal sensor after it has stabilised

5.4.3. Stability testing of mass balance plate

The mechanism of operation of the precision mass balance involves a displacement of the mass plate in vertical direction in order to measure a mass. As the displacement of the stylus is an important parameter to be measured in both experiments in this project, any displacements activities in components of the metrology loop of the experiment need to be recognised. Therefore, the movement stability of the mass plate use in this experiment must be identified and included as one of the sources of uncertainties.

To measure the stability of the mass plate, the chromatic confocal sensor was focused on the mass plate and the reading recorded every 10 seconds over a period of 40 minutes. This procedure was then repeated three times. As with previous preliminary performance testing, the value of stability error of mass plate is determined by the difference between maximum and minimum points in the results. This stability error was measured as 80 nm, 140 nm, and 141 nm with root-mean-square (rms) noise below 16 nm. The graph of displacement against time for three repeated testing is plotted and shown in Figure 5.12, Figure 5.13, and Figure 5.14. The data points of all of these graphs are close to the normal distribution.

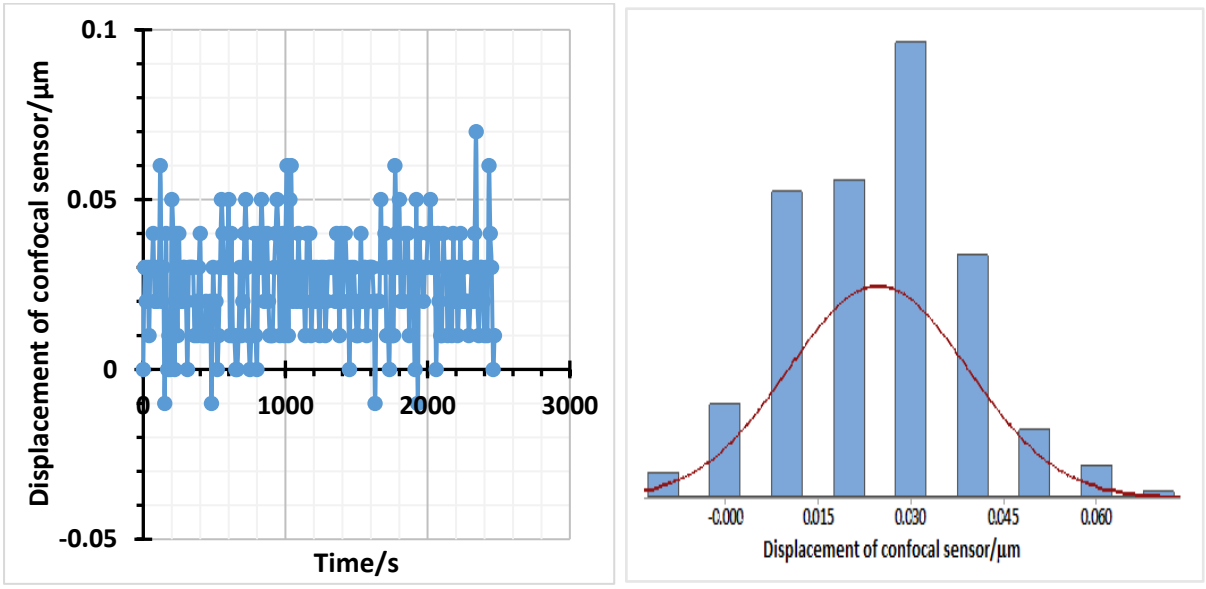

(a) (b)

Figure 5. 12: First testing result for stability of mass balance measured by chromatic confocal sensor. (a) represents a raw measurement data point while in (b) shows its distribution. With a mean of 0.024 µm, standard deviation of 0.015 µm, kurtosis of -0.03 and skewness of 0.1, the distribution of this graph is normal with slightly have right skewed.

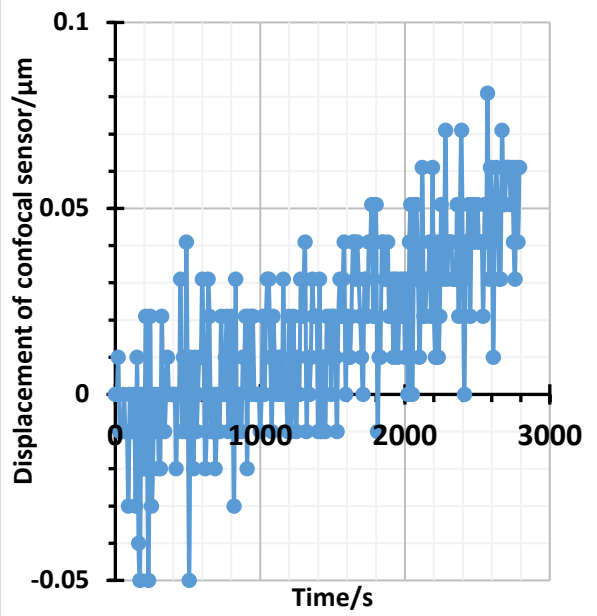

(a)

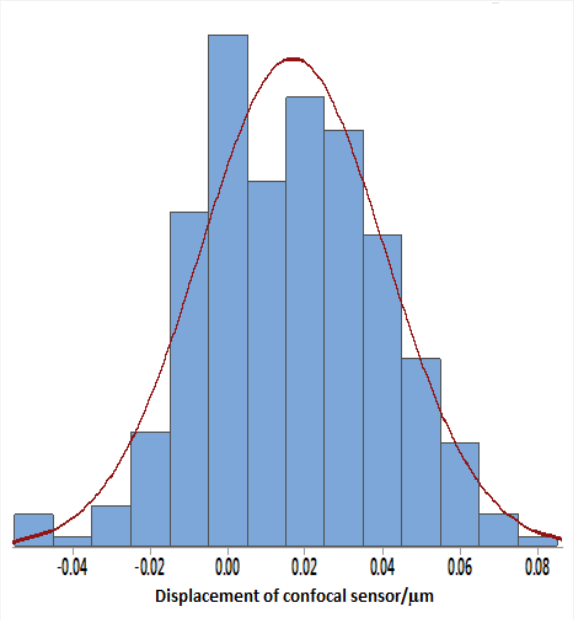

(b)

Figure 5. 13: Second testing result for stability of mass balance measured by chromatic confocal sensor. (a) represents the raw measurement data point while in (b) shows its distribution. With mean of 0.017 µm, standard deviation of 0.024 µm, kurtosis of -0.22 and skewness of -0.003, the points of this data is slightly headed to the left of distribution

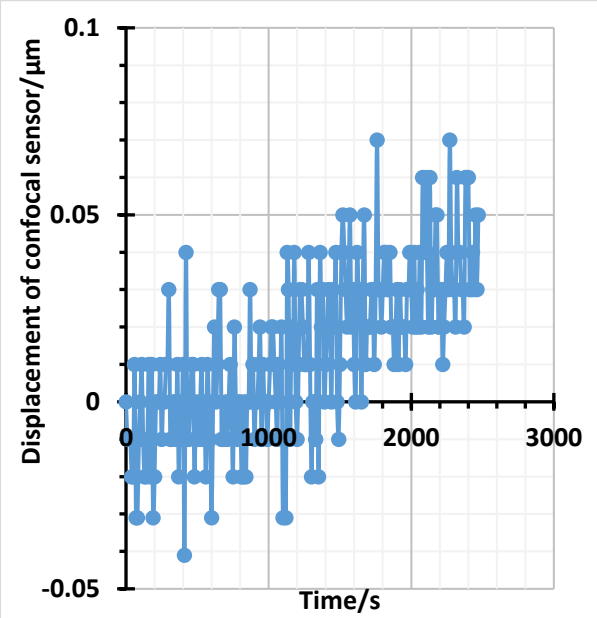

(a)

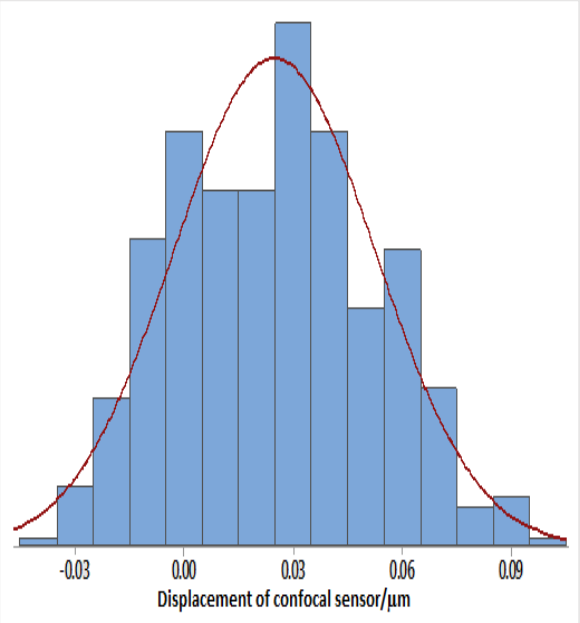

(a)

Figure 5. 14: Third testing result for stability of mass balance measured by chromatic confocal sensor. (a) is representing the raw measurement data point while in (b) shows its distribution. With mean of 0.03 µm, standard deviation of 0.027 µm, kurtosis of -0.55 and skewness of 0.15, the points of this data is slightly skewed to the right of distribution

5.4.4. Optimum parameter testing for the micro translation stage

In the main experiment procedure, the micro translation stage is instructed to move downward in vertical direction until it reaches a certain point, before returning back to its initial position. The motion of the micro translation stage is designed to be execute in a 'step pattern' where the stage will stop at several positions until the stage reaches the specified maximum point and return to the initial position. During reversal of the stage, the backlash phenomenon may affect the motion of the stage and hence it needs to be investigated. Two important parameters involved in this 'step pattern' motion are the incremental position and dwell time before the stage move to another incremental position. It is crucial to select an appropriate value for both parameters to avoid any unnecessary errors in stylus motion.

To determine the suitable incremental value, an experiment was conducted where the micro translation stage was moved up and down several times and the displacement monitored by the chromatic confocal sensor. Value of 0.05 µm and 0.1 µm were selected as representative test increments for this experiment. The results are in Figure 5.15, and Figure 5.16. Both graphs have similar general characteristic. Therefore, it can be concluded that the backlash error does not significantly contribute with either 0.05 µm or 0.1 µm increments and therefore, for the purpose of this project, 0.05 µm was selected as incremental value for stage motion.

The same experimental procedure was also conducted to determine the value of delay stopping time. Values of 20 seconds, 10 seconds, and 6 seconds were selected as the trial values for dwell time. With the incremental position value of 0.05 µm and 0.1 µm, two sets of experiments with selected values of delay stopping time were conducted. The results of both sets of experiments reveal that there is no significant difference among these tested values and the graphs obtained from each experiment show similar trends, Figure 5.15 and Figure 5.16. Hence, for the purpose of the experiment in this project, 6 seconds is chosen as the value of dwell time.

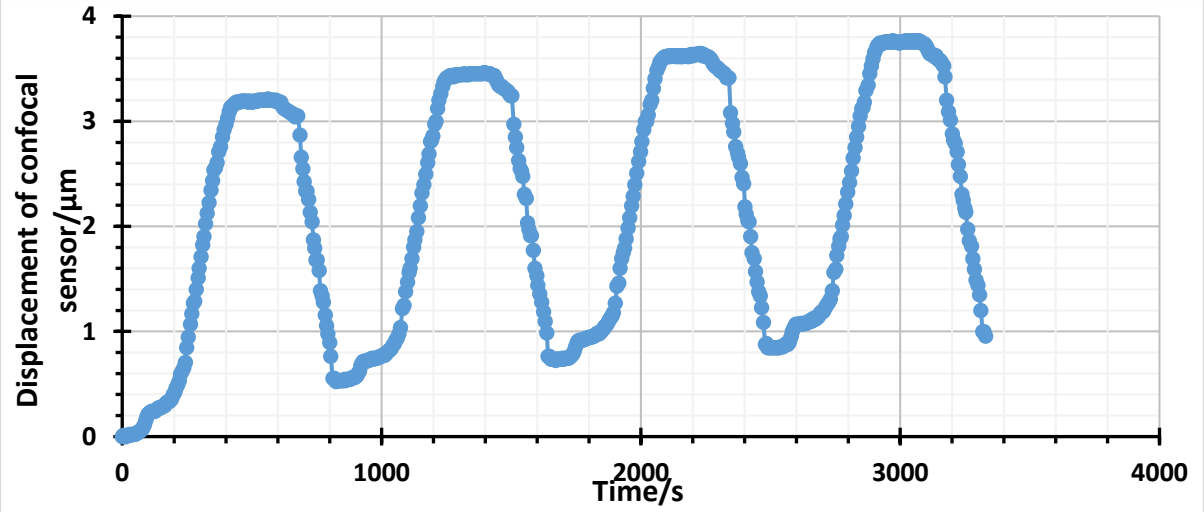

Figure 5. 15: The result of 0.1 µm of incremental value

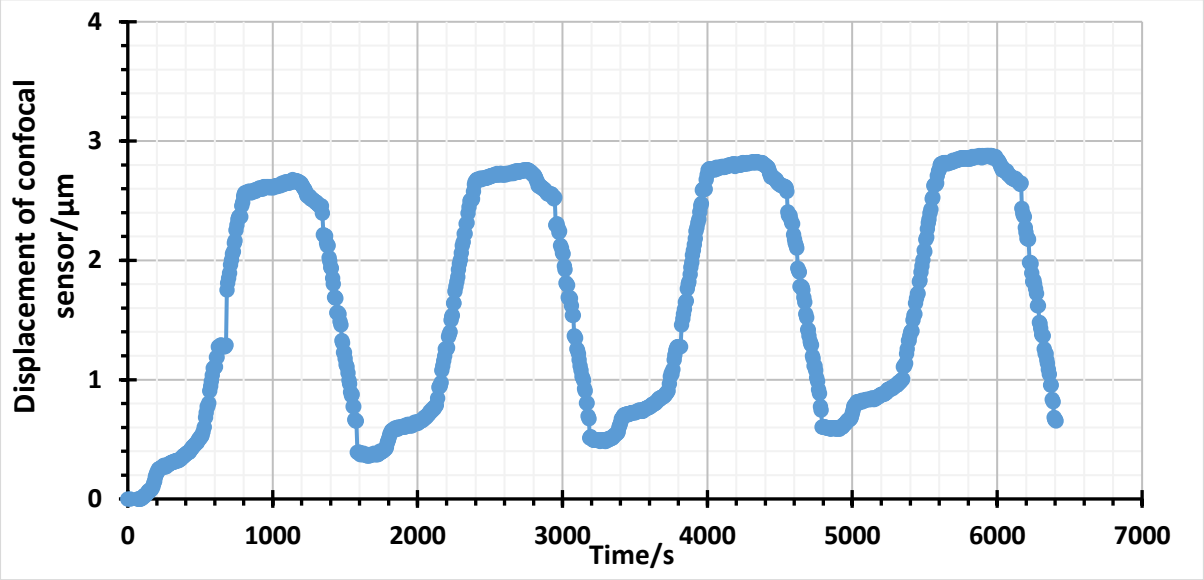

Figure 5. 16 : The result of 0.05 µm of incremental value

5.4.5. Initial testing/trial-run of the overall experimental set-up

A trial-run of the overall experimental setup is a very crucial step in this experiment procedure. It has to be conducted in the beginning of each new experiment and every time the stylus is changed. The trial-run testing indicates the ability of each functional group of components to operate as instructed by the control software. In general, the precision mass balance, precision micro translational stage and chromatic confocal sensor are expected to function throughout a test in a manner similar to that presented in Figure 5.17.

The stylus should be moving downward under the action of the precision micro translational stage to make contact with the test workpiece. When the stylus contacts the test workpiece, the force starts to be applied to it, and hence the precision mass balance starts to detect a mass reading. As the stylus moved further downward after initial contact with the test workpiece, the mass reading will increase because the force applied to the test workpiece is increased. After a certain point, the stylus will be instructed to return to its initial position before contacting the test workpiece. At this point, the applied force will be decreased and the mass reading will be also decreased. The chromatic confocal sensor is used to monitor the motion of the micro translational stage. Therefore, the confocal sensor will follow the pattern of the micro translational stage as shown in in Figure 5.17 (although, at the beginning, there are differences in slope of the both graphs, they are seen started to have similar slope when they are nearing to the condition where the stylus touch a test-workpiece and mass reading started to increase). Figure 5.17 also shows that the mass readings are instable at the region of the reversal of the micro translational stage. This confirmed that a backlash phenomenon occurs during the reversion process. However, the backlash phenomenon did not affect the measurement result as the graph in Figure 5.17 shows that the difference of the slope between the translational stage and the chromatic confocal sensor before and after the reversal region seems sufficiently small. The experimental setup was checked for each new test and troubleshooting applied if these functional group did not operated consistently to the pattern shown in Figure 5.17.

To avoid failure in trial-run testing, it was crucial to ensure the control software is fully capturing the results of each of the main components and its functions should be monitored during the trial-run testing. Also, a light beam of chromatic confocal sensor must be focused on a flat surface at the manual surface in order to obtain a stable signal. Sometimes, the micro translational stage acted somewhat erratically. In such cases, the manual stage and stylus holder were disassembled from the micro translational stage which was then tested separately and fixed, including by the use of different software.

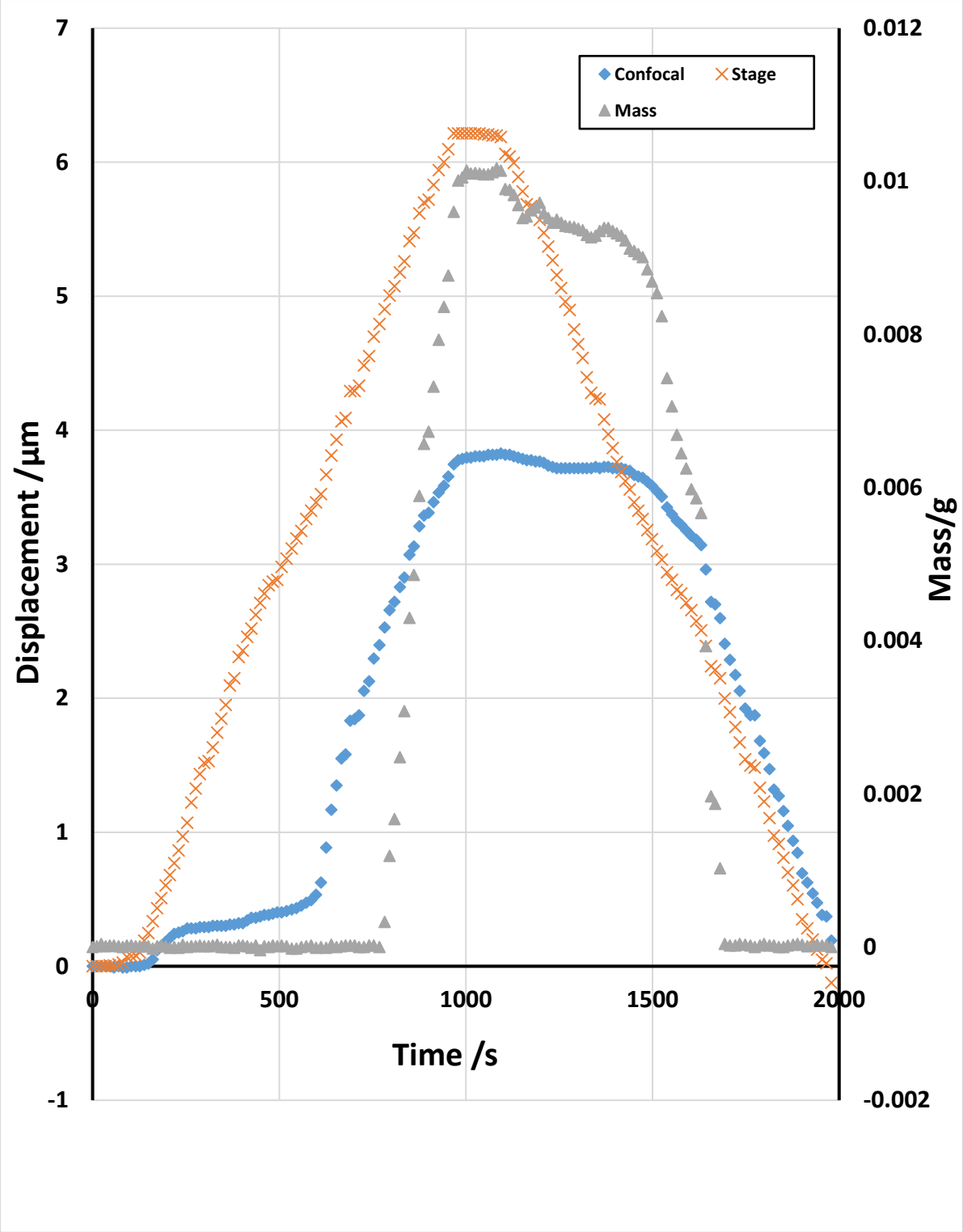

Figure 5. 17: The behaviour graph of precision mass balance, manipulation stage and precision chromatic confocal sensor in initial/trial run testing experiment

5.5. Procedure for the experiment to measure the stiffness of the stylus

As stated in the beginning of this chapter, one of the experiments conducted in this study is to determine the stiffness of the stylus. This section describes how the strength characteristic of the effective stylus shaft under a force which is perpendicular to the direction of the stylus shaft is tested. As the stylus is mounted in the horizontal position, the force occurs when the stylus is moving downward in vertical axis and its stylus tip makes a contact with the test-workpiece. The procedure of this experiment will now be explained in detail.

5.5.1. Experimental Setup.

As explained in section 5.3, the experiment was set-up according to Figure 5.5. Before a stylus was attached to the stylus holder in the set-up, the geometrical dimension of the stylus was measured separately using an optical 3D measurement machine manufactured by Alicona Imaging GmbH [134]. The length of the stylus, the effective length of the stylus shaft (the length of the lower part of stylus shaft), the length of upper part of stylus shaft, the diameter of the stylus shaft and stylus tip are all important parameters to be measured and recorded because all of these actual dimensions will be used in modelling the theoretical stiffness value as described in section 3.4.4. Each of the main components in the experimental set-up especially the micro translation stage, precision mass balance and chromatic confocal sensor was checked to be functioning well. Then, the experimental setup was left to stabilise thermally and mechanically for at least 1 hour.

5.5.2. Positioning the stylus relative to the test-workpiece

An important precautionary step is necessary in this experiment. The motion of the stylus after running a first contact with the test-workpiece, must not exceed the value of maximum deflection given in Table 5.1 in order to avoid plastic deformation and hence damaging the stylus. As the minimum value of maximum deflection stated in Table 5.1 is 1.8 µm, it was decided, as a precautionary step that, for all stylus testing in this experiment, the maximum travelled motion of the stylus after the first contact was 1 µm. Thus, this condition was set up in the control software. However, in order for the stylus tip to make a first proper contact with the test-workpiece, the control software needs to know precisely the location coordinate of the surface of the test-workpiece. It can be solved by conducted a

precautionary step procedure. Using the manual stage, the stylus was brought to a position as close as possible to the top of the surface of the test-workpiece without touching it. Having ensure that, the stylus tip is properly aligned on the top surface of the test-workpiece, this position was taken as the initial point for the main measurement sequence. Then the control software instructed the micro translation stage to move the stylus tip automatically to make a contact with the surface of test-workpiece. Once the stylus tip started contacting the surface of the test-workpiece, the reading of mass balance increased, hence, the control software could detect and record that position as the location of the test-workpiece. The stylus tip was then immediately raised up by the micro translation stage until a small vertical gap distance was achieved between the stylus tip and the surface of test-workpiece. By this means, a consistent gap distance between stylus and workpiece was established before the start of every experiment. A value of 6 µm has been selected as reasonable for this gap distance.

5.5.3. Trial-run of testing

The trial-run testing was conducted as described in section 5.4.5. It is worth mentioning that this step had to be conducted each time the stylus was changed and a new experiment conducted. After contacting the surface of the test-workpiece (it worth noting that as explained in section 5.5.2, a 6 µm gap distance had already established before contact), the stylus tip was moved downward by about 1 µm before returning to its initial position. Once the behaviour this trial-run test match that explained in section 5.4.5 (Figure 5.17), the experimental setup was deemed ready for stiffness testing.

5.5.4. Testing procedure

To determine the stiffness of the stylus (strictly, the stiffness of the effective stylus shaft), two parts of the stylus were required to make contact with the surface of the test-workpiece: the stylus tip and the upper region of the stylus shaft. Therefore, the stiffness experiment is a two-part procedure. The first part is called the ***Koverall-testing***. In this part, as shown in Figure 5.18, the stylus tip contacted the test-workpiece and so the overall stiffness will be measured and calculated from the slope of force-displacement graph. The result from this part was named as ***Koverall*** and it represented the stiffness of the entire

experimental system including the stylus itself, the stylus holder, the positioning manipulation stages and any mechanical holder that attached to the stylus.

The second part of the stiffness measurement is called ***Ksetup-testing***. This part was conducted by contacting the upper part region of stylus shaft with the test-workpiece, as illustrated in Figure 5.19. Ideally, the end of effective stylus shaft which at point B should be contacting the test-workpiece. However, as the effective stylus shaft is the smallest diameter dimension of the part in the stylus, we did not want to take any risk to damage the styli. Therefore, as precautionary step, the upper part region at point C is selected to be touched with the test-workpiece. The result obtained from this part is the stiffness result of the entire experimental system except the effective stylus shaft, known as ***Ksetup***.

By The overall stiffness arises from the serial connection of the setup stiffness and the effective stylus stiffness, so the latter can be calculated from equation 5.1 which will be explained in detail in section 5.7.1:

$$\frac{1}{K_{overall}} = \frac{1}{K_{setup}} + \frac{1}{K_{stylus}} \tag{5.1}$$

Where the ***Kstylus*** is the stiffness of the effective stylus system, ***Ksetup*** is the stiffness of entire experimental system except the effective stylus shaft where the measurement is taken at the upper region of stylus shaft, and ***Koverall*** is the stiffness of entire experimental system where the measurement is taken at the stylus tip.

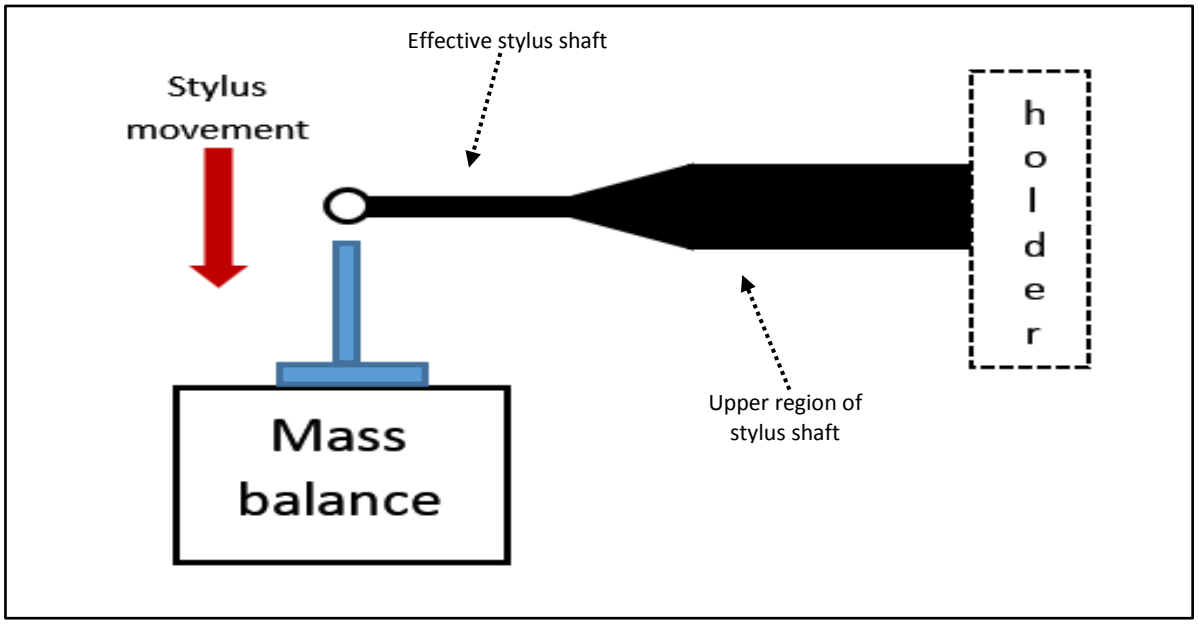

Figure 5. 18: The stylus tip contacted the test-workpiece in the **Koverall-testing** part

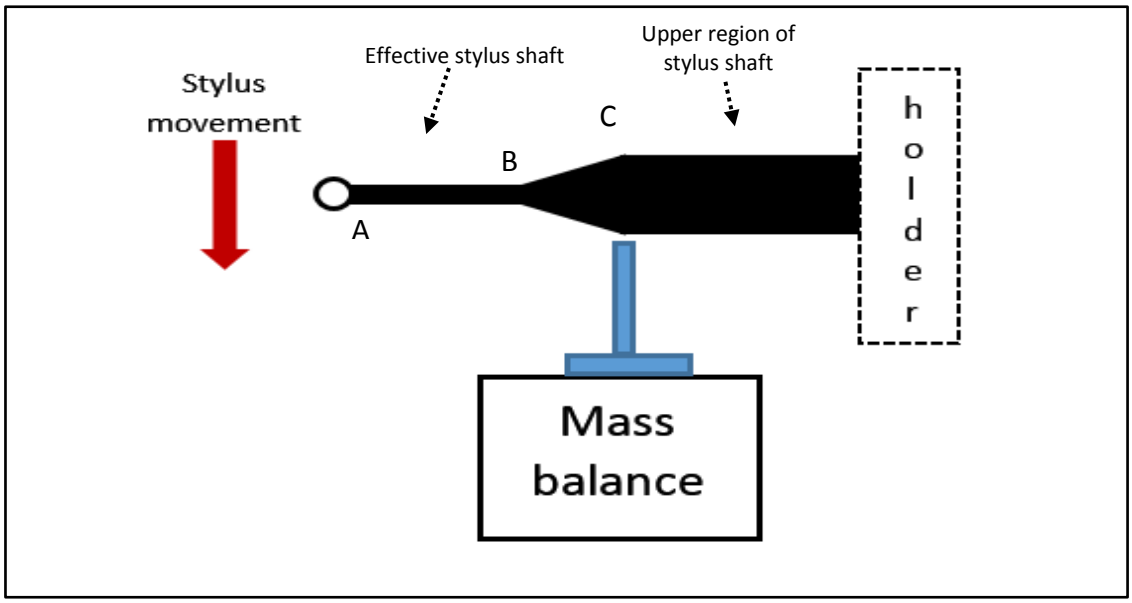

Figure 5. 19: the upper region of stylus shaft was contacting the test-workpiece in **Ksetup-testing** part

The details of testing procedures are as follows:

a) The first step was to use the method described in section 5.5.2 to ensure that the stylus tip was aligned to the top of the test-workpiece as in Figure 5.18 with the gap distance of 6 µm established between stylus tip and test-workpiece.

b) Then, the control software instructed the stylus tip to move 7 µm downward (vertical direction) in a 'step' pattern before returning to the initial position at a travel speed of 0.05 µm s^{-1}. As the gap distance between the stylus tip and test-workpiece is 6 µm, the stylus tip actually moved about 1 µm after contacting the test-workpiece before returning to the initial position. 'Step' pattern was a consistently-applied motion pattern in which the stylus was moved to a certain distance and then stopped for a certain time to stabilise and allow the control software to record the reading from mass balance and confocal displacement sensor, before continuing move downward to the next position, pausing again and so on. This process continued until the stylus had moved 7 µm downward before returning to the initial position. The distance between each stopping position and the stopping time are called the incremental displacement and delay time. Meanwhile 7 µm is called total incremental displacement. In this experiment, as determined in section 5.4.4, the optimized value for incremental displacement and dwell time were 0.05 µm and 6 s.

c) The reading of the precision mass balance, chromatic confocal sensor and micro manipulation stage were recorded at each of the incremental displacements.

d) This experimental cycle finished when the stylus completed its return to the initial position where the gap distance of 6 µm (as explained in section 5.5.2) was established.
e) Steps (a) to (d) above were repeated three times to obtain three independent sets of data.
f) For the second part of this experiment, step (a) is repeated but this time, the upper region of the stylus shaft aligned to the top of the test-workpiece as in the *Figure 5. 19* with the gap distance of 6 µm (as explained in section 5.5.2) was established between stylus tip and test-workpiece.
g) Then, steps (b) until (e) were repeated and three sets of raw data were obtained.

5.6. Procedure for measuring the maximum safe tip force

The objective of this experiment is to determine the maximum force that can be applied to the stylus in perpendicular axis to the stylus axis without damaging the functionality of the stylus itself. A stylus will have functioned as designed if it operates completely in the elastic region of its stress-strain graph. Once any plastic deformation occurs in the stylus, it could not be used anymore. Generally, in this experiment, an increasing force was applied to the stylus until the stylus is broken. Then the data was analysed and the maximum safe tip force measurement was determined. By the nature of its operational design, it is not possible for the experiment to be repeated with the same stylus. The detailed experimental procedure is explained in the following sections.

5.6.1. Experimental setup, positioning of stylus and initial/trial run

The experimental setup, precautionary steps and initial trial-run testing for this experiment were carried out the same way as explained in section 5.5.1, 5.5.2, and 5.5.3.

5.6.2. Testing procedure

After initial trial run testing had been completed and ensured the entire system functioned as intended, the main experiment was started by repeating the steps in section 5.5.2 to establish the distance gap of 6 µm between the stylus and test-workpiece. These

steps are important to confirm that the stylus tip was aligned just on top of the test-workpiece without touching it.

Then, the control software was set to have the following parameters: incremental displacement of 1 µm, delay time of 1 s and travel speed of 1 µm s^{-1}. Thus, the control software instructed the precision stage to move the stylus towards and into contact with the test-workpiece in vertical direction in step pattern. The stylus was temporarily stopped in each incremental displacement. The reading of the precision mass balance and micro manipulation stage were recorded at each incremental displacement. When the stylus made a first contact with the test-workpiece, the precision mass balance sensed an additional mass and as the stylus continued to move downward which it increased the force, so the reading of the precision mass balance also increased. The downward motion of the stylus was continued until the reading of precision mass balance suddenly drop to zero. At this moment, the stylus had been completely separated from the test- workpiece as the plastic deformation occurred which could Cause a permanent damage to the stylus for this test, the total incremental displacement was set in the control software to 'infinity'. Figure 5.20 and Figure 5.21 shows the condition of the tested styli after this experiment.

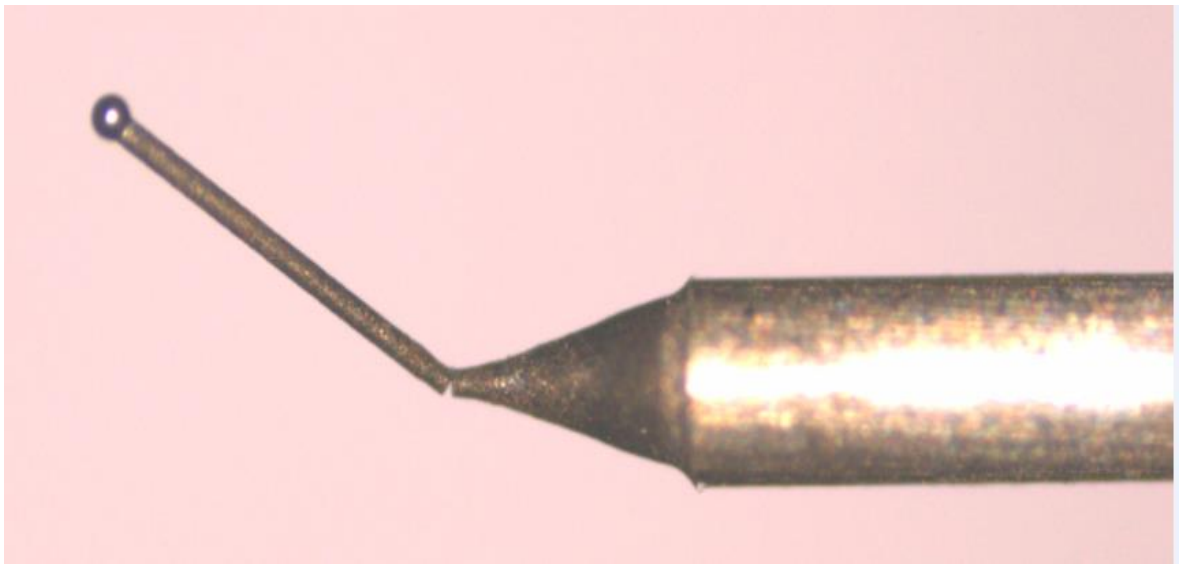

Figure 5. 20: condition of the broken stylus

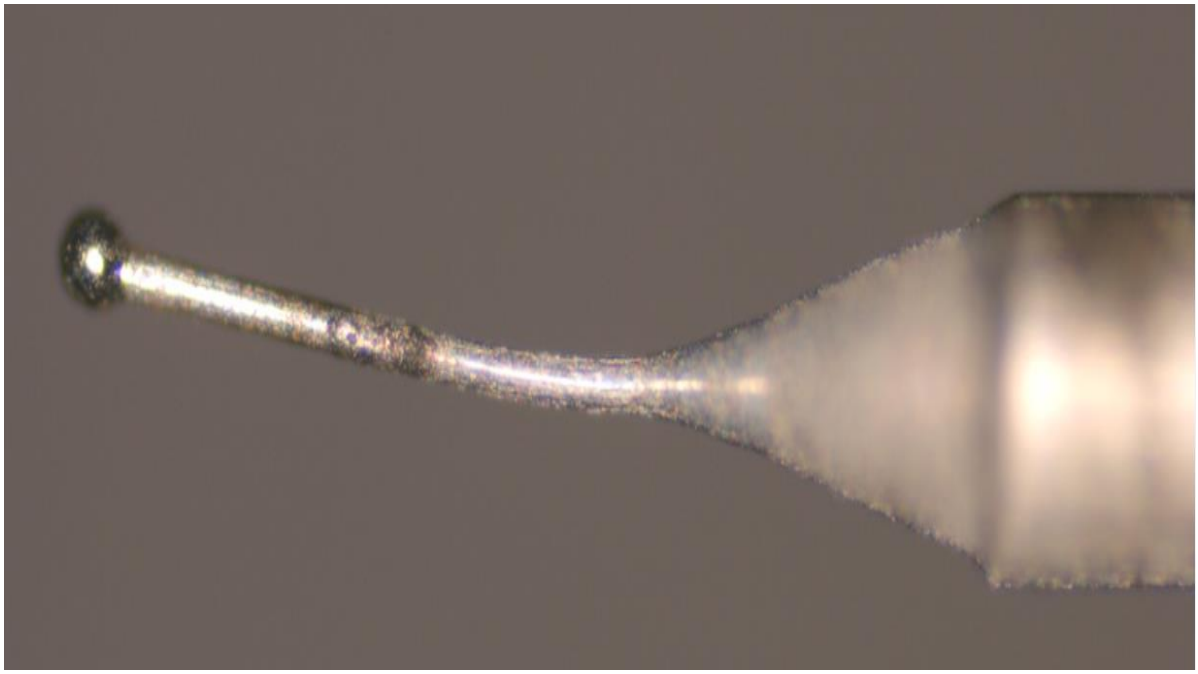

Figure 5. 21: the condition of permanent bending occurred in the stylus after testing

5.7. Post-measurement processing: Method of data analysis

The control software of each experiment is designed to collect all raw data and save the data in a comma-separated .txt format file. The data gathered in this file at every incremental displacement position is the reading of the precision mass balance, the reading of the chromatic confocal sensor, position of precision manipulation stage and the time from the computer clock. The data is then transferred to Microsoft Excel spreadsheets, where further data processing is done. The relationship between these data for majority of the test styluses is expected to be functionally similar to that shown in Figure 5.17 which was explained in section 5.4.5.

Before further analysis on the data is undertaken, a very important step in data analysis is to determine the position where the stylus first makes a contact with the top surface of the test-workpiece. This position can be detected when the reading of precision mass balance started to increase from zero. This is because until the stylus starts to contact the test-workpiece, so applying additional vertical force to it, the test-workpiece is in isolation on the pan and its weight has been tared out. This position is then defined as the initial contact position and is used throughout the entire data processing. Section 5.7.1 and 5.7.2 will describe separately the remaining methods and process flows for each of the experiment.

5.7.1. Data processing for experiment of stiffness measurement

Although there are two separate thread of raw data obtained from two stages in the stiffness measurement, their data processing is similar. Both data sets are acquired to calculate the stiffness of the system either including the stylus or without the stylus.

After the initial contact position is defined in the raw data, the next process is to determine the stiffness of the experiment by plotting the *force- displacement graph.* The slope of this graph is recognised as the required stiffness of the experiment. The data starting from the initial contacting position is used in this process. Having a gravitational acceleration constant of 9.802 m s^{-2}, the data from the precision mass balance is converted to force data in units of newton (N). In contrast, there are two methods to define the displacement data of the stylus. For the first method, the data from the confocal chromatic sensor reading is used as the displacement data for plotting the *force-displacement graph*. This method is the main method used in this experiment in processing the results data. Alternatively, the second method is employed by using the manipulation stage position (as reported by its own controller) as the displacement data. However, because the manipulation stage position is not independently calibrated, its positional data needs to be first verified with the data from the confocal chromatic sensor and a correction then applied to provide the required displacement data. This second method could be used if the confocal sensor showed too many outliers or poor consistency in particular run. Throughout these experiments, the second method was applied only to the data for stylus code *0602-5-6* of *manufacturing type 4*. Figure 5.22 shows the comparison of the force-displacement graph which the displacement data were obtained from both the chromatic confocal sensor and the manipulation stage itself from the first repetition experiment. The correction calculated from this comparison was then applied to second and third repetition results. This method was applied to this data set because the corresponding confocal chromatic sensor reading exhibited unlikely features and inconsistency in the second and third repeated runs of Koverall- *testing,* currently unexplained but assumed due to an instability of the positioning of the confocal chromatic sensor itself (the clamp that use to fix the confocal chromatic sensor might be loose after continuously used in a long time for running series of previous experiments). Noted that the displacement data in this graph is the displacement of the stylus from the initial contact position.

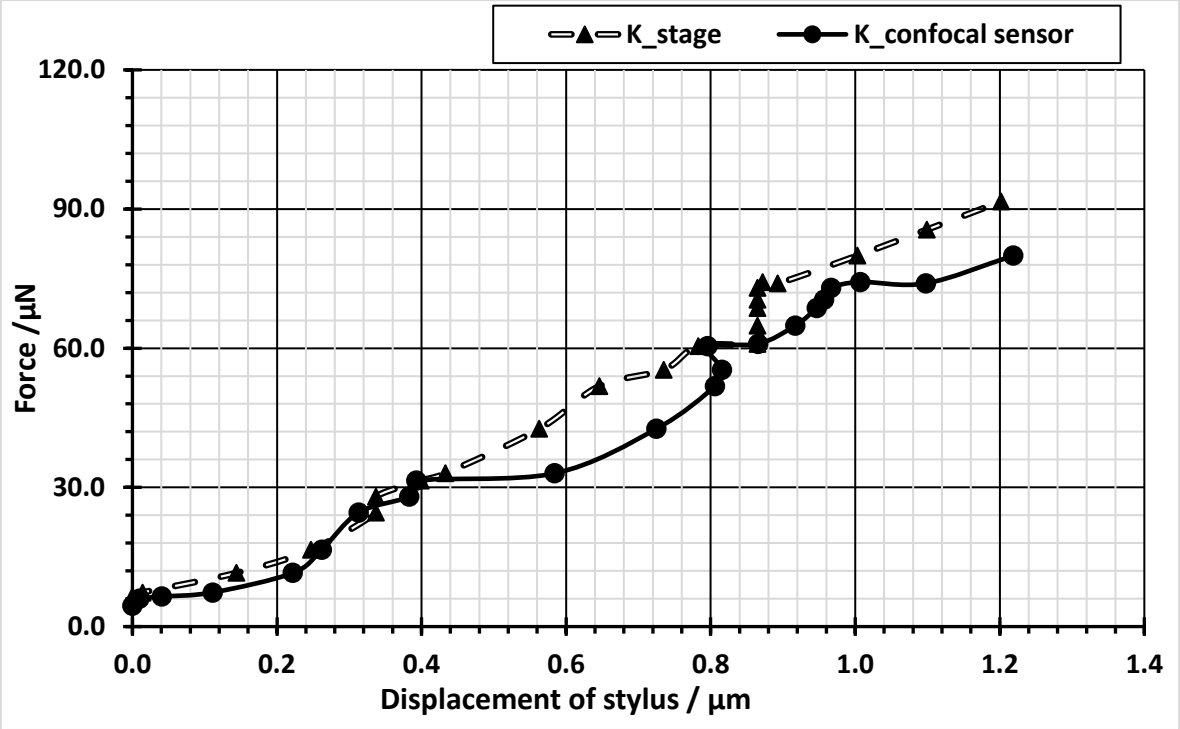

Figure 5. 22: Slope of the force-displacement graph obtained from displacement result from the precision manipulation stage is compared and verified with the displacement result obtained from the chormatic confocal sensor for stylus 0602-5-6 and correction is calculated

To demonstrate the process of data analysis in the stiffness measurement, the data from stylus code *0602-5-6*, *manufacturing type 4* (the smallest one) will be shown in this section. Figure 5.23 and Figure 5.24 display the force-displacement graph of the first-run testing for the *Ksetup-testing* experiment of stylus *0602-5-6* and a graph of the behaviour of its slope over the time of the experiment. Similar graphs for the *Koveral-testing* experiment for stylus *0602-5-6 are* shown in Figure 5.25 and Figure 5.26. All of these graphs demonstrate, a significant difference in the trend of the slope between when the stylus is moving downward and when it is returning to the initial contact position. In theory, the slope (stiffness of the stylus) should be a constants value, however, these graphs show that the motion of precision manipulation stage was not the same when returning to the initial position compared to the downward phase, due to the backlash effects in the mechanism of the stage itself. For this reason, the calculation of the stiffness in next step of data processing uses only the data taken during the downward phase.

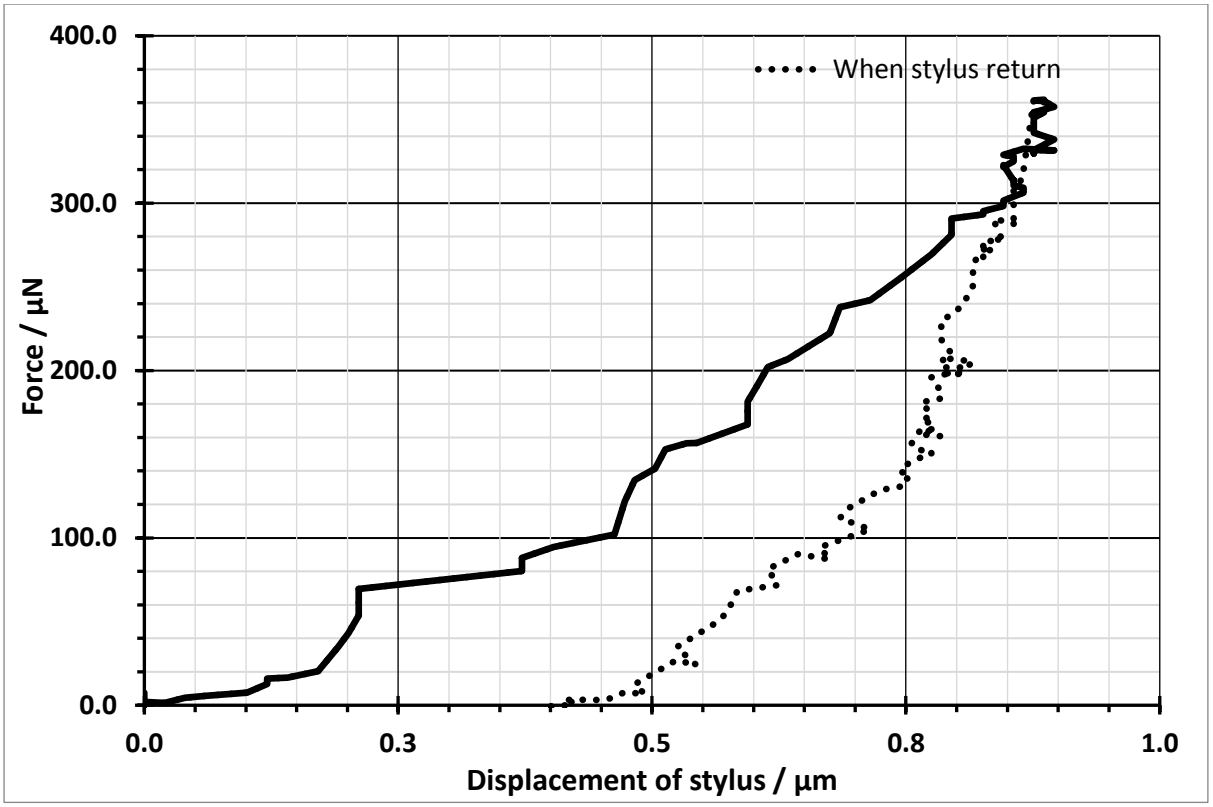

Figure 5. 23: Force-displacement for stylus 0602-5-6 in **Ksetup-testing** experiment

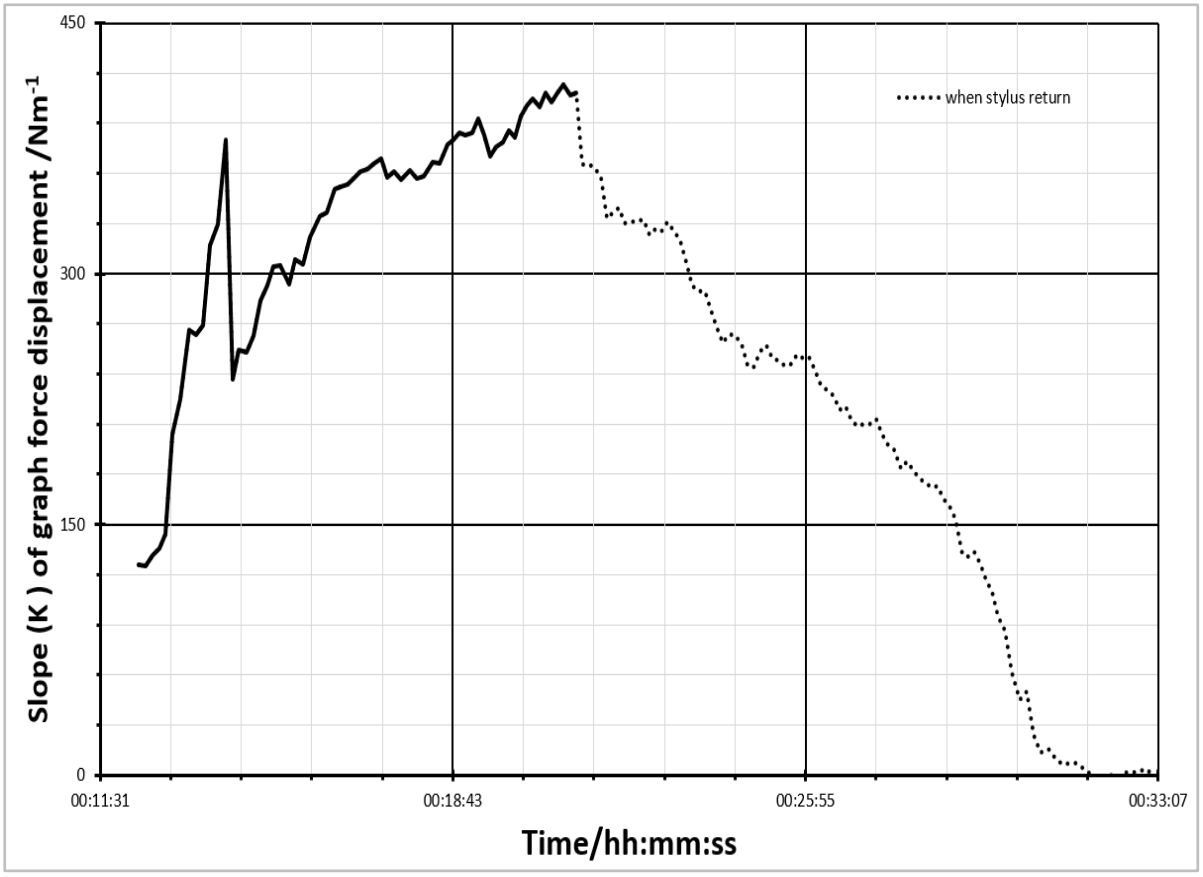

Figure 5. 24: Slope (K constant) of Force-Displacement graph for stylus 0602-5-6 in **Ksetup-testing** experiment

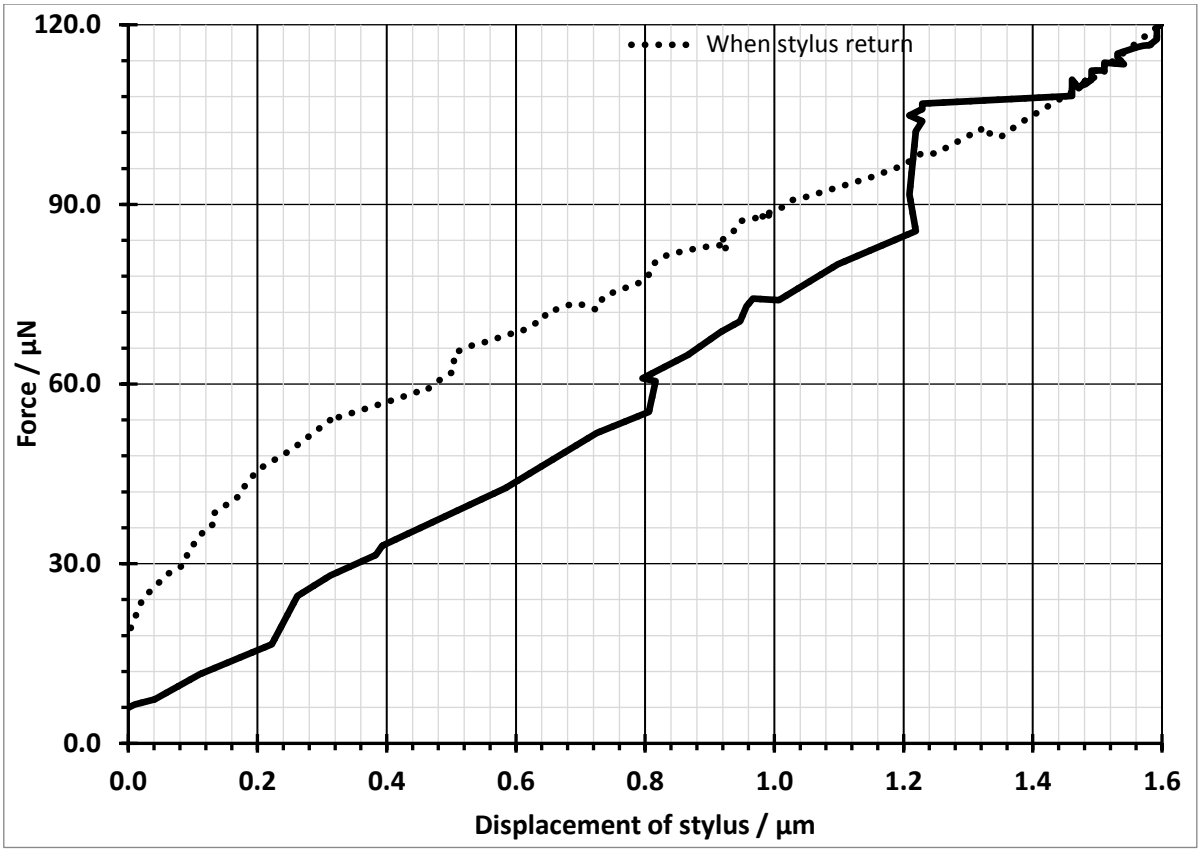

Figure 5. 25:Force-displacement for stylus 0602-5-6 in **Koveral-testing** experiment

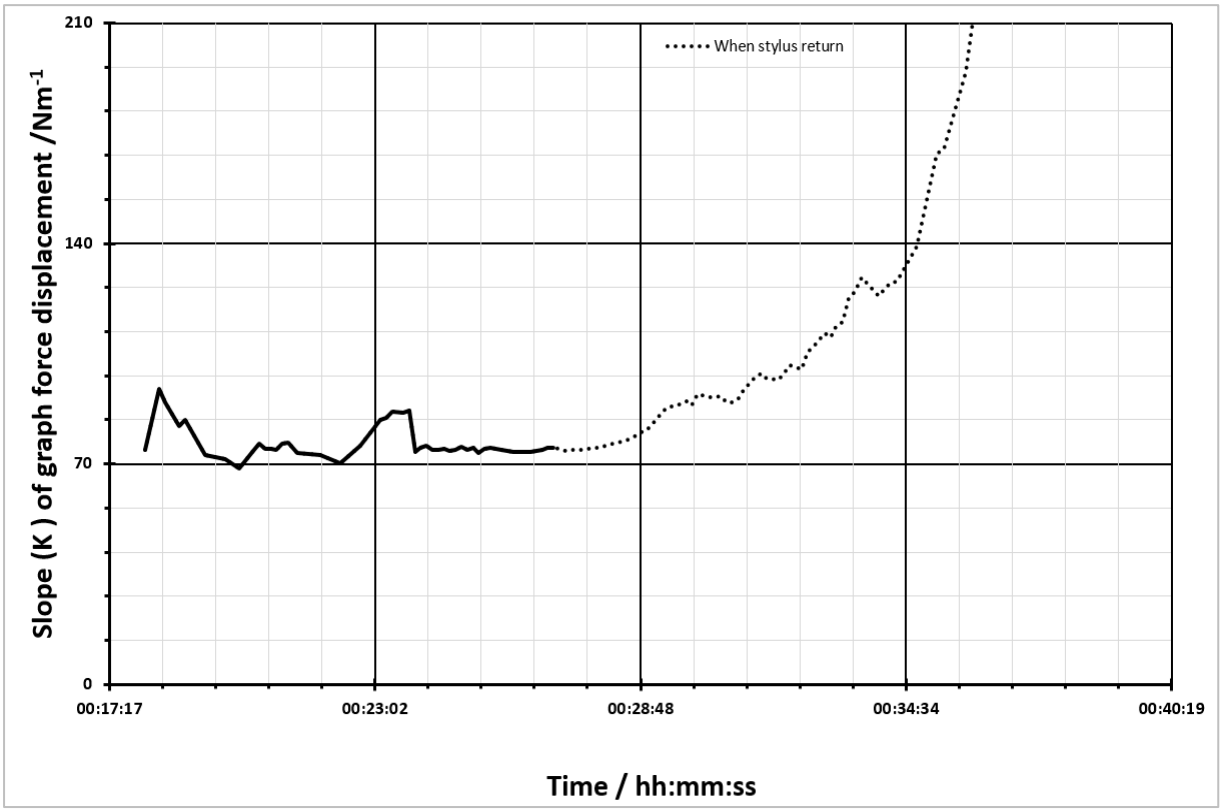

Figure 5. 26: Slope (K constant) of Force-Displacement graph for stylus 0602-5-6 in **Koveral-testing** experiment

The experiment for both part *Koverall-testing* and *Ksetup-testing were* repeated three times and these result are summarised in Figure 5.27 and Figure 5.28. As mentioned above, all of these graph cover the result data during the downward phase of the stylus. It can be seen that the behaviour at the beginning of the graphs is relatively unstable compared to the other regions. This pattern is observed to be occurred for the majority of the tested styluses. Therefore, this region is excluded from the calculation of the stiffness value (these region is approximately from 0 µm to 0.25 µm in displacement data for both graphs in Figure 5.27 and Figure 5.28). The value of stiffness i.e. the slope of these graph is calculated based on the least square best fit straight line method. The average of the three repetition experiments is taken as the value of the stiffness. Finally, the effective stiffness of the stylus is calculated based on both results value using the following equation (5.1) shown in 5.5.4.

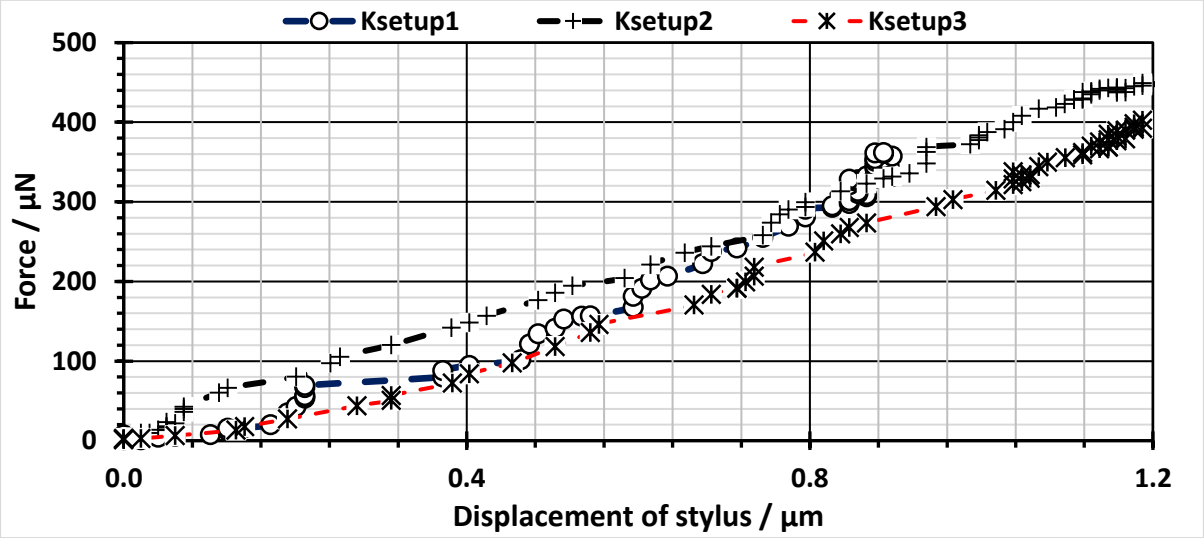

Figure 5. 27: Result of **Ksetup-testing** experiment for the stylus 0602-5-6

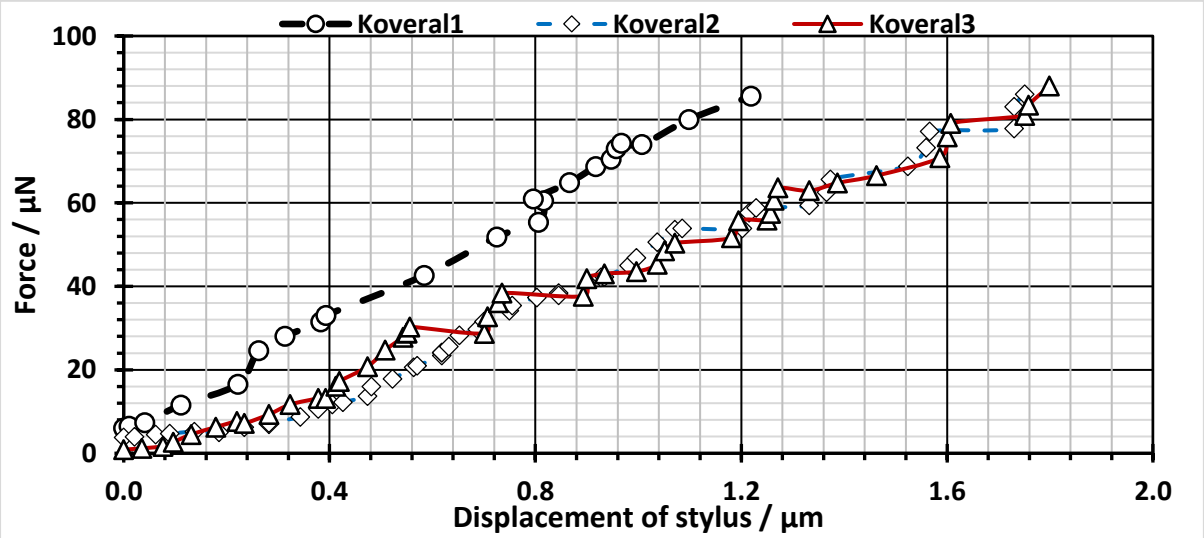

Figure 5. 28: Result of **Koverall-testing** experiment for the stylus 0602-5-6

Summary of data processing of stiffness measurement of stylus

(i) Tabulate all raw data – Reading from the precision mass balance, manipulation stage position, confocal chromatic sensor and time.

(ii) Determine the initial contact position in each data set

(iii) For each data set, convert mass data to force data and confocal chromatic sensor data to displacement data. Plot a force- displacement graph

(iv) Calculate the slope of the graph using the least square straight line method- the stiffness is recognised as the slope of force-displacement graph.

(v) Calculate the effective stiffness of stylus using equation 5.1

(vi) Evaluate the uncertainty of measurement.

5.7.2. Data processing for the measurement of maximum safe tip force

As defined in chapter 3, the maximum safe tip force is a transverse force applied on the stylus tip that causes initial plastic behaviour in the stylus. Therefore, the data analysis processing in this experiment is concerned with determining the position and force where the plastic deformation starts to occur. To calculate this force, a concept similar to that for determining the elastic limit point in a stress-strain graph is employed. In the stress-strain graph of a material, the elastic limit can be defined when the slope of the graph starts to change. However, in this data analysis a force-displacement graph is used instead of stress-strain graph.

The first steps in data analysis are similar to those in section 5.7.1: tabulated the raw data and convert units appropriately; establish the initial contact positon, and plot the force-displacement graph. The only difference is that data from the precision manipulation stage is used as the displacement data in this graph. This is because the working range of the confocal chromatic sensor is only from 0 to 300 μm which is insufficient to support the range of this experiment. From this graph, the region where the slope starts to change can, in principle, be observed and the maximum safe tip force can be reasonably estimated. However, on several tested styli, it was a challenging task to find this region and, thus, difficult to estimate the maximum safe tip force. In the force-displacement graph shown in Figure 5.29

for stylus 0506-1-2 (manufacturing type 1, stylus tip diameter of 68 µm), there are changes in the local slope of the graph at multiple locations, with several small, sudden deviations in the graph in the region of force from 0.008 N to 0.02 N and larger ones at higher forces. In contrast, it is difficult to detect the actual onset slope changing in the relatively smooth force-displacement graph for the smallest dimension stylus 0602-5-6 (manufacturing type 4, tip diameter of 21 µm) as shown in Figure 5.30. Both figures show that a 'physical slip phenomena' occurs during the experiment due to the uneven surface of the test-workpiece. Nevertheless, this physical slip phenomenon did not contribute a significant effect to the changing of the slope of the graph because after physical slip, the graph returned to same slope value as before the physical slip occurred.

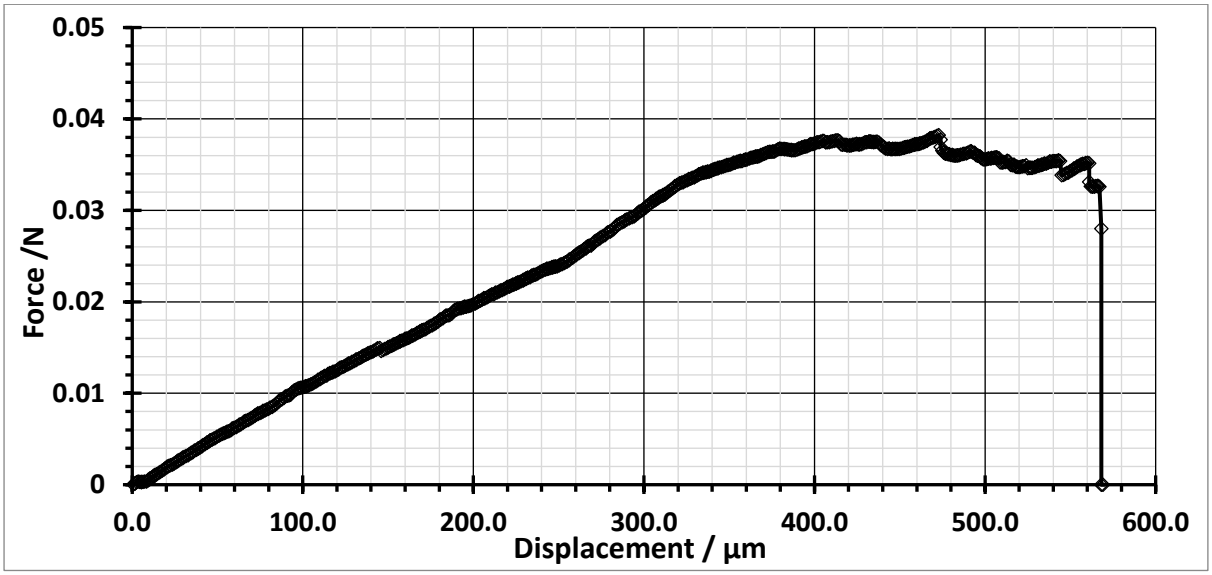

Figure 5. 29: Force-displacement graph for stylus 0506-12 type 1 experiment of maximum safe tip

Figure 5. 30: Graph of Force-displacement for stylus 0602-5-6 type 4 for experiment of maximum safe tip force

Subsequently, to determine a more consistent value of the maximum safe tip force, the gradient of the force-displacement graph is calculated and plotted against the force. For this process, the gradient over 20 successive data point of the force-displacement line is calculated based on the least square best fit line method. Then, the resultant first derivative to gradient value for successive sets of 20 data points are plotted against the force data to observe the behaviour of the slope of the force-displacement graph itself. Figure 5.31 and Figure 5.32 show these gradients of force-displacement graphs for stylus 0506-12 and stylus 0602-5-6 (smallest dimension of tested stylus).

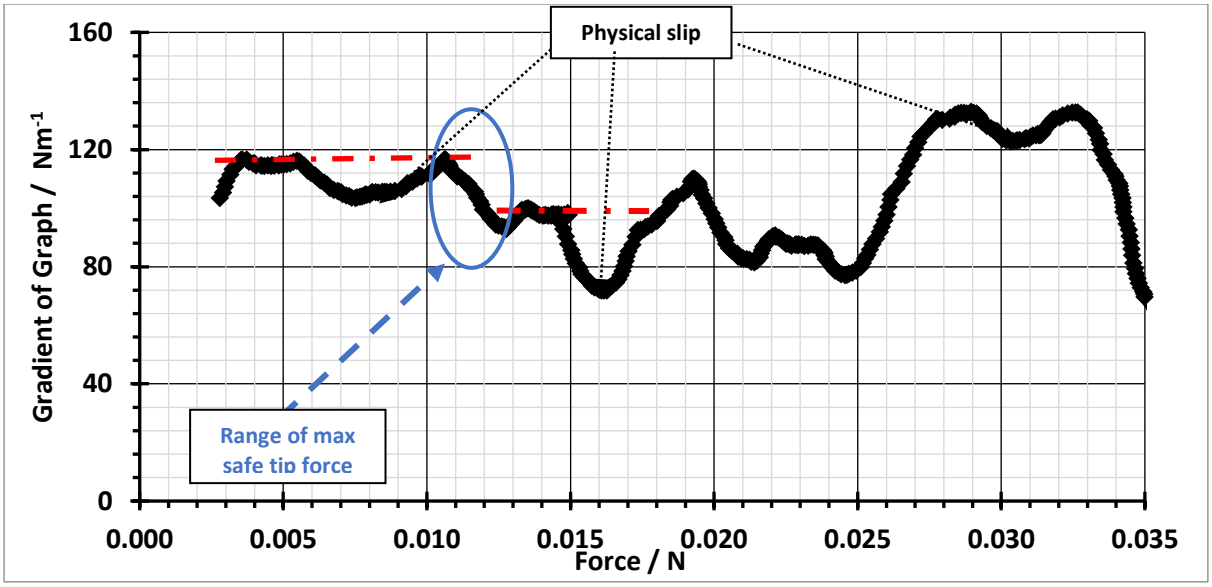

Figure 5. 31: Gradient graph to observed behaviour of the slope of force-displacement graph for stylus 0506-12 manufacturing type 1 experiment of maximum safe tip

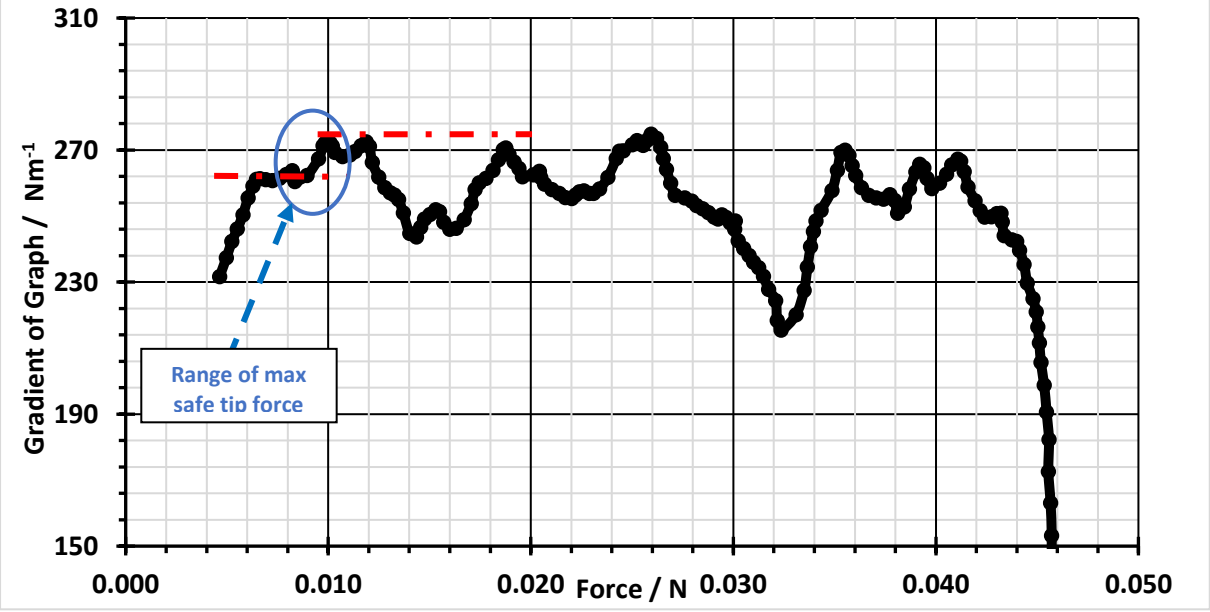

Figure 5. 32: Gradient graph to observed behaviour of the slope of force-displacement graph for stylus 0602-5-6 manufacturing type 4 experiment of maximum safe tip force

In Figure 5.31, the gradient starts to change at the force of 0.010 N and reaches another lower constant condition at a force of 0.014 N. The gradient is seen to have fluctuations at several locations in the graph, which are not considered part of its overall trends. Hence, due the definition of maximum safe tip force, the value of 0.010 N which the gradient started to change will be considered as the result value of the maximum safe tip force for this stylus. The range of force from 0.010 N until 0.014 N is the range of the value maximum safe tip force can be estimated and thus, this range shall be included in the evaluation of uncertainty of measurement which will be explained in section 5.9.2. Physical slip was seen in several locations in the graph, for instance at the range of a force of 0.006 N to 0.009 N .It can be recognised when the gradient temporarily dropped before returning to the same gradient value before it happened and therefore, at that location, it could not be considered as the value of maximum safe tip force.

The same method of data analysis is applied to the smallest stylus 0602-5-6, using the data in Figure 5.30 for which is difficult to observe the slope changing. Analysis of the slope graph in Figure 5.32 illustrates the first changing of a steady gradient (stiffness) at a force of 0.008 N, which is considered as the value of the maximum safe tip force for this stylus. The range of force from 0.008 N until 0.010 N is the range of the value maximum safe tip force can be estimated and included in the measurement uncertainty evaluation.

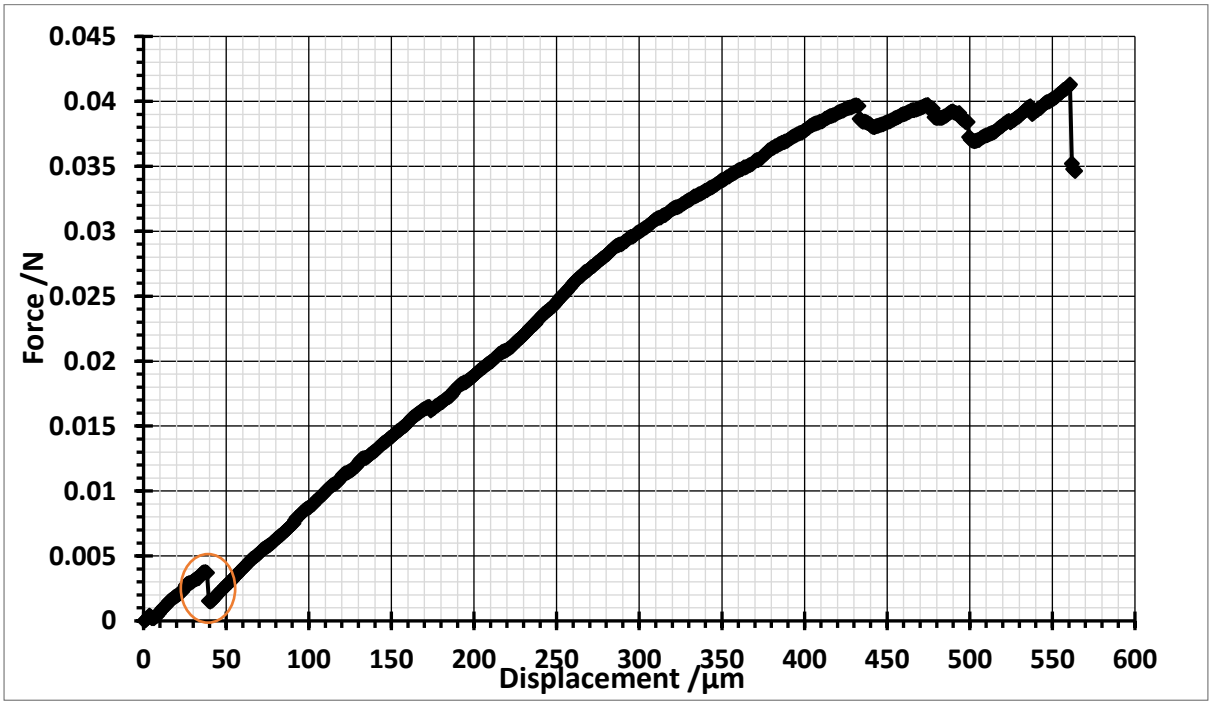

Figure 5. 33: Graph of Force-displacement for stylus 0511-1-2 manufacturing technique type 2 for experiment of maximum safe tip

In contrast, the definition of maximum safe tip force is slightly different for stylus of manufacturing technique type 2. Because the type 2 stylus uses an adhesive material to assemble a glass micro sphere to the stylus shaft, the testing procedure uses here does not, in practice, measure the maximum safe tip force as it is defined earlier in this chapter, but it measures instead the strength of the adhesive material holding the micro sphere on to the stylus shaft. It was observed that at the end of the experiment, the glass micro sphere was detached from the stylus shaft. In Figure 5.33, at the displacement of 40 µm, the force suddenly dropped and after that, it gradually increased. This dropped in force indicates that the stylus tip sphere had been broken and detached from the stylus shaft, and after that, the end of the stylus shaft was taking its place to contact with the test-workpiece and continues the experiment in terms of shaft bending, which explained the gradual increase in the graph. Therefore, for manufacturing technique type 2 stylus, the maximum safe tip force is defined as a transverse force applied on the stylus tip that causes initial separation of the stylus tip from its stylus shaft 0511-1-2.

5.8. Presentation and discussion of experimental results

The results of both experiments for all styluses in this section are presented. They address the ***Thesis Objective 2*** and the discussion of the results should be linked and compared to chapter 3 and chapter 4. The discussion that follows is crucial in determining the capability and suitability of styluses to be applied in the probing system of micro-CMM. An uncertainty evaluation is also presented in this section.

5.8.1. Experimental results of stiffness measurement

The results of stiffness measurement from all styli of all types of manufacturing techniques are presented in Table 5.2. Estimate of combined standard uncertainty and expanded uncertainty (coverage factor k=2, 95% confidence level) are also shown in the same Table 5.2. However, the details of uncertainty evaluation are not explained until in section 5.9.1.

Table 5. 2: The results of stiffness measurement for all styluses including the uncertainty estimation

	INFORMATION OF STYLUS		EXPERIMENT RESULT		
	Stylus Name	**Stylus Code**	**Result of Stiffness** $(N\ m^{-1})$	**Combined Standard Uncertainty** $\pm (N\ m^{-1})$	**Expanded Uncertainty Estimation** $\pm (N\ m^{-1})$
TYPE 1	**1a**	**0506-1-2**	309	24	48
	1b	**0430-4-5**	301	25	49
	1c	**0504-1-2**	285	20	41
TYPE 2	**2a**	**0509-1-2**	160	23	41
	2b	**511-1-2**	213	26	50
TYPE 3	**3a**	**0517-4-5**	124	49	73
	3b	**0521-3-4**	145	18	36
	3c	**0521-9-10**	169	23	59
TYPE 4	**4a**	**0602-1-2**	100	37	34
	4b	**0602-5-6**	60	35	71
	4c	**0607-2-3**	167	23	45
	4d	**0602-7**	34	19	38

Table 5.2 is quite revealing in several ways. First, there are significant differences between the stiffness predicted by the analytical modelling (presented in Table 5.1) and the experimental of stiffness measurements. For the sizes being studied, geometrical imperfections, compared to perfect models will always be a factor. However, it is worth mentioning that the analytical model calculated in Table 5.1 is slightly different than the model calculated in Table 4.2 in chapter 4. Because of the method of this experiment is conducted (*Ksetup-testing* and *Koverall-testing* in section 5.5), the calculation of effective stiffness of the stylus have to consider the effective stylus shaft with some region of the upper part of the stylus shaft (see Figure 5.19,section 5.5.4, from point A to C). Equation (3.18) in section 3.4.4 used in this calculation. In contrast, the stiffness in the analytical modelling in Table 4.2 (chapter 4) are calculated based on the effective stylus which has been determined by equation (3.16) in section 3.4.4.

The comparison between the analytical modelling (lower and upper value of predicted stiffness) and the experimental result of stiffness for each manufacturing type styli has been investigated under the influence of geometrical conditions. Figure 5.34 and Figure 5.35 shows these comparisons under the influences of mechanical aspect ratio and effective length of the stylus for *Type 1*, while the same comparison graphs are also plotted for *Type 2* (Figure 5.36 and Figure 5.37), *Type 3* (Figure 5.38 and Figure 5.39) and *Type 4* (Figure 5.40 and Figure 5.41).

The stiffness results (including measurement uncertainty) of Type 1 and *Type 2 styli* are mostly below but closely aligned to the predicted lower value of analytical modelling while *Type 3* experimental results are lower by a small but more significant distance compared to the lower value of analytical modelling. Interestingly, when comparing the experimental result and the analytical modelling value of *Type 4* styli, its experimental results are generally found between the upper and lower values of the analytical modelling. However, it is observed that the experimental result decreases to be below but nearly aligned to the lower value of analytical modelling when the aspect ratio is higher.

A divergence between these results is expected because the modelling calculation is based on the perfect geometrical dimensions of the stylus shaft, stylus tip and effective length of the stylus while the manufacture of real styli, from all variants of hybrid manufacturing techniques, will not produce perfect geometrical dimensions. Given the challenges of measuring, especially, diameter on such small delicate devices, the reasonable agreement between experimentally determined stiffness and lower-bound predictions is encouraging. However, the large deviation between analytical value and experimental results especially on *Type 3* indicates that further investigation should be conducted on Type 3.

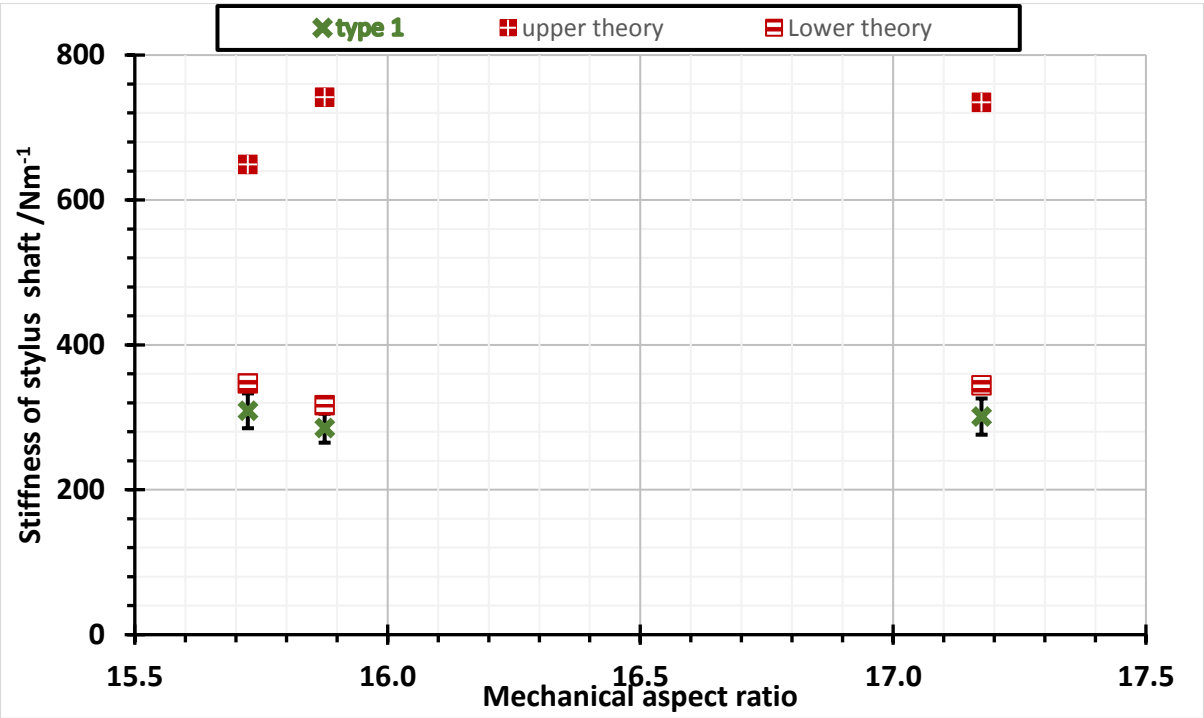

Figure 5. 34: Comparison between the experimental result and the analytical modelling for stiffness of styluses of manufacturing type 1 over the mechanical aspect ratio

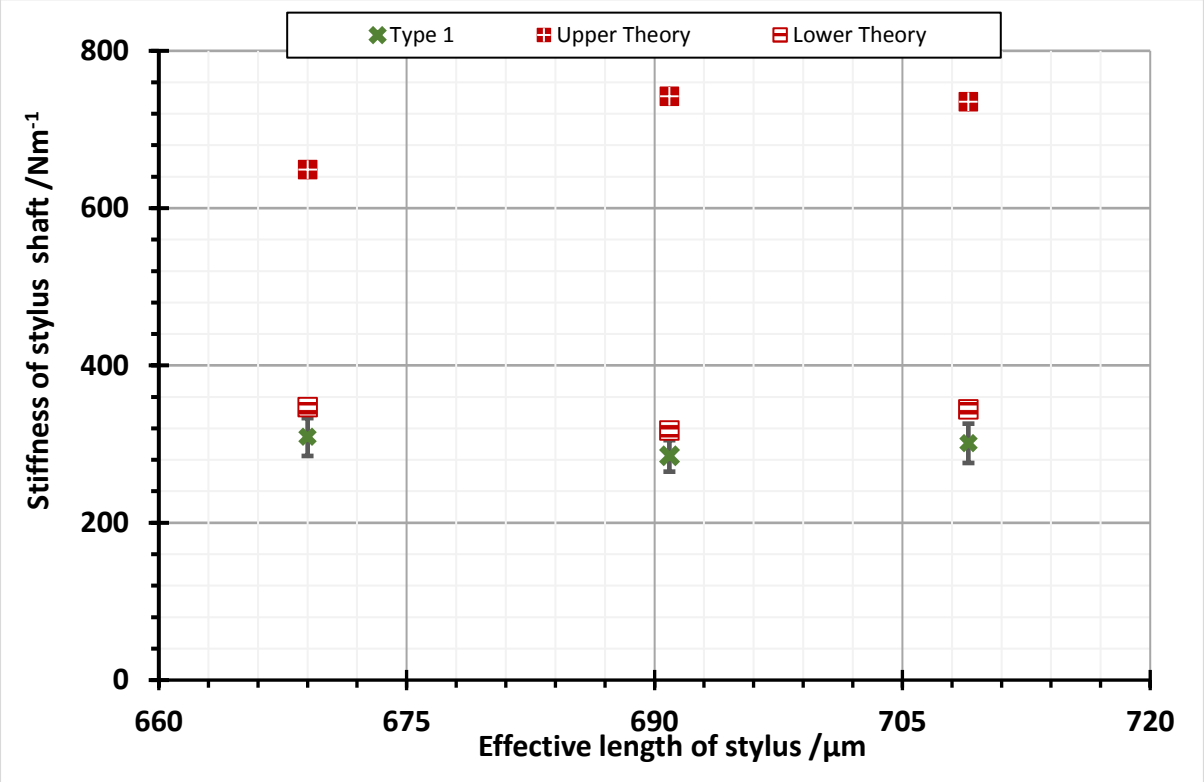

Figure 5. 35: Comparison between the experimental result and the analytical modelling for stiffness of styluses of manufacturing type 1 over the effective length of stylus

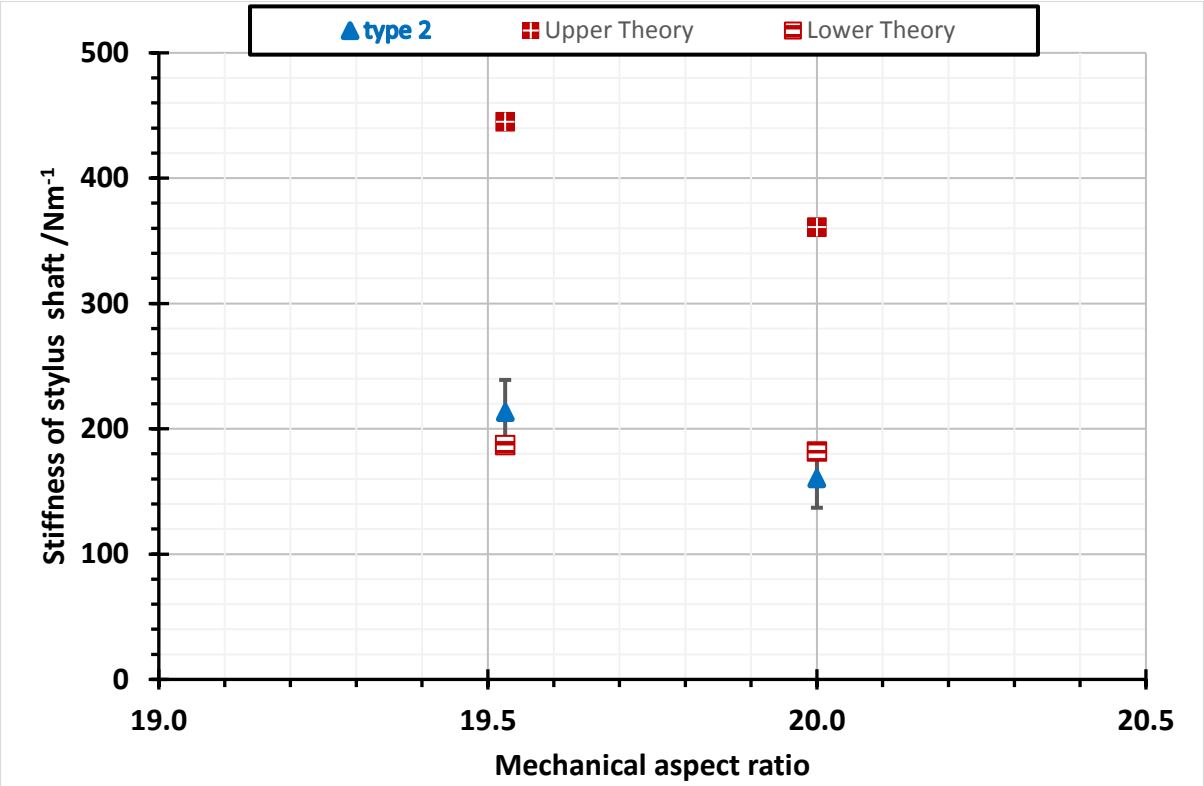

Figure 5. 36: Comparison between the experimental result and the analytical modelling for stiffness of styluses of manufacturing type 2 over the mechanical aspect ratio

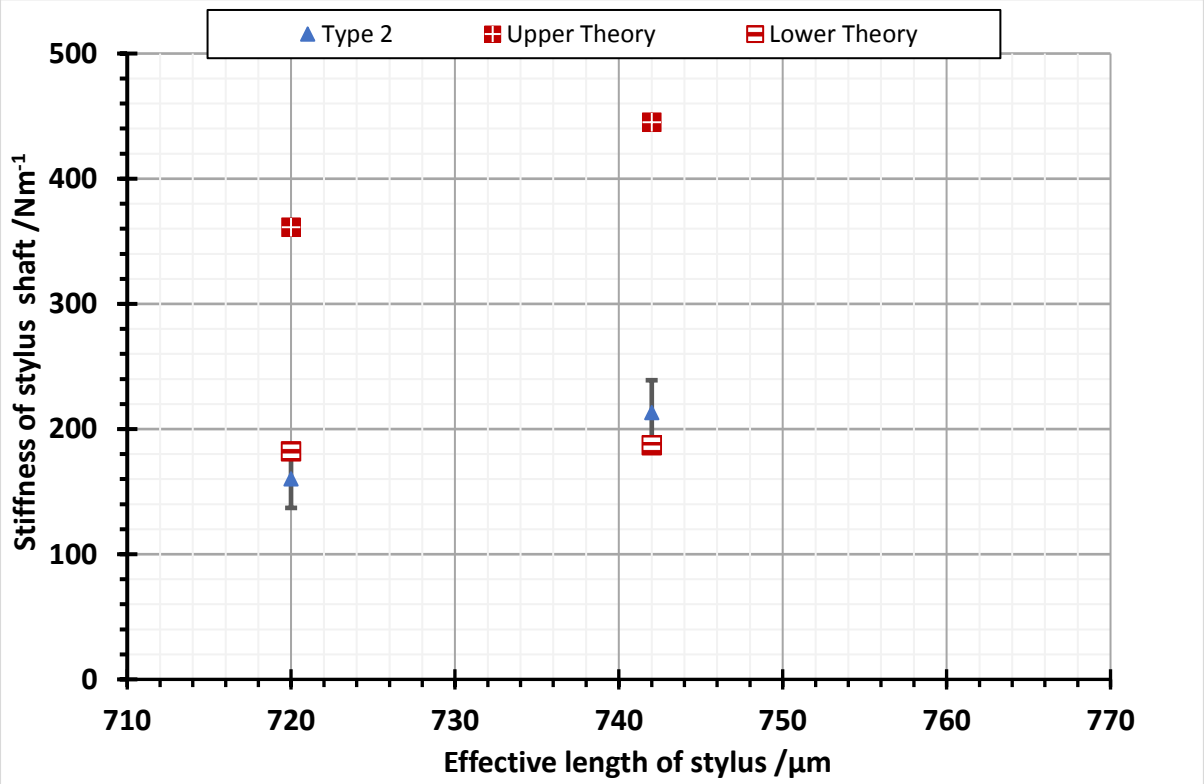

Figure 5. 37: Comparison between the experimental result and the analytical modelling for stiffness of styluses of manufacturing type 2 over the effective length of stylus

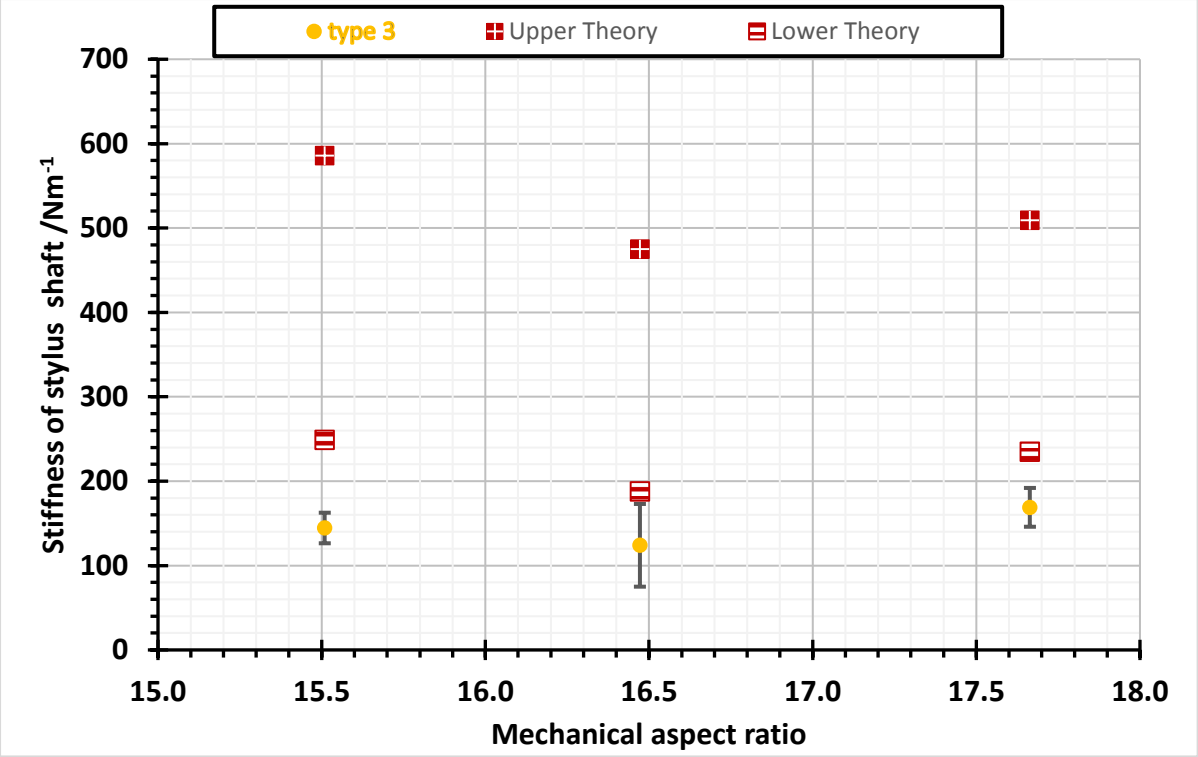

Figure 5. 38: Comparison between the experimental result and the analytical modelling for stiffness of styluses of manufacturing type 3 over the mechanical aspect ratio

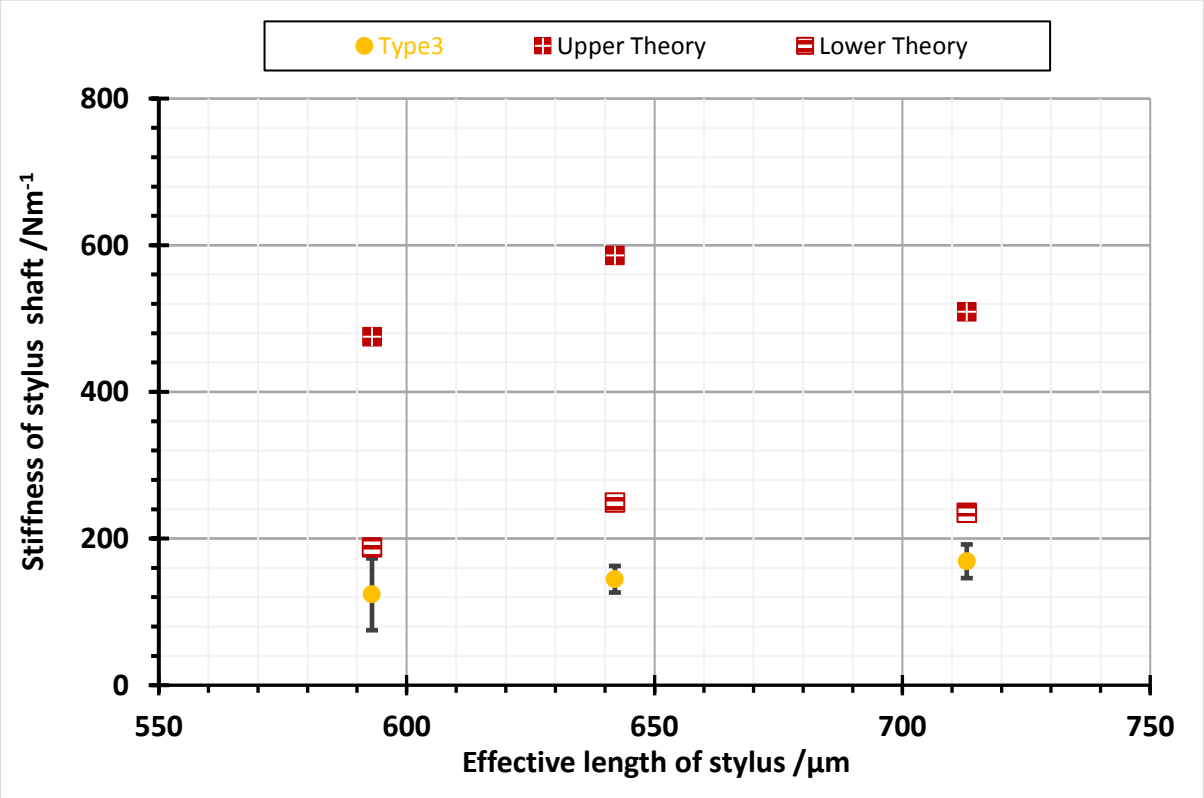

Figure 5. 39: Comparison between the experimental result and the analytical modelling for stiffness of styluses of manufacturing type 3 over the effective length of stylus

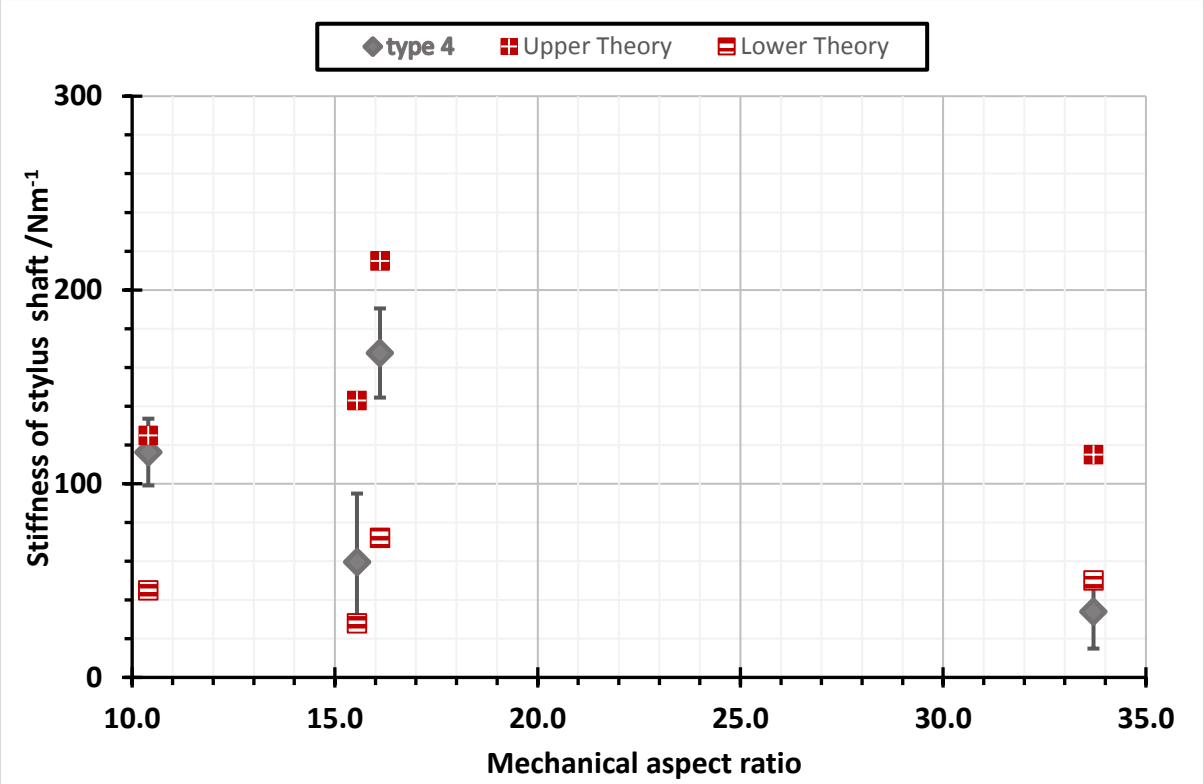

Figure 5. 40: Comparison between the experimental result and the analytical modelling for stiffness of styluses of manufacturing type 4 over the mechanical aspect ratio

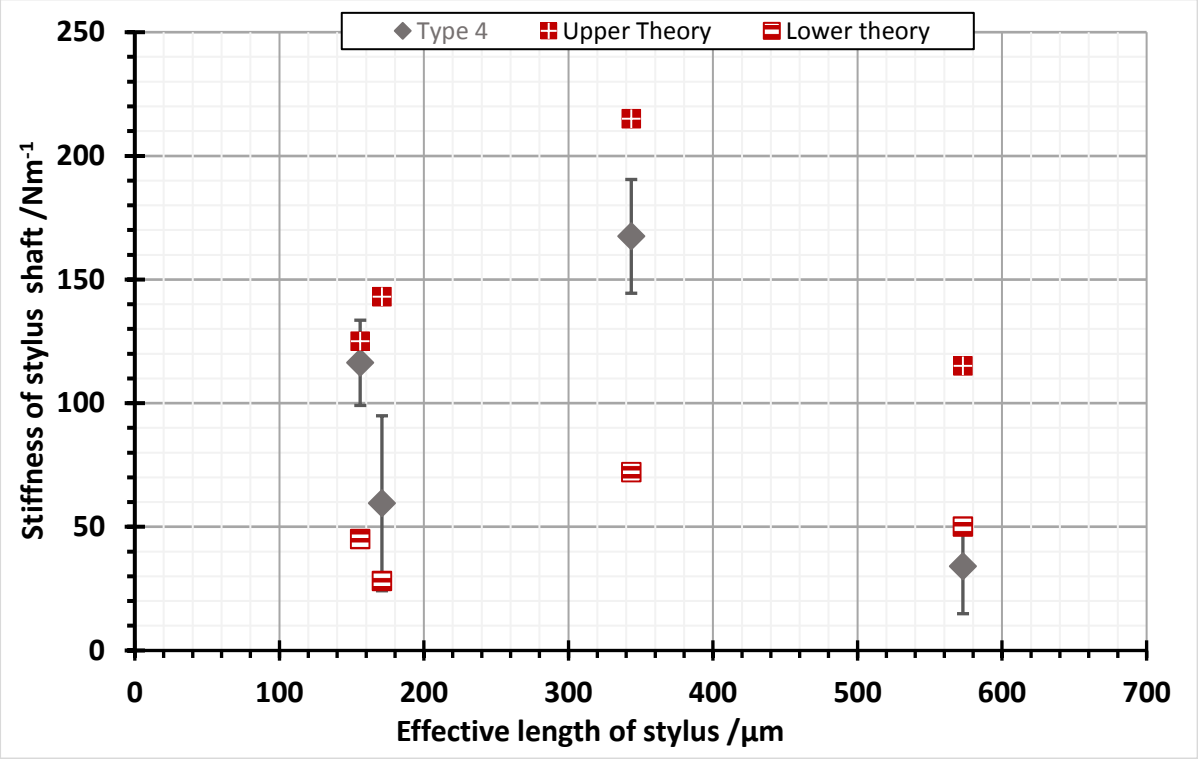

Figure 5. 41: Comparison between the experimental result and the analytical modelling for stiffness of styluses of manufacturing type 4 over the effective length of stylus

Figure 5.42 and Figure 5.43 exhibit the relationship between the measured stiffness of all styluses with the two geometrical parameters; the mechanical aspect ratio, and the effective length of stylus. These are important geometrical parameters in assessing the mechanical capability of the bending deflection of the stylus shaft. As suggested in chapter 4, section 4.3, the stiffness of the stylus shaft should have a decreasing trend in relationship to the effective length and mechanical aspect ratio. Nevertheless, the experimental results for stiffness for all types of styli do not follow this trend. At a glance, Type *1* styli show no clear trend and *Type 2* styli exhibit an increasing trend against aspect ratio in these results, while Type 3 styli remain almost constant over the small testing range and *Type 4* styli exhibit a decreasing trend. However, the stylus shafts of Type *2* styli are made by the same process as those of *Type 1* styli, and the stiffness considered here essentially indicates the capability of the stylus shaft to resist bending, so it is reasonable to consider a combination of the Type 1 and Type 2 results. This combination does suggest a decreasing trend broadly consistent with the analytical modelling.

In addition, as the styluses from *Type 1* and *Type 3* processes have approximately similar dimensions of stylus shaft and effective aspect ratio, the analytical modelling in Table 5.1 predicts that differences in their stiffness values should be small. However, these figures show clearly that the measured stiffness for *Type 1* styli is higher than that for *type 3*. This finding not only highlights a significant difference with the analytical modelling, but, most importantly, it is also contradicting the initial prediction that adding an *ECM* processed after the *WEDG* process for manufacturing of the stylus shaft in *Type 3,* would enhance the surface quality of shaft and hence produce stiffer styli compared to Type *1* styli (which only employed the WEDG process for manufacturing of stylus shaft).

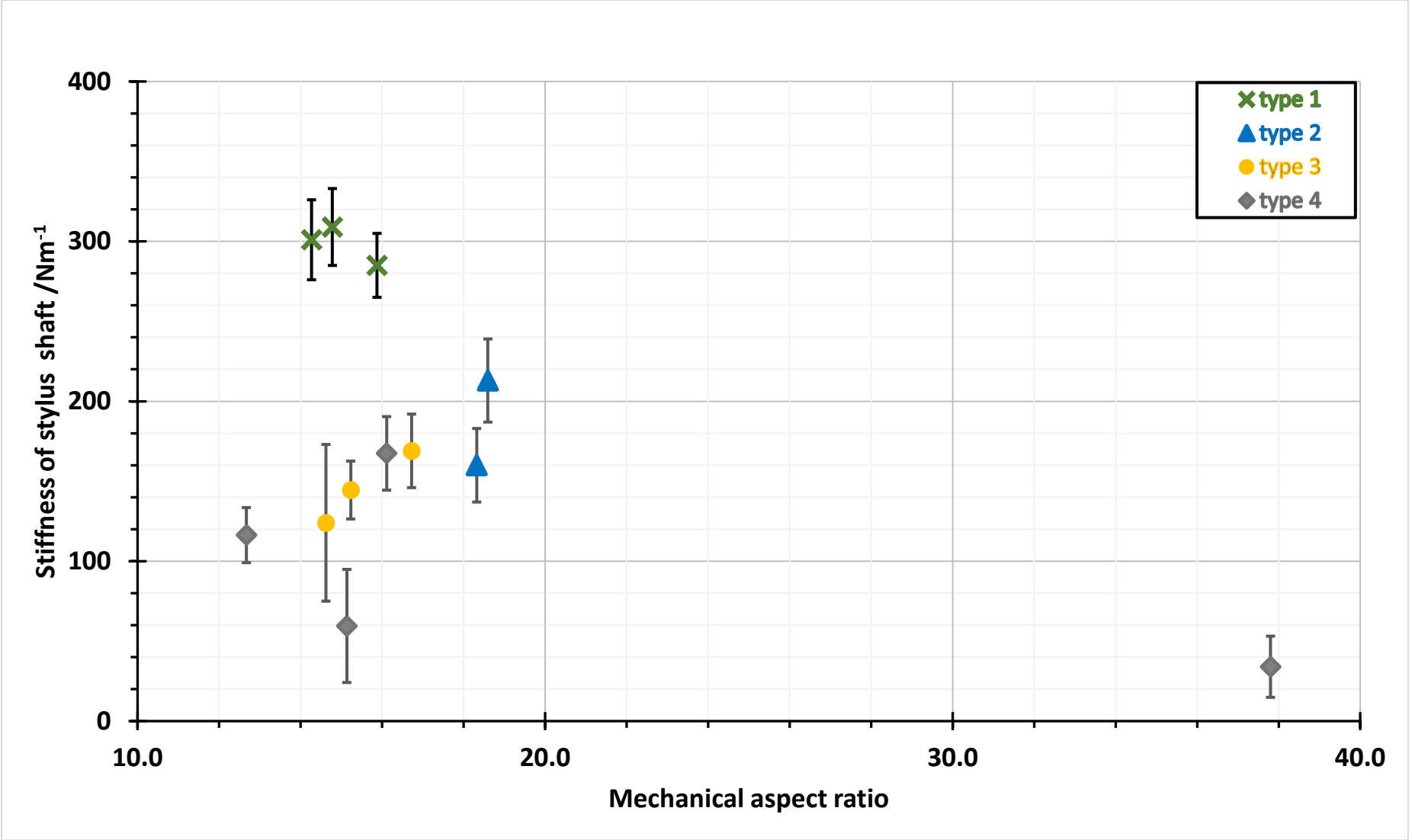

Figure 5. 42: The result of stiffness f all styluses of all manufacturing types over the mechanical aspect ratio

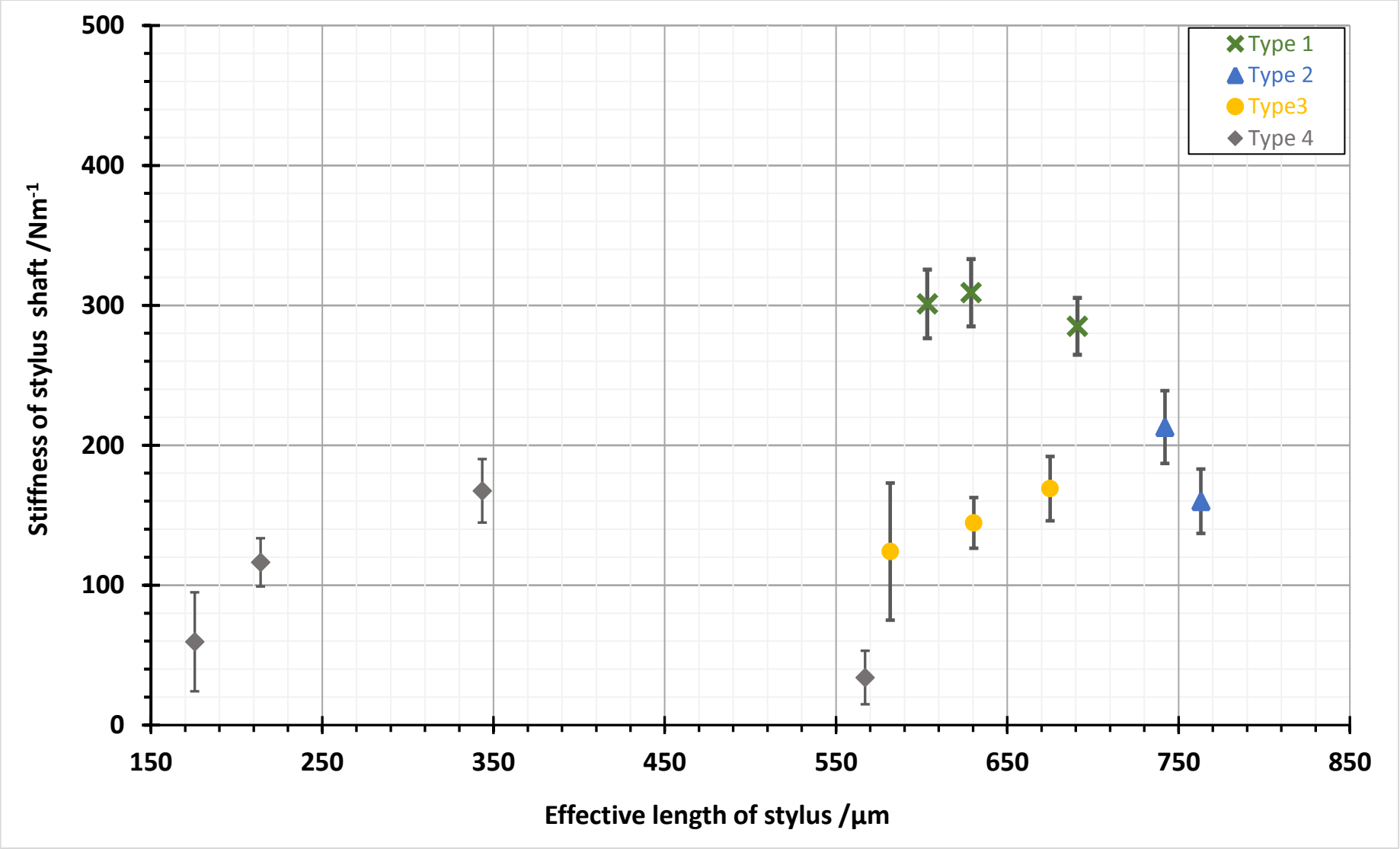

Figure 5. 43: The result of stiffness f all styluses of all manufacturing types over the effective length of stylus

The behaviour of Type *3* and *Type 4* styli are the principle focus of this study in this chapter, because the *ECM process* used in manufacturing their stylus shaft, is a promising candidate among current available technologies for making stylus shafts with the diameters less than 10 µm. Therefore, it is crucial to discuss both types in further detail. All the *Type 3 styli* demonstrate an almost constant experimental stiffness, not the expected downward trends, and have a lower stiffness compared to *Type 1* and *Type 2* styli, in contradiction of the initial theoretical prediction. There are several plausible explanations for these findings. Firstly, they may be arising from the manufacturing technique itself, in this case the *ECM* process. ECM depends importantly on several control parameters such as feeding rate, electrolyte control direction, chemical erosion rate and concentration of electrolyte. Thus, it is possible that some of these control parameters, or a specific combination of them, are not reaching the optimum state during manufacturing process and hence leading to structures for which the nominal overall dimension are misleading in terms of effective stiffness. A second possibility relates to stability of the chemical reactions when adding ECM to the WEDG process and the suitability of the electrolyte for use on the tungsten shaft; this requires further investigation beyond the scope of the current study.

An interesting finding from the experimental result is the behaviour of the *Type 4* styli. With the consideration of the uncertainty of measurement, the stiffness of these styli achieved the value and follow the trend predicted by the analytical modelling. This finding suggest that the manufacturing parameters involved in this process are reaching to their optimum condition which is not only demonstrate that ECM process is suitable and promising process to manufacture the stylus shaft with the diameters dimension less than 20 µm, but also verify the analytical modelling.

For the micro probe of a micro CMM, it is crucial to know the value of the stiffness of the stylus as this information will be used in probe calibration and thus enhancing the traceability route of the micro probe. Normally, the stiffness of a stylus with characteristic dimensions below 100 µm is estimated to be greater than the stiffness at the flexure, or other, probing sensor mechanism. Therefore, the design of micro-probe suspensions needs to be assessed in the light of the results from the present work.

5.8.2. Experimental results of maximum safe tip force measurement

The results of the maximum safe tip force measurement of all styli are presented in Table 5.3. The uncertainty value is also presented and the detail on uncertainty evaluation will be explained in 5.9.2. As pointed out in Chapter 3, it is difficult to model the maximum safe tip force by analytical calculation. Hence, these results are crucial to study of the relationship between the maximum safe force and geometrical parameter related to the mechanical strength of the stylus shaft.

Table 5. 3: The results of maximum safe tip force measurement for all styluses including the uncertainty estimation

	STYLUS			EXPERIMENT RESULT	
	Name of Stylus	**Stylus Code**	**Max Safe Tip Force**	**Standard Uncertainty (±)**	**Expanded Uncertainty (±)**
			mN	**mN**	**mN**
TYPE 1	**1a**	**0506-1-2**	*10.4*	*1.5*	*3.7*
	2a	**0430-4-5**	*10.2*	*1.1*	*2.2*
	3a	**0504-1-2**	*4.5*	*0.9*	*2.8*
TYPE 2	**2a**	**0509-1-2**	*5.5*	*0.6*	*1.8*
	2b	**511-1-2**	*3.0*	*0.7*	*1.5*
TYPE 3	**3a**	**0517-4-5**	*8.2*	*1.2*	*2.3*
	3b	**0521-3-4**	*3.9*	*0.5*	*4.2*
	3c	**0521-9-10**	*7.2*	*1.0*	*2.2*
TYPE 4	**4a**	**0602-1-2**	*3.5*	*0.3*	*2.0*
	4b	**0602-5-6**	*8.0*	*0.9*	*2.9*
	4c	**0607-2-3**	*2.1*	*0.3*	*1.2*
	4d	**0602-7**	*2.0*	*0.4*	*1.0*

Graphs in Figure 5.44 and Figure 5.45 illustrate the relationship of maximum safe tip force to mechanical aspect ratio and effective length of stylus for all styli of all types. Figure 5.46 plots the measured maximum safe tip force against the diameter of the stylus shaft for *Type 4* only. From the graphs, *Type 1* styli shows decreasing trend associated with both the mechanical aspect ratio and effective length of stylus, while no predictable trend is seen for *Type 2* and *Type 3* styli in either graphs. The interesting finding for *Type 4* styli is that there were decreasing trends in the maximum safe tip force against both effective length and diameter of stylus shaft.

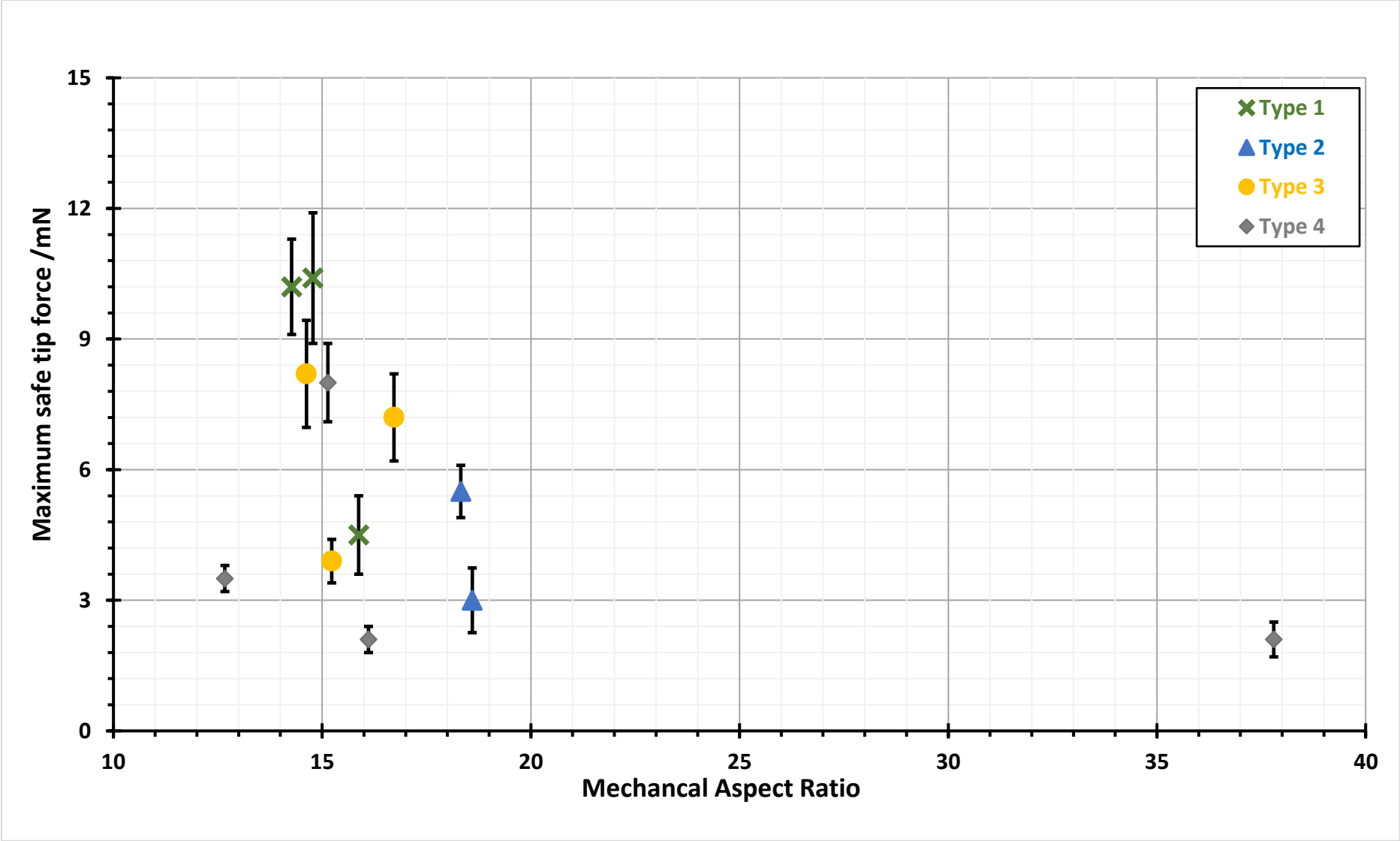

Figure 5. 44 : The result of maximum safe tip force of all styluses of all manufacturing types over the mechanical aspect ratio

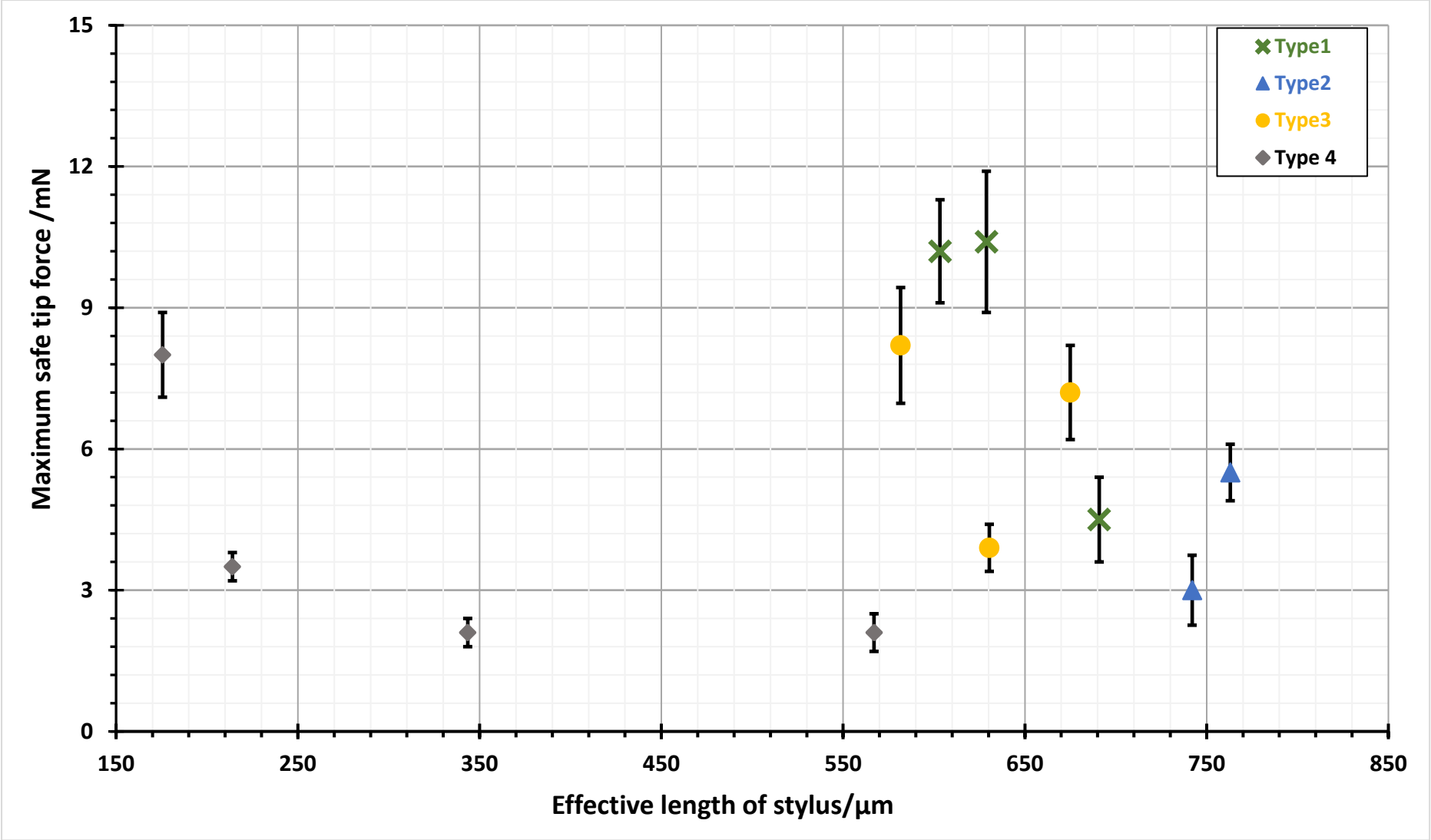

Figure 5. 45: The result of maximum safe tip force of all styluses of all manufacturing types over the effective length

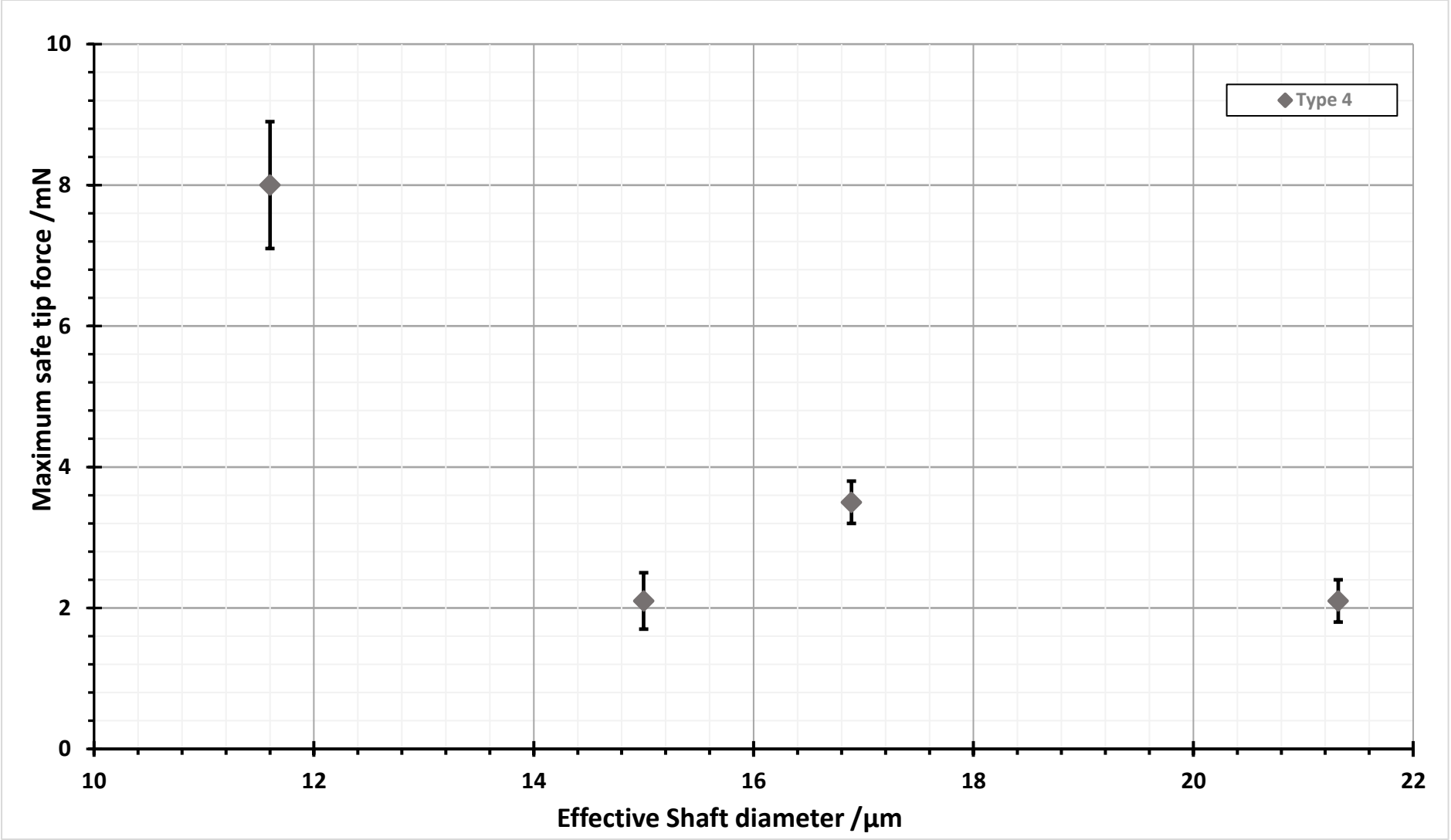

Figure 5. 46: The result of maximum safe tip force for manufacturing types 4 styli over the effective diameter of stylus shaft

The measured maximum safe tip force (Table 5.3) should be compared to the analytical model of the allowable probing force (in Table 5.1). As discussed in chapter 3, allowable probing force and maximum safe tip force are totally different forces with different definitions, either of which can be define limiting factors that determine the selection of a suitable probing force for a micro-stylus. The smaller of these two forces will be selected as a maximum force that should be applied by a stylus. In the current experiments, the maximum safe tip force for *Type 1*, *Type 3*, and *Type 4* styli are bigger than its allowable probing force. As the test workpiece is copper, which is a soft material compared to that of the stylus tip, the predicted value of allowable probing force is quite small. Therefore, in this case, the allowable probing force is the limiting factor in selection of the appropriate force for operation of the micro probe. Nevertheless, if these results of maximum safe tip force are compared to the value of allowable probing force for a case where the stylus is contacting a hard workpiece that have higher values of yield strength and Young modulus compared to the stylus tip, the experimental result for maximum safe tip force given in Table 5.3, for approximately similar dimensions and similar manufacturing techniques shall be used as the reference in selection of the operating force of a micro probe.

In contrast, *Type 2* styli exhibit experimental maximum safe tip forces that are smaller than the allowable probing force. Therefore, if this stylus type is chosen to be used in a micro probe, it has to ensure that the force applied to it must not exceed its maximum safe tip force value.

5.9. Uncertainty evaluation of the experimental result

Uncertainties in any measurement process will generally be caused by many factors. All contributing factors to a measurement process should be included in uncertainty calculation. The evaluation method in BIPM 'Guide to uncertainty of measurement' [138] is applied for the calculation of uncertainty for these experiments. The first step in the evaluation of uncertainty is to determine a mathematical equation which relates the output quantities error and influence input quantities. These influence input quantities are also recognised as the source of uncertainty or uncertainty component. After that, the standard uncertainty is calculated for each component. Then, sensitivity coefficients are determined in order to bring these components together as the combined standard uncertainty. Finally,

an expanded uncertainty is calculated and reported as suggest in the BIPM 'Guide of uncertainty of measurement' [138]. The uncertainty evaluation for stiffness measurement will be discussed in details in section 5.9.1 while maximum safe tip force will be explained in section 5.9.2.

5.9.1. Uncertainty determination and analysis of stiffness measurement

The evaluation of uncertainty of measurement starts by defining the mathematical modelled of stiffness measurement. Generally, the mathematical model in the BIPM methodology was developed by defining the output quantities *y* as a function of one or several input quantities *x*. Hence, for this experiment specifically, the mathematical model is representing the source of error in stiffness measurement. The mathematical models are:

$$E_k = \frac{m_t g}{x_t} + \ K_{rep} + K_{setup} \tag{5.1}$$

Where:

$$m_t = m_{cal} + m_{res} + m_{noise} \tag{5.2}$$

And,

$$x_t = x_{cal} + x_{res} + x_{noise} + x_{stability} \tag{5.3}$$

E_k : Error related to stiffness
m_t : Error associated with mass
x_t : Error related to displacement
g : Gravity constant
m_{cal} : Uncertainty of calibration of mass balance
m_{res} : Resolution of mass balance
m_{noise} : Noise of mass balance
x_{cal} : Uncertainty of calibration of laser chromatic confocal
x_{res} : Resolution of laser chromatic confocal sensor
x_{noise} : Noise related to laser chromatic confocal sensor
$x_{stability}$: Stability of plate of mass balance
K_{rep} : Repeatability result of stiffness
K_{std} : Standard error of slope in linear graph

The inputs quantities in equation (5.1), (5.2) and (5.3) are the individual uncertainties which express the effect of source of error in this experiment. Some of these are Type A uncertainty [138] which is calculated from the experiment itself, while other are Type B uncertainty [138], determined from other relevant sources such as from preliminary performance testing as discussed in section 5.4.

The uncertainty evaluation is continued to determine the combined standard Uncertainty. The combined standard uncertainty is a combination of several uncertainty standard or standard deviation of estimate error from several sources of measurement quantities. For this experiment, as the input quantities are independent from each other, the combined standard uncertainty for equation 5.1, based on the BIPM 'Guide of uncertainty of measurement' [138], is calculated using the following equation:

$$u_c^2(y) = \sum_{i=1}^{N} {c_i}^2 \, u^2(x_i) = \sum_{i=1}^{N} \left|\frac{\partial f}{\partial x_i}\right|^2 u^2(x_i) \tag{5.4}$$

Where c_i are sensitivity coefficients which express how the output quantity *y* varies in response to deviations of the values of input quantities x_i. The sensitivity coefficients for the individual input quantities are partial derivatives of measurement model equation. Therefore, for equation (5.1), the sensitivity coefficients for each component of uncertainty in input quantities are:

- The sensitivity coefficients related to mass including its component which is the uncertainty of mass balance, resolution of mass balance , and noise of mass balance , are

$$c_{m_t} = \frac{g}{x_t} \tag{5.5}$$

- The sensitivity coefficients related to the displacement, including the uncertainty of laser chromatic confocal, resolution of laser chromatic confocal sensor, noise that related to laser chromatic confocal and stability of mass plate ,are

$$c_{x_t} = \frac{-g(\,m_t\,)}{(x_t)^2} \tag{5.6}$$

- The sensitivity coefficients related to repeatability result of stiffness ($c_{K_{rep}}$) and standard error of slope in linear graph ($c_{K_{std}}$) is equal to 1.

Next, the details for each component of uncertainty are explained including the shape of error distribution and type of uncertainty that is appropriate to it.

Uncertainty due to the measuring instrument

The precision mass balance and chromatic confocal sensor are used as measuring instrument in this experiment. The uncertainty of these instruments ($u_{m_{cal}}$, $u_{x_{cal}}$) are essential factor for inclusion in the uncertainty evaluation. Generally, the value of instrument uncertainty is taken from its calibration certificate. However, for this experiment, based on the previous performance of both of these instrument, their uncertainty is estimated about 0.5% from the full testing range. This component of uncertainty follow a normal distribution which is divided by the coverage factor, k=2 at 95% confidence level. In this experimental work, the imported uncertainty due to laser confocal point sensor and precision mass balance are 100 nm and 250 µg respectively.

In addition, the resolution of the measuring instrument ($u_{m_{res}}$, $u_{x_{res}}$) provide further sources of uncertainty. The resolution, generally defines as the smallest capability that instrument can measure, is assumed to have rectangular distribution in this evaluation. For this work, the resolution of the laser confocal point sensor is 10 nm while resolution of precision mass balance is 10 µg.

Uncertainty related to noise of the instrument

Prior to the main experiments, the noise for both the precision mass balance and chromatic confocal sensor ($u_{m_{noise}}$, $u_{x_{noise}}$) were investigated, as reported in section 5.4.1 and 5.4.2. Both measuring instrument exhibited a drift of reading over the period of time. Therefore, drift and noise is expected to contribute a significant systematic error to the experiment, estimated from these preliminary testing result. This source of uncertainty is type B uncertainty and assumed to have rectangular distribution.

Uncertainty due to the instability of the plate of mass balance

The stability of the plate of mass balance during experiment($u_{x_{stability}}$) is expected to introduce some systematic error in the position measurement. This factor was investigated experimentally and had been reported in section 5.4.3, and the result from that test is

included in this uncertainty evaluation. As this factor is one of systematic error, the standard uncertainty is calculated based on the rectangular distribution.

Uncertainty related to repeatability of result (overall and setup)

The repeatability of the measurement is calculated based on the standard deviation of repeated measurement results. In this experiment, as explained in section 5.5.4, there are two parts of experiment of stiffness measurement which are *Koveral-testing* and *Ksetup-testing*. Both testing are conducted in three repeated measurements and the standard deviations are calculated. Standard deviation of *Koveral-testing* is recognised as the value of the repeatability error in this experiment while standard deviation of *Ksetup-testing* is represented as the standard error of the instrumental setup. Both of the error are included in the evaluation of measurement uncertainty. These components of uncertainty is assumed to have normal distribution and is categorised as Type A uncertainty.

5.9.2. Uncertainty determination and analysis of maximum safe tip force measurement

Following the same approach as in the previous section, the mathematical model equation for maximum safe tip force measurement is:

$$E_f = m_t\, g + k_{estrep} x + F_{range} \tag{5.5}$$

Where,

E_f : Error related to Maximum safe tip force measurement
k_{estrep} : Repeatability result of stiffness of *K-overall* testing experiment
x : Maximum displacement
F_{range} : Range of maximum safe tip force

The partial derivatives for each input components of equation 5.4 lead to the determination of their sensitivity coefficients. The sensitivity coefficients for each input component are:

$$c_{m_t} = g \tag{5.6}$$

$$c_{k_{estrep}} = x \tag{5.7}$$

$$c_{F_{range}} = 1 \tag{5.8}$$

The uncertainty component due to the noise of the precision mass balance and chromatic confocal sensor, and the stability of the mass plate has already been discussed in section 5.9.1. Therefore, only uncertainty components due to the range of maximum safe tip force, the estimation error for the *y*-axis in the graph and estimation of repeatability from stiffness measurement result need now be discussed.

Uncertainty due to range of maximum safe tip force($u_{F_{range}}$)

As explained in section 5.7.2, the determination of the maximum safe tip force of the stylus is based on the change of slope in the force-displacement graph of the experiment. In defining the maximum safe tip force, there are uncertainty deriving from the ranges of forces that are believed to be representative of a maximum safe tip force as shown in the circled regions in the Figure 5.31 and Figure 5.32. Therefore, this estimation range needs to be included in the uncertainty evaluation. The rectangular distribution is applied to this component. Also, from the uncertainty evaluation of the majority of the styli, this uncertainty component is observed to be one of the main contributors to the overall uncertainty in the measurement.

Uncertainty due to estimation of repeatability from stiffness measurement result($u_{k_{estrep}}$)

Due to the nature of the experiment, the maximum safe tip force can only be determined once per stylus sample. Therefore, the experiment could not be repeated at the same styli and hence uncertainty due to the repeatability result could not be calculated. However, it can be estimated using the repeatability result from the stiffness measurement of the same sample. This is because the experimental procedure for maximum safe tip force and stiffness measurement are quite similar except for the part where the stylus is loaded to destruction in the maximum safe tip testing. Because this is an estimation uncertainty component, the shape error is assumed to be rectangular distribution.

5.10. Conclusion

This chapter has presented two experiments to test parameters of mechanical properties. The first experiment is about stiffness measurement of the stylus while the other is testing the maximum safe tip force of the styli. In total 12 micro-styli from four variant of manufacturing techniques have been tested. Prior to reporting these test results, an experimental setup and experimental procedure have been explained. Moreover, the method of data processing for both experiments is also presented to address ***Research Question 2.1***, initial performance testing (or trial runs) were conducted before the main testing and are explained. Also, an uncertainty evaluation has been developed for each experiment.

The result from the stiffness measurements indicates that further improvement should be conducted on the manufacturing techniques to achieve optimum results compared to the analytical modelling. Only the stylus with highest mechanical aspect ratio has a stiffness that closely matches to the analytical modelling. Furthermore, the stylus made by the *Type 3* process, which have an additional ECM process in fabricating the stylus shaft, exhibited lower stiffness than type 1 styli which are fabricated only from the WEDG process. These results contradict to the initial prediction that the ECM process should produce stiffer result for similar dimensions. The results in this chapter constitute the first measurement of type 3 and type 4 styli, which used ECM process in their manufacturing techniques, and which were the main focus in the current testing. The measured stiffness for both of these types appear, counter-intuitively, to be nearly constant throughout the range of mechanical aspect ratios and effective stylus lengths that were examined. Therefore, it is recommended that further investigation on type 3 and type 4 styli is urgently conducted.

Chapter 6: Sphericity measurement of micro-spheres

6.1. Introduction

It is becoming critical to measure the 3D spherical form error of stylus tips used on micro-coordinate measuring machines (micro-CMMs), as the spherical form error of the stylus tip is a significant limiting factor to the accuracy of the micro-CMM itself [78]. The spherical form error of stylus tip is often neglected in conventional CMM measurement because its value is relatively small compared to the diameter of the stylus tip and can also be compensated during probe qualification. However, the presence of this error is crucial in micro-CMM measurement, especially when using a stylus with dimension less than 100 µm. As described in section 2.6, currently, there is a very limited number of traceable measuring instruments that are able to measure the form error of spherical stylus tips with nominal diameters less than 300 µm. Therefore, in addressing ***Thesis Objective 3,*** this chapter will establish the development of new technique of traceable measurement for spherical form error of micro sphere with dimension of 300 µm in diameter.

This new measurement technique has a potential to measure the spherical form error of the micro sphere with nominal diameter less than 100 µm (and is also expected to have capability to measure a sphere with dimension as small as 50 µm in diameter). However, in this project, due to limitations in the rotational and translational manipulation handling system of the sample, it is difficult to measure directly on the spherical surface of the stylus tip for the case of micro styli with dimension less than 100 µm in diameter. Thus, a micro sphere of 300 µm in diameter is selected.

The approach applied in this measurement technique is to establish the traceable form error measurement for sphere with dimension of 300 µm which then used as the reference standard for probe qualification of the micro-styli with dimension less than 100 µm in diameter. This is because, in order to compensate the form error during the qualification of the probe, the spherical form error of the reference standard sphere must first be determined. Nevertheless, in the future, with improvement and modification of the manipulation and rotation stage system, sample handling mechanism and objective lens

system, this measurement method is expected to have a potential to measure the stylus tip sphere directly to determine the spherical form error.

The explanation of this measurement technique in this chapter begins with the introduction of the major aspects of the measurement strategy used to determine the form errors of micro spheres. Then the measurement set-up and measurement procedure are described in detail in section 6.3. The important work of post-processing of measurement data, including the data stitching algorithm and the methodology in assessing the quality of the data are presented in section 6.4. Then the results of measurements were analysed and discussed in section 6.5. At the end of this chapter, some important conclusions are drawn.

6.2. Aspects of the measurement strategy for micro spheres

There are four aspects to the measurement strategy that has been employed in this work. These aspects are: the application of a coherence scanning interferometry (CSI) as the main measurement instrument; the introduction of a new rotational referencing method for more accurate measurement; the integration of sets of linked measurements with data fusion techniques; and application of mathematical data fitting modelling to determine the spherical form deviation of the entire topography of the surface.

The coherence scanning interferometry (CSI) is selected in this work because of its ability to measure a surface variations down to the nanometre scale. In addition, some of the metrological characteristics related to the instrument scale of CSI are traceable to the primary standard of length while other metrological characteristics are well-studied. Furthermore, CSI also has the capability of measuring a sphere sample with dimension less than 100 µm in diameter. However, one limitation of measurements via CSI that is relevant to this work is the limited ability to measure surfaces tilted at large angles with respect to the optical axis of the instrument. Due to this limitation, CSI is unable to measure the whole hemisphere in one field of view. To overcome this limitation, a second aspect of the measurement strategy involves the development of a rotational referencing method.

With this method, sphere is rotated about an axis nominally parallel to the optical axis of the system, the *z*-axis, and about an axis nominally parallel to the *x*-*y* plane. By doing this, the CSI instrument can measure various regions on the surface of the sphere, which ideally

can cover a hemisphere of the surface. Moreover, using this rotational referencing method, more accurate angle is expected to be obtained as it is crucial in determining the exact location of the sphere image dataset. In the third aspect of the measurement strategy, a data fusion technique is applied to combine the individual CSI measurements. In this technique, two main important processes are data stitching and data combined process of measured surfaces. With these aspects combined, the whole topography of hemisphere can be measured and mapped before the sphericity is determined. Finally, to calculate the sphericity deviation and its uncertainty, a data fitting modelling is employed as the final aspect of the measurement strategy. Figure 6.1 summarises all of this aspect of measurement strategy and, the details of all of these aspects are presented in the next section

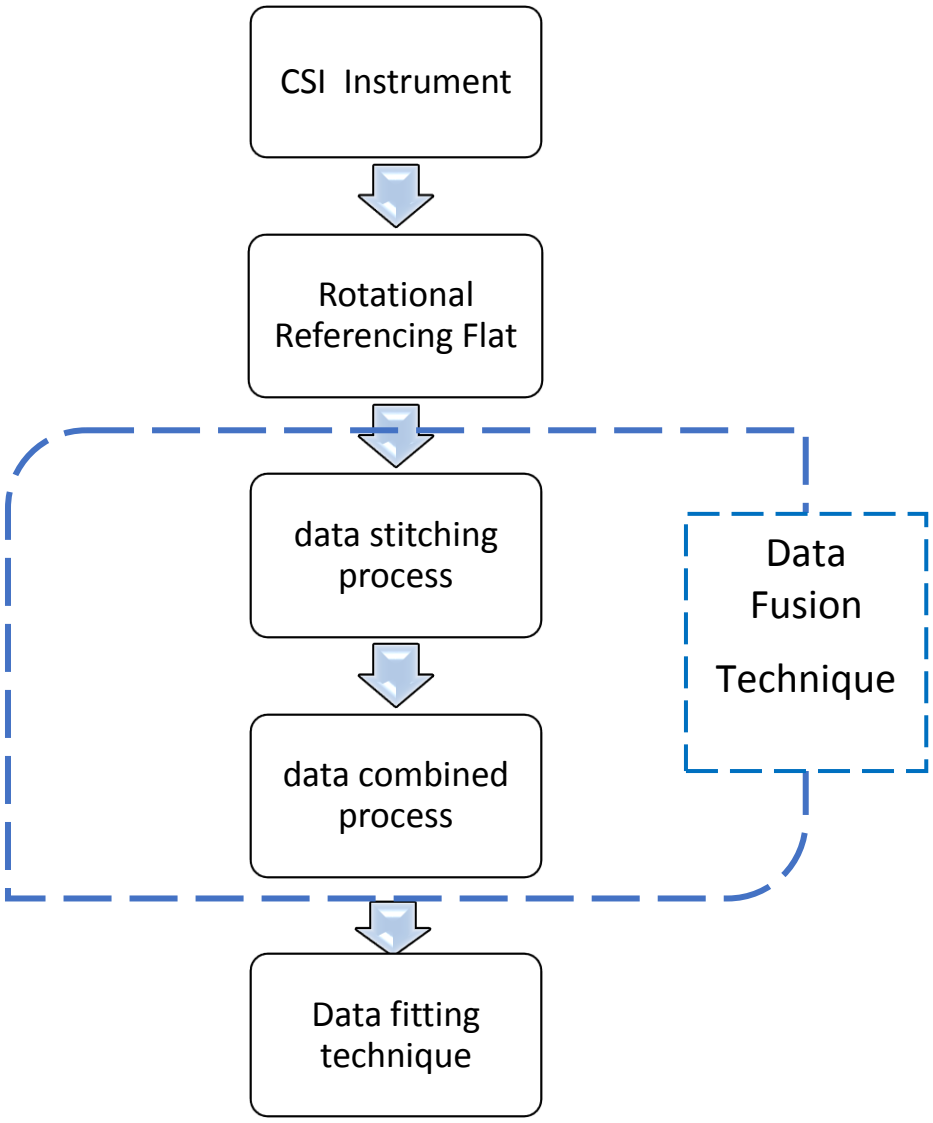

Figure 6. 1: The process flow of the measurement strategy for sphericity measurement

6.2.1. Coherence scanning interferometry

The coherence scanning interferometer (CSI) is a metrological instrument that is used in the field of areal surface topography with the capability to measure form, roughness and step heights. It combines the vertical resolution of an interferometer with the lateral resolution of a microscope [139] and these instruments have sub-nanometre resolution and repeatability in the vertical axis [1]. The technology of CSI was first demonstrated three decades ago [140] and since then, active researches have been conducted to investigated the behaviour of the CSI and improve its performance [141][142][143][144][145][146].

- General principle of operation

The basic principle and mechanism of operation for CSI can be found in many documents, for example, [147],[146],[148],[149]. In general, CSI instrument is a type of two-beam interferometer, as illustrated in Figure 6.2. In this configuration, one beam is directed to the reference mirror while other is focused on a measured workpiece. The reflected light wave front from both beams will be recombined and create a pattern of interference fringes which is captured by the CCD camera. In this configuration, the Kohler illumination optic [150] is used in order to maximise the lateral resolution and minimise the spatial coherence[146]. In addition, in this project, the Mirau interference objective type with magnification of 50x is employed as it ensures a fixed optical path length to the reference mirror.

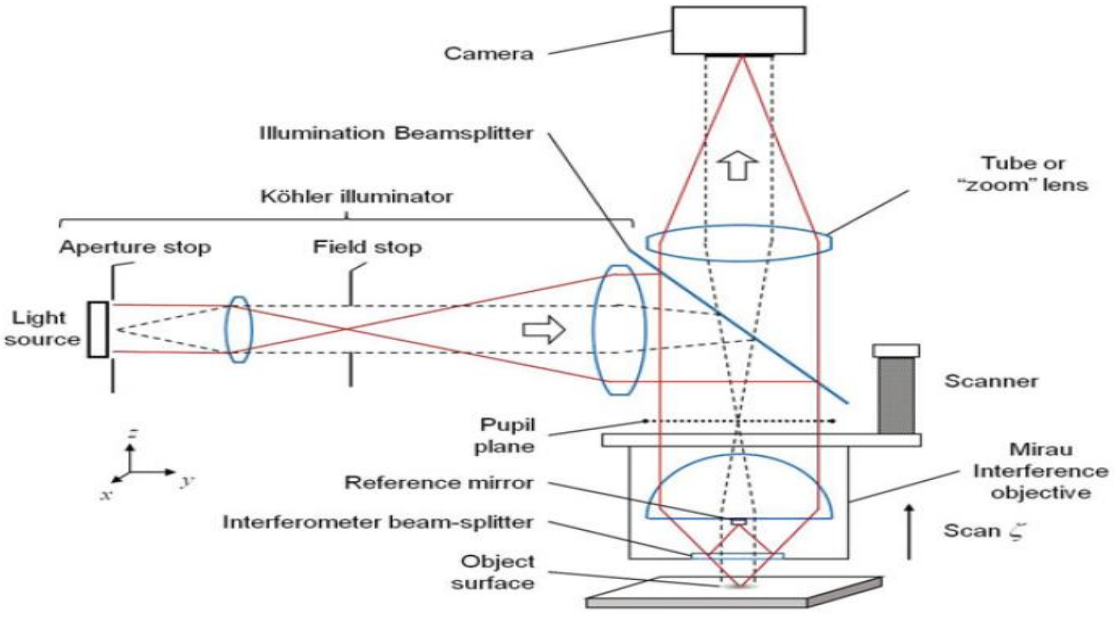

Figure 6.2: Schematic configuration of coherence scanning interferometry [146]

One of the important features of CSI instruments is the application of the wide spectrum, or bandwidth, of light (white light) as the illumination source. By using white light, the low temporal coherence localises the interference fringes seen to points where the optical path is almost equal in the measurement path and the reference path. The location of the surface can then be determined from the fringes imaged on each pixel as the *z*-scan is carried out by using one of the techniques mentioned above. Another feature of CSI is the movement of the objective lens using a mechanical scanner. As the CSI records a single surface height at a time (from each pixel), mechanical scanner is used to determine the surface height with maximum intensity of interference fringes, as illustrated in Figure 6.3. The fringes will be analysed by using one of several methods such as envelope modulation detection [140][141], phase estimation [151] or the combination of both methods [152]

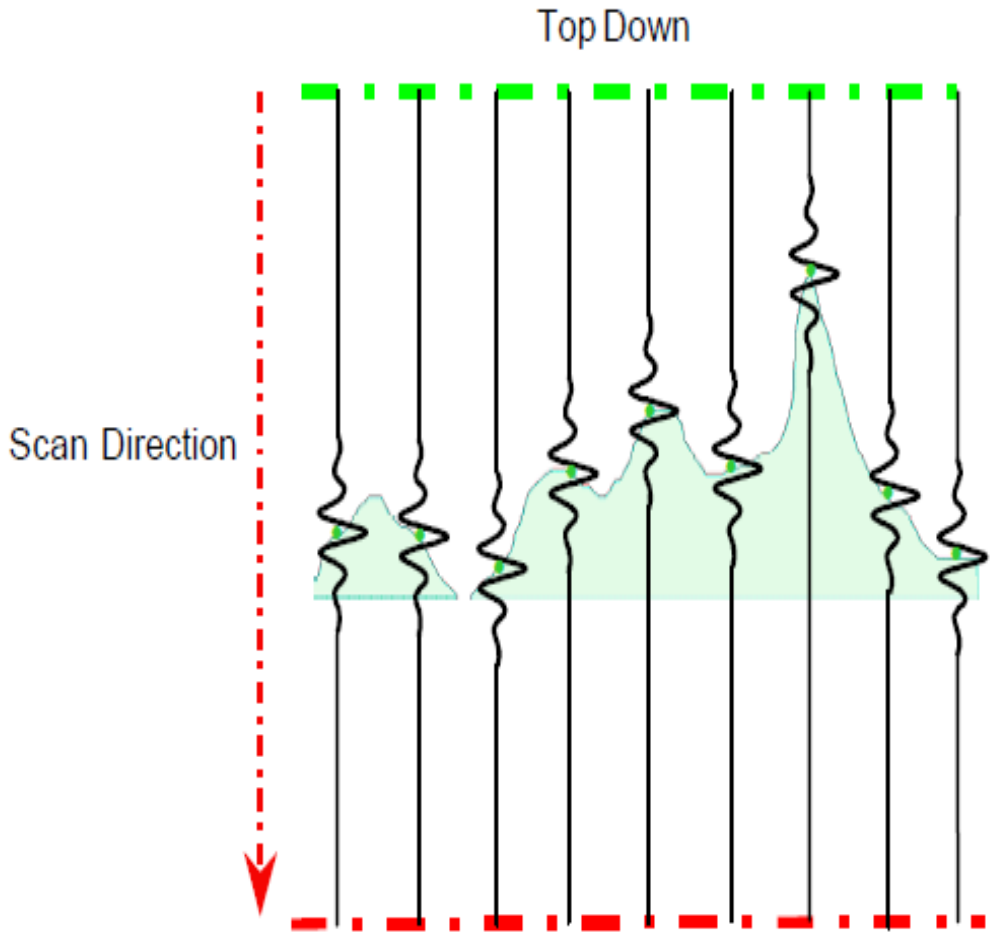

Figure 6. 3: the objective is moved in a vertical direction to find best focus and maximum contrast of interference fringe which locates the surface of measured workpiece [153]

- Sources of measurement uncertainty of CSI

Various source of errors occurs in CSI measurement are well defined and reported in the literature [154][147][1][153]. In general, the interaction behaviour of the incident lightwave with the surface of a solid workpiece, the geometry and surface condition of the workpiece, optical and instrumental components, the alignment and measurement technique and material properties are all factors that contribute to the measurement errors. Common measurement errors that are often observed are from data dropout and re-entrant features, which explanation can be found in details in other literature [147]. In summary, the data dropout in measurement might be caused from the large surface gradient, limitation of the capability of measurement range or issues with the measurement setup and alignment of workpiece. Apart from that, a re-entrant feature is a hidden feature in surface that is difficult to capture by any optical method, including CSI. These errors becoming prominent when the tilting of surface and background noise occurs during measurement.

In contrast, batwing effect and ghost step are measurement errors related to flat and stepped surfaces. The details of these error are well-explained in other literature documents [153][154][155][156][157]. Both errors occur due to the fringe order error caused by the dispersion of the incident wave and features shape on the surface (for instance, curve and step on the surface). The batwing effect can be normally observed when measuring a step discontinuity on a surface, while ghost step error is associated with a 2π phase jump when measuring a flat surface. The effect of ghost step error could be minimised by proper alignment of the instrumental setup [147].

So far, the discussion has focused on the common measurement errors occurring in CSI. In relation to this project, in which a micro sphere is used as a measured workpiece, there are several specific and important measurement errors that should be considered. The micro-sphere not only has significant regions where the surface is at a large angle with respect to the optical axis of the instrument, but because of an imperfection in surface finish process is also expected, that they may have a rough surface. Therefore, in this CSI measurement errors caused by the high slope of the geometrical surface of measured workpiece, multiple scattering error due to the surface condition of the workpiece, distortion error on the lateral axis and optical properties error of the measured workpiece are predicted to occur. When measuring the high slope surface, the numerical aperture (NA)(because of its aperture angle,

will be explained later) of the system limits the maximum slope of surface that can be measured by any optical metrological instrument, in general [158]. Theoretically, the maximum acceptable angle surface slope is half of the aperture angle. The aperture angle is the angle that determines the numerical aperture (NA) [159]. However, in practice, the maximum angle slope observed is smaller than the theory [147]. Consequently, as shown in Figure 6.4, the higher the slope of a measured surface, the greater the loss of information in the reflection wave, which leads to the error in measurement [160]. The reduced amount of light received gives a smaller signal, and hence a poorer signal to noise ratio. This makes it harder to determine the true location of the surface. For the case of complex geometry of the measured surface, typically illustrated at larger scales by a V-groove surface, there will be difficulties in defining the location of the real surfaces as multiple reflections or multiple scattering errors will [161].

Furthermore, multiple scattering could also occur when measuring the rough surface of measured workpiece as illustrated in Figure 6.5. Due to these phenomena, the result of roughness is observed to be overestimated [154]. Figure 6.6 demonstrate that from the measurement profile of V-groove, the location of the top and bottom of the sample have been determined reasonably, but the profile at the bottom of the sample shows relevant deviation from real geometry, which leads to the overestimate of the roughness result. The high noise appears in the profile due the multiple reflections at high slope angle surface of sidewall of the V-groove and the limitation of acceptance angle of objective lens. Thus, the measurement profile is unable to locate the position of the sidewall of the samples.

In addition, a distortion at the lateral axis could also occur when an optical metrological instrument is measuring a sphere surface or a tilted surface. This distortion had been first discovered by Evans [162] in 1993 when measuring the tilted plane surface by optical instrument. This distortion caused by the monochromatic third order aberration [163], where in this case, it might be caused by the spherical aberration. This lateral distortion not only alters the position of the sphere in lateral axis, but also introduces measurement error in height [164]. In recent years, research by others has demonstrated the effect of this lateral distortion on the CSI instruments [165], Wavelength scanning interferometry instrument [166] and a technique for correction to this distortion [164]. It also observed from these

research works that the lateral distortion are more significantly affected at the edge of the surfaces (lateral and height axis) within field of view of the lens [164] [165].

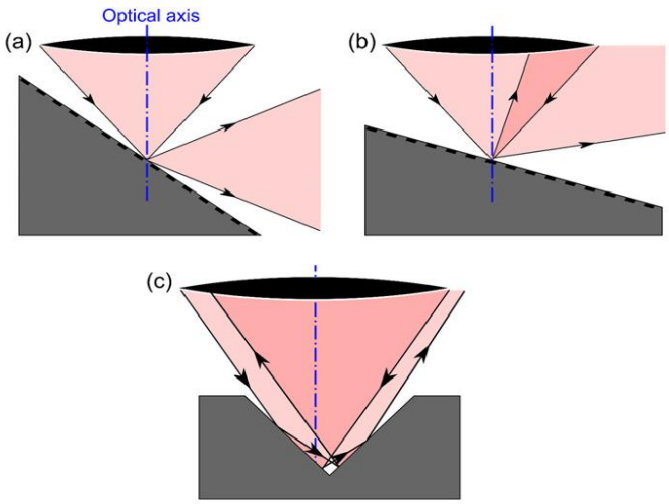

Figure 6. 4: Effect of high slope surface when interact with the incident light [160]

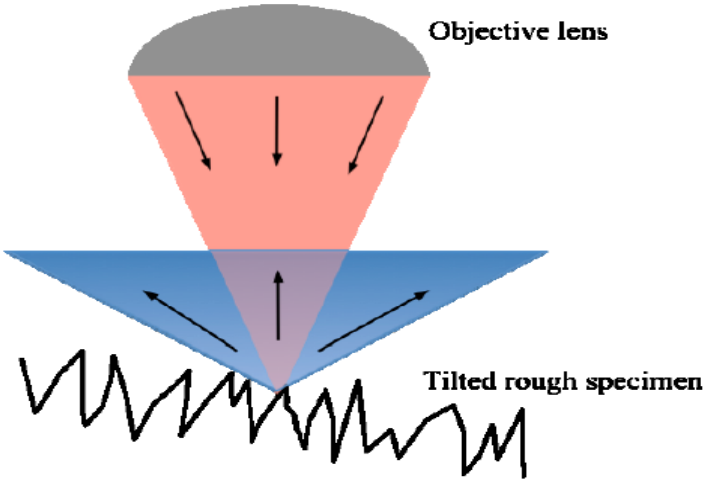

Figure 6. 5: Effect of multiple scattering error in CSI measurement [147]

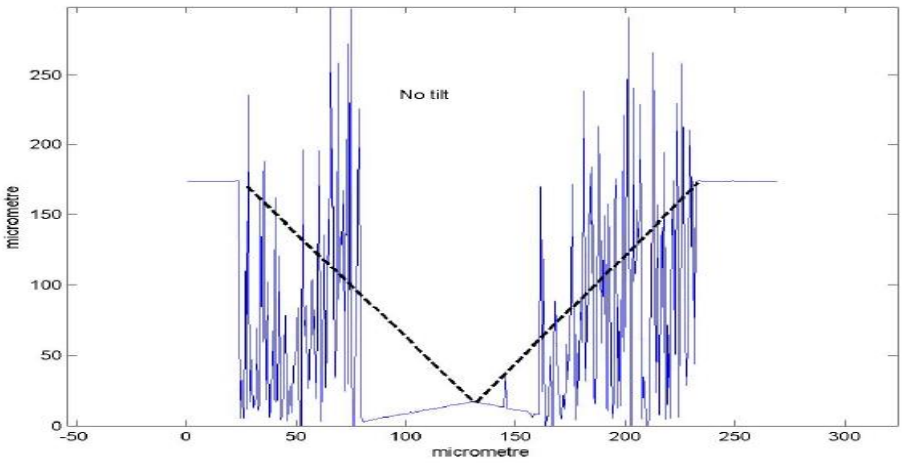

Figure 6. 6: the measurement of V-groove sample [80]

- Metrological characteristics of CSI

It is important for the instrument to be calibrated and traceable to the primary standard of length in order to provide confidence in the measurement result (and the accuracy of the instrument can be known). For CSI, the metrological characteristics, defined as the quantities measured in a calibration process, are well-studied and reported in many of the documents[167][168][169][170][171]. These metrological characteristics are associated with the calibration of the instrument scale and can be summarised as follows:

(i) Measurement noise

Measurement noise is defined as the noise arising at the output signal of the instruments [168]. It might consist of various source of noise such as internal noise of the instrument, environmental conditions, instability of electronic components, temperature fluctuation, and external electromagnetic disturbances [168]. To measure the measurement noise of CSI, an optical flat with flatness deviation less than 30 nm is used as a standard artefact [172]. Initially the value of measurement noise can be determined from the parameter *Sq*, which is the root mean square (RMS) of the signal amplitude, to give a scale limit of the surface. However, this method faces difficulties in separating the measurement noise from underlying roughness and residual flatness of the optical flat [172]. To overcome this problem, two methods have been introduced, namely the subtraction technique [168] and the averaging technique [173]. Both methods required repeated or multiple measurement at the same location on the optical flat. These methods are suitable for types of measurement noise that behave like random errors. However, when the noise is non-stationary in statistical sense [168], both methods are unable to distinguish the measurement noise from the roughness and residual flatness.

(ii) Residual flatness

Residual flatness testing is important in accessing the flatness of the reference mirror in CSI. As CSI uses a flat glass surface as a reference and any deviation from its ideal flatness, which could cause an error in the *z*-axis, should be identified. An effect indistinguishable from deviation from flatness of the reference can be produced from optical aberrations (even if the surface of reference flat is perfect) [172]. The magnitude of residual flatness can be calculated from surface areal parameter *Sz* which is the surface areal parameter associated with the maximum height of surface limit. Similar to the measurement noise testing, the optical flat is

use as a standard artefact in this testing. In order to distinguish from spurious measurement data, it is suggested that multiple repeated measurements are taken at different locations on the optical flat without changing the instrument set-up [168].To enhance the measurement result of residual flatness testing, an outlier removal method [174] and threshold method [168] have been proposed.

(iii) Amplification, linearity and squareness of the scale

It is important to calibrate all axis scales for an areal topography instrument. This can be done by establishing the metrological characteristics of amplification coefficient, linearity and squareness. Amplification coefficient and linearity parameter are determined from instrument response curve (an example of it can be seen in [175]) and they are well defined in literature[169] as *the slope of the linear regression curve obtained from the response curve (for* amplification coefficient) and the maximum local difference between the line, from which the amplification coefficient is derived, and the response curve (for linearity). The squareness is the perpendicularity deviation between any two of the x, y and z axes.

To determine the amplification coefficient and linearity of *z-axis* scale, several sizes of step height artefact are used and measured by the CSI instrument at different height positions across its range. These multiple heights measurement should cover the whole or the required range of *z-axis*. A best linear fit should be constructed from these multiple height measurement results in order to obtain the amplification coefficient and linearity of z-axis [167]. For the CSI instrument used in this project, the step height artefact of 19 nm, 350nm, 3 µm and 17 µm are employed.

In contrast, the amplification coefficient, linearity and squareness of the *x*- and *y*-axis can be tested using a cross grating [176] or a pyramidal structures artefact[177]. For the CSI instrument used in this project, a calibrated cross grating (type ACG, please refer to[169]) and was used that had been calibrated and traceable to the NPL areal topography instrument [178]. The amplification coefficient and linearity in x and y axis can be obtained by measuring the location of centre gravity of cross grating of this artefact while their squareness is achieved by measuring angle between two nominal orthogonal rows of square holes[167][169]. Prior to this, the squareness of the square holes should be specified.

(iv) Resolution

In general, the resolution is defined as the smallest change of measured quantity that can be distinguished [179]. Thus, the resolutions of all axis scales of the CSI instruments are counted as sources of uncertainty in measurement. It is currently acceptable in international standards for the resolution of each axis to be determined separately [170]. For the resolution of *z*-axis, it has been included in the measurement noise testing (as describe above in (i)), while lateral period limit (defined as the spatial period of a sinusoidal profile at which the height response of an instrument falls to 50%) testing determine the resolution in *x*- and *y*-axis [170]. This lateral period limit measurement can be conducted by using a star pattern artefact and the detail of this procedure has been described in the literature[170].

The CSI instrument used in this work is manufactured by Taylor Hobson (model name: Talysurf CCI HD). It is a part NPL dimensional metrology infrastructure which is also used as a standard calibration instrument for performing calibration services. Therefore, it has been maintained and calibrated with the high standard procedure. Based on the latest calibration certificate of this CSI instrument, the type B metrological characteristics are described in Table 6.1:

Table 6. 1: metrological characteristic of NPL CSI instrument (model name: Talysurft CCI HD) from latest calibration certificate

Metrological characteristic		**uncertainty value 20x lens**	**uncertainty value 50x lens**
Measurement noise		0.6 nm	0.6 nm
Residual flatness		2.1 nm	3.7 nm
Z-axis amplification and linearity	17 µm step height	25.9 nm	25.9 nm
	3 µm step height	3.3 nm	3.3 nm
	350 nm step height	2.2 nm	2.2 nm
	19 nm step height	1.9 nm	1.9 nm
Amplification and linearity of *Z*-axis		0.4 µm	0.3 µm
x and y resolution		4.6 µm	2.6 µm

6.2.2. Rotational Referencing technique

Since the rotation and translation of the sphere are essential steps in the measurement technique being used, the selection of rotational and translational stages is a crucial issue. It is very important to have a calibrated high accuracy rotational and translational stage system in *x*-, *y*-, and *z*-axis as an accurate position of measured surface data is required in the stitching process. The required accuracy of the stage system is estimated in the range less than the pixel width of the CSI's camera [81]. In this work, an external rotational manipulation stage system has to be employed, as the CSI does not have its own system. However, the currently available commercial rotational manipulation stage systems are not suitable for manipulating and holding the microsphere and do not reach the required accuracy. Therefore, to overcome this problem, as the third aspect of measurement strategy, a new technique of self-referencing rotational system is introduced.

The self-referencing rotational system relies on a flat reference surface, onto which the micro sphere is mounted. The flat reference surface used in this work is a gauge block surface and the micro sphere is stuck on the gauge block using adhesive material, as shown in Figure 6.7. A grade K gauge block is selected as a reference flat because of its high flatness properties. This is also means that the reference flat can be seen as a part of the measured workpiece. The CSI measurements, therefore, include the combination of the reference flat surface and the spherical surface of micro sphere. In principle, when the micro sphere is rotated about the *x*-axis (an axis parallel to the image plane), the flat will follow the rotation. Hence, the rotation angle of the flat can be determined from its reference position. The reference position is the position where no rotation is applied (where the reference flat is perpendicular to the optical axis of the objective lens of CSI). Furthermore, a special spot or line on the reference flat is used as a marker so that it can be used as reference point when the sphere is rotated about the *z*-axis. For the convenience of the discussion in this thesis, the rotation along *x*-axis will be referred to as tilt while rotation along *z*-axis will be referred to as rotation.

This new self-referencing rotational method is expected to provide a sufficiently accurate information on the angles of tilting and rotation to complete the 3D stitching process. An externally-available commercial rotational system can then be employed as a tool in manipulating the reference flat and micro-sphere because it is not involved in the metrological loop of the measurement.

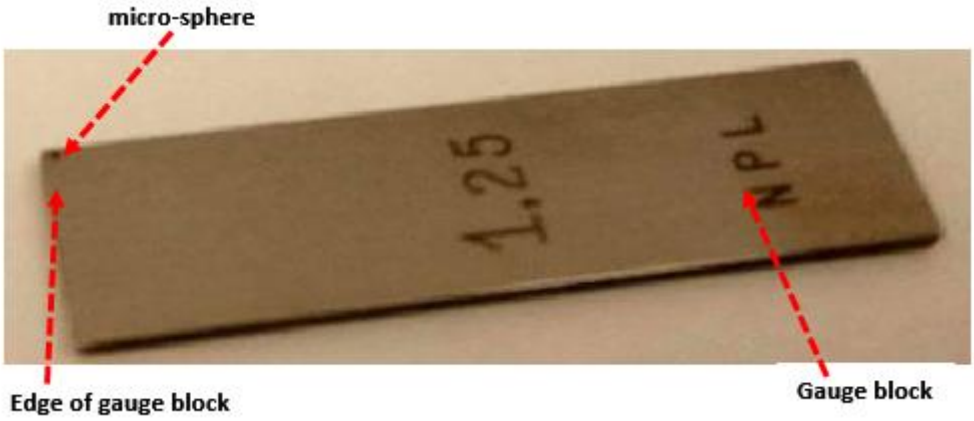

Figure 6. 7: sample preparation: microsphere is located on the gauge block using adhesive material

6.2.3. Data fusion technique- stitching technique

Due to the inability of CSI to measure the overall surface of micro-sphere in one field of view, a data fusion technique is employed in this measurement. In principle, this measurement can be conducted by rotating and translating the micro sphere so that the CSI can take measurements at each of various overlapping locations on the sphere surface. These measurement surface data are then combined using 3D data stitching process to obtain a topography map of hemisphere. The details of the data fusion methods, especially 3D data stitching, are described in the following discussion.

Data fusion is a generic name for a range of techniques used in various of fields of study such as in robotics, medical applications, space optics, non-destructive inspection, manufacturing and metrology. Although the definition of data fusion varies depending on the field of study [180], generally it can be understood as a technique of combining more than one data set from several data sources in one platform to achieve a specific purposed. In dimensional metrology, data fusion can be defined as [181]:

The process of combining data from several information sources (sensors) into a common representational format in order that the metrological evaluation can benefit from all available sensor information and data.

In metrology, data fusion techniques were initially applied to measure large component [182][183][184], including large aspheric surfaces [185][186] [187], micro and sub-micro surface [188][189] and multi sensor coordinate measurement [190][191][192]. These techniques have been employed to fulfil various purposes [193], but in this project the intention is to overcome the limitation of CSI and thus obtain a measurement result for overall hemisphere surfaces of micro-spheres.

Data fusion can be classified to four categories, namely: fusion across sensors, fusion across attributes, fusion across domains and fusion across time [194][195][196]. Fusion across sensors involve the use of several different sensors to measure same measurand, while fusion across attributes involve several different sensors in measuring different quantities, but ones related to each other, in the same experimental situation. Fusion across domains takes data from a sensor, or from several different sensors that measure the same attribute, over various ranges or domains. The last category of data fusion is that new data is fused with its historical information which is called fusion across time.

There is a common process flow normally implied in data fusion: pre-processing, registration process, data combination process and post fusion process [193][194]. Pre-processing is the process of obtaining and processing raw surface data from measurement results of the sensors. The condition of the surface data needs to be investigated, including the noise level and outlier points should be filtered before the next process takes place. Registration is an essential step in data fusion. In this process, the coordinates of multiple surface datasets will be transformed to the common coordinate system so that they can be combined and fused together. During this process, some region in a surface will share same coordinate with its adjacent surface and this region is known as the overlapping region. The gap between the surfaces in this overlapping region must be ensured to have a minimum value. Also, it is important prior to this process that the coordinate system of each surface dataset is accurately determined in the measurement. Otherwise, an error and misalignment will be occurred during registration process of overlapping region of both

surfaces. The fiducial marker method [197][198] and iterative closest point (ICP) algorithm [199][200][201] are popular methods used in registration.

One of the important techniques commonly used in registration processes is data stitching. Data stitching is classified under the type of fusion across domain. There are two categories: 2D data stitching and 3D data stitching. 2D data stitching is a process of combining two or more adjacent surface data or image data at their overlapping region under the same or multiple sensors and the same measurement setup. An overlapping region between adjacent surfaces data is an important requirement in order for both surface data to be fused together and therefore, needs to be considered during measurement of data by the sensors. This technique was first applied in interferometer measurement to measure large plane surfaces in 1994 [184]. Since then, improvements have been made and stitching techniques have become a popular solution to measure large surfaces, including large optical mirror [202][203], large aspheric surfaces [187][204], large cylindrical surfaces [205][206],and large sphere surfaces [207][101]. In contrast, 3D stitching technique, or also known as 3D data fusion [193] or point cloud fusion [181], is an extension of 2D stitching which consists of handling a three-dimensional spatial cloud surface dataset. As in this dataset, the process manipulation and fusion becomes more complex because it involves six degrees of freedom. Due to the involvement of 3D measured image data in this measurement task, the 3D data stitching technique is employed.

After registration process (using data stitching) where surfaces have been ensured to be close together, the next process is the combination of both surfaces to become one surface data so that only one dataset exists at all location of the surface. This process is called a data combination process. Many mathematical modelling methods have been developed to combine the two data sets. These include simple data averaging process, weight fusions [192][196], GP based surface fitting technique[208][209][210], and wavelet approximation technique[211][212][213] . The last process is the post fusion process which dealing with any process of output combined surface such as data reduction and format conversion of surface.

6.2.4. Sphericity calculation using data fitting modelling

As described in Chapter 2, section 2.5, sphericity or spherical form deviation can be calculated using several established mathematical data fitting models such as linear least square method, minimum circumscribed sphere, maximum inscribed sphere, minimum zone sphere and RANSAC shape detection. Therefore, as the final aspect of measurement strategy, the spherical form deviation will be determined by using consistent data fitting modelling. However, it is neither the intention nor main focus of this work to study and compare in detail each of these data fitting models. This aspect is employed as an indicator to determine the quality of this new measurement technique. For this purpose, coordinate metrological software will be used.

6.3. Measurement setup and procedure

6.3.1 Determination of measurement parameters

Before setting up the instrument and starting the measurement, several parameters need to be determined. These include the numerical aperture and magnification of the objective lens, along with the tilts and the rotations that will provide a sufficient overlap region between each of the sets of surface data. The detailed explanation of these parameters are as follows:

- ***Numerical aperture (NA) and magnification of objective lens.***

Ideally, a high NA will allow more light to be captured and the resolve finer details the surface. For the specific CSI instrument that was used, the highest available numerical aperture of the objective lens was 0.55 which has the magnification of 50x. Other objectives lenses in this CSI have magnifications of 5x, 10x, and 20x. An initial and simple measurement on the micro sphere with diameter 300 µm was conducted using the 20x lens and 50x lens. This test showed that, although the field of view (FOV) is larger, only a small area of micro sphere surface can be seen under 20x lens compared to 50x objective lens. This is because the numerical aperture (NA) of 20x lens is smaller than the 50x lens and it is unable to measure a data data as far around the sphere due to the angle of the surface, so only small region of useful data and less information can be captured by 20x lens. Therefore, the measurement

data from the 50x lens is more suitable for the purpose of this sphericity measurement and will be selected for all further measurements.

- ***Selection of tilt angle, rotation angle and percentage of overlap data and numbers of measurement data to be measured.***

Prior to measurements that exploit the stitching technique, it is important to define the way to manipulate the micro-sphere in order to ensure that each surface dataset measured by CSI instrument, partially overlaps with its adjacent surface datasets and that the combination of the data sets, theoretically, cover the entire hemisphere of the upper surface. Moreover, the coordinate frame for each surface dataset needs to be known. Therefore, the design of the manipulation stage, and the selection of tilt and rotation angles are crucial factors to be determined.

To calculate the tilt angle of the micro sphere which is defined as the angle of rotation along an axis parallel to the image plane, a simple geometrical equation for the circle and sphere are employed. Figure 6.8 illustrates a condition where only some region of the micro sphere are measured by CSI instrument. R_{sphere} is a radius of the micro sphere, d_{spot} is the diameter of the region that has been measured by CSI while m is the length of arc sector of the measured region, and , θ is the tilting angle.

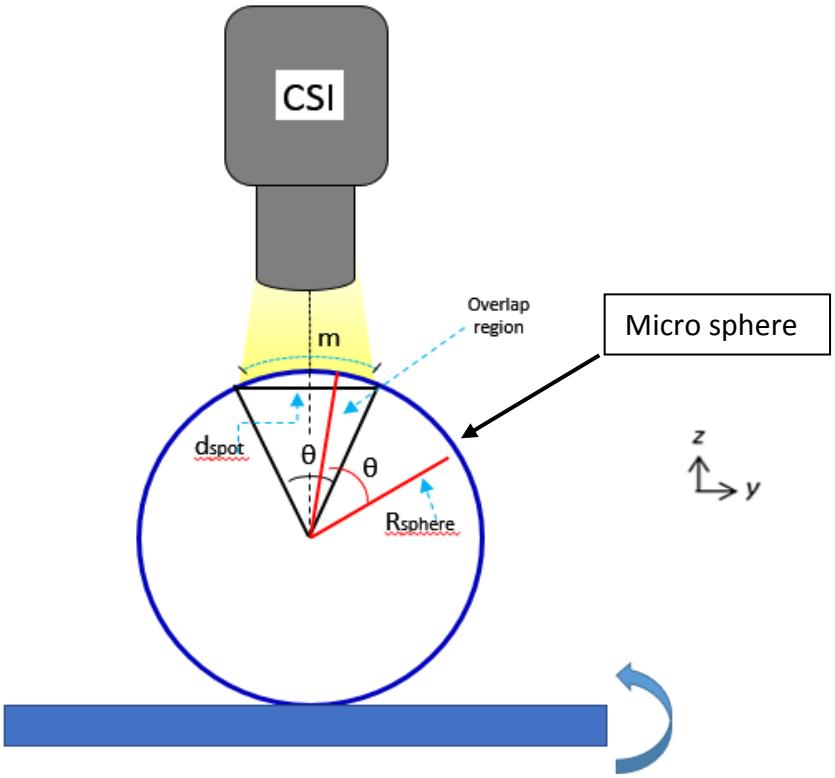

Figure 6. 8 : the micro sphere and reference flat is manipulated in order to be measured by CSI

To simplify the calculation, the microsphere is viewed as a circle. The value of *m* and d_{spot} can be determined from the measurement. The tilt angle, θ, is determined using a formula derived from the length of arc sector for circle, which can be calculated using either of the following equation (6.1) or (6.2) below:

$$m(1-f_o) = \frac{\theta^\circ}{360^\circ} \times 2\pi R_{sphere} \tag{6.1}$$

And

$$\sin(\frac{\theta^\circ}{2}) = \frac{(d_{spot}\,(1-f_o)/2)}{R_{sphere}} \tag{6.2}$$

where $0 \leq f_o \leq 1$, and f_o is referred as a fraction of the field overlapping common area or percentage overlap region of two surfaces divided by 100. Note also, while θ is formally in unit of radians, in this equations (and also the following equation which involving angle), unit of degree is used for θ and is differentiate by using the symbol of θ°.

Another rotation is needed to manipulate the micro sphere to cover the entire hemisphere surface. The orientation of this rotation depends on the design of the manipulation stage and the measurement procedure. As shown in Figure 6.9 and Figure 6.10, the rotation is either about the *z*-axis or about the tilt axis (*x*-*z* axis). In general, the angle of this rotation can be calculated as follows:

$$\sin(\frac{\theta^\circ}{2}) = \frac{(d_{spot}/2)}{R_{sphere}} \tag{6.3}$$

Circumference of a small spot = $\pi d_{spot} = 2\pi(R_{sphere} \times \sin(\frac{\theta^\circ}{2}))$ (6.4)

Number of positions = $\frac{\text{Circumference of a of a small spot}}{m(1-f_o)}$ (6.5)

Rotation angle, Φ_z° = $\frac{\text{Number of position of a small spot}}{360}$ (6.6)

As explained previously, the CSI instrument measured the surface sphere at each of position after the sphere is manipulated (by its tilting and rotating angles). Therefore, the total number of measured datasets needed to cover the whole hemisphere surfaces is crucial to be determined as it indicates how practical and time-consuming is the overall experiment. This total number of measured data depends on the design of the manipulation stage, tilting and rotating angle, diameter of the sphere and diameter of the region that has been measured by CSI instrument (d_{spot}). In this experiment, there were two options of design manipulation stage which was stage design option 1 (in Figure 6.9) and option 2 (in Figure 6.10). Due to its differences in design, the strategy (procedure) in manipulating the sphere, the rotation angle, the position pattern of sphere surface during measurement and the total number of measured data were also different between the two stage designs. In the stage design option 1, the strategy in manipulating the sample was begun by applying selected tilt angle using tilt stage and follows by measuring the surface data at that position by CSI instrument. This process continued until the sum of selected tilt angle is approximately about 180˚. Then, the sample was rotate along *z*-axis using the selected rotation angle and followed by the same tilting of sample as explained previously. After this process completed, the sample was rotated to the next position using the same value of rotation angle and the same procedures above were repeated until a 360˚ of sum of rotation angle was completed.

In contrast, for the stage design option 2, the procedure of manipulating the sample was started by tilting the sample by using the selected tilt angle and the first surface data is measured by CSI instrument. Then, the sample rotated along the tilt axis using the selected rotation angle and the surface data was measured. This rotation procedure along tilt axis was continued until the sum of rotation angle was approximately near or equal to 360˚. Next, the sample is tilted to the next position and procedures repeated with this constant value of tilt angle and the same rotations along tilt axis. This manipulation of samples is completed when the tilting angle was approximately near or equal to 90˚.

Comparing between the manipulation strategy for both stage design, it is observed that the stage design option 2 had a fewer total number of measured data while stage design option 1 involved higher data redundancy.

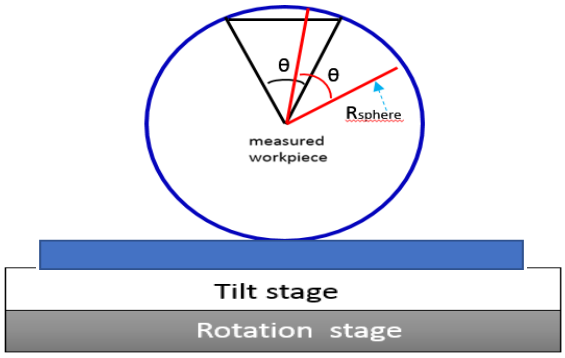

Figure 6. 9: Stage design option 1: the tilt stage will tilt the sphere along x-axis while the rotation stage will rotate the sphere along z-axis

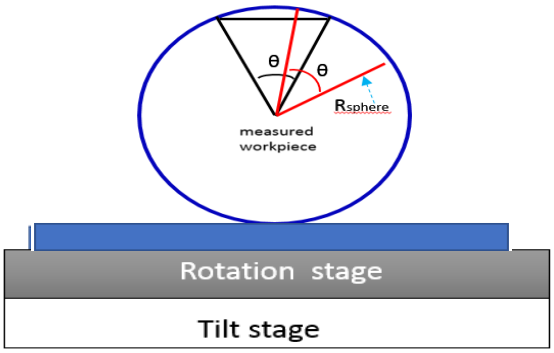

Figure 6. 10: Stage design option 2: the tilt stage will tilt the sphere along x-axis while the rotation stage will rotate the sphere along tilt-axis (x-z axis)

- ***Limitation of design manipulation stage***

Considering the apparatus and setup of equipment currently available in the laboratory, the design stage 1 shown in Figure 6.9 was selected for this project. As will be explored in detail later, selecting this stage design involved significant data redundancy but it can be compensated in the post-process data. However, a limitation is imposed by the tilting stage, which has a tilt range of only 60˚ (from -30˚ to 30˚), and, thus, the current setup is unable to cover the whole surface of a hemisphere. In addition, as the manipulation stage will be placed between the CSI stage and the underneath of the objective lens, extra precaution steps are essential to ensure the test sample or workpiece does not touch the objective lens. Because of this, the limiting tilt angle might not even reach 30˚ or -30˚ (later, in the experimental procedure, the highest safe tilt angle can be reached was below 25˚). Nevertheless, this setup is adequate to test the measurement technique and with the enhancement of the manipulation stage design in future work, the full hemisphere surface can be measured.

6.3.2 Sample preparation and handling

A micro sphere with diameter of 300 µm and made from ruby was used as a test sample or workpiece. A rectangular stainless steel gauge block, grade K, was used as the reference flat. The micro sphere was placed on the edge of gauge block and bonded to it using an adhesive material (as shown previously in Figure 6.7). The adhesive must be carefully layered underneath the micro sphere and not spill out to other areas of the surfaces that are actively within the measurement. The edge of the gauge block was selected as a marker to provide a reference point for the rotation axis. Then, the test workpiece is mounted on to manipulation stage. Care has to be taken when fixturing the test sample on to the manipulation stage in order to avoid angle distortion cause by misalignment introduced between them. Although a systematic error due to this angle distortion can be minimise or eliminated during post data processing (specifically in calculating the tilt angle), this extra precaution step is a good practise to ensure that this systematic error has been avoided in the experiment. It is also essential to clean the surface of the sample so that it is free from grease, dirt and dust.

6.3.3 Instrument and measurement setup

General guidelines on the CSI instrument setup have been well recorded in the literature [147], [153]. In principle, the steps of instrument setup can be described as follows:

a) The instrument including light source, controller and software is first turned on and left for about 30- 60 minutes to be in stabilized condition.
b) The intensity of the light source is set to the optimal value.
c) The sample/test workpiece with the external manipulation stage is placed on the CSI stage under the objective lens. It is important to ensure that the external manipulation stage is tightly fixed to the CSI stage.
d) To minimise the temperature turbulence noise, the measurement area will be shielded by an appropriate plastic box.
e) The objective lens with 50x magnification was selected for this task.
f) As the internal stage of the CSI also has an angle-related manipulation system, it is crucial to ensure that the test workpiece is in a levelled condition without any angle applied in the internal manipulation stage system. This can be done adjusting the

samples tip stage to zero tilt, focusing the CSI on the reference flat, then adjusting the instruments tip tilt stage until a single fringe is seem. Of course, the external manipulation stage should not have any angle applied.

g) After the instrument has reached the stabilised condition, it is ready to start a measurement. Prior to that, the appropriate parameters required in the software are selected.

6.3.4 Preliminary measurement and investigating the quality of measurement data

A set of preliminary measurements of the sphere were taken in order to examine the condition of the surface, and quality of the results gained. Two measurement datasets were taken on the same sphere. The first was a measurement in which no angle was applied for either the rotation or tilt stages. Then, a small tilting angle (approximately less than 2˚) was applied for the second measurement. Both measurements were conducted at the centre of the field of view (FOV) of the objective lens. This means that the peak of the spherical surface was centred in the FOV, the peak location being determined from the circular fringes seen when the top of the sphere is in focus Moreover, because the same objective lens and setup was used, the measured regions were expected to be approximately the same size. These two surface datasets were then stitched together. To examine the surface condition of the measurement data, using algorithm from CSI software, its form has to be removed from the surface and for enhancement of the surface condition, height thresholding is applied to the surfaces so that any insignificant motif height can be eliminated [214]. The result after removing the surface form and applying the height thresholding of the first measurement (measurement of surface without any applied angle) is shown in Figure 6.11 while Figure 6.12 illustrates the resultant measurement data, in terms of differences in *z*-position value when both surface datasets were stitched together. Because of only small tilting angle is applied to one of the surface datasets, when they were stitched together the majority of the region of both surface datasets are overlapped. Therefore, there is a small difference in topography area of the stitched surface dataset compares to the each of the surface dataset before stitching process, as shown in Figure 6.13 (it can also be seen in Figure 6.11 compared to Figure 6.12 where the topography of both surface dataset was observed to have approximately similar area). This was also the rationale of selecting the small angle in this

preliminary measurement as it was a simple case to be processed by the stitching algorithm (stitching algorithm will be explained in section 6.4)

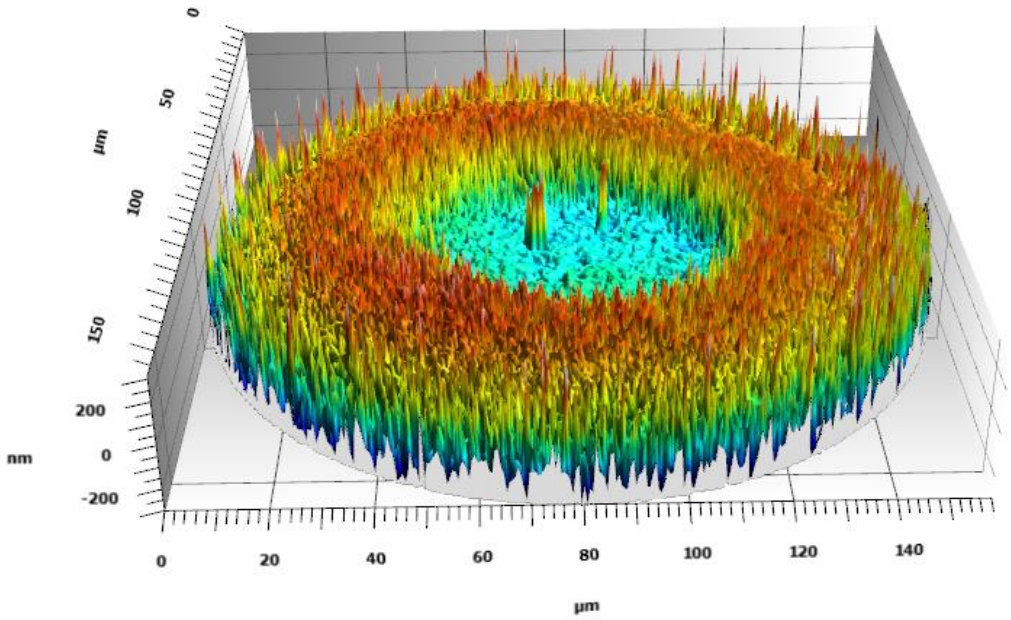

Figure 6. 11: The result data of first preliminary measurement surface. There are no tilting angle or rotation angle applied to this dataset. The form removal and surface height threshold had also been applied to this result. The result has been taken at the centre of circular fringe

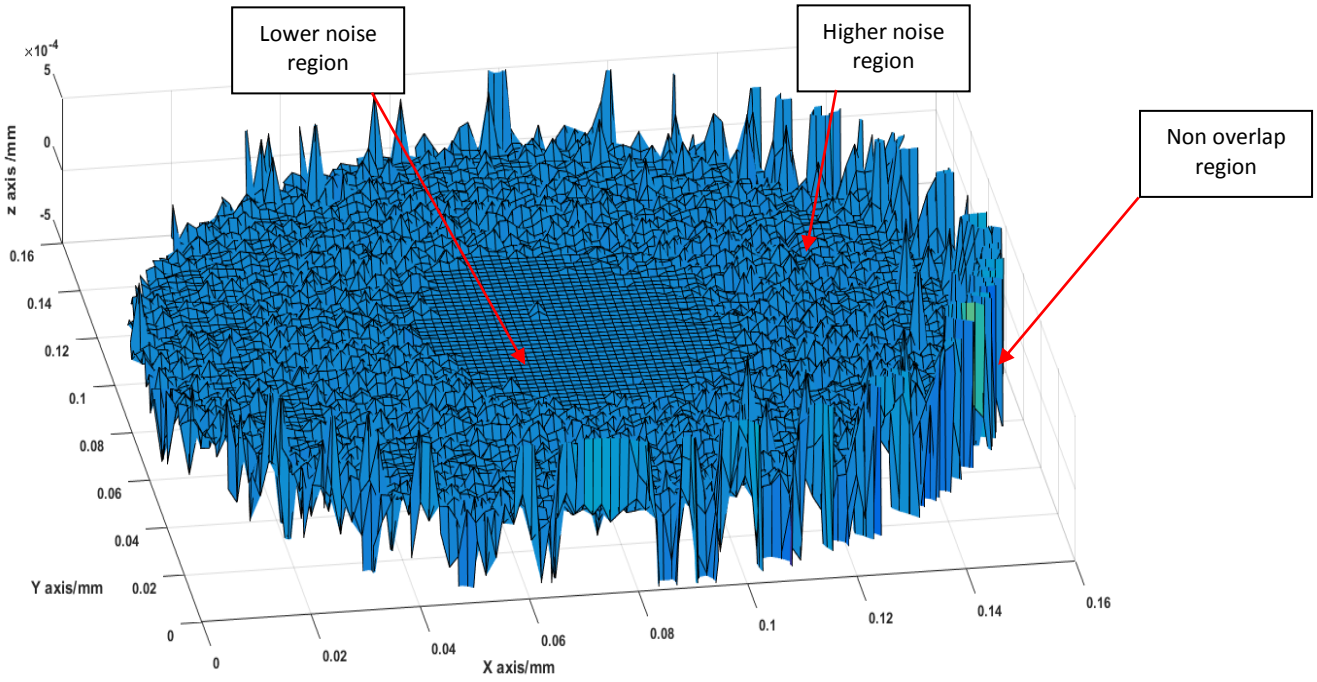

Figure 6. 12: Topography of height different of a stitched surface dataset. The form removal and surface height threshold had also been applied to this result. This result is measured at the centre of the circular fringes

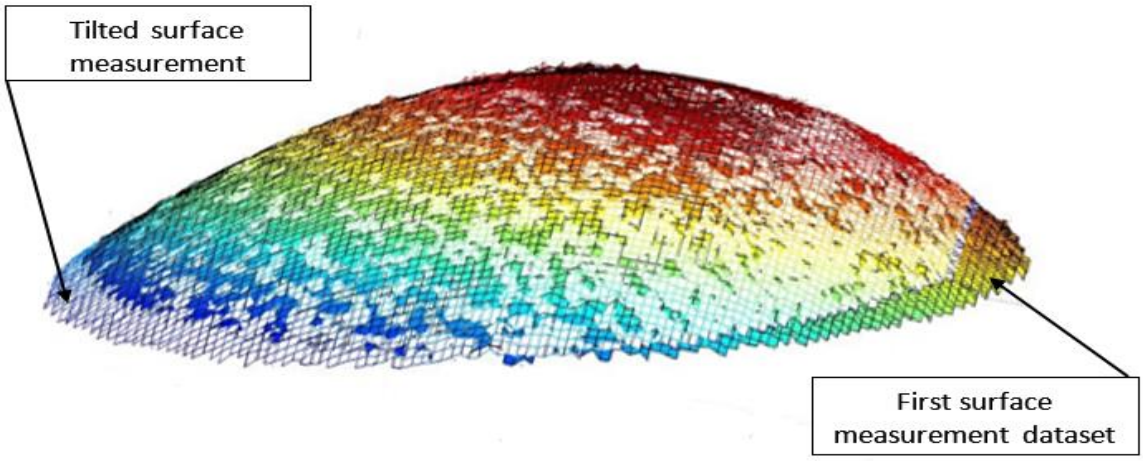

Figure 6. 13: First surface measurement dataset was stitching together with the tilt surface dataset

Figure 6.11 indicates that there is a lower noise at the centre region of the surface compared to other regions. Similarly, smaller values of difference in *z*-position in Figure 6.12 are found at the central region of measurement data image. It also worth noticing that there is a greater height difference at the edge of the measurement data. This region however is not an interest of this study as it is in the non-overlap region where the interpolation data are not accurate (the interpolation process will be further described in section 6.4.2). This noise is not the measurement noise which has been discussed in section 6.2.1 as the noise level at other regions of the surface are in the order of hundreds of nanometres which is too big for the measurement noise cause from instrumental scale of the CSI instruments. This noise resultant from this preliminary testing is related to the sample specific error in CSI measurement.

To investigate this noise, further experiments were designed and carried out with two different series of measurement data. The series of measurement are described as follows:

(i) The first measurement of the first series started similarly to the previous preliminary measurement where the centre of field of view (FOV) is located on the centre of circular fringes. After that a series of datasets were taken by translating the objective lens in the *x*-direction so that the centre of FOV was no longer aligned on the centre of the circular fringes. Several measurements were taken at different locations on the microsphere surface. In this work, the chosen locations were at the distance of 4 µm, 25 µm, 50 µm and 80 µm between the centre of FOV and the centre of circular fringes. The rotation and tilt angle were not applied in this experiment.

(ii) Similar to experiment (i), the first measurement of the second series was located with the center of circular fringes aligned to the centre of FOV. Subsequently, at the same location, a measurement dataset was taken when the sphere was tilted with small tilting angle (approximately less than 2˚). Then both these measurement datasets were stitched together. This experiment continued by repeating such pairs of measurement and stitching process at different locations on the sphere surfaces. The chosen locations were at the distance of 4 µm, 25 µm, 50 µm and 80 µm between the centre of FOV and the centre of circular fringes.

The design of both series of measurements is based on an initial prediction that the higher noise level region in the surface plots may arise from the surface slope angle error and multiple reflection error. Therefore, when the centre of FOV is shifted from the centre of circular fringe which is also at the highest point of the spherical surface, the region having a low level of noise is expected to be translated from the centre of the spherical surface. This is because, the measurement data is taken at the condition where the centre of FOV is focusing on the surface regions that have higher slopes compared to the central surface region. Another possibility from this shifting activity is the region of lower noise at the centre might become smaller due to the information losses from multiple reflection phenomena.

The results for surface condition after form removal and thresholding process of the first series of measurement are represented in Figure 6.14, Figure 6.15, Figure 6.16, and Figure 6.17 while Figure 6.18 illustrates the results in terms of measurement profiles taken across the centre of each of the surface datasets. Each of these profiles represents surface regions taken from different locations. In Figure 6.14, the lower-noise region is slightly shifted compared to the similar region in Figure 6.11 (where the data is measured at the centre of FOV), while another new region of noise level is growing in Figure 6.15 , Figure 6.16, and Figure 6.17. These results indicate that the higher noise occurred at the high gradient regions of the surfaces. Similarly, the same behaviour is found in height profiles in Figure 6.18 . Figure 6.18 (a) shows the measurement profile when the centre of FOV is measuring the centre of circular fringes (a profile through the measurement data in Figure 6.11). As the centre of FOV is shifted from centre of circular fringe, a lower noise region of the profile starts gradually to increase in gradient, as shown in Figure 6.18 (b), (c), (d) and (e) which is a profile through the measurement data in Figure 6.14, Figure 6.15, Figure 6.16, and Figure 6.17.

These measurement profiles seem similar to the profile of a measurement of a V-groove [161] where the higher noise occurs at both ends of the profile due to the high slope angle of the side wall surface.

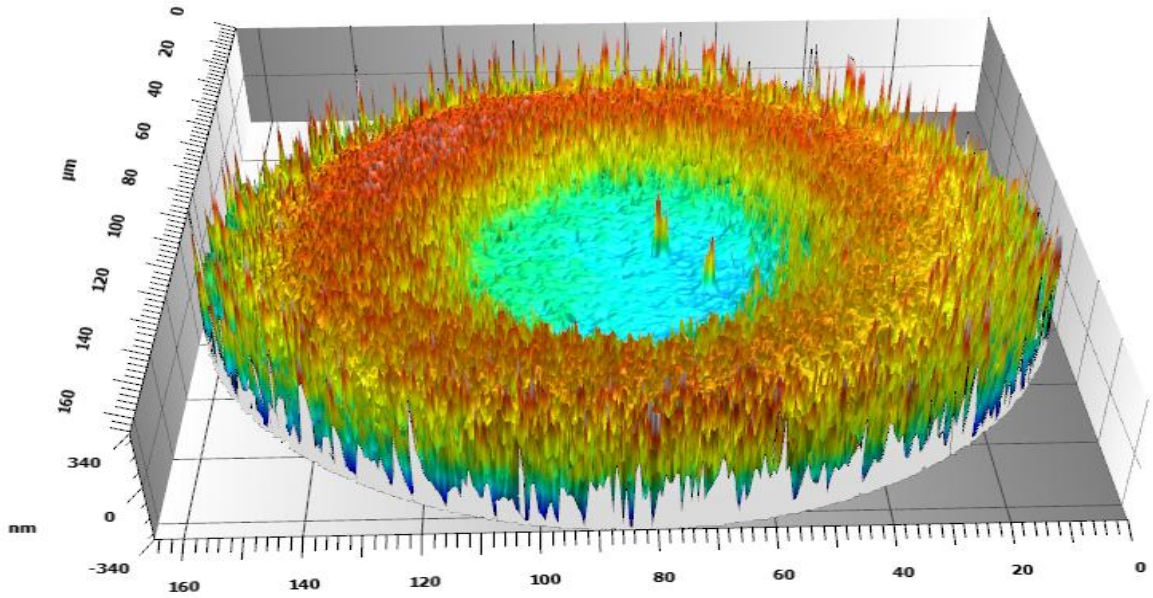

Figure 6. 14: the topography of measurement result of sphere surface, after removing form and applying height thresholding, which is similar to that in Figure 6. 11 , but taken at a location where distance between centre of FOV and Centre of circular fringes is 4 µm

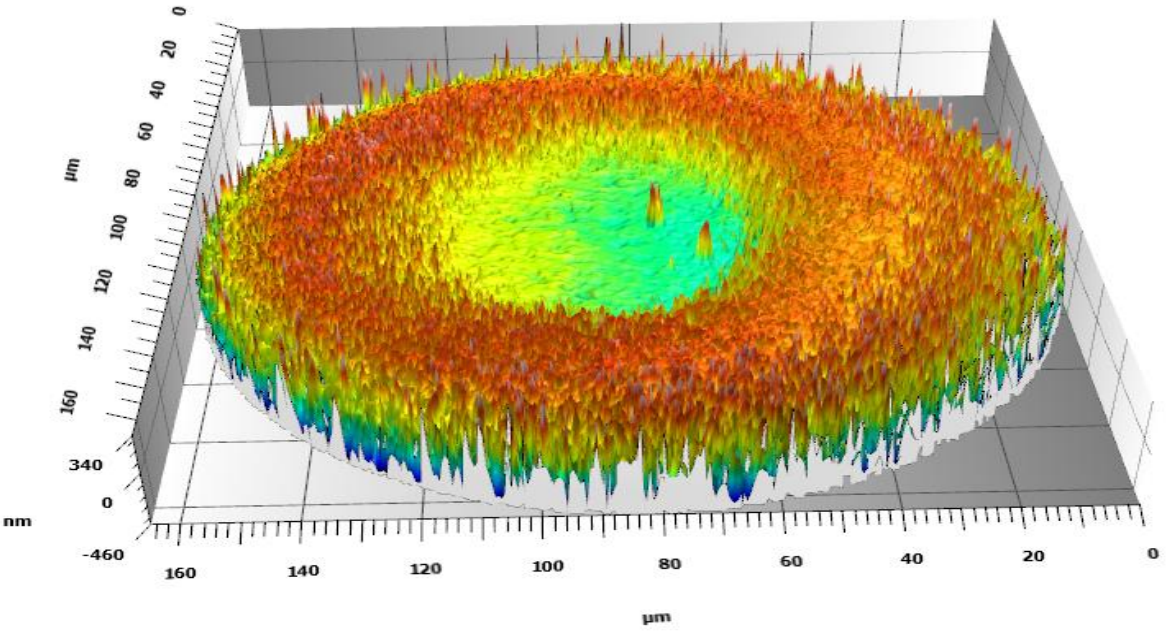

Figure 6. 15: The topography of measurement result of sphere surface, after removing form and applying height thresholding, which is similar to that in Figure 6. 11, but taken at a location where distance between centre of FOV and Centre of circular fringes is 25 µm

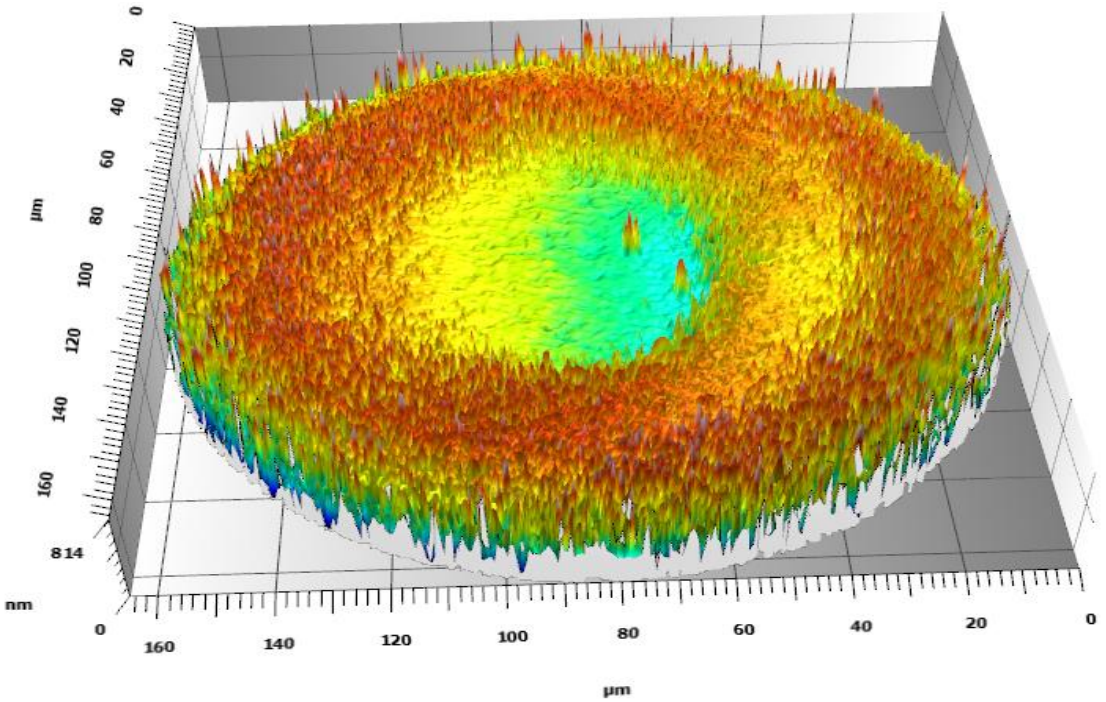

Figure 6. 16: The topography of measurement result of sphere surface, after removing form and applying height thresholding, which is similar to that in Figure 6. 11, but taken at a location where distance between centre of FOV and Centre of circular fringes is 50 µm

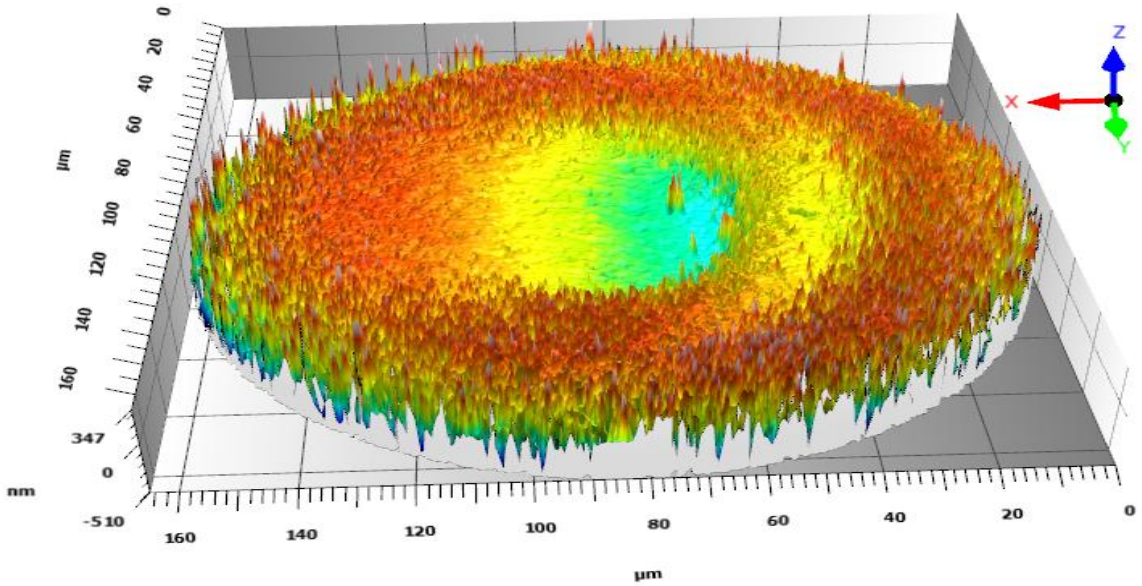

Figure 6. 17 : the topography of measurement result of sphere surface, after removing form and applying height thresholding, which is similar to that in Figure 6. 11, but taken at a location where distance between centre of FOV and Centre of circular fringes is 80 µm

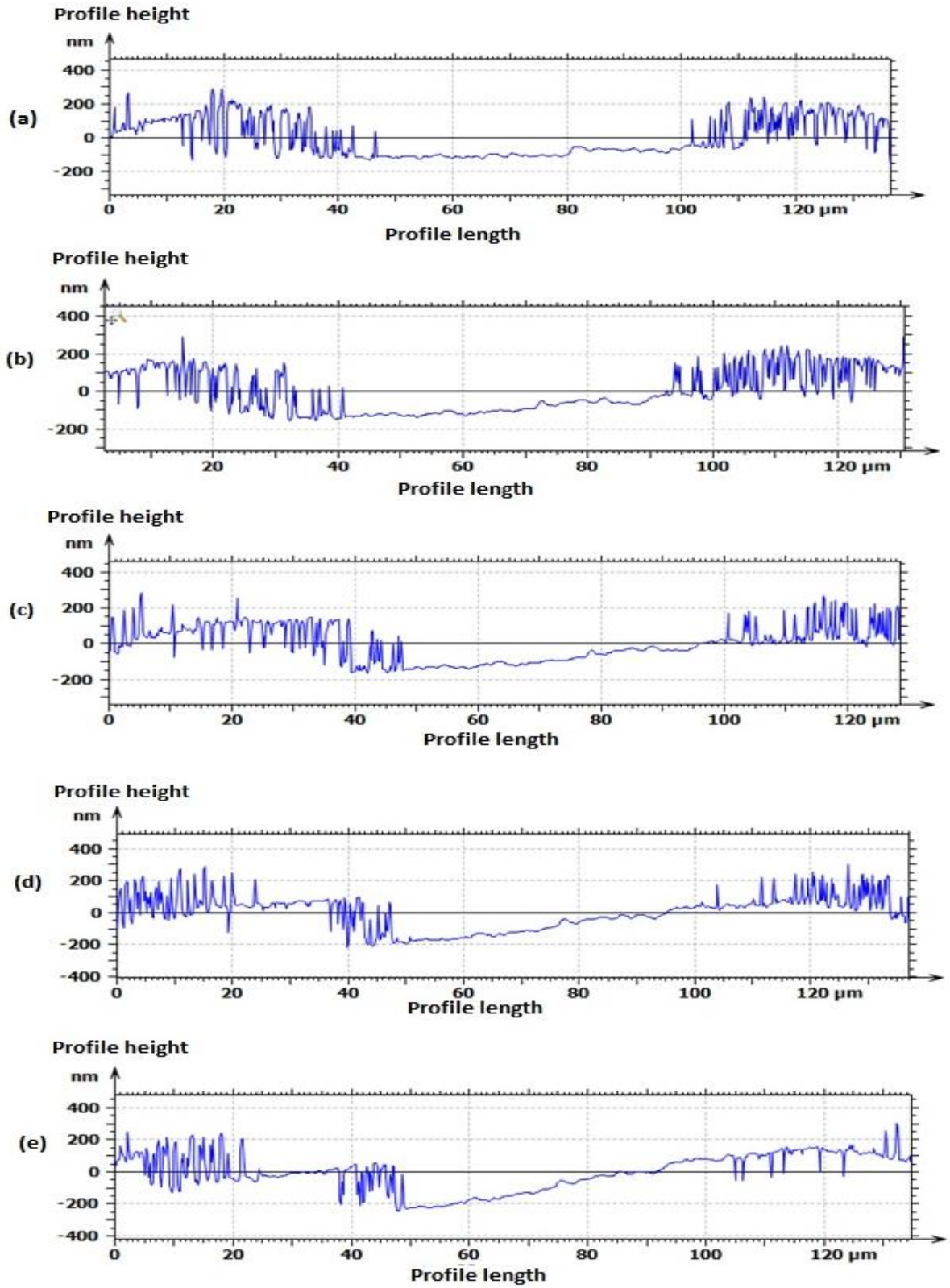

Figure 6. 18: The height profile across the centre of the measurement data image (a) The height profile of the surface measured at the location where the centre of FOV is aligned at the centre of the circular fringes. (b), (c), (d), and (e) are the height profile of the surfaces measured at the location where the distance between centre of FOV and centre of the circular fringe are 4 µm, 25 µm, 50 µm, and 80 µm.

The second series of measurements was intended to observe the behaviour at different locations between two measurement surfaces dataset (datasets at position where no tilting angle is applied and position where only small tilting angle applied) during stitching process. As explained previously, these two measurement surface datasets were measured at the same location of sphere where one of these measurements was taken without any tilting or rotating angle applied while other measurement was taken with the presented of a small tilting angle. Similar to the first series of measurement, before stitched both measurement surface data, the form removal and the height thresholding were applied to the measurement data. These results are shown in Figure 6.19, Figure 6.20, Figure 6.21, and Figure 6.22 where the surface was measured at the location where the distance between centre of FOV and centre of circular fringe was 4 µm, 25 µm, 50 µm and 80 µm. Comparing these images to Figure 6.12, where the surface was measured at the centre of the circular fringes, shows a similar trend in behaviour with the first series of measurements. The lower height different (or lower noise) region is translated when the surface is measured at the location away from the centre of circular fringes.

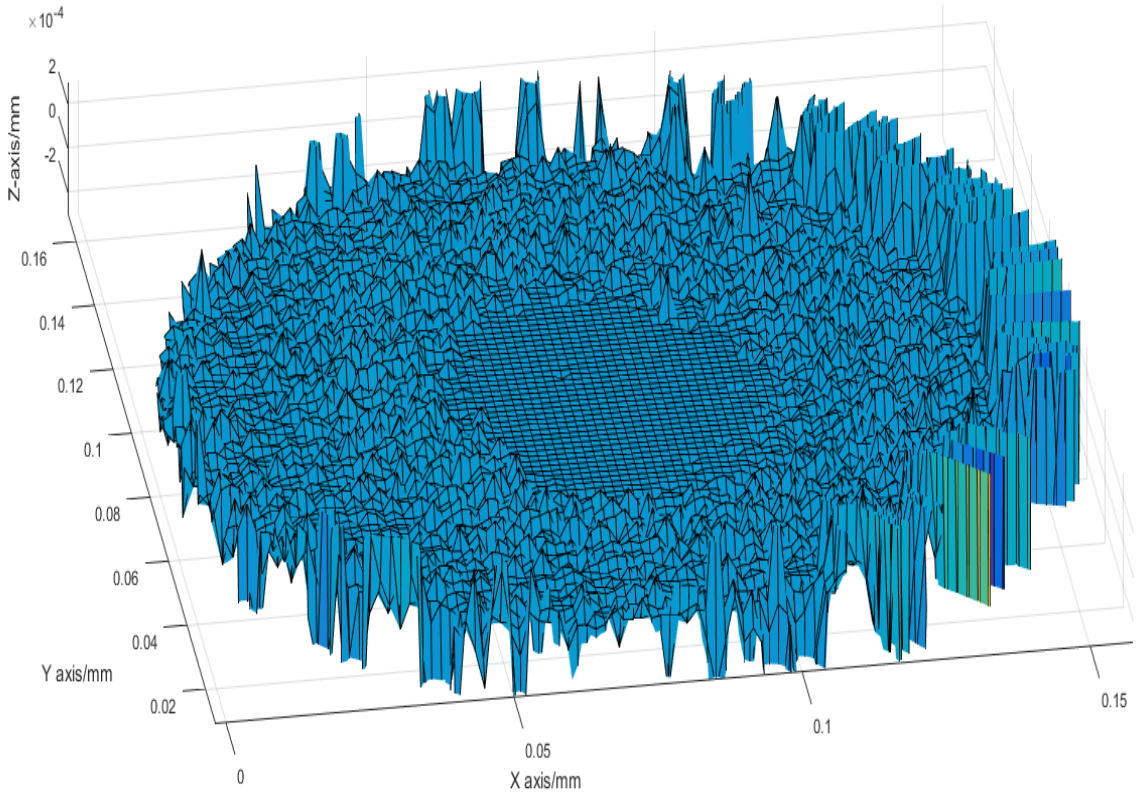

Figure 6. 19: Topography of height different of a stitched surface dataset , after removing form and applying height thresholding, which is similar to that in Figure 6. 12, but taken at a location where distance between centre of FOV and Centre of circular fringes is 4 µm

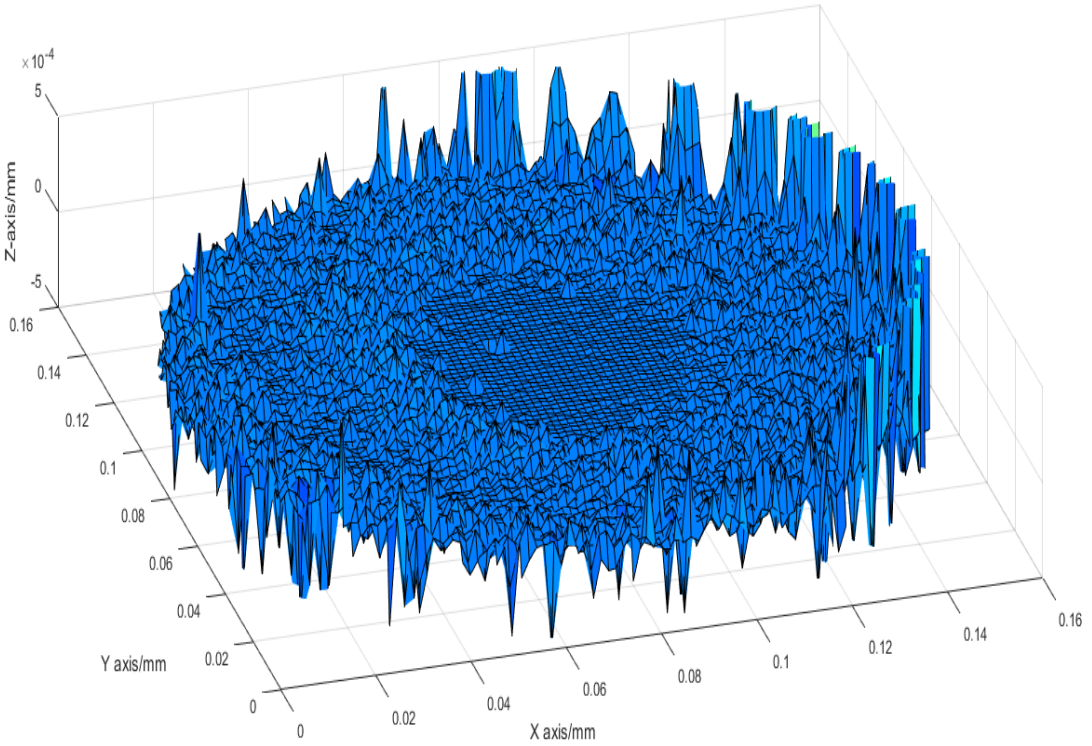

Figure 6. 20: Topography of height different of a stitched surface dataset , after removing form and applying height thresholding, which is similar to that in Figure 6. 12 , but taken at a location where distance between centre of FOV and Centre of circular fringes is 25 µm

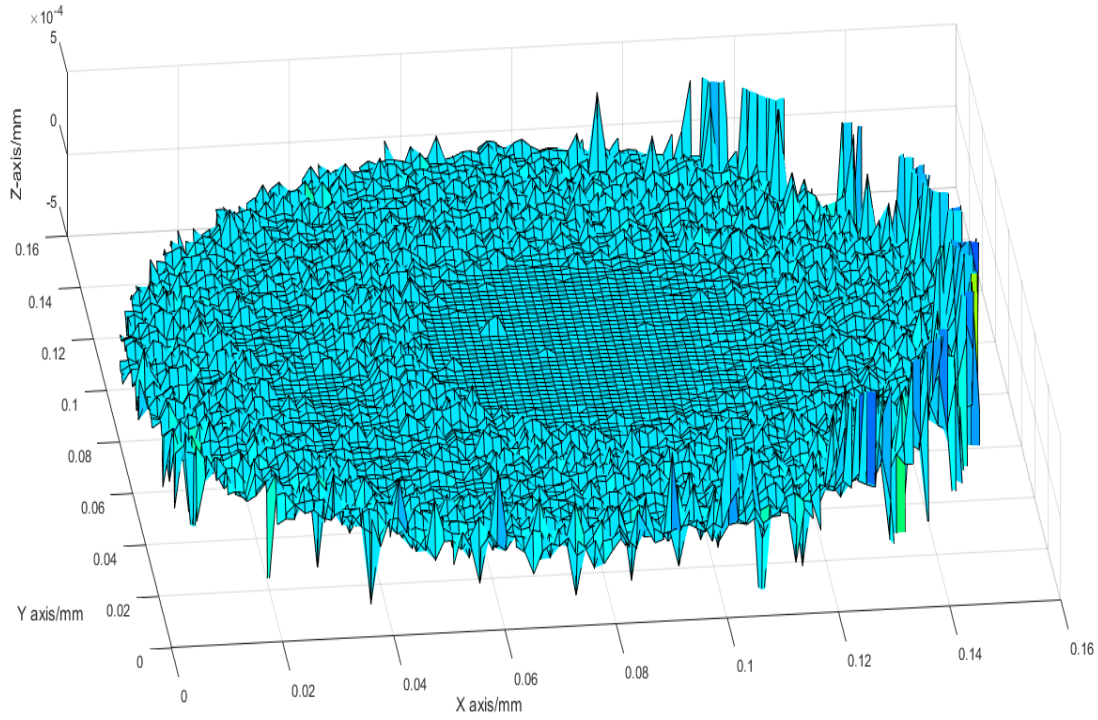

Figure 6. 21: Topography of height different of a stitched surface dataset , after removing form and applying height thresholding, which is similar to that in Figure 6. 12 , but taken at a location where distance between centre of FOV and Centre of circular fringes is 50 µm

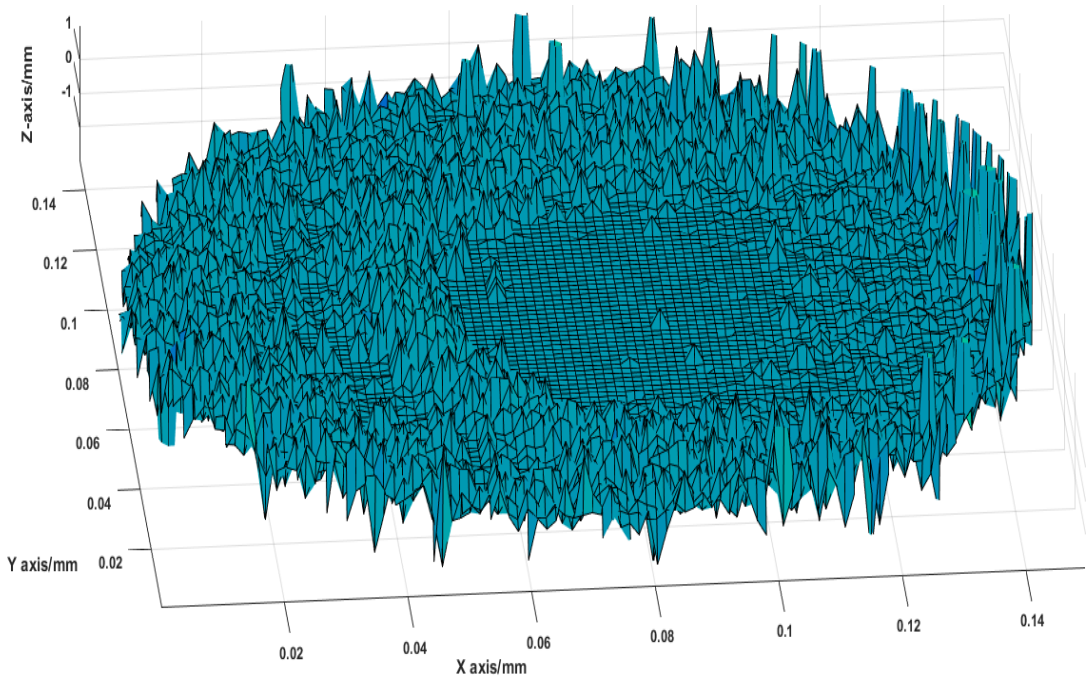

Figure 6. 22: Topography of height different of a stitched surface dataset , after removing form and applying height thresholding, which is similar to that in Figure 6. 12 , but taken at a location where distance between centre of FOV and Centre of circular fringes is 80 µm

From these two series of measurements, it can be observed that the higher noise levels seen in the surface datasets are caused by the high slope angle of the surface, which leads to the loss of information in the sensor. Based on the optical characteristics of CSI instruments, there is also a possibility that the higher noise level at the edge of the FOV is caused by the lateral distortion of the instrumental scale. Several other researchers [164][165] have observed that such lateral distortion in optical topography instruments causes measurement error at the edge of the FOV. Therefore, on the basis of these series of measurements, the procedure for further measurements in this work was modified with extra constraints. Measurements were conducted only at the location where the centre of the FOV is aligned on the centre of circular fringes and only regions with lower noise were to be considered in the stitching process for mapping the entire microsphere surfaces. Regions with higher noise level were cut and excluded in the post-measurement process

6.3.5 Decision in selection of parameter for experiment

From the finding of preliminary measurement in section 6.3.4, the measurement parameters which have been discussed in section 6.3.1 can now be specified. Referring to equation (6.4), the d_{spot} *(*diameter of the region that has been measured by CSI) can be considered as the region with lower noise observed in these results. Thus, as shown in Figure 6.18 (a), the value of d_{spot} can be estimated as 50 µm. The area of overlap region will also effect the total number of measured datasets needed to cover the measurable section of the surface of the sphere. More measurements will need to be obtained when the overlap region between adjacent surface data is bigger. In this experiment, to be safe, it is intended to have a larger area of overlap region and thus a 40% of overlap region selected in the calculation as this value is sufficient to ensure that two adjacent surface data had been stitched together. Another important parameter is the steps in the tilt angle between measurements, which can be calculated using equation (6.4). The resultant value from this calculation is 11.5˚. Similarly, from the equation (6.6) to equation (6.8), the calculated value of the rotation angle, is 68˚. Nevertheless, as a precautionary step and also considering the limitation of the tilting and rotating stages, it was decided to apply somewhat smaller tilting and rotation angles. For the further actual measurements in this work, a tilting angle of 8˚ and rotation angle of 30˚ were selected. The parameters for all further measurements (except if otherwise stated) are summarised in table 6.1.

Table 6. 2: Summary of measurement parameter

Measurement parameter	Value
Magnification of objective lens	50x
Diameter of the region measured by CSI	Region with lower noise level in surface (approximately 50 µm)
Tilting angle	-23˚, -15˚, -8˚, 0˚, 8˚, 15˚, 23˚
Rotation angle	0˚, 30˚, 60˚, 90˚, 120˚, 150˚
Number of measurements	42

6.3.6 Measurement procedure

The measurement procedure can be explained as follows:

a) For the start, the angle of rotation stage was set carefully to its 0˚ position (no rotation along z-axis is applied).
b) After ensuring that the test workpiece was levelled and no angle applied in internal stage of the CSI, the test workpiece was first tilted using the external tilting stage to the angle of -23˚(the maximum angle the micro-sphere can tilted at). It was also crucial to ensure that the test sample could not hit or approach too closely to the objective lens. If there was a risk of this happening, the initial tilting angle was reduced.
c) The objective lens of the CSI was focused on the reference flat until the optimum fringes were found at the location of the reference flat. Then, three repeated measurements on the reference flat were taken and the output data saved in the host computer
d) After that, by using the *x, y* and *z* stage, the CSI was focused on the surface of microsphere underneath the objective lens. The location of the surface was determined by finding the best contrast circular fringes concentric to the image of the sphere surface which appeared within the FOV and then three repeated measurements were taken.
e) These procedures had to be carefully conducted in order to ensure that no part of the external manipulation stage and the test workpiece ever touch the objective lens. The tilting angle should be reduced if there any possibility of hitting the objective lens. This is because the objective lens is very sensitive and readily damaged.
f) The measurement procedure continued by reducing the tilting angle to -19˚ (or maybe less). This means that a different location on the surface of microsphere was placed underneath the objective lens. This position was then measured by the CSI.
g) The same procedure from steps (c) to (e) above was then repeated.
h) Then, the above procedures were repeated with each different tilting angle. The remaining tilting angles were -15˚, -8˚, 0˚, 8˚, 15˚, and 23˚
i) The measurement then proceeded by rotating the test workpiece about the *z*-axis using the external rotation stage to an angle of 30˚. The CSI was focused on the

reference flat, specifically on the edge of gauge block to include the reference mark/point and three repeated measurements taken.

j) Then, the procedure (b) until (h) was repeated.

k) After that, the above procedures were repeated with different rotation angles. The remaining angles were 60˚, 90˚, 120˚, and 150˚.

l) All the output data had then been collected and was ready to be analysed.

6.4. Post-measurement data processing- Architecture of stitching algorithm

In this section, the workflow process of the stitching algorithm will be explained in detail. As summarised in Figure 6.23, this explanation will be based on a common process flow in data fusion which can be categorised as pre-processing, registration process, data fusion process and post processing. The stitching strategy is governed by the measurement procedure. For each of the rotation angles used, there are several measurement surface datasets obtained from several tilting angles. Therefore, all of the microsphere surface datasets from one rotational orientation will be firstly stitched together and then these stitched surface data from each of the rotation angles will be registered and combined together to build the topography of the surface for microsphere.

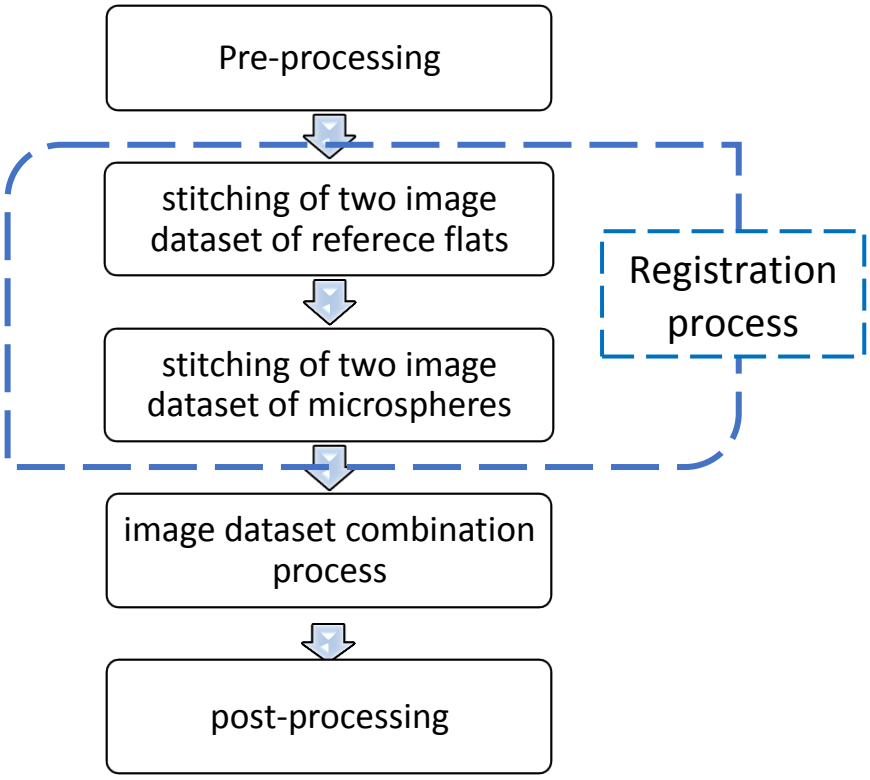

Figure 6. 23: Process workflow of stitching algorithm during post-measurement data processing

6.4.1 Pre-processing – Data processing of measurement results

The 3D stitching technique starts with pre-processing of the measurement results. The raw data from the CSI instrument's software is saved in *.txt* files and transferred to the Matlab® software environment, which is used to conduct the stitching and data fusion processes. Prior to this, as described in section 6.3.4, the quality of each of measurement data is examined and only region with lower noise will be used for further processing. For the microsphere measurement data, there was a consistent tendency for this lower noise region to cover 36% to 40% from the centre of the field of view.

6.4.2 Registration process

Registration is the process that brings adjacent surface datasets to a common coordinate system. Then, the alignment process of the surface data is important so that the overlapping region of two adjacent surface datasets can be located closely together, and hence the 'stitched error' at the overlapping regions can be determined. The stitched error indicates the distance between both surfaces and hence specified the quality of stitching process. At the overlapping region, both surface datasets shared the same ordinate values in the *x* and *y* axes but were generally different in the *z* axis. In principle, when the different in *z*-axis between both surface datasets is small, it indicates that both surfaces had been aligned closely to each other. In this project, the stitching error is defined by the average of the absolute value of the difference in z-coordinate values of the surfaces in the region where they overlap.

In this stitching algorithm, there are two parts to the registration process: the reference flat and fiducial marks are used to generate a rotation matrix to put the surfaces into the correct orientation in a common Cartesian coordinate system and then a translation of one surface with respect to the other is carried out to minimise the difference between the surfaces in the region where they overlap.

Registration of reference flat to find the tilting and rotation angle

As explained in measurement procedure in section 6.3.6, a set of rotations and tilts where applied to a workpiece, which consists of a micro sphere attached to a reference flat, such as to allow a large portion of its surface to be measured. For the simplification of the

next discussion, although there is only had one measured workpiece, each of this measured image dataset shall be viewed as separated independent measured workpiece. Figure 6.24 illustrates the measured image data from the two reference flat positions, one tilted with respect to the other. The tilt angle between the two measurements is calculated from the reference flat. A vector normal to the reference flat is calculated for each position, with the angle between these vectors corresponding to the rotation of the surface. The normal vector is obtained from the cross product of two non-parallel vectors generated from three points that lie on the surface, making sure that the vector points out from the surface in principle, this calculation of a normal vector requires the surface to have a high flatness, and otherwise an error will be introduced in the calculation. Nevertheless, this calculation method can be improved by calculating several other normal vector at different points and regions on the same surface and then averaging them for the final value.

For this task, the orientation of the flat when the tilt stage angle is zero is selected as the reference plane and hence the tilting angle of other measurement surfaces will be calculated based on this reference plane. The Matlab® code for this work is explained in Appendix A1. The rotation matrix that was generated was verified as correct by checking that after it is applied the two-surface normal are parallel. In theory, both planes should be parallel and the angle between them should be zero. Similarly, the same calculation method is applied to the rotation angle (rotation along z-axis) between two flats which is calculated according to their reference mark as shown in Figure 6.25.

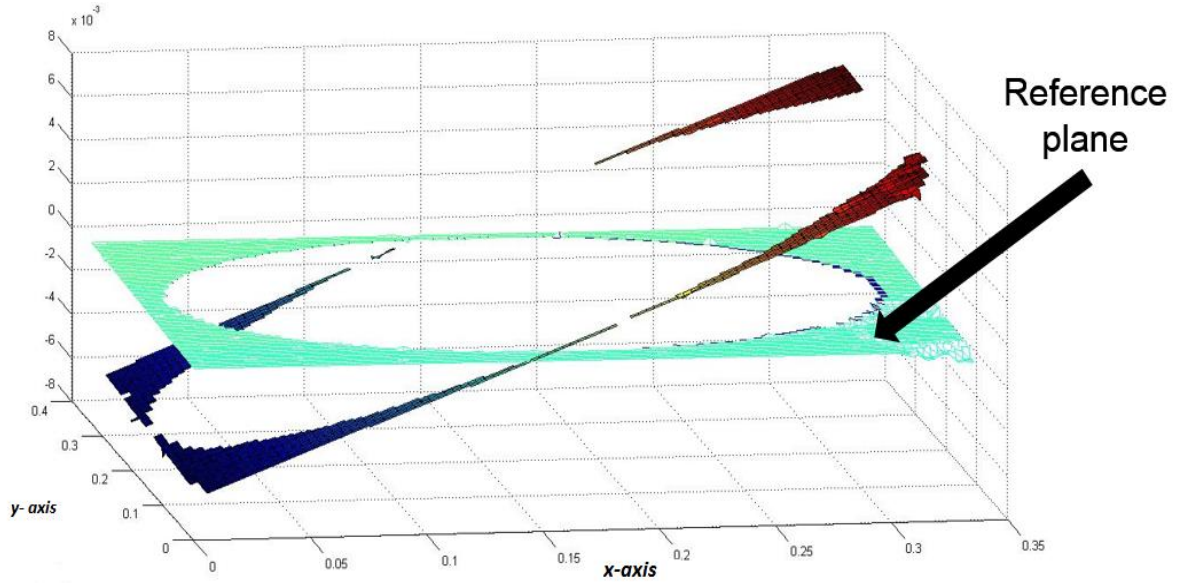

Figure 6. 24: the angle between two positions of flat surfaces, one position is when there is no tilt angle applied and other position having a tilt angle applied to it by the tilt stage

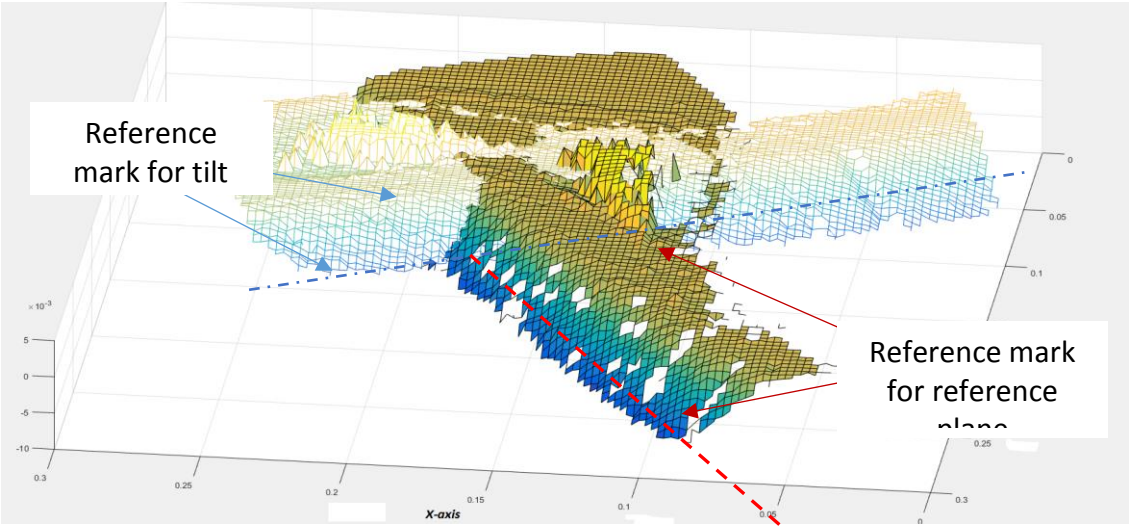

Figure 6. 25: the rotation angle is calculated based on the both reference flat by referencing the both reference mark

- ***Registration for surface of microsphere***

The second part of the registration task is the translation of the surfaces so that the difference between the surfaces in the overlap region is minimised (we can call one image dataset as 'reference surface' and other as 'tilted surface', to make simpler explanation in next discussion). To start the stitching process, both measured microsphere image datasets are aligned and brought closely together. Then, the overlap regions can be determined. This alignment is similar to the technique of *iterative closest point* (ICP) [199][200][201]. This stitched error is defined by an average of the absolute value of spacing in the *z*-values across the overlapping region. It can be minimised by translating one of the surface in *x, y* and *z-axis* as illustrate in Figure 6.26. The smallest value of stitched error is sought and reported in this task.

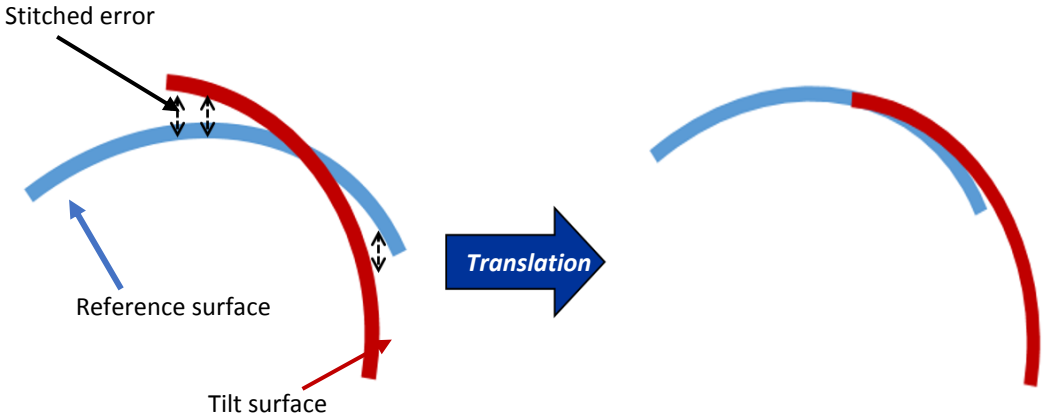

Figure 6. 26: 2D conceptual image of stitching of two surfaces. Translating in x, y and z-axis of tilt surface will minimise the stitched error and hence bring both surface close together

The stitched error is calculated using a method called sum of the absolute difference. As the *z*-coordinate is a function of *x*- and *y*-coordinates, the absolute difference in the *z*-positions of points within the overlap regions is a main interest in this calculation. Before the stitched error is calculated, the tilted surface is interpolated so that its *z*-positions can be estimated at the x and y positions of the reference surface. The Matlab® code for computing the stitched error is explained in detail in Appendix A2.

The Matlab® function '*scatterinterpolate'* is used to interpolate the data of the tilt surface. This interpolation step is crucial to be applied in this algorithm so that for each of position of *x* and *y* coordinates in overlap region, there are two slightly different *z-co*ordinates. The calculation of stitched error is then based on the differences in these pairs of z values. However, before starting this interpolation process, an overlapping region is determined and non-overlapping regions of both image datasets are excluded in this process. This is because, by using the Matlab® function '*scatterinterpolate'*, an error in the result will occur at the non-overlap region (this function is proposed to interpolate the data of a surface according to a second surface, at the non-overlap region where there is only one surface this Matlab function will not operate as intended and is unable to produce an accurate interpolation result). Therefore, the overlap region of both surfaces needs to be determined first. In this algorithm process, alignment and manipulation of the tilt surface is conducted in two stage: a coarse alignment is then optimised by using a fine alignment. Coarse alignment involved low resolution steps of translating the microsphere image dataset in *x,y* and *z* coordinates while fine alignment employed higher resolution step, but only over a small area of interest already identified by the coarse steps. In this stage of alignment, an overlap region between both measured image dataset is defined and the interpolation data and stitched error are determined. Finally, the translation of this step is stopped when the smallest value of stitched error in the overlap region is determined and the registration algorithm process is completed by reporting the smallest stitched error. The stitched error indicates the error for the new *z*-position which is applied in the evaluation of uncertainty of measurement.

6.4.3 Combination process of measured surface datasets

After the registration process, where the two surfaces are brought together, the next process is data combination of all measured surface dataset. In this process, the two surfaces will be combined to become one surface. The *z*-coordinate is a function of the *x*- and *y*-coordinates for each of the surfaces and the previous registration process has brought them both to share common x and *y* coordinates. Hence, two positions in the *z*-coordinate have been obtained at each *x*-y coordinate. To combine both surfaces at their overlapping region, each position of *x*-*y* coordinate must have only one position of z-coordinate. With the intention of combining these two position in *z*-coordinate to become one position, in general, estimation methods using statistical approaches such as mean value and weighted least squares have been used in much research that involves 2D and 3D stitching techniques [207] [215][216][217][218]. However, these statistical methods will create 'modified surface data' in the overlap region. This modified surface data is not an actual measure surface dataset but have indirect relationship toward two measured surface datasets that have been stitched together using statistical calculation.

In this work, a new fusion technique for stitching surface data is introduced. This technique is intended to eliminate the modified surface data at the overlap region. By doing this technique, only actual measured values form the surface datasets from the CSI are stitched and combined together to make the full surface topography map of the sphere. This new fusion technique is done by combining three surface datasets; the first and second surface datasets are the surfaces that are intended to combine together while the third dataset is from the surface measured at a location between them. For instance, consider when the first surface data are taken as the reference, measured at the tilt angle is 0˚, while the second surface data is measured at the tilt angle of 10˚. Then, the third surface data is obtained at the location where the tilt angle is about 5˚. The first and second surface data are stitched together and translated in order to obtain smallest stitched error. At this stage, the overlap region has been determined. Then both of these surfaces are temporarily combined using the mean value between their two positions in the *z*-coordinated. The important next step involves stitching this combined surface with the third surface, again using the registration process described above to find smallest stitched error. The third surface is intended to cover the overlap region and hence eliminate the modified surfaces data. Finally,

the whole area of third surface is involved when combining the surface datasets. Hence, the final combined surface dataset consists the whole surface dataset of the third surface and the non-overlapping region of first and second surfaces. Figure 6.27 summarises this new fusion method.

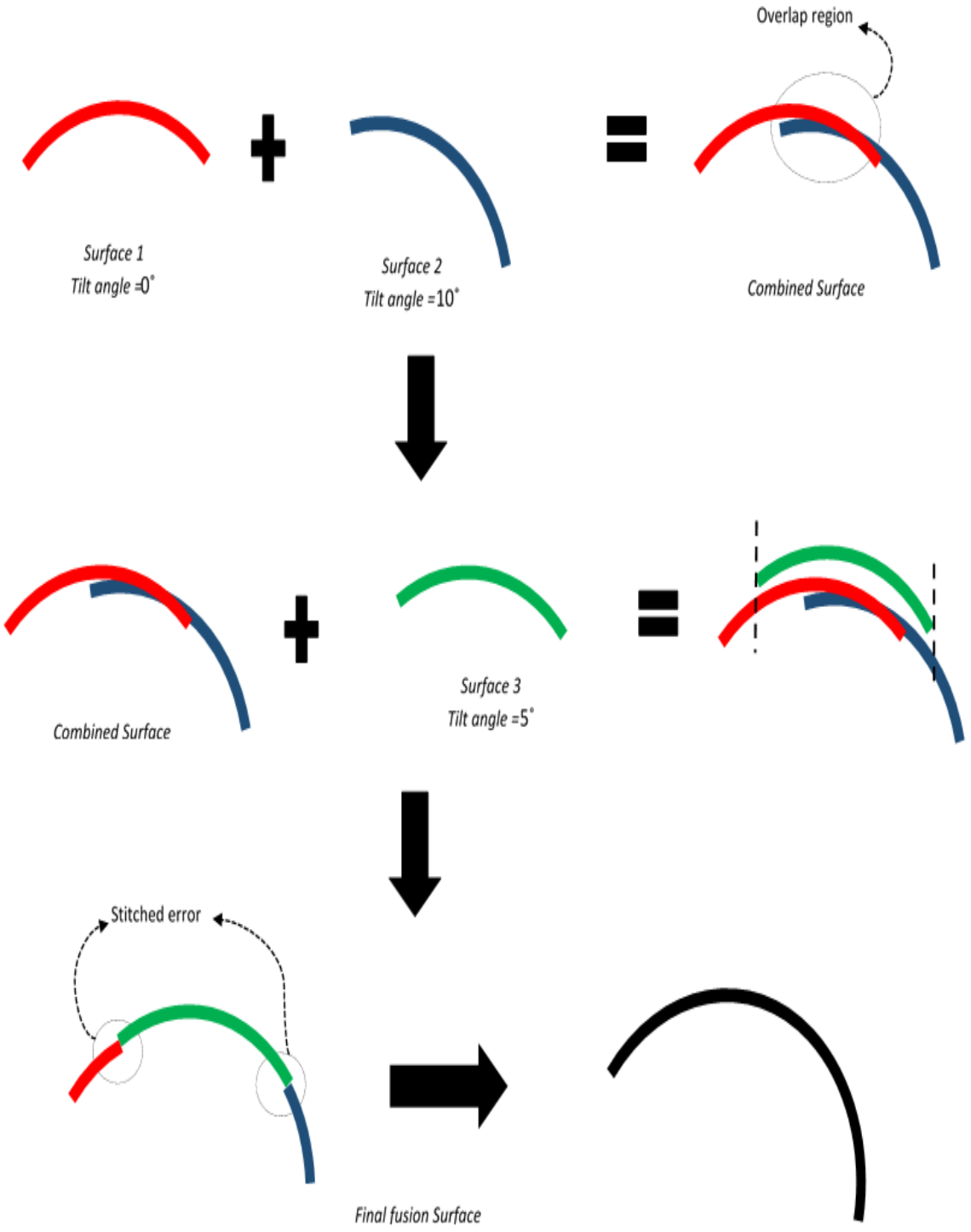

Figure 6. 27: 2D conceptual image for new technique of fusion process between 2 surfaces

6.4.4 Post-processing of data fusion

The dataset for the new surface segment is saved in a *mat.file* and a *txt.file*, ready for use for other purposes such as the next stitching process with other adjacent surfaces and transferring to other metrological software for validation with other techniques and for determining the sphericity.

6.5. Presentation and discussion of results

This section presents the measurement results from this work. It describes the development of the topography of the entire surface resulting from 3D stitching processes across the whole of the accessible region of the microsphere. The evaluations of stitched error for each individual stitching process and repeatability error of every measurement are presented and discussed. Finally, the sphericity of entire stitched surfaces is determined.

6.5.1 Topography of fusion surface and result of stitched error and repeatability error

As explained in section 6.2.2 and section 6.4, the topography of the entire measured surface dataset is developed by measuring smaller overlapping areas of the surface data at different locations around the microsphere and then using a 3D stitching process. The flow of this process is illustrated in detail in Figure 6.28. The process begins by combining two adjacent tilted surface datasets using the new fusion technique describe in section 6.4.3 (and illustrated in Figure 6.27). This process continues, using the already combined data as the reference, until all tilted surfaces under same rotation angle are completely combined. The same process is done to the other sets of tilted surfaces in other rotation angles. Then, the combined surfaces under different rotation angle are stitched together until the entire measured surface is combined.

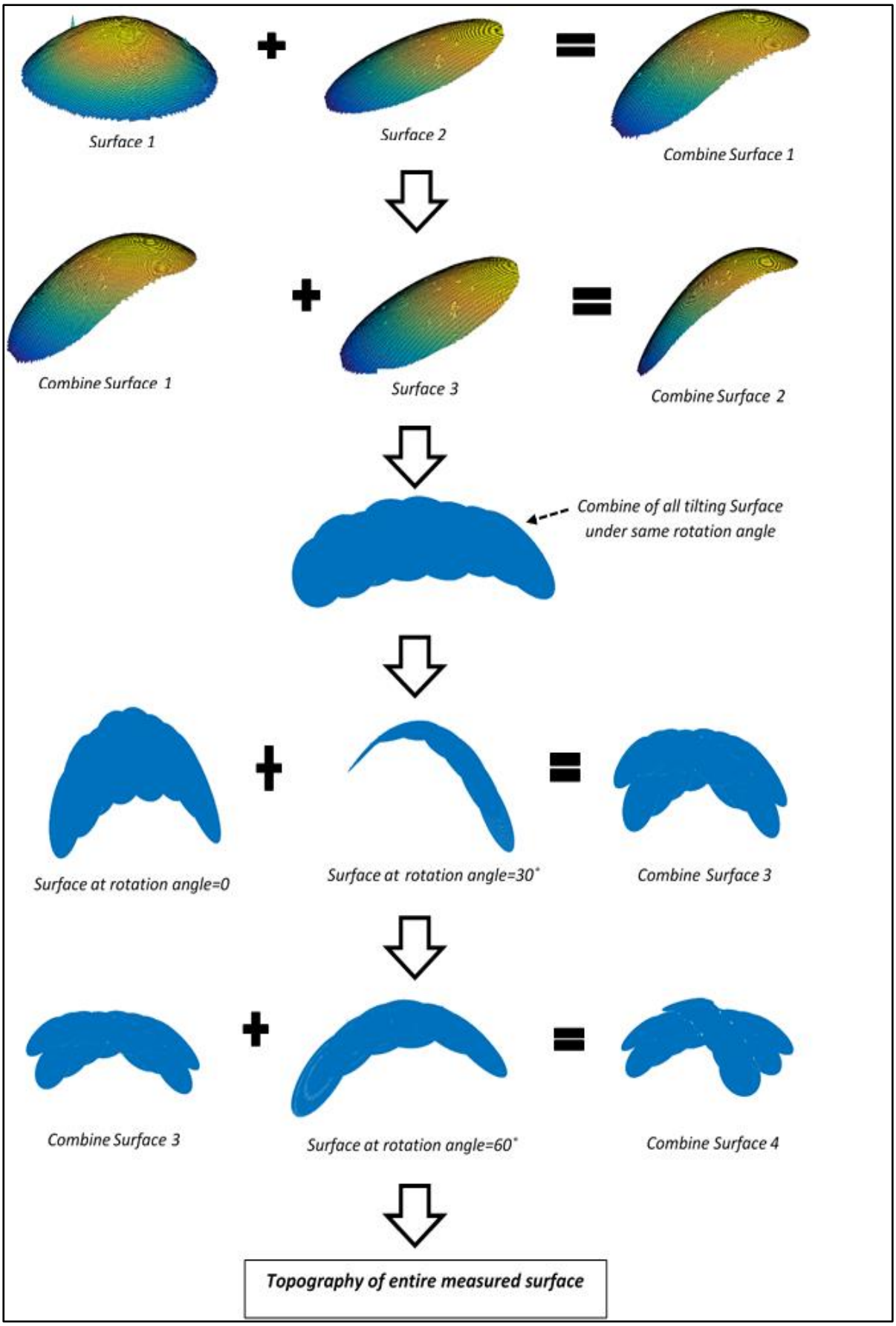

Figure 6. 28: process flow for mapping entire measured surface dataset using data stitching and combined process

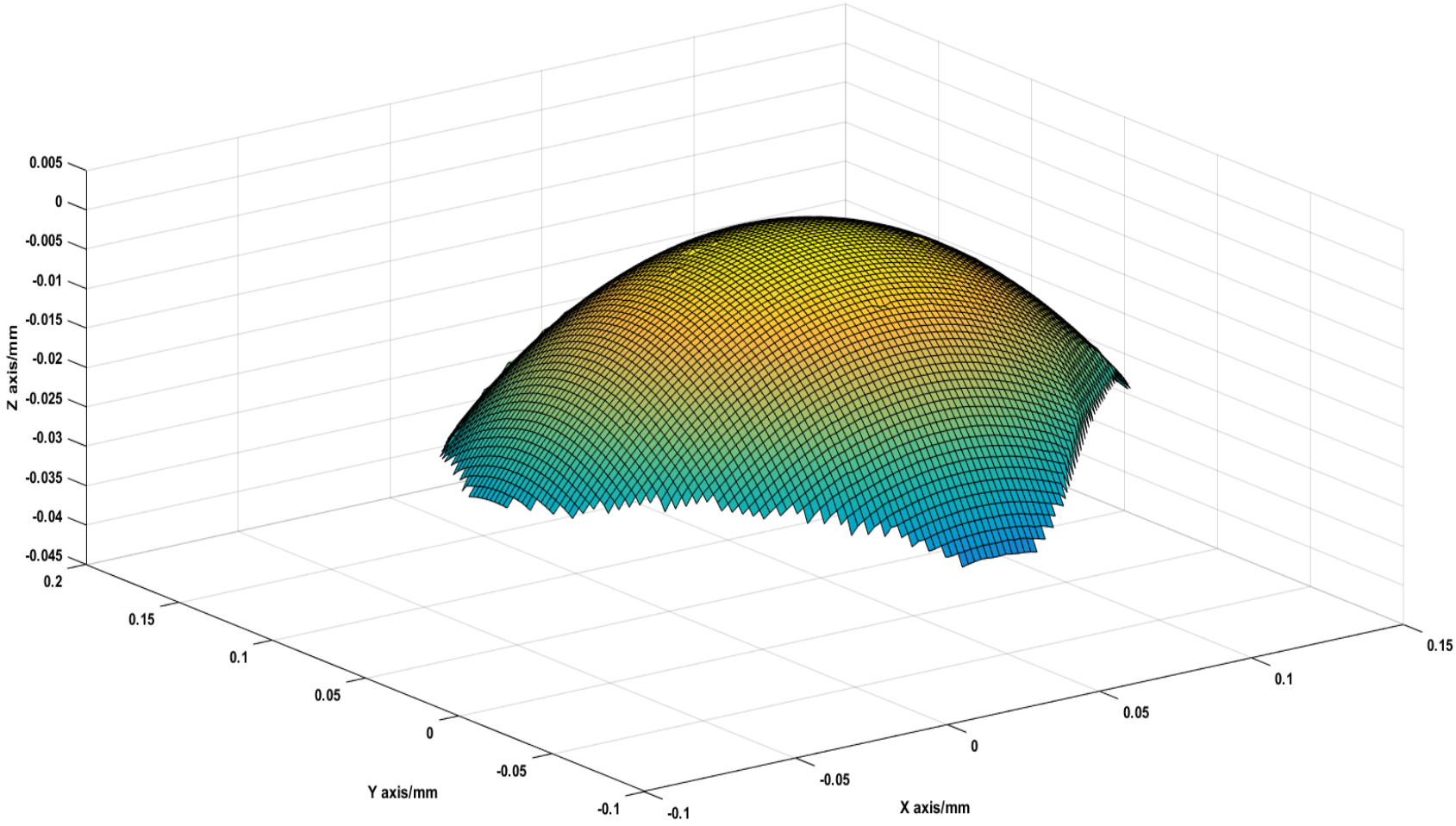

Figure 6. 29: Topography of entire measured surfaces resultant from stitching process

The topography of an entire measured surface is shown in Figure 6.29. It covers an area 0.15 mm square in the x-y plane. The spherical form error for this surface can be determined as will be discussed in next section.

The stitched errors at each location of the surface measurement are presented Table 6.3 and Table 6.4 while the repeatability errors at a single measurement location are illustrated in Table 6.5. As presented in Figure 6.28, surface A, surface B, surface C, surface D, surface E and surface F in Table 6.3 represent the combined datasets of entire tilt surfaces at rotation angles of 0˚, 30˚, 60˚, 90˚, 120˚ and 150˚. The stitched errors from the combination of these surfaces dataset are shown in Table 6.4. In all cases, they are calculated based on the fusion position in the real z-value positions at their overlap region, as explained in section 6.4.3 (with the fusion of surfaces based on the mean value between both positions). Meanwhile, the repeatability error is calculated from surface root mean square (similar to Sq parameter) of across repeated measurements. In this work, at each position two repeated measurement are taken.

Table 6. 3: Result of stitching error analysis for overall tilt surfaces measurement at rotation angles of 0˚, 30˚, 60˚, 90˚, 120˚ and 150˚

Combination Stitched surface between 3 tilt-surface	**Rotation 0˚**	**Rotation 30˚**	**Rotation 60˚**	**Rotation 90˚**	**Rotation 120˚**	**Rotation 150˚**
	Stitched error (nm)	Stitched error (nm)	Stitched error (nm)	Stitched error (nm)	Stitched error (nm)	Stitched error (nm)
Combined surface 1	*9.3*	*13.4*	*2.5*	*15.6*	*13.6*	*2.6*
Combined surface 2	*13.8*	*7.3*	*6.3*	*14.4*	*4.5*	*7.3*
Combined surface 3	*13.3*	*20.8*	*8.2*	*7.8*	*18.8*	*9.3*
Combined surface 4	*13.8*	-	*12.0*	*5.6*	-	*11.6*
Combined surface 5	-	-	*18.3*	*16.9*	-	-
Mean value	*11.9*	*13.9*	*9.4*	*12.0*	*12.3*	*7.7*
standard deviation	*2.0*	*6.7*	*6.0*	*5.0*	*7.3*	*3.8*
standard error of mean	*1.0*	*3.9*	*2.7*	*2.3*	*4.2*	*1.9*
Name of fusion tilted surfaces	surface A	surface B	surface C	surface D	surface E	surface F

Table 6. 4: Result of stitching error analysis for overall rotation surfaces measurement

Stitching between 2 surface		Stitched error (nm)	New name for fusion surface
surface A	**surface B**	*37*	surface AB
surface AB	**surface C**	*24.9*	surface BC
surface BC	**surface D**	*23.3*	surface CD
surface CD	**surface E**	*25.1*	surface DE
surface DE	**surface F**	*27.2*	All fusion surface
Mean value		*25.1*	
standard deviation		*5.5*	
standard error of mean		*2.5*	

Table 6. 5: repeatability error of each location of the measurement surface dataset. These errors are calculated from surface value of root means square (RMS)(Sq parameter) between surfaces .two repeated measurement were taken at each location

	Rotation 0˚	Rotation 30˚	Rotation 60˚	Rotation 90˚	Rotation 120˚	Rotation 150˚
individual measured surface	**Repeatability (Root Means Square (RMS) error)**					
	(nm)	**(nm)**	**(nm)**	**(nm)**	**(nm)**	**(nm)**
Tilt 0˚	*3.2*	*6.7*	*5.6*	*4.2*	*7.3*	*3.7*
Tilt (8˚)	*2.7*	*4.7*	*2.7*	*3.0*	*5.8*	*6.6*
Tilt (15˚)	*4.4*	*4.6*	**-*	*3.6*	*5.2*	*3.3*
Tilt (22˚)	*3.9*	*6.9*	*3.3*	*3.4*	**-*	**-*
Tilt (- 8˚)	*3.0*	*2.9*	*3.1*	*5.8*	*3.0*	*6.1*
Tilt (- 15˚)	*4.1*	*4.7*	*2.3*	*3.5*	*3.9*	*5.7*
Tilt (- 22˚)	*-*	*4.0*	*6.8*	*3.2*	**-*	*6.5*
Mean value	*3.5*	*4.9*	*4.0*	*3.8*	*5.0*	*5.3*
standard deviation	*0.7*	*1.4*	*1.8*	*1.0*	*1.6*	*1.4*
standard error of mean	*0.3*	*0.5*	*0.7*	*0.4*	*0.7*	*0.6*

*: repeatability at this position could not be obtained as only one measurement was taken.

The stitched errors can be considered as uncorrelated random errors. While some correlation might be expected between surface data in the stitching, because of the same process on surface of the same underlying microsphere, the individual noise, which is random, largely de-correlates them. There are two possible ways to analyse these results. The mean value of the results can be considered as the values of the stitched error and repeatability error. In contrast, the standard error of means indicates the dispersion of mean values and is normally used as standard uncertainty in considering the propagation of error when averaging has taken place. However, in this case, the stitched error defines the form deviation of the topography of the entire fusion surface, so its value should be used as the standard uncertainty of form error in sphericity measurement. Therefore, it might be wise to use the maximum mean value of stitched error and repeatability error, which are 25.1 nm (in Table 6.3) and 5.3 nm (in Table 6.4). Alternatively, due to the definition of sphericity of the surface itself, the maximum value of stitched error and repeatability error can also be considered as the standard uncertainty of the form deviation in the measurement which are 37 nm (stitched error of surface AB in table 6.3) and 7.3 nm (measured surface data location when rotation angle is 120˚ and tilt angle is 0˚) respectively.

6.5.2 Resultant sphericity of the surface

The spherical form deviation or sphericity for the entire topography of the surface can be determined using any well characterised sphere fitting model. As reviewed in Chapter 2, several common techniques of data fitting have been established to fit an ideal geometric reference to the data from which to determine the sphericity deviation of the surface. In this work, three distinct types of sphere fitting modelling were used: Gaussian least squares modelling; maximum inscribed zone; and RANSAC shape detection, as all of these data fitting types can been easily selected in the commercial software of coordinate metrology and point cloud processing. The sphericity deviation was calculated using the commercial 3D GOM Inspect software [219] and CloudCompare software [220] . The results are presented in Table 6.6.

Table 6.6: The results of sphericity deviation using three types of sphere fitting modelling

Type of data fitting modelling	Radius of sphere fitting estimation (µm)	sphericity deviation (µm)	standard deviation (µm)
Gaussian least square	199	1.9	0.062
Maximum inscribe zone	195	5.6	0.04
RANSAC detection shape	199	3.2	0.015

Table 6.6 presents the radius estimation of the fitted sphere, the sphericity deviation from it and the standard deviation for three types of sphere fitting modelling. The sphericity deviation is a peak to valley deviation relative to the data fitting while standard deviation in this contest is the root means square deviation of the measured surface data. The estimation of radius of all models is consistent between each other. However, these results are larger compared to the radius of nominal measured sphere which is 150 µm. This is due to the small amount of sphere data provided which could lead to the error in estimation of the result. This modelling analysis is expected to be improved if more data are provided and a larger sphere region is covered.

The sphericity deviations resulting from these modelling methods varied between 1.9 µm and 5.6 µm. This discrepancy is understood as they each have their own definitions and calculations of the perfect sphere and its deviation. However, this discrepancy in sphericity deviation will not be studied in further detail in this thesis because it is marginal to the scope of this work and because of time constraints. Nevertheless, from this result, with the limited measured data, it shows that the sphericity deviation is between 1% and 2% of the nominal sphere diameter.

The standard deviation of the result in Table 6.6 are also varies from 15 nm to 62 nm. As discussed earlier, the measured data supplied in this analysis might be insufficient for the model fitting to provide an accurate result. Nevertheless, this result of standard deviation is in agreement with the stitched error of 25.1 nm which is calculated in section 6.5.1. This means that the stitched errors are in the same range as the standard deviation calculated from the sphere fitting modelling. Therefore, this result also demonstrates that this new measurement technique with its 3D stitching method can be acceptable and the result of stitched error can plausibly be used as the standard error of the spherical form.

6.6. Determination of source of uncertainty in sphericity measurement

To date, the sources of uncertainty that have been determined come from the stitched error, the repeatability of the measurement and the calibration of the axis scale of the CSI (only considered for the *z* axis scale as the internal *x* and *y* axis are not employed in this work). Table 6.7 illustrates the uncertainty budget of these sources.

Table 6. 7: combined standard uncertainty of the known source of uncertainty in sphericity measurement

source of uncertainty	Type	note	value / nm	standard uncertainty /nm
Stitched error	A	Mean values as standard uncertainty		25.1
Repeatability error	A	Mean value of error	5.3	2.16
residual flatness of CSI scale	B	Uncertainty from certificate with k=2	3.7	2.14
Measurement noise of CSI	B	Uncertainty from certificate with k=2	0.6	0.35
Amplification and linearity of *Z*-axis	B	Uncertainty from certificate with k=2		
Combined standard uncertainty of known quantities				25.29

However, this uncertainty budget does not reflect the full story of evaluation uncertainty in measurement. This is because, there are other factors that need to be included as the sources of uncertainty. These factors are type B error [138] and have been identified but due to the limitation of time and the scope of this work, their values are not yet to be determined. These sources of uncertainties can be summarised as follows.

6.6.1. Uncertainty and data reduction related to lateral distortion and optical transfer function of the measured surface

The metrological quantities associated with the scale axis of the CSI which are determined in the calibration are not sufficient to characterise the metrological performance of the measurement. When measuring the rough and high slope dependant surfaces, errors arising from the interaction behaviour between the light source and measured surface have to be included in the uncertainty evaluation.

6.6.2. Uncertainty related to the rotation and tilting angles of surface data

Although in theory, the rotational self-referencing technique is expected to provide high accuracy determinations of the rotation and tilting angles, the implementation of this technique in practice still introduces a measurement error in these angles and thus in the calculated positioning of the surfaces. This is because the calculation of tilting and rotating angles in this algorithm only uses a three point on the flat algorithm to determine the normal vectors. This calculation should be enhanced by determining the overall surface normal vector or by finding and averaging the normal at different locations on the flat surface.

6.6.3. Uncertainty related to the stitching algorithm-fusion technique

The stitching algorithm developed in this work involves the solution of several mathematical models, so the uncertainty associated with their modelling should be considered in this uncertainty evaluation. Uncertainties are associated with the registration process and determining the stitched error: for instance, the ICP technique, sum of absolute difference in position technique, data interpolation and the positioning error due to the transformation matrix. The stitching condition between surfaces and the stitched error will be improved if the uncertainty due to the algorithms can be determined and corrected.

6.6.4. Uncertainty related to sphere data fitting technique in sphericity deviation calculation

The uncertainty related to the data fitting modelling employed for the calculation of the sphericity deviation should also be considered in the evaluation of overall uncertainty of measurement. The comparison between fitting modelling techniques should also be investigated in the future so that the most suitable fitting modelling can be applied to this work.

6.7. Conclusions

New measurement techniques for sphericity measurement of, especially, micro-spheres have been demonstrated and evaluated. This approach involves the use of coherence scanning interferometry (CSI) as the main traceable instrument, employs data fusion techniques, introduces a new rotational referencing technique and also applies new metrological oriented data fitting modelling.

To address ***Research Question 3.1,*** a ruby micro-sphere with dimension of 300 µm in diameter was selected. This dimension of the micro-sphere is suitable for use as a reference standard for a probe qualification for micro-styli of less than 100 µm in diameter. Therefore, the intension of this work is to measure a spherical form deviation of this micro sphere which is required in order to perform the probe qualification of the micro-styli. The form deviation of a full hemisphere cannot be obtained in this work due to some limitations in the specific rotation and manipulation stage system used. Nevertheless, the measured data are sufficient to demonstrate this new measurement technique and to acquire an estimate for the spherical form deviation of the micro-sphere.

In this new measurement technique, the coherence scanning interferometry (CSI) is used not only because of its traceability to the primary standard of length, but also due to its capability to measure rough surface features and, in principle, to work on spheres with dimension less than 100 µm. The new technique of rotation referencing also introduced, which does not rely on the external rotational and translational manipulation stage systems, including the CSI manipulation stage and other commercial systems. The external stages are only employed as tools to manipulate the micro sphere, while not being involved in the metrological loop. An accurate rotation angle is expected to be determined from this technique. A new concept for the fusion process of stitched surface data is also demonstrated in section 6.4.3. With this concept, modified surface dataset at the overlap region, resultant from the statistical approach fusion process, is replaced by an actual measured data and thus the topography of entire surface is acquired only from an actual point cloud 3D measured surface data.

As required in ***Research Question 3.2,*** the result of this measurement is explained in section 6.5. The sphericity deviation of the micro sphere is range from 1.9 µm to 5.6 µm (depend on the type of data fitting) while the uncertainty of spherical form measurement is estimated at about 25.3 nm. With the comparison to the standard deviation from the data fitting technique using 3D inspection coordinate software, this level of spherical form error is acceptably small. However, this is not the full story as there are other sources of uncertainty that need to be considered in the form error evaluation. This result for spherical form error is slightly lower than in the measurement done by *Kung et al*[102][25] and it is significantly different from the work on the qualification of micro-styli done by *Yuan Liu Chen et al* [103]. In the future, the current uncertainty is expected to be decreased when the correction of optical transfer function and lateral distortion of the instrument is applied to the measurement.

In summary, the new sphericity measurement method developed in this chapter is capable of determining the sphericity deviation and its uncertainty of a micro sphere with dimension of 300 µm and also has the potential to obtain the sphericity deviation and its uncertainty for a sphere with a diameter less than 100 µm. With improvements to the manipulation system and data fusion process, this measurement technique can be categorised as an independent technique that can be used with other optical metrological instruments. The results obtained from this measurement exhibit a promising technique for use in measuring the spherical form of micro styli with dimension less than 100 µm, either by direct measurement of the styli or through qualification of the probe. In the future, with the enhancement on the rotation and manipulation stage system, the measurement of a full hemisphere should be achievable. Investigation of optical behaviour in interaction with the surface slopes should also continue in order to reduce the resulting uncertainty in sphericity measurement. To validate the result, an independent verification measurement with precision stylus instrument is also suggested in the future

Chapter 7: Conclusion

The **Thesis aim** in Chapter 1 clearly states that:

> *"The aim of this study is to develop and characterize a contact stylus with a tip diameter below 10 µm that fit on any micro-CMM probing system and has appropriate aspect ratio to measure micro features*".

To realise this **Thesis aim**, research gaps were identified which lead to the development of three **Thesis objectives**. Then the **Research Questions** were formulated. In this chapter, the works in addressing these **Thesis objectives** and **Research Questions** will be brought together and future work will be suggested.

7.1. Conclusion on thesis objective and research question

***Thesis Objective 1*: To design a new stylus for tactile probes with a stylus tip diameter less than 10 µm and investigate the required manufacturing techniques**

- ***Research question 1.1: What are the influence factors for developing stylus in sub-10 µm dimension and how will they differ from those of a stylus above 100 µm?***

The influence factors that affect the stylus system of a micro-CMM with dimension in sub-10 µm region have been studied and identified. As reported in Chapter 3, there are 28 design rules that influenced this micro-stylus. This design rules can be categorised into five groups of influence factors: geometrical consideration; forces during measurement; physical conditions; material selection; and the influence factors from manufacturing control parameters. These design rules are interlinked between each other, with some among them having a linear relationship while most of them have non-linear relationships. Furthermore, some of them can be formulated fully using mathematical equations while others involve qualitative considerations. There are also influence factors that are ignored during measurements using conventional CMMs but are crucial during micro-CMM measurement, especially if involving micro-stylus with dimension less than 100 µm, for example, a surface interaction force and the surface quality of the stylus tip. In addition, section 4.3 is also dedicated to modelling the relationships of some of these factors.

- ***Research Question 1.2: What is the maximum workable aspect ratio that a stylus with tip dimension in sub 10 µm region could have? How could the optimum aspect ratio of stylus be determined?***

With increasing demand on a high aspect ratio measurement for micro-product, it is crucial to develop a micro stylus with high aspect ratio. Therefore, it is important to investigate the stylus with dimension in sub-10 µm is able to have high aspect ratio structure. For this reason, the section 3.2.3 and 3.2.4 are dedicated to study the factors influence the aspect ratio of styli and determine the optimum value that micro styli should have to well-functioned while modelling in section 4.4 demonstrate the relationship between the aspect ratio with the material properties of the stylus tip and measured workpiece. It can be concluded that the maximum aspect ratio of styli is varies depending on the measurement task, applied contact forces, the elastic deflection of stylus and the material properties of the stylus tip and the measured workpiece.

***Thesis Objective 2*: To characterize the mechanical properties of the new stylus and hence verify the design.**

- ***Research Question 2.1: Can the strength of the new styli under certain loads be tested? If it can be tested, how might it be possible to validate the result of the experiment?***

Chapter 5 describes the work to deliver this research question. Two mechanical parameters, namely the stiffness of the stylus shaft and the maximum safe tip force, have been identified to be tested and an experimental set up has been developed. To validate the experimental set up, preliminary performance testing (described in section 5.4) has been conducted. The purpose of this work is to identify the systematic error in the experiments. All measuring instruments involved in obtaining the results are calibrated and traceable to primary standards. For the measurement result, uncertainty evaluations are completed to demonstrate the quality of the measurement results. These can be found in section 5.9.

- ***Research Question 2.2: What is the result of this styli test? Are there any differences between high aspect ratio styli with low aspect ratio styli and how is the performance compared to the design rule?***

The results of the mechanical testing have been presented in section 5.8, which include measurements of stiffness and of maximum safe tip force. Prior to that, as explained in section 5.2, twelve styli have been manufactured using four types of hybrid manufacturing process. The smallest dimension stylus is *stylus 4b with* a stylus effective length of 176 µm, a diameter of 12 µm for stylus shaft, and 21 µm for the stylus tip. Also, the highest aspect ratio structure is *stylus 4d* which has effective and mechanical aspect ratios of 26 and 37. Its diameter of stylus shaft and tip are 15 µm and 22 µm.

For stiffness measurement, in general, except the stylus from type 4 styli, the results from all styli are low compared to the value predicted in their analytical modelling, but not too different from lower bound estimates. In addition, a number of graphs are plotted between the experimental results of stiffness and geometrical dimension parameters and comparison toward their analytical modelling value are also observed. From these comparisons, the trends vary depending on the manufacturing type. All the styli in type 4, which have the dimension less than 50 µm using ECM manufacturing process, exhibit promising and significant results. Their results are more nearly similar to the value predicted in the analytical value. From these stiffness experiments, it can be concluded that the ECM process is the promising candidate for manufacturing the stylus shaft with the diameter in less than 50 µm. The stiffness of this stylus using this manufacturing technique can be predicted from its modelling and the stylus with high aspect ratio structure can be expected to be stiffer than its modelling. However, further investigations have to be suggested for the styli with stylus shafts manufactured by the combination of ECM and other processes.

The experimental results for maximum safe tip force cannot readily be compared to analytical modelling because it is difficult to calculate using a closed-form mathematical equation. Nevertheless, as discussed in chapter 3, the maximum safe tip force and allowable probing force are two limiting factors for the force in measurement. The minimum value between these forces should be selected as the maximum force that should be applied during measurement. For these experiments (where material for the stylus and measured workpiece

are tungsten and copper, respectively), except for the Type 2 styli, the value of the results for all styli are higher compared to the value of allowable aspect ratio. Type 2 styli have stylus tips made from glass, and, considering its material properties, the value of the allowable probing force tends to be higher than for styli of other manufacturing types. Therefore, for the styli fabricate using this hybrid manufacturing technique, the maximum safe tip force needs to be determined first and is used as a guideline in selecting the appropriate forces applied in measurement.

- ***Research Question 2.3:*** **from this testing result, it is suitable for the new stylus to be fitted to current available micro-probe and can it be used to perform high aspect ratio measurement**

Among the types of styli tested in this work, *Type 4 styli* are the styli that have dimension less than 50 µm and therefore, the focus of this work. To select the suitable probing system that can operate with this stylus type, the design rules related to the allowable probing force and the stylus stiffness need to be obeyed. For the probing force, the majority of probing systems summarised in Table 2.1 can comply with the requirement of the allowable probing force of the styli (which is predicted by the modelling). However, the experimental stiffness results for *Type 4 styli* indicate that only probing systems from METAS, NPL SCMM, IBS Triskelion B-35, Xpress Gannen XM and NPL vibrating probe are suitable for practical operations with these styli. This is because the probe stiffness of these probes are smaller than the stylus stiffness. However, if the dimension of the styli shrinks down below 10 µm in diameter, as demonstrated in the modelling in section 4.2, none of these probing systems is suitable to be selected.

***Thesis Objective 3*: To reduce measurement uncertainties by developing new technique for 3D spherical form measurement of micro-sphere.**

- ***Research Question 3.1:* Can the 3D form error of the spherical surface of the stylus tip with dimension in sub-10 micrometre be examined?**

With the current available technologies, it is difficult to measure directly the spherical form error of the sphere with the diameter dimension less than 100 µm. Therefore, in this work, a new measurement technique to measure spherical form deviation of sphericity deviation of microspheres has been developed. Chapter 6 is dedicated entirely to address this objective. Section 6.2 explains the strategy of measurement for this new technique. The details of the measurement and its results presented in section 6.3 until section 6.6 prove that this new measurement technique is capable to measure the sphericity deviation of a microsphere with diameter of 300 µm. Therefore, in order to measure the spherical for error of the tip sphere of the stylus with dimension in sub-10 µm, this new measurement technique is suggested as a way to measure a standard reference sphere with a diameter of 300 µm. This standard sphere is then used as the standard artefact for probe calibration and qualification for styli with dimensions in sub- 10 µm region.

- ***Research Question 3.2*: How is the performance of the new measurement technique of micro sphere measurement?**

The results of sphericity measurement of the micro sphere with 300 µm in diameter are presented in section 6.5 and section 6.6. The uncertainty of measurement is estimated at about 25 nm. The major source of uncertainty is obtained from the stitched error. By using data fitting techniques, calculated from commercial 3D inspection coordinate software, the sphericity deviation of overall combined stitched surfaces ranges from 1.9 µm to 5.6 µm, depending on the type of data fitting. The statistical standard deviation calculated from this software is range from 15 nm to 62 nm and it is assumed to have a rectangular error distribution from which the standard uncertainty (as standard deviation) is calculated as ranging from 8.6 nm to 35.8 nm. This proves that the measurement uncertainties calculated from the stitching technique are in agreement with the standard uncertainties calculated from data fitting technique.

7.2. Future works

Throughout this research work, several improvements have been suggested for the future research work. The suggestions can be discussed in terms of two fields of research which are the stylus testing and sphericity measurement of stylus tip. These suggestions will be described below.

- ***Stylus testing***

As promising results are obtained from the styli made from *ECM* manufacturing process with the diameter of stylus tip is less than 50 µm and high aspect ratio structure, it is suggested to continue investigating the mechanical behaviour of this styli, especially those having diameters of stylus tip less than 20 nm with high aspect ratio structures. The future studies should give information about the capability of this manufacturing technique in fabricating the next generation styli with high aspect ratio structures. Nevertheless, as the experimental results from this thesis show, there are problems when the *ECM* process is integrated together with others in fabricating the stylus shaft, and further study is suggested to better understand the behaviour of this manufacturing process. In addition, finite element analysis approach is suggested to be employed as a modelling technique before conducting the experiment

- ***Sphericity measurement of the stylus tip***

Several extensions beyond the scope of this thesis need to be conducted in this field. The first suggestion is to continue research into sphericity measurement using the technique and strategy developed here with smaller microspheres. Less than 100 µm in diameter is suggested for this purpose. In order to measure the whole hemisphere of the micro sphere, a new mechanical manipulation stage has to be designed. This design must allow the sphere and the reference flat to be manipulated freely underneath the CSI without touching its objective lens. The process of data stitching and data fusion can also be enhanced by developing new mathematical modelling related to this process. In addition, the measurement uncertainty can be reduced by understanding the optical behaviour on the high slope surface and the error related to this behaviour can be defined, modelled and corrected.

Furthermore, a comparison with other independent measurement techniques, such as tactile measurement, is suggested to be conducted in order to verify this measurement technique.

7.3. General conclusion

As referred to the **Thesis Aim** of this work, it is concluded that the stylus system with dimension of sub-10 µm can be designed, manufactured and characterised to be operated in micro-CMM measurement. Not only the mechanical characteristics of the styli been explored in detail, but a promising method for determining the surface form error of the tip has also been demonstrated. In the future, with the advancement of the manufacturing technology and probing system development, this next generation styli can be operated to fulfil the demand of micro and nano dimensional measurement

Bibliography

[1] R. K. Leach, Fundamental principles of engineering nanometrology. William Andrew, 2009.

[2] A. Weckenmann, T. Estler, G. Peggs, and D. McMurtry, “Probing systems in dimensional metrology,” CIRP Annals-Manufacturing Technology, vol. 53, no. 2, pp. 657–684, 2004.

[3] A. Weckenmann, G. Peggs, and J. Hoffmann, “Probing systems for dimensional micro- and nano-metrology,” Measurement science and technology, vol. 17, no. 3, p. 504, 2006.

[4] R. Thalmann, F. Meli, and A. Küng, “State of the Art of Tactile Micro Coordinate Metrology,” Applied Sciences, vol. 6, no. 5, p. 150, 2016.

[5] R. J. Hocken, P. A. H. Pereir A, and others, “Coordinate measuring machines and systems,”2012.

[6] A. J. T. Scarr, Metrology and precision engineering. McGraw-Hill, 1967.

[7] F. T. Farago and M. A. Curtis, Handbook of dimensional measurement. Industrial Press Inc., 1994.

[8] C. L. Dotson, Fundamentals of dimensional metrology. Nelson Education, 2015.

[9] BIPM, “17th general conference on weight and measures (CGPM)- Resolution 1,” 1983.

[10] K. Takamasu, S. Ozawa, T. Asano, A. Suzuki, R. Furutani, and S. Ozono, “Basic concepts of nano-CMM (coordinate measuring machine with nanometer resolution),” in Jpn.-China Bilateral Symp. on Advanced Manufacturing Eng, 1996, vol. 155.

[11] G. Peggs, A. Lewis, and R. Leach, “Measuring in three dimensions at the mesoscopic level,” in Proc. ASPE Winter Topical Meeting—Machines and Processes for Micro-scale and Meso-scale Fabrication, Metrology and Assembly (FL, USA, January 2003), 2003, pp. 53–7.

[12] G. Peggs, A. Lewis, and S. Oldfield, “Design for a compact high-accuracy CMM,” CIRP Annals-Manufacturing Technology, vol. 48, no. 1, pp. 417–420, 1999.

[13] K. Takamasu, M. Hiraki, K. Enami, and S. Ozono, “Development of Nano-CMM and Parallel-CMM—CMM in the 21th Century—,” in International Dimensional Metrology Workshop, 1999, pp. 10–13.

[14] H. Schwenke, F. Härtig, K. Wendt, and F. Wäldele, “Future challenges in co-ordinate metrology: addressing metrological problems for very small and very large parts,” in Proceedings of IDW conference, Knoxville, 2001, pp. 1–12.

[15] K.-C. Fan, Y. Fei, and X. Yu, “Development of a micro-CMM,” in International Manufacturing Leaders Forum on Global Competitive Manufacturing, Adelaide, Australia, 2005, pp. 1–7.

[16] C. Zeiss, “F25 Measuring Nanometers,” Carl Zeiss Industrial Metrology GmbH, 2006.

[17] M. Vermeulen, P. Rosielle, and P. Schellekens, “Design of a high-precision 3D-coordinate measuring machine,” CIRP Annals-Manufacturing Technology, vol. 47, no. 1, pp. 447–450, 1998.

[18] International Organization for Standardization, “ISO 103601:2001 :Geometrical Product Specifications (GPS)- Acceptance and reverification tests for coordinate measuring machines (CMM)- Part1; ~ Vocabulary,” 2001.

[19] T. Masuzawa, Y. Hamasaki, and M. Fujino, “Vibroscanning method for nondestructive measurement of small holes,” CIRP Annals-Manufacturing Technology, vol. 42, no. 1, pp. 589–592, 1993.

[20] K. Hidaka and P. Schellekens, “Study of a small-sized ultrasonic probe,” CIRP Annals-Manufacturing Technology, vol. 55, no. 1, pp. 567–570, 2006.

[21] E. Bos, “Tactile 3D probing system for measuring MEMS with nanometer uncertainty,” PhD Thesis, Eindhoven University of Technology, 2008.

[22] W. O. Pril, “Development of high precision mechanical probes for coordinate measuring machines,” Technische Universiteit Eindhoven, 2002.

[23] M. C. van Riel and E. J. Bos, 3D Vibrating Probe for Measuring Microfeatures with Nanometer Uncertainty. Universitätsbibliothek Ilmenau, 2011.

[24] “Xpress Gannen XM probe.” [Online]. Available: http://www.xpresspe.com/probe_xm1.php. [Accessed: 12-Jan-2017].

[25] A. Küng, F. Meli, and R. Thalmann, “Ultraprecision micro-CMM using a low force 3D touch probe,” Measurement Science and Technology, vol. 18, no. 2, p. 319, 2007.

[26] F. Meli and A. Küng, “AFM investigation on surface damage caused by mechanical probing with small ruby spheres,” Measurement Science and Technology, vol. 18, no. 2, p. 496, 2007.

[27] International Organization for Standardization, “ISO 10360-2:2009 :Geometrical product specifications (GPS) — Acceptance and reverification tests for coordinate measuring machines (CMM) — Part 2: CMMs used for measuring linear dimensions,” 2009.

[28] S. Buetefisch, G. Dai, H.-U. Danzebrink, L. Koenders, F. Solzbacher, and M. Orthner, “Novel design for an ultra high precision 3D micro probe for CMM applications,” Procedia Engineering, vol. 5, pp. 705–712, 2010.

[29] G. Dai, S. Bütefisch, F. Pohlenz, and H.-U. Danzebrink, “A high precision micro/nano CMM using piezoresistive tactile probes,” Measurement Science and Technology, vol. 20, no. 8, p. 084001, 2009.

[30] T. Liebrich and W. Knapp, “New concept of a 3D-probing system for micro-components,” CIRP Annals-Manufacturing Technology, vol. 59, no. 1, pp. 513–516, 2010.

[31] J. D. Claverley and R. K. Leach, “Development of a three-dimensional vibrating tactile probe for miniature CMMs,” Precision Engineering, vol. 37, no. 2, pp. 491–499, 2013.

[32] R. K. Leach, J. Murphy, and A. Wilson, Design of a co-ordinate measuring probing system for characterising three-dimensional micro-structures. National Physical Laboratory, 2004.

[33] S. Stoyanov, C. Bailey, R. Leach, B. Hughes, A. Wilson, W. O’Neill, R. A. Dorey, C. Shaw, D. Underhill, and H. J. Almond, “Modelling and prototyping the conceptual design of 3D CMM micro-probe,” in Electronics System-Integration Technology Conference, 2008. ESTC 2008. 2nd, 2008, pp. 193–198.

[34] J. D. Claverley and R. K. Leach, “A vibrating micro-scale CMM probe for measuring high aspect ratio structures,” Microsystem Technologies, vol. 16, no. 8–9, pp. 1507-1512, 2010.

[35] “IBS Triskelion Ultra-Precision Touch Probe.” [Online]. Available: http://www.ibspe.com/category/isara-400-3d-cmm/triskelion-touch-probe.htm. [Accessed: 02-Jan-2017].

[36] R. Donker, I. Widdershoven, and H. Spaan, “Realization of Isara 400: a large measurement volume ultra-precision CMM,” in Asian Symposium for Precision Engineering and Nanotechnology, 2009, vol. 4.

[37] H. A. Spaan, R. L. Donker, and I. Widdershoven, “Isara 400: development of an ultra-precision CMM for 3D measurement of large parts,” in Proceedings of the ASPE spring topical conference, 2009.

[38] M. He, R. Liu, Y. Li, H. Wang, X. Lu, G. Ding, J. Wu, T. Zhang, and X. Zhao, “Tactile probing system based on micro-fabricated capacitive sensor,” Sensors and Actuators A: Physical, vol. 194, pp. 128–134, 2013.

[39] S.-M. Kao and D.-Y. Sheu, “Developing a novel tri-switch tactile probing structure and its measurement characteristics on micro-CMM,” Measurement, vol. 46, no. 9, pp. 3019–3025, 2013.

[40] Y. T. A. Sun, K.-Y. Tseng, and D.-Y. Sheu, “Investigating Characteristics of the Static Tri-Switches Tactile Probing Structure for Micro-Coordinate Measuring Machine (CMM),” Applied Sciences, vol. 6, no. 7, p. 202, 2016.

[41] K. Alblalaihid, T. Kirk, S. Lawes, and P. Kinnell, “Fabrication of a smart suspension structure of micro tactile probing,” Procedia Engineering, vol. 87, pp. 1164–1167, 2014.

[42] K. Alblalaihid, S. Lawes, and P. Kinnell, “Variable stiffness probing systems for micro-coordinate measuring machines,” Precision Engineering, vol. 43, pp. 262–269, 2016.

[43] K. Alblalaihid, P. Kinnell, S. Lawes, D. Desgaches, and R. Leach, “Performance assessment of a new variable stiffness probing system for micro-CMMs,” Sensors, vol. 16, no. 4, p. 492, 2016.

[44] M. Petz, R. Tutsch, R. Christoph, M. Andraes, and B. Hopp, “Tactile-optical probes for three-dimensional microparts,” Measurement, vol. 45, no. 10, pp. 2288–2298, 2012.

[45] “Werth Fiber Probe WFP/S.” [Online]. Available: http://www.werth.de/en/unser-angebot/products/sensors/werth-fiber-probe-wfps.html. [Accessed: 02-Jan-2017].

[46] Y. Takaya, S. Takahashi, T. Miyoshi, and K. Saito, “Development of the nano-CMM probe based on laser trapping technology,” CIRP Annals-Manufacturing Technology, vol. 48, no. 1, pp. 421–424, 1999.

[47] Y. Takaya, M. Michihata, T. Hayashi, and T. Washitani, “Dimensional measurement of microform with high aspect ratio using an optically controlled particle with standing wave scale sensing,” CIRP Annals-Manufacturing Technology, vol. 61, no. 1, pp. 479–482, 2012.

[48] M. B. Bauza, S. C. Woody, R. J. Hocken, and S. T. Smith, “Development of high aspect ratio microscale force probes,” Proc. of 20th ASPE, 2005.

[49] M. Bauza, S. Woody, B. Woody, and S. Smith, “Surface profilometry of high aspect ratio features,” Wear, vol. 271, no. 3, pp. 519–522, 2011.

[50] J. Tan and J. Cui, “Ultraprecision 3D probing system based on spherical capacitive plate,” Sensors and Actuators A: Physical, vol. 159, no. 1, pp. 1–6, 2010.

[51] C.-S. Goo, M. B. Jun, and A. Saito, “Probing system for measurement of micro-scale components,” Journal of Manufacturing Processes, vol. 14, no. 2, pp. 174–180, 2012.

[52] B. Goj, L. Dressler, and M. Hoffmann, “Resonant probing system comprising a high accurate uniaxial nanoprobe and a new evaluation unit,” Journal of Micromechanics and Microengineering, vol. 23, no. 9, p. 095012, 2013.

[53] B. Goj and M. Hoffmann, “Design of a biaxial nanoprobe utilizing Matlab Simulink,” in Proceedings 23rd Micromechanics Europe Workshop. Ilmenau: Verl. ISLE, 2012.

[54] International Organization for Standardization, “ISO 10360-5: 2000: Geometrical Product Specifications (GPS)—acceptance and reverification tests for coordinate measuring machines (CMM)—Part 5: CMMs using multiple-stylus probing systems,” International Organization for Standardization, 2000.

[55] Y. N. Picard, D. Adams, M. Vasile, and M. Ritchey, “Focused ion beam-shaped microtools for ultra-precision machining of cylindrical components,” Precision Engineering, vol. 27, no. 1, pp. 59–69, 2003.

[56] S. N. Bhavsar, S. Aravindan, and P. V. Rao, “A critical review on microtools fabrication by focused ion beam (FIB) technology,” in Proceedings of the World Congress on Engineering, 2009, vol. 2, pp. 1–3.

[57] C. Morgan, S. Shreve, and R. R. Vallance, “Precision of micro shafts machined with wire electro-discharge grinding,” in Proceedings of the Winter Topical Meeting on Machines and Processes for Micro-Scale and Meso-Scale Fabrication, Metrology, and Assembly. American Society for Precision Engineering (ASPE), 2003, pp. 22–23.

[58] D.-Y. Sheu, “Multi-spherical probe machining by EDM: Combining WEDG technology with one-pulse electro-discharge,” Journal of materials processing technology, vol. 149, no. 1, pp. 597–603, 2004.

[59] L.-C. Chen, “Automatic 3D surface reconstruction and sphericity measurement of micro spherical balls of miniaturized coordinate measuring probes,” Measurement Science and Technology, vol. 18, no. 6, p. 1748, 2007.

[60] A. Wilson and R. Leach, “Manufacture and testing of a micro-stylussuitable for tactile probing in dimensionalmetrology,” NPL REPORT ENG 15, 2009.

[61] T. Masuzawa, M. Fujino, K. Kobayashi, T. Suzuki, and N. Kinoshita, “Wire electro-discharge grinding for micro-machining,” CIRP Annals-Manufacturing Technology, vol. 34, no. 1, pp. 431–434, 1985.

[62] E. Uhlmann, S. Piltz, and S. Jerzembeck, “Micro-machining of cylindrical parts by electrical discharge grinding,” Journal of Materials Processing Technology, vol. 160, no. 1, pp. 15–23, 2005.

[63] J. Qu, A. J. Shih, and R. O. Scattergood, “Development of the cylindrical wire electrical discharge machining process, part 1: concept, design, and material removal rate,” Journal of Manufacturing science and engineering, vol. 124, no. 3, pp. 702–707, 2002.

[64] J. Qu, A. J. Shih, and R. O. Scattergood, “Development of the cylindrical wire electrical discharge machining process, part 2: surface integrity and roundness,” Journal of manufacturing science and engineering, vol. 124, no. 3, pp. 708–714, 2002.

[65] A. Rees, E. Brousseau, S. Dimov, H. Gruber, and I. Paganetti, “Wire electro discharge grinding: surface finish optimisation,” Manufacturing Engineering Centre, Cardiff University, CF24 3AA, UK, AGIE AG für Industrielle Elektronik, Losone, Switzerland, 2008.

[66] J. D. Claverley, D.-Y. Sheu, A. Burisch, R. K. Leach, and A. Raatz, “Assembly of a novel MEMS-based 3D vibrating micro-scale co-ordinate measuring machine probe using desktop factory automation,” in Assembly and Manufacturing (ISAM), 2011 IEEE International Symposium on, 2011, pp. 1–5.

[67] Y. Liu and H. Li, “Fabrication of Micro Spherical Electrode by One Pulse Electrical Discharge Machining,” in Digital Manufacturing and Automation (ICDMA), 2011 Second International Conference on, 2011, pp. 531–534.

[68] K. Rajurkar, D. Zhu, J. McGeough, J. Kozak, and A. De Silva, “New developments in electro-chemical machining,” CIRP Annals-Manufacturing Technology, vol. 48, no. 2, pp. 567–579, 1999.

[69] C.-F. Tsai, C.-C. Cheng, and D.-Y. Sheu, “Investigating Micro Spherical Stylus Tips Fabrication by Electro Chemical and Single Pulse Electro Discharge Processes,” Procedia CIRP, vol. 6, pp. 606–609, 2013.

[70] B. H. Kim, S. H. Ryu, D. K. Choi, and C. N. Chu, “Micro electrochemical milling,” Journal of Micromechanics and Microengineering, vol. 15, no. 1, p. 124, 2004.

[71] K. P. Rajurkar, M. Sundaram, and A. Malshe, “Review of electrochemical and electrodischarge machining,” Procedia CIRP, vol. 6, pp. 13–26, 2013.

[72] B. Bhattacharyya, J. Munda, and M. Malapati, “Advancement in electrochemical micro-machining,” International Journal of Machine Tools and Manufacture, vol. 44, no. 15, pp. 1577–1589, 2004.

[73] S. Skoczypiec and A. Ruszaj, “A sequential electrochemical-electrodischarge process for micropart manufacturing,” Precision Engineering, vol. 38, no. 3, pp. 680–690, 2014.

[74] D.-Y. Sheu, “Micro-spherical probes machining by EDM,” Journal of Micromechanics and Microengineering, vol. 15, no. 1, p. 185, 2005.

[75] D. Smale, S. Haley, J. Segal, R. Ronaldo, S. Ratchev, R. K. Leach, and J. D. Claverley, “Utilisation of FIB/SEM Technology in the Assembly of an Innovative Micro-CMM Probe,” in Precision Assembly Technologies and Systems, Springer, 2010, pp. 105–112.

[76] D.-Y. Sheu and C.-C. Cheng, “A hybrid microspherical styli gluing and assembling process on micro-EDM,” Materials and Manufacturing Processes, vol. 27, no. 10, pp. 1129–1134, 2012.

[77] D.-Y. Sheu and C.-C. Cheng, “Assembling ball-ended styli for CMM’s tactile probing heads on micro EDM,” The International Journal of Advanced Manufacturing Technology, vol. 65, no. 1–4, pp. 485–492, 2013.

[78] K.-C. Fan, N. Wang, Z.-W. Wang, and H. Zhang, “Development of a roundness measuring system for microspheres,” Measurement Science and Technology, vol. 25, no. 6, p. 064009, 2014.

[79] D. J. Whitehouse, Surfaces and their Measurement. Elsevier, 2004.

[80] B. Muralikrishnan and J. Raja, Computational surface and roundness metrology. Springer Science \& Business Media, 2008.

[81] W. Sui and D. Zhang, “Four methods for roundness evaluation,” Physics Procedia, vol. 24, pp. 2159–2164, 2012.

[82] A. Rossi, S. Chiodi, and M. Lanzetta, “Minimum centroid neighborhood for minimum zone sphericity,” Precision Engineering, vol. 38, no. 2, pp. 337–347, 2014.

[83] C.-H. Liu and C.-K. Chen, “A study on analyzing the problem of the spherical form error,” Precision Engineering, vol. 24, no. 2, pp. 119–126, 2000.

[84] M.-C. Chen, “Analysis of Spherical Form Errors to Coordinate Measuring Machine Data.,” JSME International Journal Series C, vol. 45, no. 2, pp. 647–656, 2002.

[85] T. Kanada, “Estimation of sphericity by means of statistical processing for roundness of spherical parts,” Precision Engineering, vol. 20, no. 2, pp. 117–122, 1997.

[86] H.-Y. Feng, D. H. Endrias, M. A. Taher, and H. Song, “An accurate and efficient algorithm for determining minimum circumscribed circles and spheres from discrete data points,” Computer-Aided Design, vol. 45, no. 2, pp. 105–112, 2013.

[87] R. Schnabel, R. Wahl, and R. Klein, “Efficient RANSAC for point-cloud shape detection,” in Computer graphics forum, 2007, vol. 26, no. 2, pp. 214–226.

[88] R. C. Bolles and M. A. Fischler, “A RANSAC-Based Approach to Model Fitting and Its Application to Finding Cylinders in Range Data.,” in IJCAI, 1981, vol. 1981, pp. 637–643.

[89] M. Saval-Calvo, J. Azorin-Lopez, A. Fuster-Guillo, and J. Garcia-Rodriguez, “Three-dimensional planar model estimation using multi-constraint knowledge based on k-means and RANSAC,” Applied Soft Computing, vol. 34, pp. 572–586, 2015.

[90] R. Rantoson, H. Nouira, N. Anwer, and C. Mehdi-Souzani, “Improved curvature-based registration methods for high-precision dimensional metrology,” Precision Engineering, 2016.

[91] Y. Lv, J. Feng, Z. Li, W. Liu, and J. Cao, “A new robust 2D camera calibration method using RANSAC,” Optik-International Journal for Light and Electron Optics, vol. 126, no. 24, pp. 4910–4915, 2015.

[92] “Taylor hobson series of Roundness measuring machine.” [Online]. Available: http://www.taylor-hobson.com/products/18/108.html. [Accessed: 18-Jan-2017].

[93] “Roundness measuring device Mahr MMQ200.” [Online]. Available: http://www.directindustry.com/prod/mahr/product-9205-430621.html. [Accessed: 18-Jan-2017].

[94] “Mitutoyo roundness measuring machine.” [Online]. Available: https://www.mitutoyo.co.jp/eng/products/shinen/shinen.html. [Accessed: 18-Jan-2017].

[95] J. Fleig, P. Dumas, P. E. Murphy, and G. W. Forbes, “An automated subaperture stitching interferometer workstation for spherical and aspherical surfaces,” in Optical Science and Technology, SPIE’s 48th Annual Meeting, 2003, pp. 296–307.

[96] M. Tricard, A. Kulawiec, M. Bauer, G. DeVries, J. Fleig, G. Forbes, D. Miladinovich, and P. Murphy, “Subaperture stitching interferometry of high-departure aspheres by incorporating a variable optical null,” Cirp Annals-Manufacturing Technology, vol. 59, no. 1, pp. 547–550, 2010.

[97] U. Griesmann, J. Soons, Q. Wang, and D. DeBra, “Measuring form and radius of spheres with interferometry,” CIRP Annals-Manufacturing Technology, vol. 53, no. 1, pp. 451–454, 2004.

[98] R. A. Nicolaus and C. Elster, “Diameter determination of Avogadro spheres\# 1 and\# 2,” IEEE transactions on instrumentation and measurement, vol. 54, no. 2, pp. 872–876, 2005.

[99] G. Bartl, M. Krystek, A. Nicolaus, and W. Giardini, “Interferometric determination of the topographies of absolute sphere radii using the sphere interferometer of PTB,” Measurement Science and Technology, vol. 21, no. 11, p. 115101, 2010.

[100] G. Bartl, H. Bettin, M. Krystek, T. Mai, A. Nicolaus, and A. Peter, “Volume determination of the Avogadro spheres of highly enriched 28Si with a spherical Fizeau interferometer,” Metrologia, vol. 48, no. 2, p. S96, 2011.

[101] T. Hagino, Y. Yokoyama, Y. Kuriyama, and H. Haitjema, “Sphericity measurement using stitching interferometry,” in Key Engineering Materials, 2012, vol. 523, pp. 883–888.

[102] A. Küng and F. Meli, “Self calibration method for 3D roundness of spheres using an ultraprecision coordinate measuring machine.,” in Proc. of 5th euspen Int. Conf, 2005, pp. 193–196.

[103] Y.-L. Chen, S. Ito, H. Kikuchi, R. Kobayashi, Y. Shimizu, and W. Gao, “On-line qualification of a micro probing system for precision length measurement of micro-features on precision parts,” Measurement Science and Technology, vol. 27, no. 7, p. 074008, 2016.

[104] F. Chan, E. Davis, T. King, and K. Stout, “Some performance characteristics of a multi-axis touch trigger probe,” Measurement science and technology, vol. 8, no. 8, p. 837, 1997.

[105] P. Cauchick-Miguel and T. King, “Factors which influence CMM touch trigger probe performance,” International Journal of Machine Tools and Manufacture, vol. 38, no. 4, pp. 363–374, 1998

[106] R. Aston, J. Davis, and K. Stout, “A probing question: A customer’s investigation into the directional variability of a coordinate measuring machine touch trigger probe,” International Journal of Machine Tools and Manufacture, vol. 37, no. 10, pp. 1375–1382, 1997.

[107] E. Bos, “Aspects of tactile probing on the micro scale,” Precision Engineering, vol. 35, no. 2, pp. 228–240, 2011.

[108] K.-C. Fan, F. Cheng, W.-T. Pan, and R. Li, “Analysis of the contact probe mechanism for micro-coordinate measuring machines,” Optoelectronics, Instrumentation and Data Processing, vol. 46, no. 4, pp. 340–346, 2010.

[109] H. Van Brussel, J. Peirs, D. Reynaerts, A. Delchambre, G. Reinhart, N. Roth, M. Weck, and E. Zussman, “Assembly of microsystems,” CIRP Annals-Manufacturing Technology, vol. 49, no. 2, pp. 451–472, 2000.

[110] J. D. Claverley, A. Georgi, and R. K. Leach, “Modelling the interaction forces between an ideal measurement surface and the stylus tip of a novel vibrating micro-scale CMM probe,” in Precision Assembly Technologies and Systems, Springer, 2010, pp. 131–138.

[111] F. Arai, D. Ando, T. Fukuda, Y. Nonoda, and T. Oota, “Micro manipulation based on micro physics-strategy based on attractive force reduction and stress measurement,” in Intelligent Robots and Systems 95.’Human Robot Interaction and Cooperative Robots’, Proceedings. 1995 IEEE/RSJ International Conference on, 1995, vol. 2, pp. 236–241.

[112] R. S. Fearing, “Survey of sticking effects for micro parts handling,” in Intelligent Robots and Systems 95.’Human Robot Interaction and Cooperative Robots’, Proceedings. 1995 IEEE/RSJ International Conference on, 1995, vol. 2, pp. 212–217.

[113] M. Sitti and H. Hashimoto, “Controlled pushing of nanoparticles: modeling and experiments,” Mechatronics, IEEE/ASME Transactions on, vol. 5, no. 2, pp. 199–211, 2000.

[114] J. D. Claverley, “Development and validation of a 3D vibrating contact probe for micro-CMMs,” 2014.

[115] S. Tsuchitani, S. Suzuki, M. Matsumoto, and M. Miki, “Theoretical study on the surface force in microstructures,” Transactions-Society of Instrument and Control Engineers, vol. 32, pp. 637–645, 1996.

[116] A. Küng and F. Meli, “Scanning performance with an ultraprecision µ-CMM,” Proceedings of the 6th euspen International Conference, 2006.

[117] W. P. van Vliet and P. H. Schellekens, “Development of a fast mechanical probe for coordinate measuring machines,” Precision engineering, vol. 22, no. 3, pp. 141–152, 1998.

[118] W. Van Vliet and P. Schellekens, “Accuracy limitations of fast mechanical probing,” CIRP Annals-Manufacturing Technology, vol. 45, no. 1, pp. 483–487, 1996.

[119] K.-C. Fan, H.-Y. Hsu, P.-Y. Hung, and W. Wang, “Experimental study of fabricating a microball tip on an optical fibre,” Journal of Optics A: Pure and Applied Optics, vol. 8, no. 9, p. 782, 2006.

[120] P. Kinnell and R. Habeb, “The Unpredictable Errors of Micro Tactile Metrology-Factors Affecting Stylus tip Contamination,” Measurement Science Review, vol. 13, no. 6, pp. 305–310, 2013.

[121] Renishaw, “Effects of continuous scanning on stylus balls,” Technical Paper Renishaw Resource Centre , 2006.

[122] R. Habeb and P. Kinnell, “Evaluation Tip Cleaning for a Micro CMM Touch Trigger Stylus Sensor,” Procedia Engineering, vol. 47, pp. 306–309, 2012.

[123] X. Feng, P. K. Kinnell, and S. Lawes, “Development of CO2 snow cleaning for in situ cleaning of µCMM stylus tips,” Measurement Science and Technology, vol. 28, no. 1, p. 015007, 2016.

[124] N. Ferreira, T. Krah, A. Dietzel, S. Buttgenbach, A. S. Granada, and J. Garcia, “Micro sensors with polymer membrane for accurate 3D force and displacement measurements,” in Sensors, 2013 IEEE, 2013, pp. 1–4.

[125] V. Nesterov and U. Brand, “Modelling and investigation of the silicon twin design 3D micro probe,” Journal of Micromechanics and Microengineering, vol. 15, no. 3, p. 514, 2005.

[126] R.-J. Li, S. Tao, and K.-C. Fan, “Analysis of the elastic mechanism for contact scanning probe,” in International Symposium on Precision Engineering Measurement and Instrumentation 2012, 2013, p. 87590M–87590M.

[127] R.-J. Li, K.-C. Fan, S. Tao, J.-Z. Qian, Q.-X. Huang, and F. Cheng, “Design of an analogue contact probe for nano-coordinate measurement machines (CMM),” in Seventh

International Symposium on Precision Engineering Measurements and Instrumentation, 2011, pp. 832114–832114.

[128] R. J. Roark and others, “Formulas for stress and strain 7th edition,” 2002.

[129] A. K. A. Nicolet and F. Meli, “Study of sapphire probe tip wear when scanning on different materials,” Measurement Science and Technology, vol. 23, no. 9, p. 094016, 2012.

[130] “Tables of Physical & Chemical Constants (16th edition 1995).” [Online]. Available: http://www.kayelaby.npl.co.uk/. [Accessed: 15-Jan-2017].

[131] W. D. Callister and D. G. Rethwisch, Materials science and engineering: an introduction, vol. 7. Wiley New York, 2007.

[132] D.-Y. Sheu, “ ‘Manufacturing tactile spherical stylus tips by combination process of micro electro chemical and one-pulse electro discharge technology.’ ,” The International Journal of Advanced Manufacturing Technology 74.5-8 (2014): 741-747.

[133] D.-Y. Sheu, J. D. Claverley, and R. K. Leach, “Testing the Mechanical Characteristics and Contacting Behaviour of Novel Manufactured and Assembled Sphere-Tipped Styli for Micro-CMM Probes,” in Precision Assembly Technologies and Systems, Springer, 2014, pp. 15–21.

[134] “Alicona Infinite focus instrument.” [Online]. Available: http://www.alicona.com/products/infinitefocus/. [Accessed: 16-Jan-2017].

[135] “Technical specifications and accessories of METTLER TOLEDO AT/MT/UMT Balances.” [Online]. Available: http://www.mt.com/dam/mt_ext_files/Editorial/Generic/4/AT_TeZ_0x000010083f814b3340009e92_files/at-mt-umt-tez-e-703466.pdf. [Accessed: 02-Jan-2017].

[136] “PI Compact Micro-Translation Stage M-110.1.” [Online]. Available: https://www.physikinstrumente.com/en/products/linear-stages-and-actuators/stages-with-motor-screw-drives/m-110-m-111-m-112-compact-micro-translation-stage-701650/. [Accessed: 02-Jan-2017].

[137] “National Instruments Corporation. NI LabVIEW 2010 Service Pack 1 Release Details.” [Online]. Available: http://www.ni.com/labview/release-archive/labview2010SP-1/.

[138] BIPM, IFCC, ISO, and O. IUPAP, “Evaluation of measurement data—guide to the expression of uncertainty in measurement, JCGM 100: 2008 GUM 1995 with minor corrections,” Joint Committee for Guides in Metrology,BIPM, 2008.

[139] J. Coupland, R. Mandal, K. Palodhi, and R. Leach, “Coherence scanning interferometry: linear theory of surface measurement,” Applied optics, vol. 52, no. 16, pp. 3662–3670, 2013.

[140] T. Dresel, G. Häusler, and H. Venzke, “Three-dimensional sensing of rough surfaces by coherence radar,” Applied Optics, vol. 31, no. 7, pp. 919–925, 1992.

[141] R. Windecker, P. Haible, and H. Tiziani, “Fast coherence scanning interferometry for measuring smooth, rough and spherical surfaces,” Journal of modern Optics, vol. 42, no. 10, pp. 2059–2069, 1995.

[142] A. Harasaki, J. Schmit, and J. C. Wyant, “Improved vertical-scanning interferometry,” Applied optics, vol. 39, no. 13, pp. 2107–2115, 2000.

[143] J. C. Wyant, “White light interferometry,” in AeroSense 2002, 2002, pp. 98–107.

[144] E. Sysoev, “White-light interferometer with partial correlogram scanning,” Optoelectronics, Instrumentation and Data Processing, vol. 43, no. 1, pp. 83–89, 2007.

[145] R. Dai, T. Xie, W. Gong, and S. Chang, “A high precision profilometer based on vertical scanning microscopic interferometry,” Journal of Shanghai University (English Edition), vol. 12, pp. 255–260, 2008.

[146] P. de Groot, “Coherence scanning interferometry,” in Optical Measurement of Surface Topography, Springer, 2011, pp. 187–208.

[147] J. N. Petzing, J. M. Coupland, and R. K. Leach, “The measurement of rough surface topography using coherence scanning interferometry,” 2010.

[148] W. Kaplonek and C. Lukianowicz, Coherence correlation interferometry in surface topography measurements. INTECH Open Access Publisher, 2012.

[149] C. Roychoudhuri, “Multiple-Beam Interferometers,” Optical Shop Testing, Third Edition, pp. 219–258, 2007.

[150] G. Seward, “Optical Design of Microscopes,” SPIE Press, 2010.

[151] P. Hariharan, K. G. Larkin, and M. Roy, “The geometric phase: interferometric observations with white light,” 1994.

[152] R.-J. Recknagel and G. Notni, “Analysis of white light interferograms using wavelet methods,” Optics Communications, vol. 148, no. 1, pp. 122–128, 1998.

[153] R. Leach, L. Brown, X. Jiang, R. Blunt, M. Conroy, and D. Mauger, “Guide to the measurement of smooth surface topography using coherence scanning interferometry,” NPL Measurement good practice guide, vol. 108, p. 17, 2008.

[154] F. Gao, R. K. Leach, J. Petzing, and J. M. Coupland, “Surface measurement errors using commercial scanning white light interferometers,” Measurement Science and Technology, vol. 19, no. 1, p. 015303, 2008.

[155] A. Pförtner and J. Schwider, “Dispersion error in white-light Linnik interferometers and its implications for evaluation procedures,” Applied Optics, vol. 40, no. 34, pp. 6223–6228, 2001.

[156] P. de Groot, X. C. de Lega, J. Kramer, and M. Turzhitsky, “Determination of fringe order in white-light interference microscopy,” Applied Optics, vol. 41, no. 22, pp. 4571–4578, 2002.

[157] P. Lehmann, “Systematic effects in coherence peak and phase evaluation of signals obtained with a vertical scanning white-light Mirau interferometer,” in Photonics Europe, 2006, pp. 618811–618811.

[158] P. Lehmann, “Optical versus tactile geometry measurement: alternatives or counterparts,” in Optical Metrology, 2003, pp. 183–196.

[159] W. Ehrig, U. Neuschaefer-Rube, M. Neugebauer, and R. Meeß, “Traceable optical coordinate metrology applications for the micro range,” in IS\&T/SPIE Electronic Imaging, 2009, p. 72390G–72390G.

[160] R. Leach, C. Evans, L. He, A. Davies, A. Henning, C. W. Jones, O. Daniel, and others, “Open questions in surface topography measurement: a roadmap,” Surface Topography: Metrology and Properties, vol. 3, no. 1, p. 013001, 2015.

[161] F. Gao, J. Coupland, and J. Petzing, “V-groove measurements using white light interferometry,” Photon06, Manchester, pp. 4–7, 2006.

[162] C. Evans and J. Bryan, “Compensation for errors introduced by nonzero fringe densities in phase-measuring interferometers,” CIRP Annals-Manufacturing Technology, vol. 42, no. 1, pp. 577–580, 1993.

[163] M. J. Kidger, “Fundamental optical design,” SPIE, 2001.

[164] A. Henning, C. Giusca, A. Forbes, I. Smith, R. Leach, J. Coupland, and R. Mandal, “Correction for lateral distortion in coherence scanning interferometry,” CIRP Annals-Manufacturing Technology, vol. 62, no. 1, pp. 547–550, 2013.

[165] R. Mandal, “Calibration and adjustment of coherence scanning interferometry,” PhD Thesis, Loughborough University 2015.

[166] G. Moschetti, “Development and calibration of wavelength scanning interferometry for surface topography measurement,” PhD thesis, The University of Huddersfield , 2016.

[167] C. Giusca, R. Leach, F. Helery, and T. Gutauskas, “Calibration of the geometrical characteristics of areal surface topography measuring instruments,” in Journal of Physics: Conference Series, 2011, vol. 311, no. 1, p. 012005.

[168] C. L. Giusca, R. K. Leach, F. Helary, T. Gutauskas, and L. Nimishakavi, “Calibration of the scales of areal surface topography-measuring instruments: part 1. Measurement noise and residual flatness,” Measurement Science and Technology, vol. 23, no. 3, p. 035008, 2012.

[169] C. L. Giusca, R. K. Leach, and F. Helery, “Calibration of the scales of areal surface topography measuring instruments: part 2. Amplification, linearity and squareness,” Measurement Science and Technology, vol. 23, no. 6, p. 065005, 2012.

[170] C. L. Giusca and R. K. Leach, “Calibration of the scales of areal surface topography measuring instruments: part 3. Resolution,” Measurement Science and Technology, vol. 24, no. 10, p. 105010, 2013.

[171] R. Leach, C. Giusca, H. Haitjema, C. Evans, and X. Jiang, “Calibration and verification of areal surface texture measuring instruments,” CIRP Annals-Manufacturing Technology, vol. 64, no. 2, pp. 797–813, 2015.

[172] R. Leach, Optical measurement of surface topography, vol. 14. Springer, 2011.

[173] H. Haitjema and M. Morel, “Noise bias removal in profile measurements,” Measurement, vol. 38, no. 1, pp. 21–29, 2005.

[174] M. L. Salit and G. C. Turk, “A drift correction procedure,” Analytical chemistry, vol. 70, no. 15, pp. 3184–3190, 1998.

[175] International Organization for Standardization, “ISO 25178-601 2010Geometrical product specifications (GPS)—surface texture: areal—part 601. Nominal characteristics of contact (stylus) instruments,” 2010.

[176] R. Leach, D. Chetwynd, L. Blunt, J. Haycocks, P. Harris, K. Jackson, S. Oldfield, and S. Reilly, “Recent advances in traceable nanoscale dimension and force metrology in the UK,” Measurement Science and Technology, vol. 17, no. 3, p. 467, 2006.

[177] M. Ritter, T. Dziomba, A. Kranzmann, and L. Koenders, “A landmark-based 3D calibration strategy for SPM,” Measurement Science and Technology, vol. 18, no. 2, p. 404, 2007.

[178] R. K. Leach, C. L. Giusca, and K. Naoi, “Development and characterization of a new instrument for the traceable measurement of areal surface texture,” Measurement Science and Technology, vol. 20, no. 12, p. 125102, 2009.

[179] BIPM, “The international vocabulary of metrology—basic and general concepts and associated terms (VIM), 3rd edn. JCGM 200: 2012,” JCGM (Joint Committee for Guides in Metrology), 2012.

[180] B. Khaleghi, A. Khamis, F. O. Karray, and S. N. Razavi, “Multisensor data fusion: A review of the state-of-the-art,” Information Fusion, vol. 14, no. 1, pp. 28–44, 2013.

[181] J. Wang, R. K. Leach, and X. Jiang, “Review of the mathematical foundations of data fusion techniques in surface metrology,” Surface topography: metrology and properties, vol. 3, no. 2, p. 023001, 2015.

[182] H. Yumoto, H. Mimura, S. Handa, T. Kimura, S. Matsuyama, Y. Sano, H. Ohashi, K. Yamauchi, and T. Ishikawa, “Stitching-angle measurable microscopic-interferometer: Surface-figure metrology tool for hard X-ray nanofocusing mirrors with large curvature,” Nuclear Instruments and Methods in Physics Research Section A: Accelerators, Spectrometers, Detectors and Associated Equipment, vol. 616, no. 2, pp. 203–206, 2010.

[183] Z. Zhao, H. Zhao, F. Gu, H. Du, and K. Li, “Non-null testing for aspheric surfaces using elliptical sub-aperture stitching technique,” Optics express, vol. 22, no. 5, pp. 5512–5521, 2014.

[184] M. Otsubo, K. Okada, and J. Tsujiuchi, “Measurement of large plane surface shapes by connecting small-aperture interferograms,” Optical Engineering, vol. 33, no. 2, pp. 608–613, 1994.

[185] S. Ye, P. Yang, and Y. Peng, “A profile measurement method of large aspheric optical surface based on optimal stitching planning,” Precision Engineering, vol. 45, pp. 90–97, 2016.

[186] S. O’Donohue, P. Murphy, J. Fleig, and G. Devries, “Stitching interferometry for flexible asphere metrology,” in 21st ASPE Annual Meeting, ASPE Proceedings, 2006.

[187] Y. Wen, H. Cheng, H.-Y. Tam, and D. Zhou, “Modified stitching algorithm for annular subaperture stitching interferometry for aspheric surfaces,” Applied optics, vol. 52, no. 23, pp. 5686–5694, 2013.

[188] Z. Xu, S. Li, D. J. Burns, V. Shilpiekandula, H. K. Taylor, S. F. Yoon, K. Youcef-Toumi, I. Reading, Z. Fang, J. Zhao, and others, “Three-dimensional profile stitching based on the fiducial markers for microfluidic devices,” Optics Communications, vol. 282, no. 4, pp. 493–499, 2009.

[189] Y. Chen, “Data fusion for accurate microscopic rough surface metrology,” Ultramicroscopy, vol. 165, pp. 15–25, 2016.

[190] H. Zhao, “Multisensor integration and discrete geometry processing for coordinate metrology,” 2010.

[191] B. M. Colosimo, M. Pacella, and N. Senin, “Multisensor data fusion via Gaussian process models for dimensional and geometric verification,” Precision Engineering, vol. 40, pp. 199–213, 2015.

[192] S. K. Ramasamy and J. Raja, “Performance evaluation of multi-scale data fusion methods for surface metrology domain,” Journal of manufacturing systems, vol. 32, no. 4, pp. 514–522, 2013.

[193] R. K. L. X. J. Jian Wang, “Review of data fusion for surface topography measurement,” NPL REPORT ENG 54, vol. ISSN 1754–2987, 2014.

[194] A. Weckenmann, X. Jiang, K.-D. Sommer, U. Neuschaefer-Rube, J. Seewig, L. Shaw, and T. Estler, “Multisensor data fusion in dimensional metrology,” CIRP Annals-Manufacturing Technology, vol. 58, no. 2, pp. 701–721, 2009.

[195] E. Waltz, J. Llinas, and others, Multisensor data fusion, vol. 685. Artech house Norwood, MA, 1990.

[196] R. Boudjemaa and A. B. Forbes, Parameter estimation methods for data fusion. NPL Report CMSC 38/04.

[197] M. Müller, W. Krüger, and G. Saur, “Robust image registration for fusion,” Information Fusion, vol. 8, no. 4, pp. 347–353, 2007.

[198] S. M. Yamany and A. A. Farag, “Free-form surface registration using surface signatures,” in Computer Vision, 1999. The Proceedings of the Seventh IEEE International Conference on, 1999, vol. 2, pp. 1098–1104.

[199] P. J. Besl and N. D. McKay, “Method for registration of 3-D shapes,” in Robotics-DL tentative, 1992, pp. 586–606.

[200] K.-L. Low, “Linear least-squares optimization for point-to-plane icp surface registration,” Chapel Hill, University of North Carolina, 2004.

[201] Z. Zhang, “Iterative point matching for registration of free-form curves and surfaces,” International journal of computer vision, vol. 13, no. 2, pp. 119–152, 1994.

[202] M. Sjo, B. F. Oreb, and others, “Stitching interferometric measurement data for inspection of large optical components,” Optical Engineering, vol. 41, no. 2, pp. 403–408, 2002.

[203] S. Chen, Y. Dai, S. Li, X. Peng, and J. Wang, “Error reductions for stitching test of large optical flats,” Optics \& Laser Technology, vol. 44, no. 5, pp. 1543–1550, 2012.

[204] Y. J. Fan, K. Struik, P. Mulders, and C. Velzel, “Stitching interferometry for the measurement of aspheric surfaces,” CIRP Annals-Manufacturing Technology, vol. 46, no. 1, pp. 459–462, 1997.

[205] J. Peng, H. Xu, Y. Yu, and M. Chen, “Stitching interferometry for cylindrical optics with large angular aperture,” Measurement Science and Technology, vol. 26, no. 2, p. 025204, 2015.

[206] M. Galovska, R. Tutsch, and O. Jusko, “Data fusion techniques for cylindrical surface measurements,” Advanced Mathematical and Computational Tools in Metrology and Testing IX, vol. 84, p. 179, 2012.

[207] M. Jansen, M. te Voert, and H. Haitjema, “Calibration of CMM reference spheres using stitching interferometry,” in Proc. 10th Int. EuSPEN Conference (Delft), 2010, vol. 1, pp. 79–82.

[208] K.-D. Sommer, O. Kühn, F. P. León, and B. R. Siebert, “A Bayesian approach to information fusion for evaluating the measurement uncertainty,” Robotics and Autonomous Systems, vol. 57, no. 3, pp. 339–344, 2009.

[209] H. Xia, Y. Ding, and B. K. Mallick, “Bayesian hierarchical model for integrating multi-resolution metrology data,” in best student paper competition, INFORMS Conference—Quality, Statistics and Reliability Section, Seattle, WA, 2007.

[210] Z. Weng and P. Djuric, “A bayesian approach to data fusion in sensor networks,” arXiv preprint arXiv:1303.2414, 2013.

[211] P. Kaur and M. Kaur, “A Comparative Study of Various Digital Image Fusion Techniques: A Review,” International Journal of Computer Applications, vol. 114, no. 4, 2015.

[212] Y. Song, M. Li, Q. Li, and L. Sun, “A new wavelet based multi-focus image fusion scheme and its application on optical microscopy,” in 2006 IEEE International Conference on Robotics and Biomimetics, 2006, pp. 401–405.

[213] H. Chen, Y. Liu, and Y. Wang, “A novel image fusion method based on wavelet packet transform,” in Knowledge Acquisition and Modeling Workshop, 2008. KAM Workshop 2008. IEEE International Symposium on, 2008, pp. 462–465.

[214] R. K. Leach, Characterisation of areal surface texture. Springer, 2013.

[215] P.-C. Lin, Y.-C. Chen, C.-M. Lee, and C.-W. Liang, “A subaperture stitching algorithm for aspheric surfaces,” in SPIE Optical Metrology, 2011, p. 80821G–80821G.

[216] F. Pan, X. Lu, B. Dong, X. Ma, and W. Xiao, “Subaperture stitching interferometry based on digital holography,” Optics and Lasers in Engineering, vol. 86, pp. 228–235, 2016.

[217] Y. Dai, S. Chen, S. Li, H. Hu, and Q. Zhang, “Stylus profilometry for steep aspheric surfaces with multisegment stitching,” Optical Engineering, vol. 50, no. 1, pp. 013601–013601, 2011.

[218] P. Murphy, J. Fleig, G. Forbes, D. Miladinovic, G. DeVries, and S. O’Donohue, “Subaperture stitching interferometry for testing mild aspheres,” in SPIE Optics+ Photonics, 2006, p. 62930J–62930J.

[219] “GOM Inspect Software,” 2016. [Online]. Available: http://www.gom.com/3d-software/gom-inspect.html.

[220] “CloudCompare software ver 2.7.” [Online]. Available: http://www.danielgm.net/cc/.

Appendix A

A1: Matlab code for calculation of tilting angle from the reference flat

An example of The Matlab® code to calculate a tilting angle using rotational referencing technique is shown below:

```
clear all
close all

%%%%=========================================================================
%%% load surface measured data of both flats
%%%%=========================================================================

load('S1rot150tilt0flat.mat')
load('S1rot150tilt8flat.mat')

flat00=S1rot150tilt0flat;          %%% this is the reference flat
flattilt=S1rot120tilt8flat;        %%% this is the tilted flat

%%%%=========================================================================
%%% Find angle between both plane
%%%%=========================================================================

%%% (i)find the normal vector of reference flat by determine 3 point

vsph00a=flat00(387380,:);                              %% find 3 point in the
surface
vsph00b=flat00(509861,:);
vsph00c=flat00(4175843,:);

Vnormsph00=cross  (vsph00b-vsph00c,vsph00b-vsph00a);  %%%  calculate  normal
vector

%%%%**************************************************************************
%%% (ii)find the normal vector of tilted flat by determine 3 point

vspha=flattilt (1499711,:);                             %% find 3 point in the
surface
vsphb=flattilt(2037269,:);
vsphc=flattilt(1500686,:);

Vnormsph=cross(vsphb-vspha,vsphb-vsphc);                %% calculate normal
vector

%%% (iii) calculated tilted angle between two plane its normal (unit: degree)

thetabtwnplane=            acosd((dot(Vnormsph,Vnormsph00))/(norm(Vnormsph)*
norm(Vnormsph00)));
```

```
%%%%=============================================================================
%%%Develop matrix rotation using calculated tilted angle
%%%%=============================================================================

M=Vnormsph00; N=Vnormsph;
costheta = dot(M,N)/(norm(M)*norm(N));
checktheta=acosd(costheta); doublecheck=cosd(checktheta);
rotaxis=cross(M,N)/norm(cross(M,N));

c = costheta; s = sqrt(1-c*c); C = 1-c;
x=rotaxis(:,1);y=rotaxis(:,2); z=rotaxis(:,3);
rmat = [ x*x*C+c    x*y*C-z*s  x*z*C+y*s; y*x*C+z*s  y*y*C+c    y*z*C-x*s;
z*x*C-y*s  z*y*C+x*s  z*z*C+c   ];

%% rmat : is the matrix rotation from this calculation and will be use in
further process

%%%%=============================================================================
%%Apply the rotation matrix to the tilt flat to build to ensure the
reliability of the calculation above. new rotated flat is expected to be
parallel to the reference flat
%%%%=============================================================================

sphrotpositiv = flattilt*rmat;


%%%%=============================================================================
%%%% calculated the angle between flat and new rotate flat using their normal
vector. ***(check either the both flat are parallel or not)
%%%%=============================================================================


vsphrota =sphrotpositiv(1499711,:);
vsphrotb=sphrotpositiv (2037269,:);
vsphrotc=sphrotpositiv (1500686,:);

Vnormsphrotptive=cross(vsphrotb-vsphrota,vsphrotb-vsphrotc);

thetabchecktwnplanepositiv=acosd((dot(Vnormsphrotptive,Vnormsph00))/(norm(V
normsphrotptive)* norm(Vnormsph00)));

%%%%=============================================================================
%%%% End of code
%%%%=============================================================================
```

A2: Matlab code for translation of tilted angle and calculation of stitched error at the overlap region

```
clear all
close all

%%%%=========================================================================
%%% load data of measured sphere surface from csi file
%%%%=========================================================================

load('ROTS1_rot0_tilt22.mat')
load('combinesurf__newtechniqS1_rot0_fus_8nm8_0.mat')

sphflat1=
combinesurf__newtechniqS1_rot0_fus_8nm8_0(isfinite(combinesurf__newtechniqS
1_rot0_fus_8nm8_0(:,3)),:);
sphtilt= ROTS1_rot0_tilt22(isfinite(ROTS1_rot0_tilt22(:,3)),:);


% rotatae the spheretilt back to anle betwen flat
%-------------------------------------------------------------------

rotSphere = sphtilt;
sphtiltrot = rotSphere ;
sphflat =sphflat1;

%%%%=========================================================================
% translation in x,y,z direction of the tilt surface
%%%%=========================================================================

translateinx=0;
translateiny=0;
translateinz=0;

ishiftx= sphtiltrot(:,1)+translateinx;
ishifty= sphtiltrot(:,2)+translateiny;
ishiftz= sphtiltrot(:,3)+translateinz;
shiftsphtiltrot=[ishiftx ishifty ishiftz];
rotshiftsphtiltrot= shiftsphtiltrot;

%%%%=========================================================================
%applied f scatter interpolant function to overlap region to find diffence
in z-coordinate between both surface
%%%%=========================================================================

F                                                                          =
scatteredInterpolant(rotshiftsphtiltrot(:,1),rotshiftsphtiltrot(:,2),rotshi
ftsphtiltrot(:,3));
%F can be used to interpolate the data at locations where it was not measured
%F(x,y) will return the data interpolated at (x,y)

ZRotUnrotXY = F(sphflat(:,1),sphflat(:,2));%this give z value location at x
and y of the first data which is flat data sphflat
Zdifference= sphflat(:,3) -ZRotUnrotXY;
zdiffindc=(sum(abs(Zdifference)))/(length(Zdifference))
avZdifference= Zdifference/2;
```

```
zero_ninesphzave=[sphflat(:,1) sphflat(:,2) avZdifference];


%%%%=========================================================================
%%%%              determine non-overlap region for both surface
%%%%=========================================================================

cenflaty=((max(sphflat(:,2))-min(sphflat(:,2)))/2)  +  (min(sphflat(:,2)));
%%%% find centre location x,y of flat surface
cenflatx=((max(sphflat(:,1))-min(sphflat(:,1)))/2) +(min(sphflat(:,1)));

rflaty= max(sphflat(:,2))-cenflaty;  %%% find radiius of x
rflatx= max(sphflat(:,1))-cenflatx;   %%% find radius of y
flatx=sphflat(:,1);
flaty=sphflat(:,2);


centilty=((max(rotshiftsphtiltrot(:,2))-min(rotshiftsphtiltrot(:,2)))/2)  +
(min(rotshiftsphtiltrot(:,2))); %%%% find centre point of tilt surface
centiltx=((max(rotshiftsphtiltrot(:,1))-min(rotshiftsphtiltrot(:,1)))/2)
+(min(rotshiftsphtiltrot(:,1)));
rtilty= max(rotshiftsphtiltrot(:,2))-centilty;
rtiltx= max(rotshiftsphtiltrot(:,1))-centiltx;
tiltx=rotshiftsphtiltrot(:,1);
tilty=rotshiftsphtiltrot(:,2);
%
nonv1=((((tiltx      -cenflatx).^2)+((tilty-cenflaty).^2))>(((rflatx)^2)));
%%%%%formula to find overlap region
sphtiltnonoverlap1=rotshiftsphtiltrot(nonv1,[1,2,3]);


nonv2=((((flatx -centiltx).^2)+((flaty-centilty).^2))>(((rtiltx)^2)));
sphflatnonoverlap2=sphflat(nonv2,[1,2,3]);

%%%%=========================================================================
%%%%%      determine overlap region of common area of both surface  %%%%%%%%
%%%%=========================================================================

over2=((((flatx -centiltx).^2)+((flaty-centilty).^2))<(((rtiltx)^2)));
overlapsphflat=sphflat(over2,[1,2,3]);

ZRotUnrotXYoverlap     =     F(overlapsphflat(:,1),overlapsphflat(:,2));%%%
scaterinterpolant for tilt surface and only overlapregion on sphflat
overZdifference= overlapsphflat(:,3)-ZRotUnrotXYoverlap;
zdiffindcoverlapsurf=(sum(abs(overZdifference)))/(length(overZdifference))

interpolantsurfaceover=[overlapsphflat(:,1)             overlapsphflat(:,2)
ZRotUnrotXYoverlap];

Zaverageoverlap=(overlapsphflat(:,3)+ ZRotUnrotXYoverlap)/2;
comboverlapZav1= [overlapsphflat(:,1) overlapsphflat(:,2) Zaverageoverlap];


%%%%=========================================================================
%%%%     combine all surface overlap and non-overlap      %%%%%%%%%%%%%%%%%%
%%%%=========================================================================

combinesurf__newtechniqS1_rot0_fus_8_22=[sphtiltnonoverlap1;sphflatnonoverl
ap2;comboverlapZav1];
```

```
%%%%=============================================================================
%                                  display surface sphere
%%%%=============================================================================
figure (1);
xnewsphtilt= rotshiftsphtiltrot(:,1);
ynewsphtilt= rotshiftsphtiltrot(:,2);
znewsphtilt= rotshiftsphtiltrot(:,3);
xnewsphtiltlin=linspace(min(xnewsphtilt),max(xnewsphtilt));
ynewsphtiltlin=linspace(min(ynewsphtilt),max(ynewsphtilt));
[Jnewsphtilt,Knewsphtilt]=meshgrid(xnewsphtiltlin,ynewsphtiltlin);
Lnewsphtilt=griddata(xnewsphtilt,ynewsphtilt,znewsphtilt,Jnewsphtilt,Knewsp
htilt,'cubic');
mesh(Jnewsphtilt,Knewsphtilt,Lnewsphtilt)
% surf(Jnewsphtilt,Knewsphtilt,Lnewsphtilt)
xlabel( 'X axis') % x-axis label
ylabel('Y axis')
hold on

%figure;
x00= sphflat(:,1);
y00= sphflat(:,2);
z00= sphflat(:,3);
x00lin=linspace(min(x00),max(x00));
y00lin=linspace(min(y00),max(y00));
[J00,K00]=meshgrid(x00lin,y00lin);
L00=griddata(x00,y00,z00,J00,K00,'cubic');
mesh(J00,K00,L00)
surf(J00,K00,L00)
xlabel( 'X axis') % x-axis label
ylabel('Y axis')
hold on

figure(2);
x001= combinesurf__newtechniqS1_rot0_fus_8_22(:,1);
y001= combinesurf__newtechniqS1_rot0_fus_8_22(:,2);
z001= combinesurf__newtechniqS1_rot0_fus_8_22(:,3);
x001lin=linspace(min(x001),max(x001));
y001lin=linspace(min(y001),max(y001));
[J001,K001]=meshgrid(x001lin,y001lin);
L001=griddata(x001,y001,z001,J001,K001,'cubic');
mesh(J001,K001,L001)
xlabel( 'X axis') % x-axis label
ylabel('Y axis')


figure(4);
x003= sphflatnonoverlap2(:,1);
y003= sphflatnonoverlap2(:,2);
z003= sphflatnonoverlap2(:,3);
x003lin=linspace(min(x003),max(x003));
y003lin=linspace(min(y003),max(y003));
[J003,K003]=meshgrid(x003lin,y003lin);
L003=griddata(x003,y003,z003,J003,K003,'cubic');
mesh(J003,K003,L003)
surf(J003,K003,L003)

%%%%=============================================================================
%%%% End of code
%%%%=============================================================================
```